

Establishing a Process for the Fabrication of High-Quality HTc SQUIDs

P.A. Rottier

Thesis presented in fulfilment of the requirements for the degree of
Master of Engineering at the University of Stellenbosch



Supervisor: Prof. W.J. Perold
December 2002

DECLARATION

I, the undersigned, hereby declare that the work contained in this thesis is my own original work and that I have not previously in its entirety or in part submitted it at any university for a degree.

P.A. Rottier

ABSTRACT

High-temperature (HTc) SQUID magnetometers are used in the biomedical field of magneto-cardiography (MCG). The use of MCG enables a much earlier diagnosis of potentially dangerous conditions than the use of electrocardiography (ECG). For the use of MCG, high-quality HTc SQUIDs are necessary. These SQUIDs can only be realised if the design and fabrication processes are well defined and understood. In this thesis an extensive literature review on the design process explains all the concepts necessary to understand and design a high-quality HTc SQUID. Then the fabrication process is redefined and characterised.

The SQUIDs are fabricated with YBCO thin films on MgO substrates. The relevant steps in the process are the pulsed laser deposition (PLD), UV lithography and argon ion milling. The characterisation of the fabrication process is based on a statistical method called Design of Experiment (DOE). This enables more information to be obtained about the fabrication process than before. For the PLD process the important parameters are determined and an initial optimisation is done. During the characterisation process it is proven that the use of ozone during PLD has a positive effect on the quality of the YBCO thin film. On the PLD apparatus the substrate heater and laser-beam profile is improved. The UV lithography process is analysed and a DOE is proposed for optimisation. A temperature bath is added to the process to enable better reproducibility. An rf multicusp ion mill is built for argon-ion milling, this device is tested and shown to provide the required etching capability.

SINOPSIS

Hoë-temperatuur (HTc) SQUID magnetometers word in die biomediese rigting vir magneto-kardiografie (MKG) gebruik. Met MKG kan 'n mens potensieel gevaarlike toestande heelwat vroeër diagnoseer as wat moontlik is met elektrokardiografie (EKG). HTc SQUIDs van hoë kwaliteit word benodig vir MKG. Sulke SQUIDs kan slegs vervaardig word as die vervaardiging en ontwerpsprosesse goed gedefinieer en verstaan word. In hierdie tesis verduidelik 'n omvattende literatuurstudie oor die ontwerpsproses al die konsepte wat nodig is om 'n SQUID van hoë kwaliteit te verstaan en te ontwerp. Verder word die vervaardigingsproses geherdefinieer en gekarakteriseer.

Die SQUIDs word vervaardig met YBCO-dunfilm op MgO-substrate. Die relevante stappe tydens die vervaardiging is: gepulseerde laser deposisie (PLD), UV-litografie en argon-ioonstraling. Die karakterisering van die vervaardigingsproses is gebaseer op 'n statistiese metode genaamd "Design of Experiment" (DOE). Hierdie metode laat 'n mens toe om meer inligting oor die proses te verkry as wat voorheen moontlik was. Gedurende die karakterisering word bewys dat die gebruik van osoon gedurende die PLD-proses 'n positiewe invloed op die kwaliteit van die YBCO-dunfilm het. Die PLD-apparaat se substraatverwarmer en laserstraalprofiel word verbeter. Die UV-litografieproses word geanaliseer en 'n DOE word voorgestel vir die optimisering daarvan. Daar word 'n temperatuurbad by die proses gevoeg om die herhaalbaarheid te verbeter. 'n "Rf multicusp ion mill" word gebou, die toestel word getoets en daar word aangetoon dat dit die nodige etsvermoë het.

ACKNOWLEDGEMENTS

There are a few people without whom this thesis would not have been possible. To my study leader, Prof. W. J. Perold: thank you for your enthusiasm, for always finding the resources somewhere to allow this research to continue and for all the help with the final graphics included in this document.

To Ulrich Büttner, my fellow researcher and assistant: thank you for all the time and skill you invested in this project, for always being available to repair and rebuild, for your help with the experiments themselves, for all the work you put into the building of the Ar-ion mill and for always having that one more idea.

To Elani Strydom, my friend and companion through it all: thank you for your emotional, spiritual, physical and linguistic support – without you I would not have been able to finish such an enormous piece of work.

Thank you to my family who has been very supportive in many ways; special thanks to my mother, Martie, for all the technical photographs and to my father, Johan, for a lot of essential help and advice, both during the working process and with the final document.

I'd like to thank Pieter de Kock, for his help with the ion mill electronics and the UV lithography; Petrus Pieterse and Dr J.P. Holtzhausen, for their help with and advice on the high-voltage side; Sue van Rensburg and Dorothea van Vuuren, for doing the AFM measurements; Niel Steenkamp, for the SEM measurements and helping us to obtain the old TEM; Prof. R. Pretorius for the use of the PLD chamber.

I'd also like to thank the laser people: Christina Steinmann, Uli Deutschländer and Prof. H. von Bergman. Furthermore I'd like to thank Dr T. von Molte from the University of Pretoria, for the use of their AFM apparatus; Dr D. Boonyawan from Chain Mai University, for the designs of the ion mill as well as his advice on getting it to work; and the people at iTemba Labs: Chris Theron, Carl Springhorn and especially Tshepo Ntsoane, for the X-ray diffraction measurements.

I would also like to thank the NRF and Mushroom Biomedical systems for making this research possible through their funding .

And finally and most important: thank you to my Lord and God, Jesus Christ, for everything.

Contents

1	Introduction	8
2	Superconductivity - a brief introduction	10
2.1	A brief history of Superconductivity	10
2.1.1	Low-temperature superconductivity	10
2.1.2	High-temperature superconductivity	11
2.2	Fundamental considerations	11
2.2.1	The Meissner effect	12
2.2.2	The Two-Fluid model	12
2.2.3	The London equations	13
2.2.4	The Macroscopic Quantum Model	14
2.2.5	The BCS theory	15
2.2.6	Type I and II superconductivity	16
2.2.7	High-temperature superconductors	17
2.3	Summary	17
3	The theory of Josephson junctions	19
3.1	Josephson Junction structure and types	19
3.2	Junction theory	19

<i>CONTENTS</i>	2
3.2.1 Tunnelling junctions	20
3.2.2 High transition temperature junctions	25
3.3 Junction properties and fabrication	32
3.3.1 Bicrystal Junction	32
3.3.2 Step-edge Junction	32
3.3.3 Noise in junctions	36
3.3.4 Interface engineered junctions	37
3.3.5 The improvement of Josephson junctions	37
3.4 Summary	39
4 SQUIDS	40
4.1 Basic theory	40
4.1.1 The dc SQUID	40
4.1.2 The rf SQUID	41
4.2 The physical structure of a SQUID	41
4.2.1 Pickup loops	42
4.2.2 rf SQUIDS	46
4.2.3 dc SQUID	47
4.2.4 Alternative SQUID arrangements	47
4.3 Modelling	48
4.3.1 The RSJ model revisited	49
4.3.2 Equivalent circuit models	51
4.3.3 Other useful equations	52
4.4 Parameter extraction	52

<i>CONTENTS</i>	3
4.4.1 dc SQUIDs	52
4.4.2 rf SQUIDs	53
4.5 Reducing SQUID Noise	54
4.5.1 Narrow linewidths	55
4.5.2 Flux Dams	56
4.5.3 Other physical noise prevention measures	57
4.5.4 Electronic noise reduction by modulation schemes	58
4.5.5 Typical noise values	59
4.6 Electronic Compensation	59
4.6.1 Series and parallel configurations	59
4.6.2 Vector reference SQUIDs	61
4.7 Readout Electronics	63
4.7.1 Additional Positive Feedback Scheme (APF)	64
4.7.2 rf Bias current reversal	65
4.8 Improving SQUID performance	69
4.8.1 Ion-beam etching	69
4.8.2 SQUID Baseline	70
4.9 Summary	72
5 Biomagnetism - theory and application	74
5.1 Biomagnetic Measurements	74
5.1.1 Magnetoencephalanography (MEG)	74
5.1.2 Magnetocardiography (MCG)	77
5.1.3 Magnetoneurography	78

<i>CONTENTS</i>	4
5.1.4 Gastroenterology	78
5.1.5 Magnetopneumography	79
5.1.6 Liver iron susceptometry	79
5.1.7 Conclusion	79
5.2 High-temperature SQUID implementation	80
5.3 Summary	81
6 The Fabrication process	82
6.1 The deposition of YBCO thin films	82
6.1.1 The PLD process	83
6.1.2 Improvements to the PLD process	89
6.2 Photolithography	92
6.3 Etching	93
6.3.1 Wet Etching	93
6.3.2 Ar-ion milling	94
6.4 Summary	96
7 Design of Experiment	99
7.1 Motivation	99
7.1.1 Terminology	99
7.1.2 Comparison of experimental design with the previously used method	100
7.2 Designing experiments	101
7.2.1 Basic concepts	101
7.2.2 Statistical foundation	101
7.2.3 The design process	102

<i>CONTENTS</i>	5
7.3 Factorial designs	104
7.3.1 The 2^k factorial design	104
7.3.2 Fractional factorial designs	105
7.3.3 Taguchi method	107
7.4 Analysis	108
7.4.1 The analysis of variance (ANOVA)	108
7.4.2 Models	109
7.5 Summary	113
8 Characterisation of the manufacturing process	114
8.1 The PLD process	114
8.1.1 The PLD setup	114
8.1.2 Improvements to the system	115
8.1.3 Experimental setup	118
8.1.4 Design of Experiment for the PLD process	118
8.2 The patterning process	127
8.3 The etching process	130
8.3.1 Principles of ion milling	130
8.3.2 Ion-mill design	131
9 Improvements to existing SQUID designs	136
9.1 Requirements	136
9.2 Evaluation of previous designs	137
9.2.1 Pickup loop design	137
9.2.2 SQUID loop design	138
9.2.3 Simulation	138
9.3 Possible alternatives	138

<i>CONTENTS</i>	6
10 Experimental Results	140
10.1 PLD results	140
10.1.1 The experiment, parameters and responses	140
10.1.2 Results	141
10.1.3 Analysis of the results	141
10.2 Patterning results	145
10.3 Etching results	148
11 Conclusions	168
11.1 The Literature review	169
11.1.1 Josephson junctions and SQUIDs	169
11.1.2 Biomedical applications of SQUIDs	170
11.2 Design of experiment	170
11.3 The PLD process	170
11.3.1 The improvements	170
11.3.2 The application of DOE	171
11.3.3 Dealing with equipment failures	171
11.3.4 Measurements conditions	171
11.3.5 Parameter interactions	172
11.3.6 Optimisation with fractional-factorial experiments	172
11.3.7 Treatment of other noise sources.	173
11.4 The development of the ion mill	173
11.5 Final remarks	174

<i>CONTENTS</i>	7
12 The way forward	175
12.1 Finalising the fabrication process	175
12.1.1 Optimising the PLD process	175
12.1.2 Robust design of the PLD process	176
12.1.3 Monitoring and improving the PLD process	177
12.1.4 Characterisation of the UV lithography and Ar-ion milling process	177
12.2 New developments and research	178
12.2.1 Electron-beam lithography	178
12.2.2 Future research proposals	179
A PLD deposition instructions	192
A.1 Preperation Procedure for YBCO thin film Deposition	192
A.2 Depostion Procedure for YBCO thin film deposition	193
A.3 Post deposition annealing procedure.	194
B Taguchi method	196
C DOE for the PLD process	199
D DOE for the UV Lithography process	203
E Design of rf multicusp ion mill	204

Chapter 1

Introduction

In this thesis the successful development, re-definition and characterisation of a fabrication process for high-temperature SQUIDs are described. A comprehensive literature review on Josephson junctions, SQUIDs and the biomedical application of SQUIDs are presented, introducing recent research and findings. Some of these results have not yet been included in any textbooks. The rest of the thesis focuses on the fabrication of high-temperature YBCO SQUIDs, especially the, up to now poorly characterised, pulsed laser deposition (PLD) process. This includes an extensive literature study on SQUID fabrication. This is followed by an introduction to experimental design and the technique used to characterise and optimise the PLD process. Then the actual characterisation process is described followed by the results and the analysis of the results. In this last section a description of the manufacturing and testing of an rf multicusp ion mill are also presented. This information and the practical achievements serve to develop and enhance the capacity for superconducting research at Stellenbosch University as well as adding to the field of academic knowledge.

The University of Stellenbosch has been involved in superconducting research since 1989 and with high-temperature superconductors since 1997. Most of the research were done in the field of superconducting digital logic, with a smaller amount of research on high-temperature superconductors. Although relatively little work has been done on high-temperature superconductors, the facilities for the fabrication seemed to exist. Some effort has also been put in to optimise these facilities [26, 25, 128].

One of the possible application areas of SQUID technology in the biomedical field is magnetocardiography. In the South African context magnetocardiography would be extremely useful, both for research and emergency medical treatment. In chapter 5 it will be shown that the magnetocardiogram have many advantages over the traditional electrocardiogram and that the high-temperature SQUID is a good candidate for the measurement of magnetic heart signals.

With this in mind the thesis started out as a study into the biomedical applications of SQUID sensors, with the aim to develop a SQUID magnetocardiograph. However, it turned out that the work already

done at the University of Stellenbosch on the fabrication of high-temperature superconductors has been insufficient for establishing the capability to routinely fabricate high-temperature SQUIDs.

Therefore this thesis establishes a foundation for the development of SQUID magnetocardiography sensors. This foundation consists of a knowledge base of SQUID technology, a well-characterised fabrication process and the necessary education of technical staff to obtain competence and institutionalised knowledge.

The knowledge base was established through an extensive literature study on all the aspects of the design and fabrication of a SQUID capable of detecting biomedical signals from the heart. This knowledge is presented in this document as background, as well as a foundation on which further (PhD) research can be based.

The redefinition, enhancement and characterisation of the fabrication process constitute the bulk of the practical work done in this thesis. An experimental design approach was used. This experimental design approach maximises the amount of data gathered per experiment during the characterisation process. It also gives a good indication of the reliability of the results. This experimental design methodology is established for the characterisation of processes and the initial results are given, confirming the success of this methodology.

The education of the technical staff was a continuous process. Although not specifically discussed, this is considered one of the important contributions of this thesis.

This thesis will have the following structure. Firstly, a brief account of the basics of superconductivity is presented. This is followed by the theory of Josephson junctions and SQUIDs. The theory includes the basic design considerations as well as the different types of junctions and SQUIDs. Then biomagnetism, its theory, its application and the specific use of SQUID magnetometers in this area will be given. This is followed by a description of the work done to establish the fabrication process. This work includes the characterisation and modification of the PLD process and the characterisation of the photolithography process. The building, testing and characterisation of an argon-ion (Ar-ion) mill will also be described. Then an evaluation of the existing SQUID designs will follow. Finally the results and conclusions will be presented. The thesis ends with suggestions for future research projects.

Chapter 2

Superconductivity - a brief introduction

This chapter is a brief introduction to the field of superconductivity, consisting of a brief history followed by the fundamental concepts of superconductivity.

2.1 A brief history of Superconductivity

Superconductivity is a very young field as its development was determined by the development of cryogenic technology. Therefore with the advent of the liquefaction of helium came the discovery of the first superconductors.

2.1.1 Low-temperature superconductivity

Superconductivity was discovered in 1911 by Heike Onnes, the same person that first succeeded in liquefying helium. He found that mercury loses all resistance at 4.2K [2]. This was followed by the discovery of a multitude of other metallic elements and alloys. At this time, however, any practical applications of superconductivity were impossible, because these superconductors lost all their superconductivity in a very low magnetic field.

In 1933, Walter Meissner and Robert Ochsenfeld discovered that magnetic flux is expelled from a superconductor. Later this was called the Meissner effect [3]. This effect was the first evidence that superconductivity was fundamentally a magnetic phenomenon. Their discovery was followed by the London phenomenological theories of superconductivity, the work of the London brothers Heinz and Fritz London, published in March 1935 [4]. The Gorter-Casimir “two-fluid model” was also developed during this period [1, pp 7]. The London brothers were also the first to realise that superconductivity is in essence a macroscopic quantum mechanical phenomenon.

Next came the development of the BCS theory in 1957, named after the researchers Bardeen, Cooper and Schrieffer. This was a microscopic theory describing the behaviour of superconductors under all circumstances. Their breakthrough came through realising that electron pairing occurred in the ground state. This phenomenon was later known as "Cooper pairs" [5].

On the more practical side, Alexei Abrisokov proposed in 1952 the separation of superconductors into two types. Type I superconductors were the pure metal superconductors and Type II the metal alloy superconductors. Type II superconductors were the first practically usable superconductors, because they allowed much higher field strengths and their associated currents than Type I superconductors. The first high magnetic field superconductive alloy was developed by Bernd T. Matthias and Ted Geballe. It was a tin niobium alloy and in 1960 Eugene Kunzler and his associates tested this material up to a field of 88 kG [1, pp 14-15].

Also in 1960, Ivar Giaever discovered single-electron tunnelling through an isolating barrier [6]. This was followed by the theory of Brian Josephson in 1962. His theory predicted that a dc current would flow through an isolating barrier with no applied voltage. He also predicted that an oscillating current would flow when a small dc voltage is applied across the barrier [7].

2.1.2 High-temperature superconductivity

The age of high-transition-temperature (HTc) superconductors commenced in April 1986 with a report by Alex Müller and Georg Bednorz on superconductivity in lanthanum-barium-copper-oxide at 30K [8]. The discovery of the familiar yttrium-barium-copper-oxide (YBCO) was made by the Wu-Ashburn-Torng team in 1987 [9]. In the years that followed various other substances were discovered, including thallium and bismuth compounds. Thallium provides very stable superconductors below 125 K and bismuth is an extremely suitable compound for superconducting wires and other large-scale applications [1, pp. 30-37].

Despite the success of these high-temperature superconductors the BCS-theory (dealt with in section 2.2.5) does not apply in the same way that it does to low-temperature superconductors. At present there is no accurate theoretical description for the superconductivity in high-temperature superconductors.

2.2 Fundamental considerations

The discussion in this section will be limited to low-temperature superconductors. However most of the macroscopic principles apply to high-temperature superconductors as well.

2.2.1 The Meissner effect

All superconductors have zero dc resistance and pronounced diamagnetic properties below a transition temperature T_c . This phase transition point is determined by the temperature as well as the size of the magnetic field perpendicular to the surface of the superconductor. For every superconductor there is a critical magnetic field H_c , with an associated current density J_c , that will destroy the superconducting properties if either is exceeded. When in a superconducting state, all magnetic flux are expelled from a superconductor and the internal static electric field is zero. This property distinguishes superconductivity from a phenomenon such as negligible resistance in a normal metal. To distinguish these two we will first consider the case of a normal metal with negligible resistance and then a true superconductor.

Consider a conducting cylinder with its long axis parallel to the magnetic field. Faradays' law,

$$\Delta \times \mathbf{E} = -\frac{\partial \mathbf{B}}{\partial t} \quad (2.1)$$

describes the relationship between the applied vector magnetic field \mathbf{B} and the resulting electric field vector \mathbf{E} . From the relationship

$$\mathbf{J} = \sigma \mathbf{E} \quad (2.2)$$

where \mathbf{J} is the vector current density, it can be seen that an infinite conductivity σ would require that the electric field $\mathbf{E} = 0$. This would lead to

$$\frac{\partial \mathbf{B}}{\partial t} = 0. \quad (2.3)$$

This means that the magnetic induction inside the perfect conductor cannot change. Any magnetic flux present inside the conductor at the time of its resistance becoming negligible would thus be trapped [1, pp. 42-45].

Superconductors are different – they expel the flux (as long as the magnetic flux is smaller than the critical flux H_c) when entering the superconducting state. The superconducting behaviour can still be described by Maxwell's equations, but with an important addition, covered in section 2.2.3.

2.2.2 The Two-Fluid model

The current transport in the superconducting state is the result of the flow of a combination of paired electrons and unpaired electrons. As the temperature of the superconductor falls below T_c the ordinary electrons “condense” into superconducting pairs (also see section 2.2.5).

For temperatures above 0 K only a part of the electrons participate in the superconducting behaviour. As the temperature approaches 0 K however, the number of unpaired normal electrons dwindle as more and more of the electrons go into pairing mode. At 0K all the electrons are in the paired state.

The density of normal electrons compared to superconducting electrons is expressed as

$$n_s = n_0 \left\{ 1 - \left(\frac{T}{T_c} \right)^4 \right\} \quad (2.4)$$

where n_s is the superelectron density and n_0 is the normal electron density. T is the temperature for values of $T \leq T_c$, with T_c the critical/transition temperature [10, pp. 94-97].

2.2.3 The London equations

In accordance with the two-fluid model, the total current flowing in the superconductor is the sum of the normal and superconducting components and is written as

$$\mathbf{J} = \mathbf{J}_s + \mathbf{J}_n. \quad (2.5)$$

The normal electron current \mathbf{J}_n obey Ohm's law (2.2). The supercurrent \mathbf{J}_s on the other hand is described by the first London equation (2.10). This equation is derived below.

Consider an electron with mass m and charge q in the presence of an applied electric field \mathbf{E} . Newton's law combined with Lorentz's equation state that

$$\mathbf{F} = m \frac{d\mathbf{v}}{dt} = q\mathbf{E} \quad (2.6)$$

where \mathbf{F} is the force on the electron and \mathbf{v} is the electron velocity. The current density \mathbf{J} is $nq\mathbf{v}$, where n is the number of electrons. Thus, in (2.6)

$$\frac{d\mathbf{v}}{dt} = \frac{1}{nq} \left(\frac{d\mathbf{J}}{dt} \right) = \frac{q}{m} \mathbf{E} \quad (2.7)$$

which gives

$$q\mathbf{E} = \frac{m}{nq} \frac{d\mathbf{J}}{dt} \quad (2.8)$$

and finally

$$\frac{d\mathbf{J}}{dt} = \left(\frac{n(q)^2}{m} \right) \mathbf{E} = \left(\frac{1}{\Lambda} \right) \mathbf{E} \quad (2.9)$$

where $\Lambda = \frac{m}{n(q)^2}$. From this the equation known as the first London equation can be written as

$$\mathbf{E} = \frac{\partial}{\partial t}(\Lambda \mathbf{J}) \quad (2.10)$$

where $\mathbf{J} \equiv \mathbf{J}_s$, the supercurrent density in equation 2.5

The second London equation stems from the Meissner effect discussed in section 2.2.1. From Maxwell's equations the following relationship can be derived:

$$\left(\frac{1}{\lambda^2} + \nabla^2\right) \frac{\partial \mathbf{B}}{\partial t} = 0 \quad (2.11)$$

with $\lambda = \sqrt{\frac{\Lambda}{\mu_0}}$ (the London penetration depth), where μ_0 is the permeability of free space [10, pp. 60]. The London brothers postulated that, for a superconductor, this should be changed to

$$\left(\frac{1}{\lambda^2} + \nabla^2\right) \mathbf{B} = 0 \quad (2.12)$$

where the time derivative of the magnetic flux density $\frac{\partial \mathbf{B}}{\partial t}$ is replaced by the magnetic flux density \mathbf{B} to allow for the expulsion of flux, which (2.11) didn't allow. Working backward from this equation we find that

$$\nabla \times (\Lambda \mathbf{J}) = -\mathbf{B} \quad (2.13)$$

[10, pp. 79-80].

2.2.4 The Macroscopic Quantum Model

“Superconductivity is an inherently quantum mechanical phenomenon that manifests itself on macroscopic scales”, according to Fritz London [10, p. 219]. This important realisation made it possible to derive the London equations treated in the previous section. It is also largely this fact that accounts for the strange behaviour observed in superconducting materials.

The macroscopic quantum model is based on the coherent phenomenon between superelectrons which enables all carriers to be described by a single macroscopic wavefunction

$$\Psi(\mathbf{r}, t) = \sqrt{n^*(\mathbf{r}, t)} e^{i\theta(\mathbf{r}, t)}. \quad (2.14)$$

Using this equation, the entire ensemble, when subjected to an electromagnetic field, can be described using an equation similar to Schrödinger's equation for a single particle. This allows the macroscopic

supercurrent to be expressed as

$$\Lambda \mathbf{J}_s = - \left(\mathbf{A}(\mathbf{r}, t) - \frac{\hbar}{q^*} \nabla \theta(\mathbf{r}, t) \right) \quad (2.15)$$

where q^* is the superelectron charge and $\theta(\mathbf{r}, t)$ is a real function representing the phase of the macroscopic wave function. $\mathbf{A}(\mathbf{r}, t)$ is the magnetic vector potential from Gauss's magnetic law and $\Lambda \equiv \frac{m^*}{n^*(q^*)^2}$ is the isotropic London coefficient. The time derivative of equation 2.15 yields the first London equation as

$$\frac{\partial}{\partial t}(\Lambda \mathbf{J}_s) = \mathbf{E} - \frac{1}{n^* q^*} \nabla \left(\frac{1}{2} \Lambda \mathbf{J}_s^2 \right). \quad (2.16)$$

This equation includes the effects of the magnetic field created by the motion of carriers. Taking the curl of equation 2.15, we find the second London equation (equation 2.13).

The final important result from the macroscopic quantum model is that of flux quantisation. This is found by integrating the supercurrent equation 2.15 around a closed path:

$$\oint_C (\Lambda \mathbf{J}_s) \cdot d\mathbf{l} + \int_S \mathbf{B} \cdot d\mathbf{s} = n \Phi_0. \quad (2.17)$$

Equation 2.17 proves that the magnetic flux in a closed superconducting loop can only change by integer multiples of a flux quantum Φ_0 , where $\Phi_0 = \frac{h}{2e}$.

2.2.5 The BCS theory

The BCS theory was the first theory that was able to predict the behaviour of low-temperature superconductors under all circumstances. When the temperature falls low enough, the electrons move into a ground state where they form so-called Cooper pairs or superelectrons. This is called the extraordinary ground state.

The Cooper pairs have twice the mass of normal electrons and consist of two electrons with opposite spin and momentum. This means that the net spin and momentum of these pairs are zero. Therefore they tend to move in exactly the same way. This explains why all the electrons can be described by a single wave function and why the electrons never experience scattering or resistance. To reduce the momentum of a single Cooper pair the momentum of all the other pairs need to be reduced simultaneously.

Cooper pairs are formed because, in the ground state, the electrons experience an attractive force instead of a repulsive one. As the free-moving electrons move in the crystal lattice, the positively charged atoms cause a localised attraction between an electron and the atoms. This causes a temporary net-positive charge in that area, which attracts the other electron of the Cooper pair to its partner.

Not all electrons in a superconductor form Cooper pairs. Electrons with enough energy to raise into the next state are not bound into Cooper pairs. This is consistent with the predictions of the two-fluid model (section 2.2.2).

A certain amount of energy is needed to break the bond of a Cooper pair and raise the electrons into the next energy state. In the BCS theory, this energy is described as the energy gap Δ . The BCS energy gap exists only in superconducting materials and not in normal metals. The smaller the energy gap, the lower the critical temperature of the material, since it can only become superconducting once thermal agitation does not raise the electrons to an excited state.

Temperature, however, is only one of the three limiting factors determining whether a material is superconducting or not. The other two factors that could raise the electron energy high enough are applied magnetic flux H_c and current density J_c .

The idea of a Cooper pair introduces another parameter called the coherence length ξ . This determines the range of coherence between the electrons, i.e. the mean distance between electrons in a Cooper pair. This parameter was first introduced by the Ginzburg-Landau theory and can be expressed as

$$\xi(T) \equiv \xi_{GL} = 0.74\xi_0 \sqrt{\frac{1}{1 - \frac{T}{T_c}}} \quad (2.18)$$

where ξ_0 is the coherence length in a pure metal at 0 K. The coherence length is dependent on the mean free path of the electrons. This changes with the amount of impurities in the metal [25, pp. 15-17].

2.2.6 Type I and II superconductivity

As mentioned in section 2.1.1 there are two distinct types of superconductivity.

Type I superconductors are always pure metals with perfect diamagnetic properties, but easily quenched in magnetic fields below 1000 G. Since currents generate magnetic fields, this also implies a low current-carrying ability. The exact amount of magnetic flux that would cause the superconductor to normalise is determined by how far the temperature is below the T_c . Type I superconductivity is characterised by an abrupt change from non-superconducting above T_c to superconducting with total diamagnetism below T_c . There is a single critical magnetic field H_c . As long as these conditions apply there is no dc resistance inside the material and no internal magnetic field (except in certain special circumstances) in an applied magnetic field.

Type II superconductors allow flux to penetrate the superconductor in the form of an internal array of normal state flux tubes. These tubes are called “vortices”, because they are surrounded by a circulating supercurrent. This frees the energy that is used in Type I superconductors to expel the

magnetic flux and enables much higher levels of applied magnetic flux and also higher current density. Type II superconductivity shows a more gradual change in magnetic properties and three regions can be distinguished: H_{c1} , H_{c2} and H_{c3} . For the magnetic field smaller than H_{c1} , the material is in a perfect diamagnetic state and all the flux are expelled. In the range $H_{c1} \rightarrow H_{c2}$ the material is in a mixed state, the resistance is still zero but the internal magnetic field is nonzero and penetrates the material in the form of flux vortices. This phenomena has important implications for the noise performance and the critical current of superconductors (see section 3.3.3). When a superconductor is cooled in a magnetic field, field lines normal to the surface can become trapped in vortex tubes, which have the ability to move around in the superconductor. Therefore it is very important to stabilise these tubes. In the range $H_{c2} \rightarrow H_{c3}$ a superconducting sheet remains on the surface of the superconductor [1, pp. 45-46,79-82].

2.2.7 High-temperature superconductors

According to the theory of low-temperature superconductivity, the maximum temperature of superconductors is about 30 K, but this was proved invalid by the discovery of high-temperature superconductivity.

Most high-temperature superconductors are copper-oxide perovskites. As mentioned above, high-temperature superconductivity cannot be described by conventional superconducting theory, although most of the macroscopic relationships apply.

Most of the work in this thesis will deal with high-temperature superconductors, especially with YBCO. Yttrium-Barium-Copper-Oxide is one of the most common high-temperature superconductors and is most commonly used in the manufacturing of high-temperature SQUIDs.

The superconducting properties of YBCO depend strongly on the oxygen content. The molecular structure of $\text{YBa}_2\text{Cu}_3\text{O}_{7-\delta}$ is either orthorombic (for $\delta < 0.6$) or tetragonal (for $0.6 < \delta < 1.0$). In the tetragonal state YBCO is not superconducting. In order to obtain superconducting YBCO thin films of a high quality a lot of care must be taken in the production process. The manufacturing of the thin films will be discussed in Chapter 6 and the various factors influencing the quality of the thin film in section 6.1.

2.3 Summary

In this chapter we briefly covered the basic principles of superconductivity. The most important equations are those of the London brothers and the macroscopic quantum model. These will be used in the next chapter to analyse the behaviour of Josephson junctions.

CHAPTER 2. SUPERCONDUCTIVITY - A BRIEF INTRODUCTION

18

For more information on the topics discussed in this chapter, the books by Orlando et al [10] and Doss [1] can be consulted.

Chapter 3

The theory of Josephson junctions

The Josephson effect is responsible for most of the applications of superconductors as we know it today. A SQUID consists of one or more Josephson junctions connected in a superconducting loop. In this chapter the various types of Josephson junctions will be discussed. This will be followed by a discussion of the tunnelling junction, this type of junction is the easiest to analyse and provides a good understanding of the junction phenomenon. Then a closer look will be taken at high-temperature Josephson junctions. Although the tunnelling junction theory predicts the behaviour of these junctions to a certain extent, there are still many discrepancies. The different high-temperature junctions and their fabrication will also be discussed, followed by a comparison of their properties.

3.1 Josephson Junction structure and types

Low-temperature Josephson junctions can be divided into two main types: tunnelling junctions and proximity junctions, also called weak links. The tunnelling junction is formed by a Superconductor-Insulator-Superconductor (SIS) junction. The weak link is formed by various methods, like Superconductor-Normal-Superconductor (SNS) junctions, point contacts and microbridges, to name just a few [25, pp. 31]. In high-temperature superconductors there are uncertainty as to the type of junction (see section 3.2.2 for more detail).

3.2 Junction theory

The tunnelling junction's name stems from the fact that the electrons tunnel coherently through the insulating layer separating the two superconductors. In weak links, the Cooper pairs move through the barrier region by the proximity effect. The effect of both types of conduction can be described by the

same basic equations, see section 3.2.1.1. The main difference as far as application is concerned, lies in the capacitance of the junctions. Because it is considered more intuitive, the tunnelling junction will be used to explain the Josephson effect.

3.2.1 Tunnelling junctions

A tunnelling junction consists of two superconductors separated by a thin isolating layer. In figure 3.1 the basic tunnelling junction is shown. Tunnelling occurs when the separate wave functions of the Cooper pairs penetrate the junction to such an extent that they interact. This is called coupling. When the coupling energy of the wave functions rises above the thermal activation energy, the phases of wave functions become locked. Consequently Cooper pairs can pass from one conductor to the other without energy loss. Unlike normal electron tunnelling, there is no excitation involved – it can even occur without a voltage applied across the junction. When a voltage is applied to the junction, the pairs can still tunnel. The phases are not locked together, however, but slip relative to each other at a constant rate determined by the applied voltage [11, pp. 159].

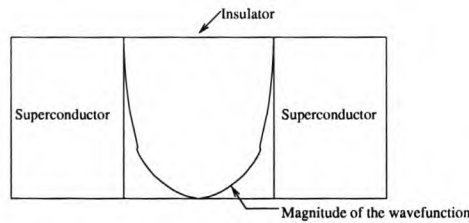


Figure 3.1: A basic superconductor-insulator-superconductor (SIS) tunnelling junction

In the following sections the mathematical equations for this tunnelling will be described. Then the behaviour of these junctions in certain circumstances will be predicted.

3.2.1.1 The basic Josephson junction

The behaviour of the so-called lumped junction can be obtained by assuming that the current density is uniform and restricted to be lower than the Josephson critical current. It is assumed that the temperature is low enough that all the current is carried by Cooper pairs.

The equations for the macroscopic quantum model are

$$\mathbf{J}_s(\mathbf{r}, t) = -\frac{1}{\Lambda} \left[\mathbf{A}(\mathbf{r}, t) + \frac{\Phi_0}{2\pi} \nabla\theta(\mathbf{r}, t) \right] \quad (3.1)$$

and

$$\frac{\partial}{\partial t} \theta(\mathbf{r}, t) = -\frac{1}{\hbar} \left[\frac{\Lambda \mathbf{J}_s^2}{2n^*} + \mathbf{q}^* \phi(\mathbf{r}, t) \right] \quad (3.2)$$

where equation 3.1 is the supercurrent equation describing the current density of the superelectrons in a single piece of material. In this equation \mathbf{A} is the magnetic vector potential and θ is the phase of the quantum mechanical waveform. The energy-phase relationship (3.2) shows how the phase of the wavefunction changes in time and how this change is influenced by the energy of the superelectrons. Here ϕ is the scalar electric potential (for the derivation see [10, pp. 219-239]).

These equations enable us to relate the current density of the current through the Josephson junction, to the magnetic and electric fields across the junction. This relationship can be expressed as

$$\mathbf{J}_s(\mathbf{r}, t) = \mathbf{J}_c(y, z, t) \sin \varphi(y, z, t), \quad (3.3)$$

where \mathbf{J}_s is the current density as a function of position and time. The critical current density \mathbf{J}_c can be expressed as

$$\mathbf{J}_c = \frac{e\hbar\sqrt{n_1 n_2}}{2m\zeta \sinh(\frac{2a}{\zeta})}, \quad (3.4)$$

where \hbar is the reduced Planck's constant, n_1 and n_2 is the electron density on the two sides of the insulator and a is the thickness of the insulator. ζ is known as the decay length and is a property of the insulator. This is something different than ξ , the coherence length of the superconductor. The factor φ is known as the gauge invariant phase difference and is given by

$$\varphi(y, z, t) = \theta_1(y, z, t) - \theta_2(y, z, t) - \frac{2\pi}{\Phi_0} \int_1^2 \mathbf{A}(\mathbf{r}, t) \cdot d\mathbf{l}, \quad (3.5)$$

where θ_1 and θ_2 are the phases of the quantum mechanical wave function on the different sides of the insulator. The voltage-phase relationship is

$$\frac{\partial \varphi(y, z, t)}{\partial t} = \frac{2\pi}{\Phi_0} \int_1^2 \mathbf{E}(\mathbf{r}, t) \cdot d\mathbf{l}, \quad (3.6)$$

where \mathbf{E} is the electric field across the insulator.

The relationship for the lumped basic Josephson junction can be derived as follows:

By integrating (3.3) for a uniform current density, the current-phase relation is found to be

$$i = I_c \sin \varphi(t). \quad (3.7)$$

The gauge invariant phase difference is still given by (3.5). The voltage-phase relation can be obtained by noting that $\int_1^2 \mathbf{E}(\mathbf{r}, t) \cdot d\mathbf{l}$ in equation 3.6 is simply the voltage across the junction. Therefore equation 3.6 becomes

$$\frac{d\varphi}{dt} = \frac{2\pi}{\Phi_0} v \quad (3.8)$$

[10, pp. 398-406].

This model can be extended to the short Josephson junction by allowing the current density and gauge invariant phase difference to vary. The short junction can be modelled as two Josephson junctions that are a very small distance apart and connected by a superconductor on both sides. This gives an analysis similar to that of a SQUID (see section 4). From this analysis and the assumption that the self-field from the currents is negligible, the total current through the junction is expressed as

$$i(\Phi_J, \varphi(0)) = I_c \frac{\sin \frac{\pi \Phi_J}{\Phi_0}}{\frac{\pi \Phi_J}{\Phi_0}} \sin(\varphi(0)), \quad (3.9)$$

for a constant J_c over the area of the junction. Here $\Phi_J = \mathbf{B}_0 h_{eff} d$ is the flux through the junction and $I_c = J_c w d$ is the maximum critical current through the junction. The maximum supercurrent that can be put through the junction is a function of $\varphi(0)$ and occurs when $\sin \varphi(0) = \pm 1$. This can be expressed as

$$i_{max}(\Phi_J) = I_c \left| \frac{\sin \frac{\pi \Phi_J}{\Phi_0}}{\frac{\pi \Phi_J}{\Phi_0}} \right|. \quad (3.10)$$

and is shown in figure 3.2. This modulation of the maximum current is a typical phenomenon for high-temperature Josephson junctions because they usually have relatively large junction areas.

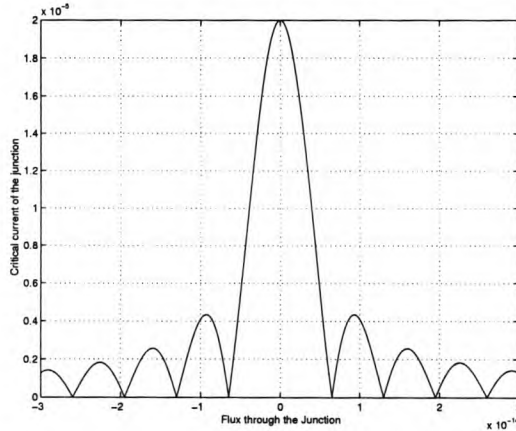


Figure 3.2: $i_{max}(\Phi_J)$ for a Josephson junction with $I_c = 20\mu\text{A}$.

The modulation can be understood by examining the plot of $J_s(z)$ for the Josephson junction (see figure 3.3). As the external flux density is increased from zero, the phase $\varphi(z)$ varies linearly with the size of Φ_J according to the relationship

$$\varphi(z) = \frac{2\pi \Phi_J}{\Phi_0} \frac{z}{d} + \varphi(0) \quad (3.11)$$

where d is the width of the junction [10, pp 420-426]. The supercurrent J_s varies with $\sin \varphi(z, t)$. Thus, as the applied flux increases, the supercurrent is modulated in space with a sinusoidal function

of increasing frequency. This causes flux vortices to appear in the junction. The vortices consist of circulating currents. These Josephson vortices are the cause of the interference pattern seen in figure 3.2. They are also the cause of noise, especially in high-temperature superconductors.

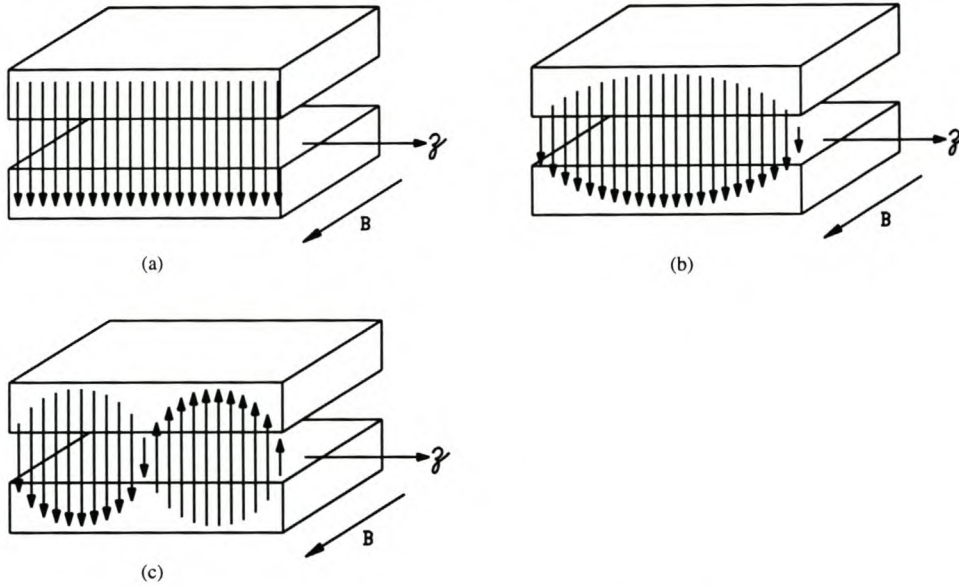


Figure 3.3: The current density distribution for $i_{max}(\Phi_J)$ for a single short Josephson junction [10, p. 425] (a) $\Phi_J = 0$ (b) $\Phi_J = 1/2\Phi_0$ (c) $\Phi_J = \Phi_0$.

3.2.1.2 Junction Resistance and Capacitance

Even at 0 K there are normal electrons due to the breaking up of Cooper pairs by the applied voltage. At temperatures above 0 K normal electrons exist in accordance with the two fluid model. In order to accurately model the behaviour of a Josephson junction, the tunneling of the normal electron needs to be addressed as well. This tunneling is modelled by allowing for two additional channels to conduct the excess current: the capacitive and conductive channel.

The first channel is capacitive because of the parallel structure of the junction. The insulator is seen as an ideal insulator with a permittivity ϵ . In the second channel conduction takes place through tunnelling of normal electrons through the perfect insulator [10, pp. 450].

For tunnelling junctions the capacitance can be found through the normal parallel plate formula

$$C = \frac{\epsilon_0 \epsilon_\mu A}{d} \quad (3.12)$$

[11, pp. 193]. The conductance is represented by a piecewise-linear model

$$G(v) = \begin{cases} \frac{1}{R_{sg}(T)} & \text{if } |v| < 2\Delta(T)/e \\ \frac{1}{R_n} & \text{otherwise} \end{cases}, \quad (3.13)$$

where $G(v)$ is the conductance as a function of voltage. The sub-gap resistance $R_{sg}(T)$ gives the resistances for temperatures greater than 0 K. The exact resistance is a function of the ratio of normal electrons to Cooper pairs. The condition for this region is that the absolute voltage should be lower than the sub-gap voltage $\frac{2\Delta(T)}{e}$. If the voltage is higher, the conductance can be modelled by a resistance R_n . R_n can be found from the so called $I_c R_n$ product. This product is constant for each Josephson junction and is determined by

$$I_c R_n = \frac{\pi \Delta_0}{2e} \quad (3.14)$$

where $\frac{2\Delta_0}{e}$ is the steady-state voltage when the current is slightly greater than I_c at 0 K [10, pp. 453-456].

For other (non-tunnelling) junction types the situation is more complicated. For metal barrier and coplanar junctions the capacitance is very small compared to the conductance. Although the conduction of metal barrier and coplanar junctions have different mechanisms, they are usually modelled by a constant conductance [11, pp. 192-195].

If we assume that the conduction is constant, we can simply replace $G(v)$ with $\frac{1}{R}$. This is called the resistively shunted junction (RSJ) model, the RSJ model is one of the most common models used for the analysis of junction. If the conduction is assumed non-constant, as mentioned in the above, the model is called the non-linear resistively shunted junction (NRSJ) model. Figure 3.4 shows both these models. If we implement the RSJ model, we find the second-order differential equation for the current through the junction as

$$i = I_c \sin \varphi + \frac{1}{R} \frac{\Phi_0}{2\pi} \frac{d\varphi}{dt} + C \frac{\Phi_0}{2\pi} \frac{d^2\varphi}{dt^2}. \quad (3.15)$$

This equation will be used in the next section to evaluate the responses of the Josephson junction to DC and AC driving sources.

3.2.1.3 Response to various sources

The response of a Josephson junction to various driving sources will now be considered. In this section only the basic arguments and the results will be presented. For a more complete discussion see Orlando et al [10, pp. 458-470].

Response to a dc driving source The model in (3.15) driven with a DC current source can be written as

$$\frac{i}{I_c} = \sin \varphi + \frac{d\varphi}{d\tau} + \beta_c \frac{d^2\varphi}{d\tau^2} \quad (3.16)$$

where

$$\tau = \frac{t}{\tau_J} \quad (3.17)$$

$$\tau_J = \frac{\Phi_0}{2\pi I_c R} \quad (3.18)$$

and

$$\beta_c = \frac{RC}{\tau_J} = \frac{\tau_{RC}}{\tau_J}. \quad (3.19)$$

Here β_c is called the Stewart-McCumber parameter. β_c is the ratio of the capacitive time constant to the time constant τ_J , which is associated with the basic Josephson junction. For $\beta_c \ll 1$ and $\beta_c \gg 1$, the equation can be solved; $\beta_c \ll 1$ can be solved in the limiting case of the Josephson time constant determining the behaviour and $\beta_c \gg 1$ can be solved in the limiting case of the capacitive time constant determining the behaviour. The typical behaviour of a SQUID for $\beta_c \ll 1$, $\beta_c \gg 1$ and $\beta_c \approx 1$ is shown in figure 3.5 [10, pp. 458-466].

Response to an ac driving source With an ac driving source the solution for (3.15) becomes more complex and numerical solutions are required.

3.2.2 High transition temperature junctions

In low-temperature superconductors the fabrication of a layered structure like an SNS or SIS junction is reasonably easy. In high-temperature superconductors however, the fabrication of these extrinsic junctions is very difficult. Some of the difficulties are the requirement of a fully epitaxial layer structure, the short coherence length of the Cooper pairs (1-2 nm in the ab-direction and 0.2 nm in the c-axis direction) and the sensitivity of the superconductor to structural and chemical changes.

Because of these difficulties, most of the junctions in high-temperature materials make use of special properties of the material to create intrinsic Josephson junctions. These properties include the intrinsic Josephson effect in the c-axis direction and the existence of grain boundaries which supplies a junction layer.

Because of the complicated nature of these junctions, the detailed transport mechanism has not yet been identified for most Josephson junctions. Furthermore, the transport mechanism can vary strongly within a few lattice constants because of variations in the oxygen content or because of oxygen disorder, strain or chemical reactions. Possible transport mechanisms include direct tunnelling, resonant tunnelling, hopping or diffusion. The type of tunnelling depends on things like the amount of degradation of the material and the length-scale of the degraded region.

Most of the material presented below are based on an extensive literature study done by Gross et al [12].

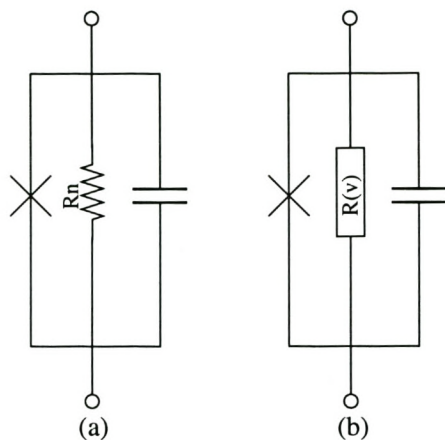


Figure 3.4: The (a) RSJ and (b) NRSJ models

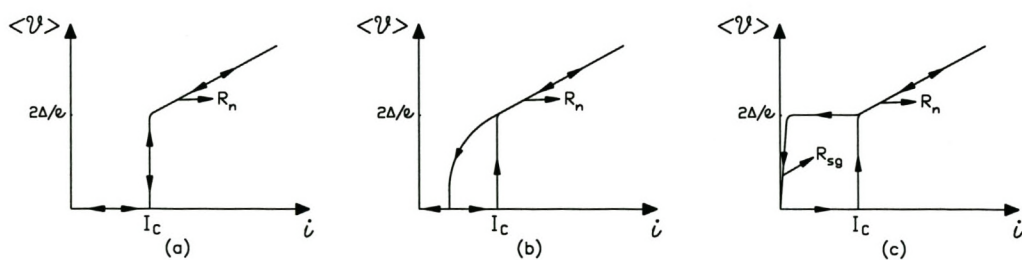


Figure 3.5: Average voltage versus current for a) $\beta_c \ll 1$, b) $\beta_c \gg 1$ and c) $\beta_c \approx 1$.

3.2.2.1 Classification of Junctions

Because of the lack of knowledge of the transport mechanism, it is difficult to divide the high-temperature Josephson junctions into the usual categories of tunnelling junctions, proximity effect coupled junctions or constriction junctions. A better classification of the junctions would be according to the interface. This would divide junctions into three groups: junctions without interfaces, junctions with intrinsic interfaces and junctions with extrinsic interfaces.

Junctions without interfaces These junctions have no well defined interface and the Josephson effect is achieved by weak coupling. Constriction junctions like nano-bridge junctions and weakened structure junctions fall into this category. The weak coupling is achieved through local damage to the junction. This is done through focused electron-beam or ion-beam irradiation. Because of the strong sensitivity of the material to structural changes as well as to oxygen deficiency this irradiation leads to degradation of the superconducting properties in the targeted region. The weak coupling can also be achieved by concentrating the local current sufficiently to destroy the superconducting properties in a certain region. These junctions are based on single-layer technology, therefore they are simple to fabricate. They also have the advantage of no topological constraints as well as a controllable J_c . However the junctions do not yet show long term stability and the $I_c R_n$ products at 77K is still too low for practical application.

Junctions with intrinsic interfaces These are the most common type of high-temperature Josephson junctions and consist of three main types of grain boundary junctions (GBJs): bicrystal junctions, step-edge junctions (SEJ) and epitaxial grain boundary junctions. The weak link behaviour of grain boundaries results from an insulating layer at an oxygen deficient and disordered grain boundary interface with a thickness in the order of a few nanometers. The critical current density is determined by the orientation of grains and the coupling between the grains. This current density is very sensitive to the misorientation angle of the grains.

The bicrystal junction is perhaps the most common GBJ –it consists of a single crystal substrate which is cut at a certain angle after which the edges are then fused back together. The critical current density decays approximately exponentially with an increasing misorientation angle. The $I_c R_n$ products of these junctions are in the order of $400\mu V$ at 77K and the spread of their characteristic parameters is about 10-15% on the same chip.

For step-edge junctions the step edge is manufactured by milling a substrate to create a sharp step before the deposition of YBCO. This step causes one or more grain boundaries across the step which can be used to create a Josephson junction. For step-edge junctions in MgO, it seems that the grain boundaries are mainly regions of disorder, with no oxygen deficiencies. The thickness of these regions increases as the step-edge angle increases. The bicrystal and step-edge junction will be discussed in more detail in section 3.3.

The epitaxial grain boundary junction is asymmetric 45° junctions fabricated by the in-plane rotation of the HTS film by using an extremely thin epitaxial template layer.

Junctions with extrinsic interfaces In these junctions artificial barriers are used. The most common junctions are ramp edge junctions. The fabrication requires advanced multilayer fabrication technology. However, quite uniform junctions have been produced by some researchers [12].

3.2.2.2 Common Properties

Most Josephson junctions that couple along the ab-plane have the following properties:

- $V_c \ll \frac{\pi\Delta_0}{2e}$, typically $V_c < 500 \mu\text{V}$ at 77 K, where V_c is the voltage associated with the Josephson critical current.
- $\beta_c < 1$ – this means most junctions are overdamped with non-hysteretic current-voltage curves.
- The current-voltage curves can usually be modelled by the RCSJ (resistive and capacitively shunted junction) model.
- The temperature dependence of the critical current is almost linear over a wide range of temperatures.
- $V_c \propto (J_c)^p$ where $p \simeq 0.5$.
- The junction shows a large amount of low-frequency $\frac{1}{f}$ noise due to fluctuations in the critical current and the normal resistance.
- $S_R = \left| \frac{\delta R_n}{R_n} \right|^2 \propto R_n$ which means that the normalised fluctuations of the normal resistance scale linearly with the normal resistance.
- The critical current J_c is spatially inhomogeneous on the length scales from a few micrometer down to the nanometer range.

Most of these properties have been proven by different researchers on various types of high-temperature superconducting materials. Properties like the scaling behaviour of $I_c R_n$ are in contrast with the SIS-type junctions where $I_c R_n$ is independent of J_c and equal to $\frac{\pi\Delta_0}{2e}$. The high $\frac{1}{f}$ noise at low frequencies is also a unique property to high-temperature superconductors. It is suggested that this noise is related to the same phenomenon responsible for the $I_c R_n$ behaviour because it shares the same scaling behaviour [12, pp. 2932]. In the next section a model that might explain this behaviour is presented.

3.2.2.3 Transport Mechanism and Models

Most high-temperature Josephson junctions were considered to be proximity effect coupled SNS-type Josephson junctions, because of their low $I_c R_n$ and their overdamped RSJ model-like current voltage curves. However, the phenomenon considered in the previous section cannot be explained by this simple model. Research have shown that only a few junctions fit this simple proximity effect theory [13].

Models have been suggested that include the effect of the finite boundary resistance i.e. the SINS and SINIS models. Constriction-type models like ScNS and SNcNS have also been proposed, where c denotes the constriction. These models are covered by Gross et al [12] and will not be discussed in this section.

A completely different approach is based on the tunnelling type transport mechanism. This model assumes an isolating barrier that contains a large density of localised states. These states force quasi-particle tunnelling to take place through resonant tunnelling. In contrast with this Cooper pairs can only tunnel directly, due to Coulomb repulsion. The resonant channel is viewed as an intrinsic resistive shunt.

This model explains the low values and the scaling behaviour of the $I_c R_n$ product. The trapping and releasing of charge carriers in the localised sites result in a fluctuation of the barrier height and this effects both the critical current I_c and the normal resistance R_n . It also results in increased low-temperature noise. This is exactly what is observed for most high-temperature junctions [12].

To understand how this theory describes the scaling property, the behaviour of bicrystal junctions will be investigated. It was found [105] that $I_c R_n^{1.5} = const$. According to the tunnelling type transport model, the normal current flow has two components; a direct tunnelling current and a resonant tunnelling current. If the direct current dominates, the relationship $I_c R_n^2 = const$ holds; if resonant tunnelling dominates, the relationship is $I_c R_n = const$. The $I_c R_n^{1.5} = const$ serves as evidence that both types of current flow are present. The normal current conduction in this case is given as

$$G_n = G_{do} \exp(-2ad) + G_{ro} \exp(-ad) \quad (3.20)$$

where $1/a$ is the decay length of the wave function, d is the barrier thickness, G_n is the conductance with $G_n = \frac{1}{R_n}$ and G_{do} and G_{ro} are the amplitude of the direct and resonant tunnelling respectively. The superconducting current, however, can be assumed to flow only by direct tunnelling. The critical current can thus be written as

$$I_c = C \exp(-2ad) \quad (3.21)$$

where C is the amplitude of the supercurrent. Substituting equation 3.21 into equation 3.20, we get

$$G_n = \frac{G_{do}}{C} I_c + \frac{G_{ro}}{\sqrt{C}} \sqrt{I_c}. \quad (3.22)$$

This result compares well with the experimental results obtained by Minotani et al [105] for misorientation angles between 24 and 33°. The results for a misorientation angle of 36.8° deviate from this theory; it shows a linear relationship between I_c and G_n which indicates that $I_c R_n = \text{const}$.

3.2.2.4 Determining the normal resistance

There are various parameters associated with Josephson junctions, of which the critical current I_c and normal resistance R_n are probably the most important.

To determine the normal resistance, a method of measurement is needed. It was suggested by Gross et al [93] that, if an RSJ model is assumed, the current voltage characteristics can be fitted to an RSJ model provided that the finite thermal noise current is included in the model. Using the RSJ model an R_n can be chosen to fit the model to the measured curve. In HTc junctions R_n is almost independent of temperature at temperatures between 4.2K and T_c .

The RSJ model can be assumed in most cases, especially for bicrystal junctions. These junctions usually show RSJ-model-like behaviour. A typical example is the results of Minotani et al [104]. These results show good agreement between the measurements on a 30° bicrystal junction and the RSJ model with the excess current I_{ex} , the effect of the strip line resonance (formed by the inductance) included. The inclusion of an excess current means that the junction current I_J is assumed to be $I_J = I_c \sin \phi + I_{ex}$. The excess current I_{ex} is the I-axis intercept of the high voltage portion of the I-V curve extrapolated back to zero voltage [35].

3.2.2.5 RSJ-like behaviour

Although the RSJ model can be frequently used to model the behaviour of an HTc GBJ, there are often large discrepancies between the model and the actual junction behaviour. The magnetic modulation data can be used as a measurement of how well the RSJ model will describe the behaviour of the junction. The magnetic modulation data of a junction is used to determine the relationship between the uniformity of the current flowing through the SNS Josephson junction and the shape of the I-V curve that is measured on the junction. The magnetic modulation data are expressed in terms of a depth-of-modulation curve. The depth of modulation corresponds to the uniformity of the current flowing through the junction. As this current comes closer to a uniform current, the RSJ model becomes a better approximation of the junction.

To see how this is possible consider a uniform current density through a junction. This current will result in a Fraunhofer diffraction pattern for I_c versus \mathbf{B} . The question is whether the inverse, although not theoretically true, could be used to gather some more information about the uniformity of the current in the junction.

From this magnetic modulation data the depth-of-modulation curve is defined as:

$$M = \left[1 - \frac{I_c(\min)}{I_c(\max)} \right] * 100\% \quad (3.23)$$

where $I_c(\min)$ is the first minimum and $I_c(\max)$ is the value of I_c at the central maximum. Theoretically this voltage modulation depth ΔV can also be written as

$$\Delta V = \frac{4}{\pi} \frac{I_c R_n}{1 + \beta} \exp \left[\frac{-3.5\pi^2 k_B T L_s}{\Phi_0^2} \right] \quad (3.24)$$

where $\beta = 2L_s I_c / \Phi_0$ is the inductance parameter, k_B is the Boltzmann constant and Φ_0 is the flux quantum. Perfect RSJ-like curves give 100% modulation. If the modulation factor (3.23) is plotted in relationship to I_{ex}/I_c , which is an indication of the type of curve, there is a 66,5% correlation. If the junctions belonging to the separate samples are separated this correlation increases to 70% and 90% for the separate samples. It is thus clear that there is a direct relationship between how the junctions respond to an external magnetic field and their I-V curve shape. RSJ-like curves show large depth of modulation; flux-flow-like curves show small depth of modulation and this small depth of modulation implies non-uniform current [104].

From these observations the theory was formed that these non-uniform currents are due to micro-shorts across the Josephson junction. It was concluded that RSJ-like curves are associated with a more uniform current flow than flux-flow-like curves.

This research applies to SNS-type junctions, while our research focuses more on step-edge and bicrystal junctions. We believe, however, that the same correlations could be made. This issue needs further investigation. There are other ways, however, of determining the homogeneity of the junction, one of these are discussed in the next section.

3.2.2.6 Measures of junction quality

The field dependence on critical current gives a good indication of the homogeneity of the junction as well as the field stability in SQUID magnetometer applications.

Vaupel et al [67] derived this dependence as a function of junction width for small junctions. The period of field dependence for an ideal vertical Josephson junction can be written as

$$\Delta B_0 = \frac{\Phi_0 t}{2\lambda w}, \quad (3.25)$$

where w is the width of the junction and λ is the penetration depth. In small Josephson junctions w is in the order of and smaller than the Josephson penetration depth λ . Thus equation 3.25 is valid for $w = 2.5 \mu\text{m} \approx \lambda_j$ down to $w = 0.5 \mu\text{m} \ll \lambda_j$, where λ_j is the Josephson penetration depth.

The dependence of the critical current on the applied magnetic field $I_c(B)$ is measured in a magnetic field perpendicular to the film surface. For small junctions $w < \lambda_j$, the graph resembles a Fraunhofer pattern with a period ΔB_0 . For thin films the flux focusing effects due to vortex trapping lead to deviation from the ideal junction. In this case a dependence of

$$\Delta B_0 \approx \frac{(1.9 \pm 0.2)\Phi_0}{w^2} \quad (3.26)$$

was obtained.

For a $10\mu\text{m}$ wide junction the period of the pattern is roughly equivalent to the magnetic field of the earth. This would cause rotation of the junction in the magnetic field of the earth to result in large variation in the critical current of the junction. The smaller the junction width, the better the stability in the earth's magnetic field.

The effects of flux penetration into the junctions and flux trapping are also visible from the Fraunhofer pattern of $I_c(B)$ as shifts and partial suppressions of maxima. These suppressions were observed to occur at external fields where exactly one flux quantum entered the effective junction area.

3.3 Junction properties and fabrication

3.3.1 Bicrystal Junction

As already mentioned bicrystal junctions are fabricated by cutting a single crystal and fusing the edges back together at an angle. These junctions are purchased from specialised suppliers and are available with certain common misorientation angles. The misorientation angle refers to the angle at which the crystal is fused back together. This is one of the important factors in the fabrication of bicrystal junctions. It was found that devices using 30° misorientation bicrystal junctions show better magnetic field noise than devices with 24° junctions, for devices fabricated with the same layout.

This is mainly because the critical current of the 30° junction is approximately half the average value of the 24° junctions, while at the same time having a comparable large $I_c R_n$ product. This is only for bicrystals on SrTiO_3 ; no similar results have been reported for MgO [54, 49].

3.3.2 Step-edge Junction

A step-edge junction is much more complicated to manufacture than a bicrystal junction, but it has the added advantages of freely positionable junctions as well as better control over the critical current of

the Josephson junctions. Step-edge GBJ on MgO are known to provide good control of critical current density. The excess noise levels (measured as critical current fluctuations) of the best MgO step-edge junctions are comparable to (if not better) than that of bicrystal junctions [72, 67]. Step-edge junctions with their tunable junctions also solve one of the biggest problems with dc SQUIDs – the parameter variation between the two Josephson junctions in the SQUID loop. In this section the exact method of fabricating such a step as well as the various parameters influencing the resulting Josephson junction are discussed.

3.3.2.1 Step preparation

rf SQUIDs based on single-layer step-edge Josephson junctions (SEJs) are superior to SQUIDs based on other technologies. This is because of higher flexibility in design and ease of application. However, the problem with this technology is the lack of reproducibility in the fabrication of stable SQUIDs [66, 50].

Below the various parameters that must be considered for an optimal step are presented. The steps are normally prepared using ion-beam etching (IBE). The $\frac{1}{f}$ noise spectra and optimum operating temperature depend strongly on the IBE process used for step preparation. The optimum operating temperature dependence is due to the influence of the step height and step sharpness on the critical current I_c . Firstly the influence of the step angle and the t/h ratio of the step itself will be briefly discussed. The t/h ratio is the ratio of the superconducting film thickness to the height of the step. This will be followed by a discussion on the influence of the various IBE parameters on the step structure.

Dependence on step structure Foley et al [72] did a study on the influence of step angle on junction behaviour. They found step-edge junctions usually have two junctions in series. The exception is step edges with a step-angle of 19° where there is only one clear grain boundary with a tilt boundary along the $\langle 102 \rangle$ crystalline plane. The lower edge of the slope has no observable boundary [71].

It seems that the I_c , R_n and J_c of MgO step-edge GBJs are mainly influenced by the c-axis tilt and in-planar orientation (c-axis rotation) of the step. Three different types of step morphologies were found to be associated with the different step angles (see table 3.1) There are, however, no distinct boundaries

Type	morphology	angle	t(nm)	h(nm)	$J_c(\text{A}/\text{cm}^2)$
a	deep trench	45°	200-350	300-500	2×10^3
b	double junction	32°	200-350	250-400	4×10^4
c	single junction	19°	200-350	300-500	1×10^4

Tabel 3.1: Three different step morphologies and their associated step angles (taken from Foley et al [72, pp. 3185 (Table 1)]).

between these step morphologies, since the morphology of the lower step edge is very sensitive to the orientation of the MgO in the ion beam.

Foley et al [72] found that for $t/h > 0.4$, RSJ behaviour is always observed. They note that the previously reported, strong influence of t/h on J_c is actually a result of the morphology, non-uniformity and the quality of the YBCO film. They found that J_c is only dependent on the step angle. This differs from the results reported by other researchers. For instance, Francke et al [38] reports that for $t/h > 0.85$ the I-V characteristics are flux-flow-like and for $t/h < 0.8$ the characteristics are RSJ-like. The same behaviour was also found by Vaupel et al [67]. They reported that for a $t/h \approx 0.5$ the I-V characteristics show RSJ-like behaviour and as the ratio decreases $t/h < 0.33$, T_c decreases. Flux flow behaviour is observed for $t/h > 0.67$.

A possible reason for this discrepancy might be that both Francke et al [38] and Vaupel et al [67] used SrTiO substrates with Ar-ion etching, and resist edges with angles of 80-85°. Foley et al [72] used different angles and MgO substrates.

Foley et al [72] also found the best junction uniformity is achieved for step heights greater than 300nm. This might be because the grain size of YBCO is in the order of 300nm. It was found that the higher step angles had corresponding higher voltage noise, but that the critical current fluctuations were similar for all junctions. It was also found that the deeper the step, the lower the optimum operating temperature of resulting SQUID gradiometers [66].

Francke et al [38] found that the critical current density also differs for the two ranges, for $t/h > 0.85$ it is 0.10 MA/cm² and for $t/h < 0.8$ it is 0.008MA/cm². The frequency dependence follows a $\left(\frac{1}{f}\right)^{0.5}$ dependence.

Optimal IBE parameters Some of the essential factors to producing low $\frac{1}{f}$ noise devices are: sharp and clean steps, high film quality and reproducibility [37]. Fardmanesh et al [66] investigated the effect of step structure on noise and reproducibility of rf SQUIDs, while Schubert et al [50] proposed an alternative etching procedure that gives much higher reproducibility.

The various approaches and a brief discussion of their results are presented below. Fardmanesh et al [66] prepared substrates with 200nm YBCO on LaAlO and SrTiO using PLD. They used two SQUID structures for the measurements: the magnetometer structure with a 3mm washer diameter and a loop of 150x150 μm^2 (230pH), and the gradiometer structure with a 1.5mm baseline and a loop of 75x75 μm^2 (490pH). The steps for the junctions were prepared with Ar-ion etching. Schubert et al [50] used only LaAlO substrates with a washer-type rf SQUID similar to the one described by Zhang et al [79]. The etching was done through chemical wet etching [80].

The following IBE parameters were used:

Normal incident ion beam: Some substrate material were re-deposited on the side walls of the steps. The thickness of this redeposition was found to be about 90nm and up to a few hundred nanometers in height. This effect was less pronounced on SrTiO substrates than on LaAlO. The redeposition reduces the yield of SQUIDs to less than a few percent and gives SQUIDs with a large spread in noise behaviour in the low- frequency regime. The redeposition also causes high $\frac{1}{f}$ noise in the SQUIDs. The reason for this noise figure is found in a fence of redeposited material grown during the ion-beam etching process which consists of amorphous substrate material [66, 38].

IBE angle of 45⁰: With the substrate rotation the result was clean substrates, with a higher yield and lower $\frac{1}{f}$ noise. But the optimum operating temperature (the temperature which gives the highest signal voltage) of these substrates were higher than 77K due to the higher I_c of the junction. They also found a higher $\frac{1}{f}$ noise. Both effects are due to a curved structure at the trench, caused by the substrate rotation.

Combination of two etching angles: Using two etching angles with different energies, a sharp edge with high yield and low $\frac{1}{f}$ noise was obtained. First a stationary, angled ion beam along the trench with a higher beam energy was used to obtain the desired depth. Then a rotating angled ion beam was used to modify the surfaces of the steps. The flux noise was below $80 \frac{\mu\phi_0}{\sqrt{Hz}}$ for LaAlO and below $60 \frac{\mu\phi_0}{\sqrt{Hz}}$ for SrTiO [66]. Schubert et al [50] confirmed that the best results were obtained through the use of a combination of the two ion-beam etching processes. They also started by forming a trench, using a fixed ion beam which was adjusted parallel to the long edge of the trench. They created a 270 nm deep trench using a fixed Ar-beam with 500 eV beam energy and a current of 0.5 mA/cm². The incident angle of the beam was 40⁰ with respect to the substrate surface. Then they cleaned the edge surface using a rotating substrate with a beam energy of 300 eV, a current density of 0.5 mA/cm² and an angle of incidence of 45⁰. A drastic improvement in the low-frequency noise performance was seen and the noise spread also reduced.

Alternative fabrication technique Up to now the assumed way in which a step is etched in a substrate, is through ion-beam etching. However, there are other options –we briefly touch on one of these options. It is a method developed by Nie et al [39] and it involves a lift-off technique.

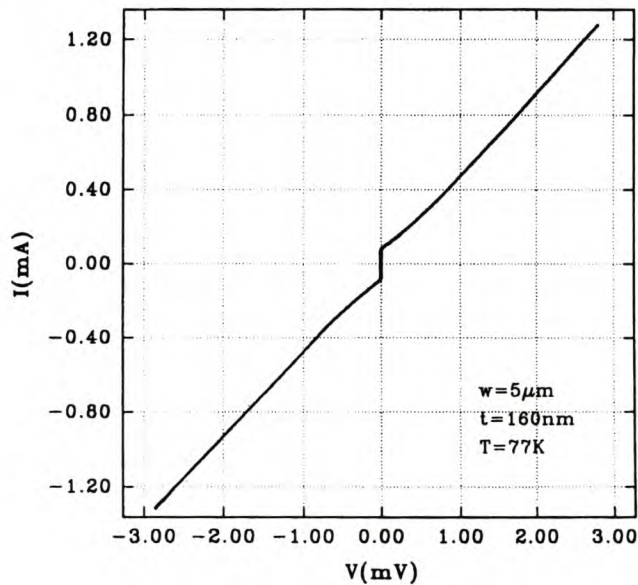
In short, the process consists of dissolving the YBCO film underneath and lifting the top SrTiO₃ film off (in fragments) from half the substrate surface.

In more detail the steps of the process are:

- A layer of YBCO film of 300 nm is deposited on a SrTiO₃ substrate by DC magnetron sputtering.
- Half of the YBCO film is covered with a mask (Shipley AZ 1350 photoresist), the other half is dissolved with dilute phosphoric acid.

- A SrTiO_3 layer is deposited by RF sputtering on the whole substrate. In this experiment the deposition temperature was 760°C and the sputtering atmosphere consisted of 5×10^2 mbar of O_2 and 2.5×10^{-1} mbar of Ar.
- The YBCO film underneath the SrTiO_3 was dissolved by phosphoric acid.
- With this process half of the SrTiO_3 layer could be lifted off, leaving the other half of the SrTiO_3 film stuck to the substrate surface.
- The substrate was covered with YBCO deposited by DC magnetron sputtering.
- Patterning was done by wet etching with dilute phosphoric acid.

The results of the Josephson junctions formed by this process are shown in figure 3.6. The T_c was 89-91 K.



Figur 3.6: I-V characteristics of a step-edge YBCO junction at 77K, where the step was fabricated by the lift-off process [39].

3.3.3 Noise in junctions

According to Fardmanesh et al [66] the temperature-dependent $\frac{1}{f}$ noise can be separated into two categories. The first type of noise is associated with the precipitate density that increases with increasing temperature. This is speculated to be due to increasing flux hopping through the precipitates due to thermal activation. The second type increases with decreasing temperature and is caused by precipitates close to the Josephson junction, both due to the PLD process and due to redeposition caused by normal incident IBE during the patterning of the YBCO.

3.3.4 Interface engineered junctions

One of the challenges in manufacturing high quality SQUIDs is achieving a small spread of junction parameters. A possible solution is to treat the interface in such a way that it creates a natural barrier instead of using an epitaxially-grown barrier layer. Dittmann et al [33] and Horstmann et al [32] used ion-beam etching in a ramp-type junction to damage the interface – this reduced the critical current density. Ramp-type junctions, however, are more suitable for digital circuits. As this type of junction requires a complex multilayer process, it will not be considered in this thesis.

There is, however, a method of creating interface-engineered junctions in a planar arrangement. This is done through scribing by a high-brightness electron source. The electrons are used to selectively damage an area on a microbridge in order to form a junction. However, the only reference found to this method shows that the critical temperature is too low for practical application [92]. It might be useful to investigate the use of this method.

3.3.5 The improvement of Josephson junctions

3.3.5.1 Ozone treatment

Sydow et al [31] found that ozone annealing treatment achieves a greater level of oxygenation in stressed YBCO systems than the level provided by normal O_2 annealing. Both, however, could be used to tune the I_c and R_n parameters of the Josephson junctions.

The process consisted of samples mounted with silver paste to an alloy block that was heated with an enclosed halogen lamp. The chamber was pumped down to 5×10^{-6} Torr and then backfilled to slightly over 1 atm. The ozone was provided by a commercial ozone generator creating an O_2/O_3 mix with ~2% O_3 . Upon cool-down the ozone flow was maintained until the sample was near room temperature.

For grain boundary junction, the ozone annealing increased the I_c from 0.8mA to 1.78mA (at 4.2K) and the R_n was decreased from 1.63 to 0.57 Ω (at 4.2K), decreasing the $I_c R_n$ product from 1.31 to 1.02mV. This is thought to be caused by the fact that the GBJ consists of at least two components; a relatively immutable barrier layer closely associated with the physical grain and regions of deoxygenated YBCO on either side of the grain boundary. The first boundary does not change with increased oxygenation; the second does change, having an impact on I_c and R_n but not the $I_c R_n$ product or the intrinsic RSJ behaviour of the device. The operating temperature is not effected by the ozone annealing. From this it was concluded that the effect of the ozone annealing is to increase the amount of completely oxygenated YBCO material adjacent to grain boundary. Therefore the effective junction area is increased, which increases I_c and decreases R_n while holding $I_c R_n$ constant.

For the interface-engineered junction the effect of the ozone treatment is that the I_c increases from 0.65 to 3.46mA while R_n decreases from 2.32 to 0.45 Ω . $I_c R_n$ remains fairly constant, increasing from 1.51 to 1.56 mV (all at 4.2K). There is an increase in excess current but the RSJ behaviour remains almost unchanged. A slightly higher uniformity of the junction characteristics was also achieved.

3.3.5.2 Trimming by degassing and ion milling

Related to the process of ozone treatment is the process of trimming a Josephson junction in order to get a higher normal resistance, R_n . Since the spectral density of the flux noise should be inversely proportional to R_n , this improves the performance of the junction. Another parameter affected by this trimming is β_L , the SQUID parameter.

Before the trimming process is started the junction is first annealed in an oxygen atmosphere to ensure that it is completely oxygenated (see section 3.3.5.1). When the trimming process start, the junction is heated in an argon atmosphere; this allows diffusion of oxygen out of the junction, thereby lowering the critical current, I_c . This step is repeated until the target critical current I_c is reached.

Due to the scaling law $I_c R_n \propto I_c^q$ the lowering of I_c increases the normal resistance, it also lowers β_L . This can be used to trim R_n to the highest possible value and β_L to its optimal value which is between 0.5 and 1. It was found that during storing the critical current, I_c decreases by ~25%. This should be accounted for when using this optimisation technique.

In step-edge junctions it has been found that ion-beam etching can be used to raise the $I_c R_n$ product. In a step-edge junction the $I_c R_n$ product is determined by the t/h ratio. By thinning the junction, the junction thickness is decreased leading to an increase in the $I_c R_n$ product. It was found that R_n can be increased from 10 Ω (as deposited) to 100 Ω and $I_c R_n$ to 1mV by additional ion milling [67].

3.3.5.3 Substrate re-use

Yu et al [36] investigated the degradation of the bicrystal line in a re-used substrate and the effect this has on the junction quality. They found that the bicrystal line becomes deeper with re-using of the substrate. This causes the $I_c R_n$ product and R_n to drop. They also reported a meandering GBJ line (seen in AFM images) consisting of various irregularly shaped islands. As a consequence of this, a single grain boundary may be considered as junctions in parallel with different crystal orientations. This could lead to inhomogeneous current distributions when current flows across the junction, which results in a non-Fraunhofer-like pattern. This is thought to be due to the interference of currents flowing across the small junctions.

3.4 Summary

In this chapter the basics of the Josephson junction were very briefly discussed (for more on this see Orlando et al [10], as well as Knox-Davies [26] and Conradie [25]). Then we discussed high-temperature Josephson junctions in more detail.

Important things that were mentioned are:

- The depth-of-modulation data can be used to determine how well the RSJ model will approximate the junction.
- The period of the field dependence ΔB_0 determines the magnetic stability of the junction. This is inversely proportional to the square of the width of the junction.
- Step-edge junctions are in many respects preferable to bicrystal junctions as long as they are manufactured correctly.
- The best way of fabricating an SEJ is by using a two-step Ar-ion milling process.
- Ion milling together with ozone treatment can be used to tune junctions to a desired R_n value.

In the next chapter the use of junctions in SQUIDs will be discussed.

Chapter 4

SQUIDS

SQUID is an acronym for Superconducting QUantum Interference Device. It is currently the most sensitive detector of magnetic field available. A SQUID consists of one or more Josephson junctions connected in a superconducting loop. The basic SQUID as described by the RSJ model will be briefly discussed. Then the high-temperature SQUID will be presented, both the theory and practical design aspects.

4.1 Basic theory

4.1.1 The dc SQUID

The dc SQUID consists of two Josephson junctions connected in a superconducting loop. Using the RSJ model and the assumption that the inductance of the SQUID loop is negligible, the current in the loop can be expressed as

$$i = \mathbf{I}_c \sin \varphi + \frac{1}{R} \frac{\Phi_0}{2\pi} \frac{d\varphi}{dt}, \quad (4.1)$$

where

$$\mathbf{I}_c = 2\mathbf{I}_{c1} \cos \left(\frac{\pi \Phi_{ext}}{\Phi_0} \right). \quad (4.2)$$

The average voltage can be expressed as

$$\langle v(t) \rangle = iR \sqrt{1 - \left(\frac{i_{max}}{i} \right)^2}, \quad (4.3)$$

where i_{max} is the maximum amount of current that can be sent through the two basic Josephson junctions in parallel. These formulas are only valid in the case of a negligible inductance. For most SQUIDS used

in practice the inductance L cannot be neglected. The circuit behaviour is then covered by a set of coupled, time dependent nonlinear equations that are usually solved numerically [10, pp. 471-474]. The numerical analysis can be done with simulation programs like WRSPICE [14].

4.1.2 The rf SQUID

The one-junction SQUID consists of a single Josephson junction in a superconducting loop. When analysing the structure we find

$$I = -I_c \sin \left[\frac{2\pi\Phi_{ex}}{\Phi_0} + \beta_L \left(\frac{I}{I_c} \right) \right] \quad (4.4)$$

where Φ_{ex} is the external flux penetrating the superconducting loop and

$$\beta_L = \frac{2\pi LI_c}{\Phi_0}. \quad (4.5)$$

Here L is the inductance of the superconducting loop [11, pp. 256-260].

This one-junction SQUID can be used as an rf-SQUID magnetometer. The magnetometer is formed by coupling the one-junction SQUID to a tuned circuit that is driven by an rf current source (called a tank circuit). As the flux applied to the SQUID is changed, the circulating flux increases until the applied flux reaches $\frac{\Phi_0}{2}$ and then the junction opens to allow one flux quantum to enter the loop. This causes periodic variation of the loading to the tank circuit, which leads to a change in the voltage across the tank circuit. A feedback arrangement is used to determine the amount of flux (see figure 4.1). Using

$$\Phi_1 = \Phi_{ex} - LI_c \sin \frac{2\Phi_1}{\Phi_0}, \quad (4.6)$$

where Φ_1 is the flux inside the loop, the operation of the SQUID can be divided into two different regions. When $\frac{2\pi LI_c}{\Phi_0} > 1$, the device is in the so-called hysteretic mode. As the external flux is varied the output shows hysteretic behaviour. For $\frac{2\pi LI_c}{\Phi_0} < 1$, the device operates in the inductive mode and the output is more linear [11, pp. 280-283]. The inductive mode is preferred for rf-SQUID operation. Usually the critical current I_c is chosen so that $LI_c \approx \Phi_0$. The rf SQUID can also be modelled by the numerical program WRSPICE [14].

4.2 The physical structure of a SQUID

In a SQUID loop the inductance will determine the hysteresis of the loop. The inductance also has an influence on the thermal noise of the SQUID. To keep the inductance low, a SQUID loop should be as

small as possible. In order to have a small sensor loop but a very sensitive sensor, a pickup loop is needed. This loop usually couples inductively with the SQUID loop, although some high-temperature SQUID configurations use a directly coupled pickup loop. Apart from the sensor some readout electronics are also needed. There are various readout schemes but the most commonly used is either a flux-locked loop or a current-locked loop.

The pickup loop can consist of a single loop, in which case the SQUID system is called a magnetometer, but it can also consist of two or more loops where the shielding currents flow in such a way that a magnetic field passing through both coils cancel and only the difference gets amplified (fig 4.2).

High-temperature SQUIDs are limited compared to low-temperature SQUIDs in that it is very difficult to fabricate multilayer devices. We are confined to the use of planar gradiometers since there is no practical HTc wire. This section will start off by describing the coupling of pickup loops to SQUID structures. Then dc and rf SQUIDs will be considered. Finally some of the newer SQUID arrangements will be presented.

4.2.1 Pickup loops

One reason for using pickup loops in SQUID magnetometers is that these devices are usually operated in a static ambient field (like the magnetic field of the earth). Because of the Fraunhofer-like dependence of the critical current on the magnetic field (see figure 3.2), devices fabricated with large SQUID loops tend to suppress the critical current. This can be overcome by reducing the junction dimensions to the sub-micrometer range. A much simpler solution, however, is to use an external pickup loop and reduce the SQUID loop dimensions [99].

There are two types of pickup loops: an integrated multilayer structure with inductive coupling and a single-layer directly coupled magnetometer.

In the directly coupled pickup loop the loop injects the circulating current directly into the SQUID loop. The coupling can be compared to an auto-transformer coupling. The directly coupled magnetometer is simpler and cheaper to manufacture, but has very inefficient coupling to the pickup loop. Thus a larger

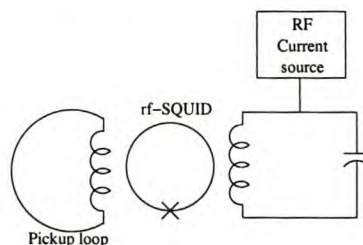


Figure 4.1: Basic configuration of an rf-SQUID magnetometer.

pickup loop as well as low noise SQUIDs are needed for good magnetic sensitivity. By reducing the inductance of the pickup loop, much higher effective areas can be achieved for directly coupled designs. This can be done by fabricating multiple narrow pickup loops in parallel. For example, Dilorio et al [64] used four pickup coils of $100 \mu\text{m}$ each in parallel to reduce the inductance of the pickup coil. In addition, by locating a separate flux dam in series with each pickup loop, the flux penetration and subsequent noise can be limited. This will be discussed in more detail in section 4.5.

4.2.1.1 Flip-chip inductively coupled pickup loops

A variation on the integrated multilayer structure is the flip-chip inductively coupled pickup loop. Here the pick-up loop is patterned on a separate substrate. This pickup loop is bonded to the SQUID with the superconducting layers facing each other and a thin isolating layer in-between. Faley et al [97] showed that this significantly reduces the effective SQUID inductance and provides better inductance matching. In practical terms this means that the inductive coupling provides better flux sensitivity for a given pickup-loop size.

For directly coupled loops the relationship between loop size and flux sensitivity can be approximated by

$$S_{dc} \approx \frac{1}{a}, \quad (4.7)$$

while for flip-chip loops

$$S_{ind} \approx \frac{1}{a^{3/2}} \quad (4.8)$$

where S is the flux sensitivity and a is the loop area in mm^2 .

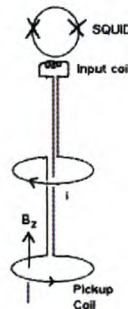


Figure 4.2: The gradiometer configuration for low-temperature SQUIDs.

CHAPTER 4. SQUIDS

4.2.1.2 Pickup loop Hysteresis

For proper sensor design it is important to determine the magnetic field change limits beyond which the pickup-loop response becomes either nonlinear or hysteretic. Vortices are created when type II superconducting materials are cooled below their transition temperature in an external magnetic field. They are also created when the applied field becomes large enough to make their formation energetically favourable.

The concentration of the shielding current at the outer edge of the pickup-loop structure increases the magnetic field strength at the edge, resulting in the nucleation of new vortices (primarily at the edge). The Lorentz force from the current is the strongest on these nearby edge vortices and acts to displace them further into the film [45].

Purpura et al [45] studied this magnetic hysteresis in high- T_c test samples which had various pickup-loop linewidths. They found that the circulating currents induced in the magnetometer pickup loops varied linearly with the applied magnetic field up to a particular threshold value. Beyond this threshold value the field response of the samples became hysteretic. Therefore flux penetration can be measured by magnetic hysteresis [85]. Figure 4.3 shows this hysteresis for various linewidths. For higher values of applied field, the bending at the ends of the hysteresis loops increase.

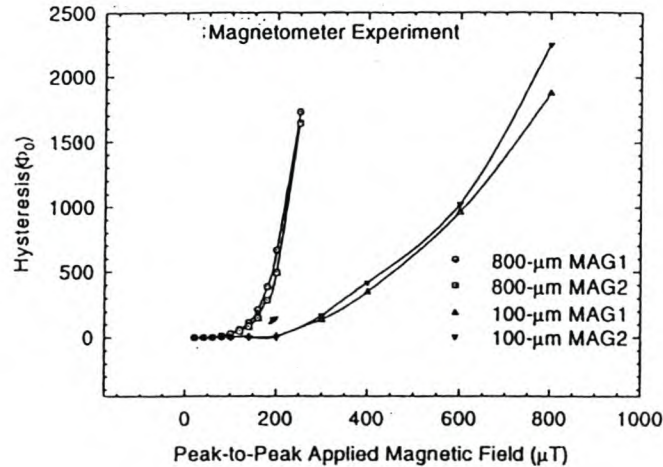


Figure 4.3: Magnetic hysteresis as a function of line width [45].

It is clear from figure 4.3 that the amount of hysteresis depends on the linewidth. It was also found that the flux vortices do not penetrate the pickup loops for linewidths smaller than $4 \mu\text{m}$ (see section 4.5).

4.2.1.3 Second-order Gradiometers

A gradiometer is a device that is only sensitive to local magnetic field and cancels out far and uniform fields.

Most SQUID gradiometers are first-order gradiometers. To realise a second-order gradiometer one usually has to use electronic gradiometry (for more on this see section 4.6).

Lee et al [101], however, considered the design of a second-order hardware gradiometer, using a directly coupled SQUID structure with three loops (see figure 4.4). The right loop and left loop have the same area and inductance. When a uniform field \mathbf{B} is applied to either loop, a shielding current $I = \mathbf{B}A/L$ will flow, coupling a flux Φ_S to the SQUID loop, $\Phi_S = \alpha \mathbf{B}AL_s/L$. For the central loop the only difference will be that the inductance will be L_c instead of L and the fraction of SQUID inductance through which the current flows will be α_c instead of α . Thus, for a uniform field coupled to all three loops the output will be zero if

$$\frac{A_c L}{A L_c} = \frac{2\alpha}{\alpha_c}, \quad (4.9)$$

where α and α_c is the fraction of the loop through which the current flows for the side and center loops respectively. Here the assumption has been made that the left and right loops are identical.

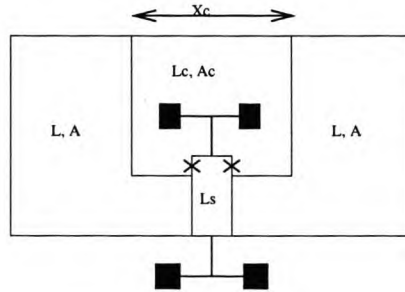


Figure 4.4: Schematic of a directly coupled second-order gradiometer.

In balancing it is easier to design a device with $\alpha_c A_c / L_c$ larger than $2\alpha A / L$ and then trim the centre loop by adjusting a small piece of YBCO placed in the centre loop. Lee et al [101] calculated the sensitivity of their gradiometer to be $\approx 1.3 \times 10^{-9} \text{T/m}^2 / \sqrt{\text{Hz}}$ using the formula

$$\left(\frac{\partial^2 B}{\partial x^2} \right) = \frac{1}{\alpha_c A_c} \frac{L_c \phi_n}{L_s l^2} \frac{1}{1 + \kappa}, \quad (4.10)$$

where l is the distance between the centre of the left and right loops and the centre of the centre loop and ϕ_n is the SQUID noise. $\kappa = \frac{1}{3} \left(1 - \frac{x_c}{l} \right)$, where x_c is the geometric mean width of the centre loop. They implemented this design and found the off-balance to be about 0.6% for a uniform field and 1.4% for a first-order gradient.

4.2.1.4 Alternative flux transformers

If it were possible to shield the SQUID magnetometer from an external magnetic field while just allowing the magnetic field to be measured, a lot of the noise could be eliminated. It is not possible to use a superconducting pickup loop because it not possible to fabricate high- T_c wire at present. It might however be possible to use a copper flux transformer. Firsov et al [100] investigated this possibility and found that the flux transformer does not significantly increase the noise value of the magnetometer itself. They estimated the gradiometer field resolution to be $6 \times 10^{-11} \text{T}/\sqrt{\text{Hz}}$ at 1kHz.

4.2.2 rf SQUIDS

Rf SQUIDS are inductively coupled to the readout electronic using a tank circuit. In this case the tank circuit is a tuned circuit driven by an rf current source. Some of the critical parameters of these circuits are: the pumping frequency f_0 , the quality factor Q and the coupling coefficient k . The requirements are the highest possible f_0 , a high Q and $k^2Q > 1$.

Some of the circuits suggested to achieve these requirements are: $\lambda/2$ resonators, modified microstrip hairpin resonators and coplanar resonators. The $\lambda/2$ resonators have the advantage of high pumping frequencies, but the field resolution is limited due to small SQUID loop areas. The microstrip hairpin resonators solved this by allowing larger SQUID loops. Microstrip structures, however, contribute excess low-frequency noise due to the usage of a metallic ground plane. Coplanar resonators solved this problem by removing the ground plane. Zhang et al [82] investigated the use of coplanar resonators structures.

A typical coplanar resonator is a flip-chip assembly of a single-layer SQUID with a step-edge junction and a single-layer flux concentrator with a resonator. For a 14 mm diameter, it has a field sensitivity of $16 - 20 \text{fT}/\sqrt{\text{Hz}}$ at 1kHz at 77 K, deteriorating to $60 - 80 \text{fT}/\sqrt{\text{Hz}}$ at 1Hz [40]. Figure 4.5 shows a coplanar resonator integrated with a flux concentrator. The resonant frequency of this resonator is between 600 and 850 MHz, depending on the configuration. The frequency is determined by the angle θ ; decreasing the angle increases the frequency. This is a non-linear dependence with a faster decrease for small θ values. The Q for this resonator is between 4000 and 5000 at 77K. Because of the high Q and frequency a matching circuit between the readout electronics and the tank circuit is usually needed.

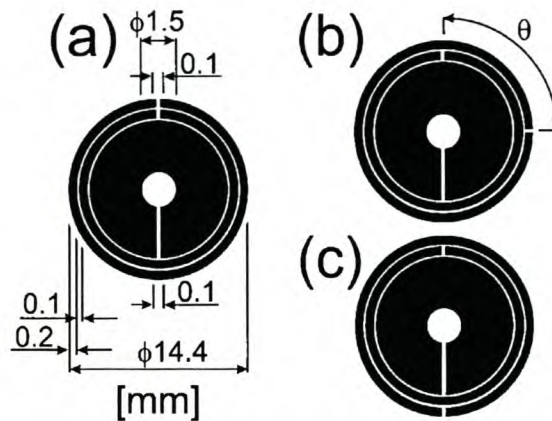


Figure 4.5: Schematic of three flux-concentrator / coplanar-resonator configurations for different resonant frequencies [40].

The SQUID and the resonator were coupled inductively via a flux concentrator (centre loop in figure 4.5). In this case a small diameter (3.5 mm) rf SQUID was used. The coupling coefficient k between the SQUID with the concentrator and the coplanar resonator is given by $k^2 = A_{eff}/A_{t,c}$. Here A_{eff} is the effective area of the SQUID loop and $A_{t,c}$ is the area surrounded by the tank resonator. This coupling is not effected by the variation of θ .

This structure, although much better than the modified hairpin resonator, still shows excess low-frequency noise, which is probably the result of flux hopping in the large concentrator. The flux hopping could be reduced by the use of a higher resonant frequency (with a corresponding smaller focusing area) or by pinning the flux vortices.

4.2.3 dc SQUID

The dc SQUID is the most popular SQUID configuration for low-temperature SQUID electronics. The dc SQUID was discussed in section 4.1.1. As mentioned in section 4.2.1 the pickup loop is usually coupled directly to the dc SQUID. This is also the case for the second-order gradiometer discussed in section 4.4.

The design of the basic dc SQUID has been treated in both the previous theses written at the University of Stellenbosch, in Chapter 9 these designs will be critically analysed.

4.2.4 Alternative SQUID arrangements

Various other SQUID arrangements have also been proposed, for instance the three-junction SQUID proposed by Enpuku et al [88]. An attempt was made by Schultze et al [49] to test and compare some of

these arrangements.

For the three-junction SQUID they found that the voltage swing can be double the size of the two-junction SQUID. However, because the period for one modulation is also doubled, there is no effect on the flux-to-voltage transfer function when the SQUID is used in a directly coupled magnetometer.

Another configuration tested by Shultze et al [49] is that of two dc SQUIDs being connected in series in a directly coupled magnetometer. When both SQUIDs have equal critical currents, the SQUID modulations superimpose. The modulation period remains the same; therefore the flux-to-voltage transfer function is enhanced.

A problem arises when the coupling inductance kL_{SQ} of the two SQUIDs are different. Here k denotes the part of the SQUID inductance L_{SQ} , which carries the screening current from the pickup coil. A difference in the two coupling inductances causes a “beat” in the SQUID modulation. When the difference between the two coupling inductances is smaller than 2%, more than 50 SQUID modulations with a large voltage swing are available. Shultze et al [49] reported that 45% of the 18 SQUIDs they investigated have identical critical currents and show a spread lower than 2% in the coupling inductances. When more than two SQUIDs were tried, it was found that only about three SQUIDs always work together. Apart from the fact that this is just a small improvement on two SQUIDs in series, there is also the problem that an array with more than two SQUIDs can not be used in a directly coupled configuration.

The conclusion Shultze et al [49] reached was that the best configuration is a directly coupled pickup loop with two dc SQUIDs in series. As pickup loop they recommended a washer configuration.

4.3 Modelling

There are various models that can be used for the simulation of SQUID magnetometers. Some of the models stem from material and physical considerations while others are more focused on equivalent circuit models. Since the purpose of this thesis is both research and design, some consideration to both types must be given.

It seems, however, that at present the equivalent circuit models are approaching usefulness while the physical models are still in their infancy. Still even the equivalent models are at the moment more useful for understanding the behaviour of SQUIDs than predicting and designing SQUIDs with required parameters. This is because of a lack of understanding of the influence of parameters during the manufacturing process as well as a lack of understanding of the actual mechanism of high- T_c superconductivity.

4.3.1 The RSJ model revisited

In the original RSJ model of low-temperature SQUIDS the Nyquist noise (thermal noise), originating in the Josephson junction shunt resistance, is treated as a small perturbation in the equations describing the dynamic behaviour of the SQUID. This means that the Josephson coupling energy,

$$E_J = \frac{\Phi_0 I_c}{2\pi} \quad (4.11)$$

is assumed to be larger than the thermal fluctuation energy, given by $T_f = k_B T$. If we define $\Gamma \equiv k_B T / E_J$ as the noise parameter, it means $\Gamma \ll 1$. Furthermore the magnetic energy per flux quantum is assumed to be large compared to T_f . This means $\beta\Gamma \ll 1$, where β is the SQUID parameter. $\beta\Gamma$ can be written as the ratio of the SQUID loop inductance L_s over a fluctuation-threshold inductance L_F where

$$L_F = \frac{(\Phi_0/2\pi)^2}{k_B T}. \quad (4.12)$$

This gives $\beta_{rf}\Gamma = L_s/L_F$ and $\pi\beta_{dc}\Gamma = L_s/L_F$. For low-temperature SQUIDS, L_s must be much smaller than L_F [103].

These assumptions, however, does not apply to high-temperature SQUIDS that are operated at 77 K. At 77 K, L_F is much smaller than at 4.2 K. For HTc SQUIDS $\beta\Gamma \geq 1$ and Γ are close to unity. This is equivalent to a Josephson current being close to the thermal current I_{th} , where

$$I_{th} = \frac{2\pi k_B T}{\Phi_0} \quad (4.13)$$

Typically $I_{th} \approx 3.3\mu\text{A}$ at 77K. It could also be seen as the SQUID inductance L_s being close to the fluctuation-threshold inductance L_F which is typically $L_F \approx 100\text{pH}$ at 77K. For rf SQUIDS with their larger loop holes (for increased magnetic sensitivity) $\Gamma \geq 1$ and $L_s > L_F$ [106].

Therefore in the case of HTc SQUIDS it is more appropriate to use probabilistic equations like the Fokker-Planck equation to describe the behaviour analytically [103]. This approach has been used by Chesca et al [124] to predict the behaviour of rf SQUIDS. This approach gives an exact solution for $\beta_{rf} \ll 1$ and an approximate one for $\beta_{rf} < 3$. These solutions are valid for $\Gamma > 1$. This theory was extended by Greenberg et al [122] and used to determine the I_c , R_n , k and Q_L of the SQUID from the L_s and rf voltage versus frequency characteristics of the SQUID at low pumping power. The results were checked by measurement, deviations in the order of 10% for I_c and 15-25% for R_n was found [103].

Later Chesca et al [123] also solved the equations for the dc SQUID (two-dimensional Fokker-Planck equations), again only for $\beta_{dc} < 1/\pi$ and $\Gamma > 1$. The solution predicts $\beta_{opt} \cong 1/\pi\Gamma$. These restricted ranges severely limit the usefulness of these solutions since the most practical dc SQUIDS have $\Gamma \approx 0.1 - 1$ and $\beta \geq 1$. To address this problem, an approximate first-order solution to these equations was

found by Greenberg et al [107] using a perturbation method. Their approximation is valid for any value of β and Γ as long as $\alpha \geq 1$, where $\alpha = L/L_F$. This is fulfilled as long as $L \geq 100\text{pH}$. They predict the transfer function of a symmetric dc SQUID as

$$\frac{1}{RI_c} \frac{\partial V}{\partial \varphi_X} = e^{(-\alpha/2)} \sin(2\varphi_X) f(i, \Gamma) \quad (4.14)$$

where R is the normal resistance of the Josephson junction, V is the voltage across the SQUID, $i = I_b/I_c$ with I_b the bias current and $\varphi_x = 2\pi\Phi_X/\Phi_0$. The function $f(i, \Gamma)$ can be written as

$$f(i, \Gamma) = 32\pi^3 J_0^3 \Gamma^2 e^{(-\alpha/2)} \sum_n \frac{(-1)^n I_n I_{n+1} \left[A \left[\left(\frac{i}{2}\right)^2 - n(n+1)\Gamma^2 \right] + B \left(\frac{i}{2}\right)^2 (2n+1) \right]}{\left[\left(\frac{i}{2}\right)^2 + n^2\Gamma^2 \right] \left[\left(\frac{i}{2}\right)^2 + (n+1)^2\Gamma^2 \right]} \quad (4.15)$$

where

$$A = \sum_n \frac{(-1)^n n I_n I_{n+1}}{\left(\frac{i}{2}\right)^2 + n^2\Gamma^2}, \quad (4.16)$$

$$B = \sum_n \frac{(-1)^n n I_n I_{n+1}}{\left(\frac{i}{2}\right)^2 + n^2\Gamma^2} \quad (4.17)$$

and

$$(-2\pi J_0)^{-1} = \frac{2I_0}{i} + i \sum_{n=1}^{\infty} \frac{(-1)^n I_n^2}{\left(\frac{i}{2}\right)^2 + n^2\Gamma^2}. \quad (4.18)$$

Here I_n and I_{n+1} are modified Bessel functions of the argument $1/\Gamma$: $I_n(1/\Gamma)$, $I_{n+1}(1/\Gamma)$. The summations are from $n = -\infty$ to $n = \infty$, but it was found that $N=100$ gives sufficient accuracy. For the equations for the asymmetric dc SQUID, the reader can go to the references [107].

Although these equations give a better prediction than most numerical simulations, there are still about 70% percent of measured values that deviate substantially from the theory. However, the allowance this approximation made for asymmetrical current proved that the asymmetrical current is not the reason for the deviation of the measurements from the theory. Still this theory could be used to try and do some predictions as to the expected behaviour of the SQUIDS designed at this University.

Chesca et al [124] also predicted that, when $\Gamma > 1$, the SQUID energy resolution

$$\varepsilon = \frac{S_\Phi}{2L_s} \quad (4.19)$$

is a minimum at $L_s \cong L_F$, where S_Φ is the thermal flux noise

$$S_\Phi = \frac{S_v}{V_\Phi^2}. \quad (4.20)$$

When comparing the prediction for the rf and dc SQUIDS it seems that the rf SQUID should perform

better than the dc SQUID for high $\Gamma > 1$ levels, since the dependence of V_{Φ} on Γ is weaker than that of the dc SQUID. V_{Φ} is the transfer function $\partial V/\partial\Phi$ [103].

4.3.2 Equivalent circuit models

One model that is used for directly coupled dc-SQUID magnetometers is the model developed by Minotani et al [95]. This model is also used by Beyer et al [54] where there is an excellent diagram (figure 4.6) with the model in relation to the physical layout of the SQUID.

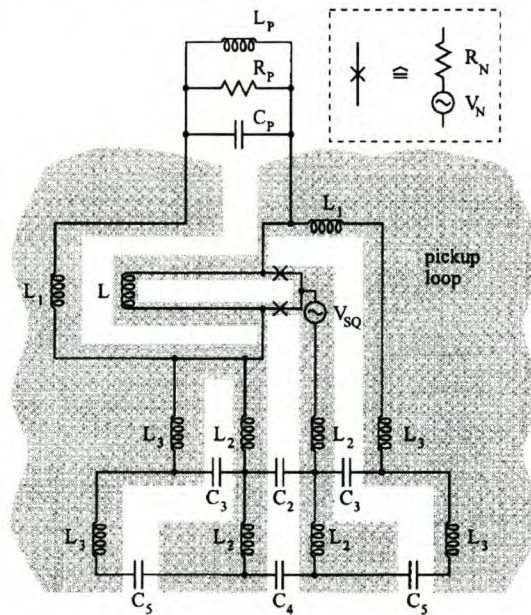


Figure 4.6: The equivalent circuit model of a directly coupled dc SQUID magnetometer with magnetometer layout [54].

The pickup loop is modelled as a parallel $L_p - C_p - R_p$ resonant circuit, where L_p is the pickup loop inductance, C_p is the stray capacitance across the pickup loop and R_p represents the rf losses of the resonant circuit. The voltage source

$$V_{SQ} = \frac{V_{pp}^0}{2} \left\{ 1 - \cos \left(\frac{2\pi\Phi(t)}{\Phi_0} \right) \right\} \quad (4.21)$$

represents the SQUID, where $\Phi(t)$ is the flux threading the SQUID loop and V_{pp}^0 is the peak-to-peak modulation voltage without noise. L is the SQUID inductance, $R_{N1} = R_{N2} = 2R_{SQ}$ are the junction resistances and the junction noise is represented by V_{N1} and V_{N2} . From this circuit the $V - \Phi$ curve can be simulated. For the simulation, R_{SQ} need to be determined experimentally while the inductance and capacitances can be estimated from the circuit layout. Then V_{pp}^0 and R_p remain as fitting parameters, which can only be determined by fitting the simulated curve on the measured curve.

4.3.3 Other useful equations

For the design of SQUID inductance, formulas like those of Jaycox and Ketchen [70] can be used but only for a square washer-type SQUID. The Ketchen formulas are

$$A = 1.1dD \quad \text{and} \quad L = 1.25\mu_0d \quad (4.22)$$

where d and D are the side lengths of the hole and the washer respectively [49].

According to Enpuku et al the voltage transfer function is predicted by the equation

$$V_\phi = \frac{4}{\Phi_0} \frac{I_c R_n}{(1 + \beta_L)} \exp \left[-3.5\pi^2 \frac{k_B T L}{\Phi_0^2} \right]. \quad (4.23)$$

The accuracy of this model was confirmed by Dillman et al [98] on step-edge junctions, they found good agreement between the predictions and the measurements for variation of both the resistance R_n and the SQUID inductance L .

4.4 Parameter extraction

In order to use some of the model described in section 4.3 and in determining the accuracy of some of the models, a way is needed to extract these parameters from the experimental SQUIDS.

According to Enpuku et al [102] the current fluctuations can be determined from the flux noise measurements using the formula

$$S_\Phi(dc) - S_\Phi(ac) = \frac{(LI_0)^2}{2f} \frac{S_{I_0}}{I_0^2}, \quad (4.24)$$

where $S_{I_0}^{1/2}$ is the current fluctuation, L is the SQUID inductance, f is the frequency and I_0 is the critical current. $S_\Phi(dc)$ and $S_\Phi(ac)$ are the flux noise determined with the dc and ac bias methods.

4.4.1 dc SQUIDS

For the dc SQUID the parameters can be extracted using the equivalent circuit model mentioned above or using the formula in equation 4.23. Because measurement can be made directly across the parallel junction pair the method in section 3.2.2 can also be applied to dc SQUIDS.

4.4.2 rf SQUIDS

For rf SQUIDS the extraction of parameters is much more tricky than that of the dc SQUID because of the inductive coupling of the SQUID. Zeng et al [108] introduced the use of SQUID amplitude versus frequency curves (AFCs) and the use of the predictions of Chesca's theory to extract the parameters of $\beta(I_c)$, R_n , k^2 and Q_L .

The rf SQUID together with its flip-chip flux concentrator and coplanar resonator was placed between two single turn-copper coils. The coils were connected to a Network analyser through an attenuator and a pre-amplifier (figure 4.7). It is important to have a high quality factor for the resonator, thus the influence of the antenna coils must be minimised. To achieve this they were very weakly coupled to the resonator. This means that no matching was used.

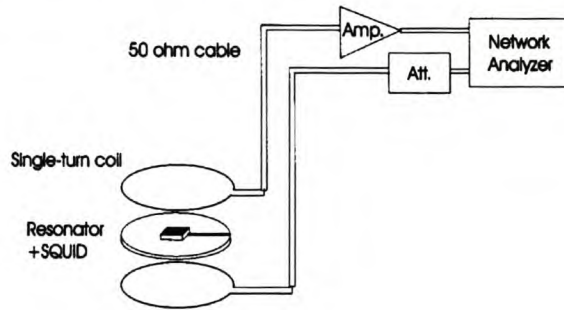


Figure 4.7: Experimental setup for the determination of the amplitude-frequency characteristics of an rf SQUID [108].

Using this setup the two resonant frequencies ω_1 and ω_2 corresponding to an external magnetic flux value of $\Phi_e = n\Phi_0$ and $\Phi_e = (n + 0.5)\Phi_0$ were determined. These two frequencies must be determined very accurately. This means that the rf power bias should approach zero. To achieve this the AFCs were measured with a input power around 1 mW with an attenuation of -95 dB. All measurements must be done in a shielded environment, with a field coil to enable the application of an external field.

An rf SQUID operating in non-hysteretic mode can be seen as a non-linear inductance, with the resonant frequency and the damping rate dependent on the external magnetic flux and the external power level. If the rf power is kept low enough, the external magnetic flux determines the resonant frequencies. This gives two distinct peaks for the two magnetic flux values, situated around the resonator frequency ω_0 . For a SQUID operating in hysteretic mode the two fields have the same resonant values but different amplitudes.

The SQUID parameters can be determined using the formulas

$$\Gamma = x \frac{(1 - x^2)}{\Omega} \left[1 + \frac{\Omega^2}{4(1 - x^2)^2} \right], \quad (4.25)$$

$$k^2 = \frac{\omega_1 - \omega_2}{\omega_0 \beta x} \quad (4.26)$$

and

$$q = \frac{Q_2^{-1} - Q_1^{-1}}{2k^2 \beta x [1 + (g(l) - x(1 - x^2))/\Gamma]} \quad (4.27)$$

where

$$x = \exp\left(\frac{-L_s}{2L_F}\right), \quad (4.28)$$

$$\Omega = \frac{2\omega_0 - \omega_1 - \omega_2}{\omega_1 - \omega_2}, \quad (4.29)$$

$$l = \frac{L_s}{L_F}, \quad (4.30)$$

Q_1 and Q_2 are the loaded quality factors at $n\Phi$ and $(n + 0.5)\Phi$,

$$q = \frac{\omega_0 L_s}{R_n} \quad (4.31)$$

and

$$g(l) = l\left[1 - \frac{1}{2}l + \frac{13}{72}l^2 - \frac{7}{244}l^3 + \frac{31}{3600}l^4 - \frac{1}{1200}l^5 + \frac{1}{35280}l^6\right]. \quad (4.32)$$

Thus with the values of ω_0 , ω_1 , ω_2 , Q_1 and Q_2 , the parameters Γ , β , k , and R_n can be determined. When checked against measured values of these parameters, which were obtained by destroying the loop, good agreement was obtained.

An interesting result from this study was the experimental confirmation that rf SQUIDS remain in non-hysteretic mode until $\beta \approx 3$ which is much higher than $\beta \approx 1$ for low T_C rf SQUIDS.

4.5 Reducing SQUID Noise

The noise in high-temperature SQUIDS is dominated by the uncorrelated motion of thermally activated flux vortices that hop between pinning sites in the SQUID washer, with a wide distribution of time constants, producing a $1/f$ spectrum. This is aggravated by cooling a SQUID in a low magnetic field ($50\mu\text{T}$), and exposing the SQUID to a moderate magnetic field ($100\mu\text{T}$) after cooling.

A changing magnetic field applied to a magnetometer pickup loop will induce a circulating current. This shielding current exerts a Lorentz force that can drive flux vortices into the washer. These vortices lead to the degradation of the low-frequency noise properties of the device and also to a time drift in the magnetometer output [53, 89].

Because SQUIDS are usually operated in high magnetic fields (Earth field) this flux-induced noise is of much concern. For example, the temporary increase of the uniform magnetic field by 1 G for plain

directly coupled SQUIDS (rf or dc) can cause the noise spectral density to increase 10 times at 10Hz. Even after the removal of this field, the noise can take hours to return to its original level [99].

In this section we will discuss various methods to reduce this noise.

4.5.1 Narrow linewidths

One way to eliminate this $\frac{1}{f}$ noise is to design the device with narrow linewidths, so that vortices are not trapped in the washer when cooling in magnetic fields below a certain threshold. Dantsker et al [86] showed that SQUIDS with narrow lines, with linewidths nowhere greater than $4 \mu\text{m}$, display no increase in flux noise at 1Hz when cooled in static fields of up to $100 \mu\text{T}$. Slots and holes in the bodies of SQUID washers also reduce the level of $\frac{1}{f}$ noise, providing that the superconducting thin films are of high quality, especially at the edges. This has been confirmed by quite a number of researchers [43, 49, 45, 44, 51]. This is because the narrow linewidth prevents the flux vortices from penetrating the SQUID washer. Also, in comparison with a solid-washer SQUID, an effective area gain of up to 24% is possible depending on geometry and the number of slots[60].

A directly coupled magnetometer consists of a SQUID connected in parallel to a large-area pickup loop. While noise due to vortex motion in the SQUID itself can be eliminated by using a narrow-linewidth SQUID washer, it is still possible for the pickup loop to cause excess $\frac{1}{f}$ noise in the device.

There are two ways in which the motion of vortices in the pickup loop might couple flux to the SQUID. Firstly, vortex motion might couple flux directly by causing field lines to move into or out of the SQUID washer. Secondly, vortex motion might couple indirectly to the SQUID through screening supercurrents. This indirect contribution of vortex motion in the pickup loop to flux noise in the SQUID can be calculated using

$$S_{\Phi}^{(in)}(f) = 4NS_r(f) \frac{\Phi_0^2 L^2 \alpha_d^2}{L_p^2} \left(\frac{D_p + d_p}{D_p - d_p} \right), \quad (4.33)$$

where N is the number of uncorrelated flux vortices, each with a spectral density $S_r(f)$ for radial motion. D_p and d_p are the outer and inner dimensions of the pickup loop, L_p and L are the inductances of the pickup loop and the SQUID respectively and α_d is the fraction of the SQUID inductance that the current couples to.

For directly coupled loops, the large mismatch between L and L_p means that flux noise contributed by the pickup loop is negligible in most cases. For indirectly coupled loops, however, the better matching causes extra flux noise to couple. This noise can be removed by using the same method used for the SQUID itself. Cho et al [53] repatterned a solid-washer magnetometer to convert the whole area of the pickup loop to a mesh of $4 \mu\text{m}$ wide lines. They determined that the noise remains relatively flat for cooling fields up to $100 \mu\text{T}$. The effective area of this repatterned device is also slightly larger than that of the solid-washer devices.

4.5.2 Flux Dams

There is also the possibility to limit the shielding currents in directly coupled magnetometers by flux dams, so that no flux vortices penetrate the SQUID loop as the ambient field is increased. A flux dam is a weak link or Josephson junction in the pickup loop of the magnetometer. Each flux dam limits the maximum circulating current. Therefore the Lorentz force driving the vortices into the superconducting material is also limited. When the current induced in the pickup coil exceeds a certain value determined by the critical current of the flux dam, the flux dam junction enters the resistive state and damps the circulating current. This protects the SQUID from exposure to large currents. The protection consequently limits $\frac{1}{f}$ noise and longterm drift coming from the vortex entry into the film edges. Low magnetic fields, typically the fields to be measured, do not exceed the current limitations and as such they are not affected by these flux dams [53, 60, 89, 64].

The critical magnetic field that would inject flux quanta into the perimeter of a pickup loop is determined by

$$B_c = \frac{1.17 \times 10^{-6} \sqrt{w}}{R} \left[\frac{(J_c d)^3 \Phi_0}{\mu_0} \right]^{\frac{1}{4}} \log \left(\frac{16R}{w} - 1.75 \right), \quad (4.34)$$

where R is the radius of the pickup loop, w the width, d the thickness and J_c the critical current density. The J_c is typically 10^9 A/m², which is a bit lower than regular J_c values because the critical current density at the edge of the pickup loop is usually smaller than the average value. For most common configurations this equation gives values about ten times less than the earth's magnetic field. Therefore flux quanta will be injected into the films.

The exact choice of critical current for the flux dam depends on the required dynamic range and frequency response of the magnetometer. The current must be much larger than the currents induced in the loop by normal operation of the SQUID. It must also be several times larger than $\frac{\Phi_0}{2M}$, where M is the mutual inductance between the pickup loop and the SQUID.

Another parameter that must be taken into account is the relaxation time of the current in the pickup loop. When there is a change in the magnetic field too sudden or large for the feedback loop (in flux feedback configuration) to track, the junctions will open and allow flux to enter the loop. The time it takes for the circulating current caused by this extra flux to relax back to zero is called the relaxation time. The relaxation time is given by

$$\frac{dI}{dt} = \frac{-V_J}{L_P}, \quad (4.35)$$

where V_J is the voltage across the flux dam junction and L_P is the inductance of the pickup loop. This can be approximated as

$$\frac{dI}{dt} \approx -4 \times 10^{-8} \frac{T}{I_0 t} \text{ (A/s)}, \quad (4.36)$$

where T is the operating temperature and I_0 is the critical current of the pickup loop [89].

Koch et al [89] found that, by using these flux dams, they could operate magnetometers in moderate magnetic fields at performance levels that are competitive to similar-sized devices operated in a zero magnetic field. They verified this for both flux-locked loop and bias current reversing. Ludwig et al [51] used slotting of their 3 mm wide pickup loop into 150 parallel loops of $10\mu\text{m}$ linewidth. Since all these slotted lines have to pass the grain boundary of the bicrystal substrate, they obtained 150 so-called "flux dams". Ludwig et al reported: "devices with slotted pickup loops show significantly improved performance when exposed to a magnetic field comparable with the earth's field. These properties make them attractive for low-noise systems that can be operated in moderately shielded or even unshielded environment." Carr et al [60] suggested the use of flux dams in the SQUID loop as well as an extra $5\mu\text{m}$ loop with flux dams in parallel to the washer-type loop. This configuration had a better noise resistance when cooled in an external magnetic field than both thin ($5\mu\text{m}$) and solid-washer SQUID loops.

4.5.3 Other physical noise prevention measures

Although flux dams can reduce the $\frac{1}{f}$ noise, Cho et al [53] have shown that in a directly coupled pickup loop the flux noise can also be minimised through designing the magnetometer in such a way that it keeps the SQUID far enough (about $100\mu\text{m}$) from any wide films of the pickup loop. They used a design where the SQUID was separated on three sides (by a $120\mu\text{m}$ -wide gap) from the wide film of the pickup loop. They found the noise to be suppressed up to fields of $100\mu\text{T}$. At a $100\mu\text{T}$ field, the $\frac{1}{f}$ noise (at 1Hz) increases again as flux begins to penetrate the $4\mu\text{m}$ washer of the SQUID. Flux dams are not needed, because the large mismatch of the inductances ensures that the flux noise in the pickup loop is so tightly attenuated that it contributes negligibly to the flux noise in the SQUID. For inductively coupled pickup loops, however, flux dams will have to be used.

For their wide gap SQUIDs Cho et al [53] observed an abrupt increase in $\frac{1}{f}$ noise when the cooling field is increased from zero to a few micro-Tesla, after which the noise is more or less unchanged. This unusual dependence on field strength below $100\mu\text{T}$ comes from the tapered outer edges of the magnetometer pickup loop, an artifact of the deposition process. After re-patterning where they removed the thinner material where the substrate had been clipped to leave a sharp edge, this behaviour disappeared. This can be taken one step further: if sub- μm patterning technology is used, the onset of magnetic flux penetration is further increased by one order of magnitude to about $300\mu\text{T}_{pp}$. This effect is due to steeper edges in the superconducting structures which hinder the penetration of flux [87].

A common way to prevent flux noise is to use a heating coil integrated in the SQUID package. This heater is used to heat the SQUID after cooling to remove the trapped flux caused by movement while cooling [60].

4.5.4 Electronic noise reduction by modulation schemes

Once the noise caused by the flux vortices is reduced there is another noise source that starts to dominate. This is noise due to critical current fluctuations in the Josephson junction.

According to Grundler et al [81], there are at least two separate sources of noise in Josephson junctions: current fluctuation noise and the motion of flux lines trapped in the body of the SQUID. Critical current fluctuations is the dominant source of low-frequency noise in high-T_c dc SQUIDs [52].

The voltage noise spectral density can be separated into two different parts. The first is a frequency-dependent contribution that scales with $\frac{1}{f}$ and is most apparent at the lower frequency. The second part is a frequency-independent part called white noise that dominates at higher frequencies. This part can be attributed to the nyquist noise of the effective SQUID resistance.

For Low T_c SQUIDs the following model is used

$$S_{v,f} = \frac{S_{I_{0,f}}}{2} \left[\left(\frac{V}{I_0} - \frac{I\delta V}{I_0\delta I} \right)^2 + \left(L_s \frac{\delta V}{\delta \Phi} \right)^2 \right]. \quad (4.37)$$

This model gives the power spectral density with both the critical currents I_{c1} and I_{c2} assumed to be independent and equal to $S_{I_{0,f}}$. The first term represents the voltage noise coming from “in-phase” critical current fluctuations and the second term represents voltage noise from “out-of-phase” critical current fluctuations. The “out-of-phase” fluctuations lead to flux noise that develop because of circulating currents.

It was found that the use of a flux-locked loop results in the suppression of the “in-phase” noise and the use of the bias current reverse mode suppresses the “out-of-phase” noise contribution (see figure 4.8) [68, 69]. More detail will be given in section 4.7.

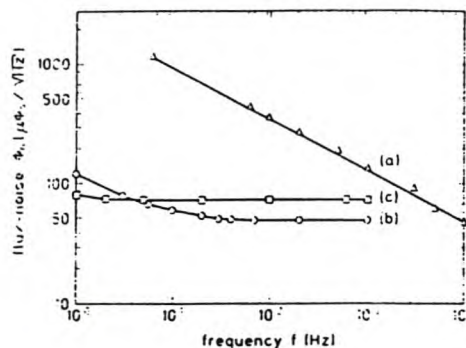


Figure 4.8: Flux noise for different measurement techniques: (a) small signal measurement, (b) flux-locked loop measurement and (c) bias current reverse technique [81].

4.5.5 Typical noise values

Typical noise values for dc SQUIDs are $8 \mu\text{V} \Phi_0^{-1} \text{Hz}^{-1/2}$ for the white noise level, $63 \mu\text{V} \Phi_0^{-1} \text{Hz}^{-1/2}$ at dc bias and $8.4 \mu\text{V} \Phi_0^{-1} \text{Hz}^{-1/2}$ with bias current modulation at 1Hz. This is for SEJ SQUIDs with a t/\hbar ratio of 0.63. The inductance is 25-35 pH and the junction width 3-6 μm , with transfer functions between 55 and 102 $\mu\text{V} \Phi_0^{-1}$. The noise levels were measured at optimum bias. This means that most of the noise is attributable to critical current fluctuations of the grain boundary Josephson junctions. All these measurements were made with the SQUID operating in a flux-locked loop.

4.6 Electronic Compensation

In order to get rid of background fields electronic gradiometry is frequently used. With electronic gradiometers longer baselines can be obtained than with hardware gradiometers. The basic electronic gradiometer uses two SQUID magnetometers. The one magnetometer is situated close to the subject being measured and it is called the "signal SQUID". The second magnetometer is placed in the same vertical axis as the signal SQUID but a distance y above it and it is called the "background SQUID". The background fields will contribute equally to the signal in both SQUIDs but the field from the subject will contribute mainly to the signal SQUID. Therefore by subtracting the output of the background SQUID from the output of the signal SQUID the influence of the background field is attenuated. As a measure of performance of these devices the balance level is often used. The balance level of a SQUID is defined as the ratio of the amplitudes of a uniform field, measured by the signal SQUID with and without gradiometry.

There are two factors that limit the balance level in gradiometers: how well matched the amplitudes of the signals being subtracted are and any time delays between them. In hardware gradiometers the signal amplitudes depend on geometry, but there is no time delay between the signals. In electronic gradiometers the signal amplitudes can be easily adjusted to very high precision, but the signals may be out of phase due to time delays caused by the electronics. Both the wire-wound and the electronic gradiometers, however, must be carefully aligned.

4.6.1 Series and parallel configurations

Two of these electronic gradiometer configurations, parallel and series, were compared by Espy et al [65].

In parallel gradiometry, the output of both the background and signal SQUID go to a summing amplifier where the gains are adjusted and the difference taken. In series gradiometry, the output of the background

SQUID is sent to the amplifier for gain adjustment and then added to the signal SQUID using a feedback coil. The effect of this is that the background field is suppressed at the signal SQUID while the dynamic range is preserved.

As already mentioned, the electronic gradiometer requires a finite amount of time for the source magnetic field (detected by a SQUID) to be converted to a voltage at the output of the SQUID electronics. The time delay causes a phase difference between the source signal and the SQUID response. The phase difference is a function of the signal frequency.

In the case of the parallel gradiometer the existence of these time delays is not problematic. The time delays, however, must be identical for the two SQUIDs so that the signals will be in phase at the amplifier when they are subtracted. For the series gradiometer any time delays in the electronics degrade the gradiometer performance, because the output of the background SQUID has to propagate through the electronics to the signal SQUID in order to cancel the real-time background field. Thus for the parallel configurations the challenge is to keep the delays identical, and for the series configuration the challenge is to minimise the delay.

The delay can be estimated by considering the small-signal closed-loop frequency response of the flux-locked loop circuit. The loop contains a one-pole integrator. This can be written as

$$A(f) = \frac{G_f}{(1 + G_f)} \quad (4.38)$$

where G_f is the open-loop gain defined as a complex number:

$$G_f = \frac{V_\Phi G_I(f) M_{fb}}{R_{fb}} = \frac{f_1}{if}, \quad (4.39)$$

V_Φ is the SQUID transfer function at the point of operation, $G_I(f) = \frac{1}{i2\pi f RC}$ is the gain of an ideal one-pole integrator where $i = \sqrt{-1}$ and R_{fb} and M_{fb} is the feedback resistance and inductive coupling respectively. From this the small signal phase shift can be calculated. This is found to be $\theta \approx \frac{f}{f_1}$ and it can be related to the time delay by

$$t_{delay} = \frac{\theta}{2\pi f} = \frac{1}{2\pi f_1} \quad (4.40)$$

For any time delay in the system there is a corresponding phase difference that increases with increasing frequency.

Matching the time delays is achieved by matching the small-signal cut-off frequency for both background SQUID and signal SQUID electronics. To minimise the delays, one has to make the small-signal cutoff frequency as large as possible.

If it is possible to measure the time delays, the balance level between two SQUIDs can be determined as

$$\gamma(t_{delay}, a) = \frac{1}{\sqrt{(1-a)^2 + \omega^2 \delta t_{delay}^2}}, \quad (4.41)$$

where a is the scaling variable for the signal levels that do not match exactly and δt_{delay} is the difference between the two time delays for the SQUIDs. The derivation of equation 4.41 can be found in [65].

The parallel and series configurations described above were characterised in an unshielded laboratory. The noise of both were dominated by 60 Hz and its harmonics, caused by the power lines. The parallel configuration performed better; the 60 Hz peak was ~25 times smaller than when no gradiometry was used. The series method reduced the 60 Hz peak by ~9 times. Even with exceptionally high balance levels, first-order gradiometry is only effective for unshielded applications where the gradient of the ambient field noise is small. Usually one cannot assume that power-line noise is uniform; therefore first-order gradiometry might not always be effective enough.

4.6.2 Vector reference SQUIDs

Still there is the problem of alignment of the magnetometers (mentioned earlier) – the common-mode rejection ratio (CMRR) (the so-called balance), is not high if the SQUIDs are not orientated sufficiently in parallel. The balance for a first-order gradiometer cannot be better than $\frac{1}{2 \sin(\theta/2)}$, where θ is the angle between the sensitive directions of the two magnetometers. The traditional approach to this problem of mechanically adjusting the reference SQUID is often impractical and unreliable [46].

An alternative is to use a vector reference, which allows electronic adjustment of the balance. The reference SQUID in the first-order axial gradiometer is replaced by an arrangement of three SQUIDs orientated in such a way that they form an orthogonal triplet. The signals of the three reference magnetometers are added and the coefficients are adjusted in such a way that their effective sensitive direction and gain compensates the sensing magnetometer exactly. Borgmann et al [42] as well as He et al [46] investigated this compensation technique. The focus of both studies were on HTc rf SQUIDs, with a three-magnetometer reference system.

For comparison Borgmann et al [42] used a normal electronic gradiometer consisting of two sensitive rf-SQUID magnetometers, connected to create an electronic gradiometer with a baseline of 5 cm. For compensation they used a less sensitive compensating SQUID. The signal of this SQUID was fed back to the feedback inductances of the other two magnetometers via a tunable resistor. This was done to compensate for the environmental disturbances and strong changes to background field. The compensating SQUID was tested at two different axial positions (see figure 4.9 (a)). The common mode rejection of homogeneous magnetic fields for the first-order gradiometers was 200 for the first configuration (figure

CHAPTER 4. SQUIDS

4.9 a(i)) and more than 1500 for the second configuration (figure 4.9 a(ii)). In the second configuration superconducting plates were used for balancing [84].

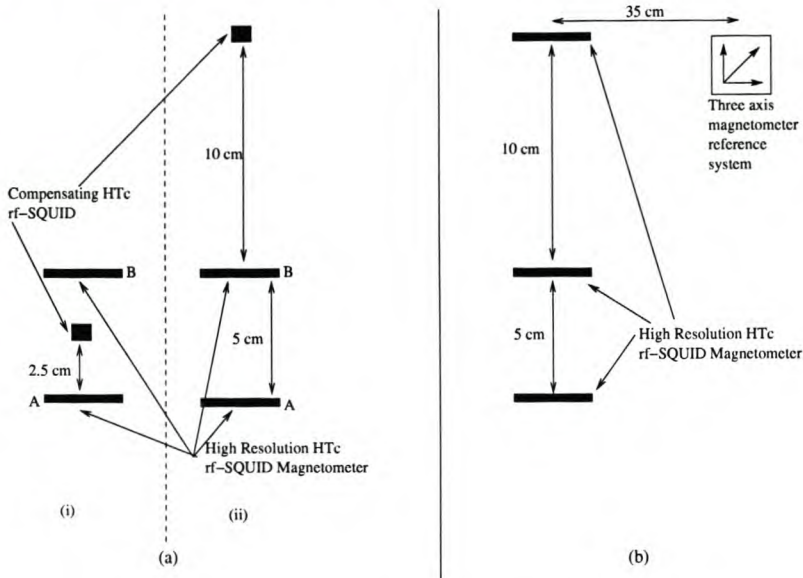


Figure 4.9: (a) Electronic gradiometer with the compensating SQUID in two different configurations. (b) Three-SQUID gradiometer with vector reference system configuration.

They proposed an axial three-SQUID gradiometer with a three-axis reference system. This system is shown in figure 4.9(b). The three SQUIDs are arranged in an asymmetric baseline configuration, in order to form an electronic second-order gradiometer. This setup was tuned in the axial direction using a homogeneous AC field of 1Hz generated by a Helmholtz-type coil system (the first-order gradiometer system was tuned the same way). The reference system consisted of a three-axis fluxgate magnetometer at a distance of 35cm from the SQUID.

Despite the higher noise level in the second-order gradiometer signal, the spatial filtering allows the efficient rejection of strong environmental disturbances during measurements in shielded environments. In an unshielded environment with low disturbance, only the 50 Hz line frequency and its harmonics show an increase by a factor of 20. By adding the signals of the reference system to the gradiometer, the line frequency interference peaks were suppressed by a factor of 10, but the overall noise performance remained the same. In unshielded environments with strong disturbances the spectral noise is strongly increased in the magnetometers and the unbalanced second-order gradiometer. In this environment the addition of signals from the reference magnetometers improved the output significantly. The reference signal and the output of the two lower SQUID magnetometers were added to the second-order gradiometer signal, with fixed coefficients in an averaged adaptive process. This gave an averaged common mode rejection of up to 76 dB for the 50 Hz and 66 dB for the 150 Hz disturbances. For the lower frequencies it was 55 dB [84]. This is much better than the first-order magnetometer presented above.

He et al used only a single sensing SQUID located close to the source with the orthogonal reference triplet placed at a distance of 8 cm from the sensing SQUID. In this case all the sensors were rf-SQUID magnetometers. Figure 4.10 shows the electronics that were used to adjust the balance of the gradiometer. The adjustment “potentiometers” were adjusted with the setup inside a uniform magnetic field generated by Helmholtz-like coils. By applying the field in the various axial directions the reference SQUIDs were aligned exactly to the sensing SQUID. He et al [46] found a common mode rejection of 4000 with a baseline of 8 cm. The field sensitivity can be improved by using flux concentrators or coplanar resonators.

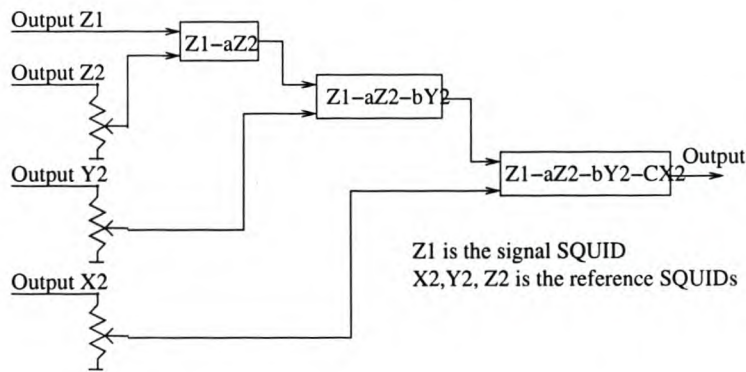


Figure 4.10: Schematic of the balance adjustment electronics.

One of the limiting factors in the scheme of He et al [46] may be the low-frequency cross-talk between the channels of the gradiometer. As the SQUIDs are operated in flux-locked loop configuration, the field produced by the feedback cable and compensation coil of one SQUID is observed as a signal by the other SQUIDs. This crosstalk can be minimised by choosing an appropriate sensor configuration, e.g. by arranging all sensors precisely in line, or by a certain planar arrangement of the reference triple. Another form of cross-talk is the high-frequency cross-talk generated by the high-frequency pumping of the tank circuit. This pumping of one SQUID could influence another nearby SQUID. This can reduce the SQUID amplitude, leading to an apparent increase in the white noise. High frequency cross-talk can be eliminated by proper matching of the tank circuit [46].

4.7 Readout Electronics

In section 4.5.4 the suppression of the SQUID noise by the use of modulation schemes was discussed. It was shown that the $\frac{1}{f}$ noise has two sources. Two modulation schemes were suggested to treat these two noise sources: the flux-locked loop and bias reversal. These methods will be discussed in more detail in this section. The flux-locked loop will not be explicitly treated but additional positive feedback (APF) will be presented. APF is a refinement of the flux-locked loop.

4.7.1 Additional Positive Feedback Scheme (APF)

For dc SQUIDs there are two types of connections between the SQUID and the readout electronics. They are direct coupling and connection via an impedance transformer. With direct coupling the pre-amplifier noise dominates the system noise. The pre-amplifier noise is much larger than the SQUID noise [109]. To enhance the SQUID voltage, a modulation scheme like APF is needed. Drung et al [52] proposed some refinements to this scheme to overcome some of the noise problems caused by the lack of modulation in the original scheme. This lack of modulation meant that low-frequency critical current or resistance fluctuations in the Josephson junctions were not suppressed. The use of a bias current reversal scheme was suggested to reduce these fluctuations.

The system consists of an APF flux-locked loop with a flip-chip magnetometer. The APF circuit consists of a resistor (R_a) and a coil (L_a) in series, connected in parallel with the SQUID as shown in figure 4.11. A constant bias current I_b maintains a voltage V across the SQUID, which is equal to the bias voltage V_b of the SQUID at its operating point. A small increase in the magnetic flux Φ at the SQUID produces a small change in V . The resulting current change in the APF circuit induces an additional flux in the SQUID via the mutual inductance M_a between the APF coil and the SQUID, thereby increasing the flux-to-voltage transfer function to

$$V_{\Phi} = \partial V / \partial \Phi = \frac{V_{\Phi,i}}{(1 - G_a)}, \quad (4.42)$$

where $V_{\Phi,i}$ is the transfer function without the APF and

$$G_a = \left(M_a + \frac{\partial \Phi}{\partial I} \right) \frac{V_{\Phi,i}}{R_a} \leq 1 \quad (4.43)$$

is the APF gain. The spectral density of the total flux noise with APF at frequency f is expressed as

$$S_{\Phi}(f) = S_{\Phi,i}(f) + 4k_B T R_a \left(\frac{G_a}{V_{\Phi,i}} \right)^2 + \frac{S_{V,amp}(f)}{V_{\Phi}^2} + S_{I,amp}(f) \left(\frac{\partial \Phi}{\partial I} \right)^2, \quad (4.44)$$

where $S_{\Phi,i}$ is the intrinsic noise of the SQUID without APF, the second term represents the Nyquist voltage noise of the APF resistor, the third and fourth term is the voltage and current noise of the pre-amplifier and $-\partial \Phi / \partial I$ is the current sensitivity of the SQUID. Equation 4.44 demonstrates that APF reduces the effects of the pre-amplifier voltage noise by increasing the flux-to-voltage transfer function V_{Φ} , whereas the effect of the current noise remains unchanged, since $-\partial \Phi / \partial I$ is not affected by APF. G_a chosen as 0.9 is a good compromise between low noise and high bandwidth.

For all the magnetometers a 7-turn APF coil and a single-turn feedback coil of 0.05mm diameter varnish-insulated Copper wire were used. The metal-film APF resistor was selected for each SQUID to make $G_a \approx 0.9$. The bias voltage V_b , was generated by passing a bias current I_b through a cooled metal film resistor R_v . The deviation between the SQUID and bias voltages was amplified, integrated, and fed back

as a current into the feedback coil. With a static bias current the APF scheme does not suppress the critical current fluctuations of the two junctions. Therefore the low-frequency noise is higher than with the flux modulation scheme, which does suppress these fluctuations. To rectify this bias current reversal is used (discussed in detail in section 4.7.2). With bias reversal both in-phase and out-of-phase fluctuations are suppressed, and the low-frequency noise is strongly reduced for frequencies below a few kHz. With bias reversal, the white noise of the flip-chip was $16.2 \text{ fT}/\sqrt{\text{Hz}}$. In the case of a static bias, the white noise was slightly lower.

4.7.2 rf Bias current reversal

Bias reversal can be implemented both for a directly coupled setup and an inductively coupled setup. The directly coupled setup requires additional techniques to enhance the SQUID voltage, while the inductively coupled setup transforms the SQUID voltage in such a way that it is well above the pre-amplifier noise. This is done through impedance matching. Both techniques with refinements suggested by Zhang et al [61, 109] will be discussed below.

4.7.2.1 Bias reversal in directly coupled dc-SQUID magnetometers

Bias reversal is implemented by using a square wave to bias the SQUID (see figure 4.12). The square wave generates two currents, i_b and i_r ; i_b flowing as a bias current through a resistance R_b and the SQUID. The current i_r flows through resistor R_r and an external coil with an inductance L_r in such a way that it couples half a flux quantum to the SQUID loop. That is $i_r \times M = \phi_0/2$, where M is the mutual inductance. Thus, through adding half a flux quantum for the negative bias current, a $V - \phi_e$ curve that is in phase with the positive bias current is obtained. Here V is the voltage across the SQUID and ϕ_e the external magnetic flux. The load seen by the two currents differ, thus the phases will also differ. This difference in phase will increase with the bias reverse frequency f_r . The bias reversal frequency is therefore limited to a few kHz.

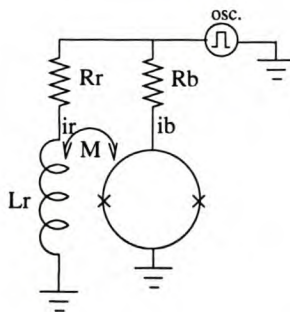


Figure 4.12: Bias reversal with additional $\frac{\phi_0}{2}$ phase shift for negative bias (redrawn from [61])

Zhang et al [61] overcame this limitation by proposing a simple design for the bias reversal which can increase f_r to the radio frequency (rf) range. They suggested that, instead of adding half a flux quantum, one should use a multiplier to obtain the in-phase $V - \phi_e$ curve for the negative and positive bias currents. The circuit illustrating this principle is shown in figure 4.13. For a negative bias current, the output voltage of the SQUID, i.e. the input signal for the multiplier, is negative. However, the reference voltage V_{ref} , for the multiplier, which comes directly from the oscillator, is also negative. Therefore the output voltage from the multiplier is positive, while the voltage amplitude remains unchanged. Thus, identical $V - \phi_e$ curves should be obtained for the positive and negative bias currents without considering the $\frac{1}{f}$ noise from the SQUID.

This solves the phase problem of the previous circuit so that f_r can be increased to the RF range. The out-of-phase noise from the two junctions produces an apparent flux in the SQUID loop. This flux shifts the $V - \phi_e$ curve of the SQUID to the left or the right. Over a small time period these phase shifts are in opposite directions but they have equal amplitude, provided that the reversal frequency f_r is much higher than the corner frequency f_c of the SQUID. The corner frequency f_c is normally between 100Hz and many kilohertz. Thus a low-pass filter can be used to get the average of the out-of-phase noises from the positive and negative bias currents. The higher the f_r the better the averaging – a good guideline is to make f_r at least three orders of magnitude higher than f_c .

Another advantage of this scheme is that the demodulation of the SQUID signal is independent of the flux modulation scheme, which makes the readout electronics much simpler.

To decrease the noise temperature of the pre-amplifier, the SQUID and the pre-amplifier are normally connected via a resonant circuit. For their rf bias reversal scheme, Zhang et al used a quarter wavelength transmission line, connected on one side to the SQUID and terminating on the other side in a FET. This has the following advantages:

- No lumped elements are used for the resonant circuit.
- The coaxial cable simultaneously transports the rf signal and serves as the resonant circuit.
- The distribution of the rf current and voltage for the $\lambda/4$ transmission line is fixed at f_0 , and the analysis of the circuit is thus similar to a dc circuit.
- The coaxial cable has a very good resistance to the external rf disturbances.

Zhang et al [61] were able to demonstrate that this design does indeed reduce $\frac{1}{f}$ noise in dc SQUIDs. Note, however, that this is only the case for $\beta \leq 1$ for sine-wave bias reversal; for a square wave it should be possible to obtain this for all values of β . Thus, rf bias reversal using a 50MHz signal can be achieved and the bandwidth of the SQUID can be greatly increased while the $\frac{1}{f}$ noise is reduced.

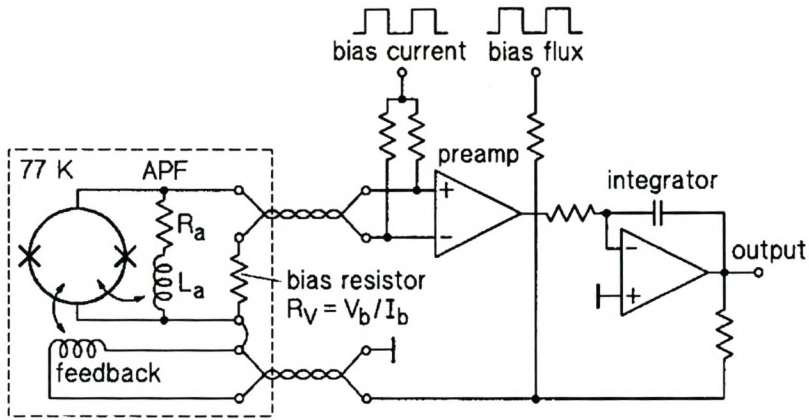


Figure 4.11: Circuit diagram of the APF modulation scheme with bias current feedback [52].

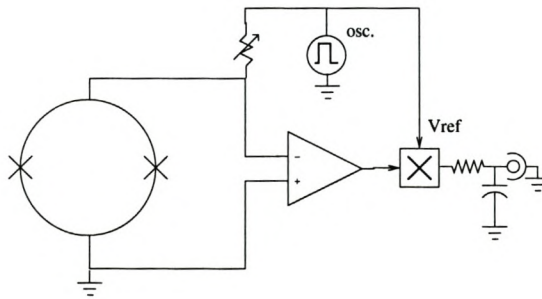


Figure 4.13: Circuit diagram of the rf-bias current reversal scheme using a multiplier (redrawn from [61]).

4.7.2.2 Bias reversal in inductively coupled dc-SQUID magnetometers

With the inductively coupled magnetometer one of the big drawbacks is that the bias reversal frequencies have to be chosen low to prevent the appearance of transient currents caused by the inductance of the primary side of the transformer. These transients lead to an increase in the SQUID noise. In order to prevent this, Zhang et al [109] suggested the use of a non-constant bias current that compensates for the transient. Hereby a perfect square wave current I_s through the SQUID can be obtained, which allows the bias reversal frequency to be raised to several hundreds of kHz without an increase in the SQUID noise.

They obtained the equations for the non-constant compensating current through a simple analysis of a lumped element circuit for the inductively coupled SQUID loop. This circuit is shown in figure 4.14. In this circuit the primary coil forms an inductive element that connects in parallel to the SQUID. The bias current I_b is usually rectangular, with a period T and an equilibrium amplitude A . At each reversal the current through the SQUID I_s gets a peak A' which is generated by the parallel inductance. Thus, for a short time τ after the reversal, the current through the SQUID is not constant, where $\tau = L/R$, with R the bias resistor and L the inductance of the primary transformer. The magnitude of the additional noise is determined by the ratio of the times τ/T and the amplitudes A'/A . Thus, as the frequency is increased, the noise increases.

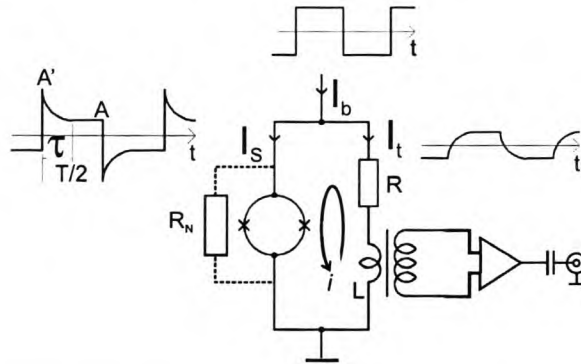


Figure 4.14: Transformer scheme for dc-SQUID operation. The time transients of the bias currents I_s , I_b and I_t are shown as well [109].

The circuit can be written as

$$L \frac{\partial}{\partial t} (I_b - I_s) + (I_b - I_s)R = I_s R_N. \quad (4.45)$$

Because the current I_s must be held constant, the equation can be rewritten as

$$L \frac{\partial I_b}{\partial t} + R I_b - I_s (R + R_N) = 0. \quad (4.46)$$

With the initial condition

$$I_{b0} = I_A \frac{R_N - R}{R_N + R}, \quad (4.47)$$

the solution of equation 4.46 is

$$I_b = I_A - 2I_A \frac{R_N}{R + R_N} \exp\left(-\frac{t}{\tau}\right), \quad (4.48)$$

where I_A is the maximum amplitude of the bias current. From this solution it is clear that only the ratio $R_N/(R + R_N)$ has to be adjusted and τ is independent of the dynamic resistance R_N of the SQUID. This means that R_N is independent of thermal fluctuations of the junctions.

Zhang et al [109] suggests the following circuit (figure 4.15) for the compensation of the bias :

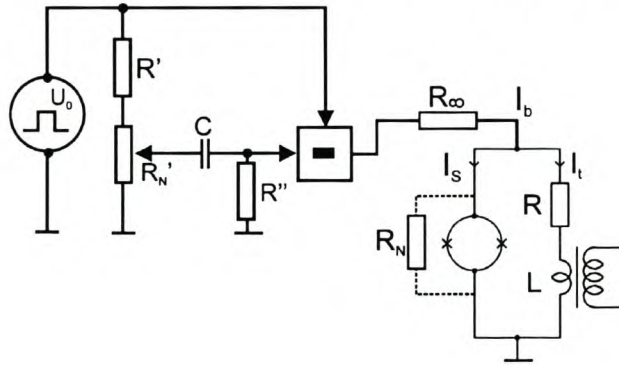


Figure 4.15: Diagram of an electrical circuit for generating the non-constant bias current I_b [109].

1. An oscillator generates a rectangular-shaped ac voltage of variable frequency.
2. This voltage is fed to a voltage divider and a differentiation circuit.
3. The differentiated voltage is subtracted from the original oscillator voltage by an operational amplifier.
4. This voltage source forms the bias current source through a large resistor R_∞ . The divider $R'_N/(R'_N + R')$ should be adjusted to equal the ratio $R_N/(R_n + R)$. The time constant must be adjusted to match $\tau = R''C = L/R$.

4.8 Improving SQUID performance

4.8.1 Ion-beam etching

In the design of SQUID structures the critical current I_c and the normal resistance R_n are the parameters that have the biggest influence on the performance. This can be related to the β_L parameter according to

$$\beta_L = \frac{2I_c L}{\Phi_0}, \quad (4.49)$$

where L is the inductance of the SQUID loop. The best performance is seen in SQUIDs where the junction resistance, R_n , is high and β_L is in the order of 1. One way to adjust these parameters is through ion-beam etching [47].

The etching changes the electrical parameters of the grain boundary of bicrystal Josephson junctions. Wunderlich et al [47] investigated this on grain boundary Josephson junctions. Simulations of the penetration depth of the Ar⁺ ions into the superconducting film show a damaged area of about 2 up to 5 nm on the surface of the film during ion-beam etching.

For the trimming of the junctions, the whole sensor apart from the region of the Josephson junctions is covered by a mask of amorphous YBCO. This etching mask prevents the lowering of the mutual inductance between the SQUID and the gradiometer antennas.

This technique trim the gradiometer sensor by lowering the film thickness only in the parasitic part of the SQUID. Therefore it restricts the increase of the SQUID inductance to the parasitic part. The parasitic part of the SQUID is seen as the part of the inductance that does not contribute to the galvanical coupling of the screening current of the gradiometer to the dc SQUID (this is for directly coupled pickup loops). The film thickness in this area was lowered from 130 nm with a parasitic inductance of 25 pH, to a thickness of 50 nm with a parasitic inductance of 41 pH. The increase of the whole SQUID inductance from 67 pH to 83 pH (a 24% increase) is moderate compared to the reduction of the critical current which was reduced by one order of magnitude. This decrease of the critical currents from 450 to 40 μ A corresponds to an increase of the normal resistance R_n from 0.84 to 4.20 Ω .

The most important parameter, however, is the $I_c R_n$ product. For good SQUIDs this value must be as high as possible. The $I_c R_n$ product was also found to depend strongly on the film thickness. The lattice mismatch between YBCO and the substrate results in imperfections and stress in the film near the YBCO-substrate interface. This results in a moderate increase of electrical parameters like $I_c R_n$ for film thicknesses above 50nm, as the stress relaxes and the number of imperfections decrease. Although the $I_c R_n$ product will decrease with decreasing critical current I_c , the white noise levels will be improved, up to the level where the SQUID parameter $\beta_L = \frac{2I_c L}{\Phi_0}$ has a value above one. Table 4.1 serves to illustrate the dependence of the various parameters on the film thickness of a dc SQUID on a SrTiO₃ bicrystal substrate with a misorientation angle of 24°.

4.8.2 SQUID Baseline

One of the limiting factors in SQUID design is the baseline; this is the distance between two gradiometer loops and plays an important part in determining the efficiency of common-mode rejection. Some of the results of Pegrum et al [43] are useful when trying to optimise this factor.

There are two main techniques for forming a long baseline HTS SQUID gradiometer. The first approach is that of electronic gradiometry; the advantage of these systems is that they can have large baselines

and a high degree of balance. Still electronic subtraction imposes stringent requirements on the system linearity, slew rate and the synchronisation of the multichannel electronics [51]. These methods are discussed under electronic compensation (section 4.6). The second approach for forming a long baseline HTc SQUID gradiometer is to form a planar gradiometer by coupling two symmetric pickup loops to a SQUID. The size of such single-layer gradiometers (SLGs) is restricted to 10x10mm. This limits the baseline to typically 4mm and the area of the two pickup loops to small values and this leads to low gradient sensitivities. An additional disadvantage is the SQUID in the centre of the structure that acts as a sensor of uniform fields. This gives rise to a parasitic effective area of the order $\approx 500\mu\text{m}^2$. An alternative to the SLG is to couple a large flip-chip flux transformer to a single-layer magnetometer or gradiometer. This greatly enhances the gradient sensitivity but requires very accurate manual alignment [43].

Pegrum et al [43] suggests a device that combines the two approaches mentioned above. In order to achieve a longer baseline a $30\times 10\text{mm}^2$ substrate and a novel two-SQUID coupling scheme is suggested. This design employs simple electronic gradiometry – because of the smaller area of the SQUIDs (compared to magnetometer SQUIDs) the requirements on the electronics are less demanding. The gradiometer consists of two symmetric and approximately rectangular pickup loops to which four identical SQUIDs are directly coupled. The SQUIDs are arranged in two pairs (the one pair is shown in greater detail in figure 4.16). The linewidth of the SQUIDs were restricted to $4\mu\text{m}$ to prevent magnetic flux penetration when the device is operated unshielded. The width of the junctions was $3\mu\text{m}$ and the SQUID slit had a length of $108\mu\text{m}$ and a width of $4\mu\text{m}$ giving an estimated SQUID inductance, $L_{\text{SQ}} \approx 100\text{pH}$.

d[nm]	$I_c[\mu\text{A}]$	$R_n[\Omega]$	$I_c R_n[\mu\text{V}]$	$V_{\text{pp}}[\mu\text{V}]$	L[pH]	β_L	$\sqrt{S_{\Phi}}[\mu\Phi_0/\sqrt{\text{Hz}}]$
130	446	0.84	375	24	67	14.5	10.5
112	371	1.00	371	25	69	12.4	8.6
94	282	1.22	344	29	71	9.7	6.6
77	209	1.51	316	32	74	7.5	5.9
60	86	2.73	235	36	78	3.2	4.2
51	37	4.20	155	31	83	1.5	5.1

Table 4.1: SQUID parameters as a function of film thickness for a dc SQUID.

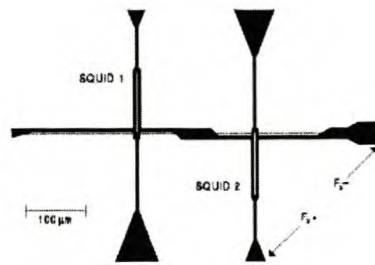


Figure 4.16: The arrangement of a pair of SQUIDS with antiparallel coupling to the gradiometer loops [43].

The arrangement seen in figure 4.16 shows how the SQUIDS are coupled in opposite senses to the pickup loops. This causes that, for any given combination of uniform and first-order fields, the gradiometric and magnetometric signals add for one SQUID while they subtract for the other SQUID. This is only for perfectly symmetric pickup loops – in practice, the effective areas of the two SQUIDS will be slightly different. These differences can however be compensated for by using electronic balancing. In order to fabricate the long baselines, the PLD process was modified by focusing the laser to a spot with a horizontal dimension of ~ 10 mm and a vertical dimension of ~ 0.5 mm. This caused a plume that expanded a little in the horizontal direction but significantly in the vertical direction.

4.9 Summary

This chapter started with a very brief introduction to the theory of SQUIDS. The book by Orlando et al [10] treats this subject in more detail. However, for the purpose of designing and implementing an Htc SQUID, this theory is only of limited use. The theory is mainly concerned with low-temperature SQUIDS and the behaviour of HTc SQUIDS deviates from this theory in many ways.

For the typical SQUID magnetometer and gradiometer we have to consider the pickup loop, the SQUID structure and the readout electronics. The most important aspect in the design of these SQUID structures is the noise. Because of the extremely sensitive nature of the SQUID, one must try to reduce the noise in every part of the system.

For the SQUID structure itself the rf SQUID with a coplanar resonator performs very well and has the advantage of being much more reproducible than the dc SQUID. If more than one SQUID are considered, the best results are obtained by using two dc SQUIDS in series coupled to a washer-type pickup loop.

In modelling SQUIDS the RSJ model is based on an assumption that the magnetic energy per flux quanta is large compared to the thermal energy. This is not the case for HTc SQUIDS, therefore other models

must be considered. These models are based on the solution of the Fokker-Planck equation describing the behaviour of the system. These models describe the rf SQUID adequately, but for the dc SQUID the deviations from the theory are still large. For the dc-SQUID, equivalent-circuit models are a better option. Parameter extraction is necessary to check the accuracy of the models as well as for refinement of the equivalent circuit models.

We also investigated various improvements to the physical structure of the SQUID, to reduce the noise. For the pickup loop we saw that the use of multiple thin lines ($4 \mu\text{m}$) with the possible inclusions of flux dams in the loops improves the noise. It is also important to keep the pickup loop at least $100 \mu\text{m}$ away from the SQUID. It was also seen that the use of certain readout schemes like the flux-locked loop, bias feedback and additional positive feedback suppresses certain types of noise.

To overcome the limitation on the baseline of physical gradiometers, the use of electronic gradiometers was considered and we saw that the use of a vector reference system provides good background field rejection. We also saw that ion etching can be used to tune the $I_c R_n$ product of a SQUID. Finally some ways to overcome hardware gradiometer limitations were presented.

Chapter 5

Biomagnetism - theory and application

The purpose of this chapter is to provide an overview of the application areas of superconductors in medicine. After a brief outline of the various applications each of the applications will be discussed along with the major benefits of and major limitations of SQUID magnetometry. The biomedical application of superconductivity is mostly in the area of biomagnetism.

5.1 Biomagnetic Measurements

One of the major achievements of superconductivity is the SQUID magnetometer (the theory of operation of the SQUID device has been discussed in section 4.2). This measurement device is capable of measuring magnetic fields in the order of femto Tesla. This makes it one of the most sensitive magnetic measurement devices known. To provide an idea of the sensitivity of the SQUID, figure 5.1 shows the relative sizes of various magnetic fields.

The human body generates extremely small magnetic fields, but the measurement of these fields is of great diagnostic value. Because of its sensitivity the main device for measuring these fields is the SQUID magnetometer. SQUIDs can be used in the fields of magnetoencephalography, magnetocardiography and other biomagnetic applications.

5.1.1 Magnetoencephalography (MEG)

The most common source of biomagnetic signals is intra-cellular current flow. This flow is the result of muscular or neural excitation. The cells can be represented as a current source and the current flows outside the cell through a volume conductor (surrounding fluids). This current flow causes electric fields that can be measured by electroencephalography (EEG) techniques. The current flow also causes a

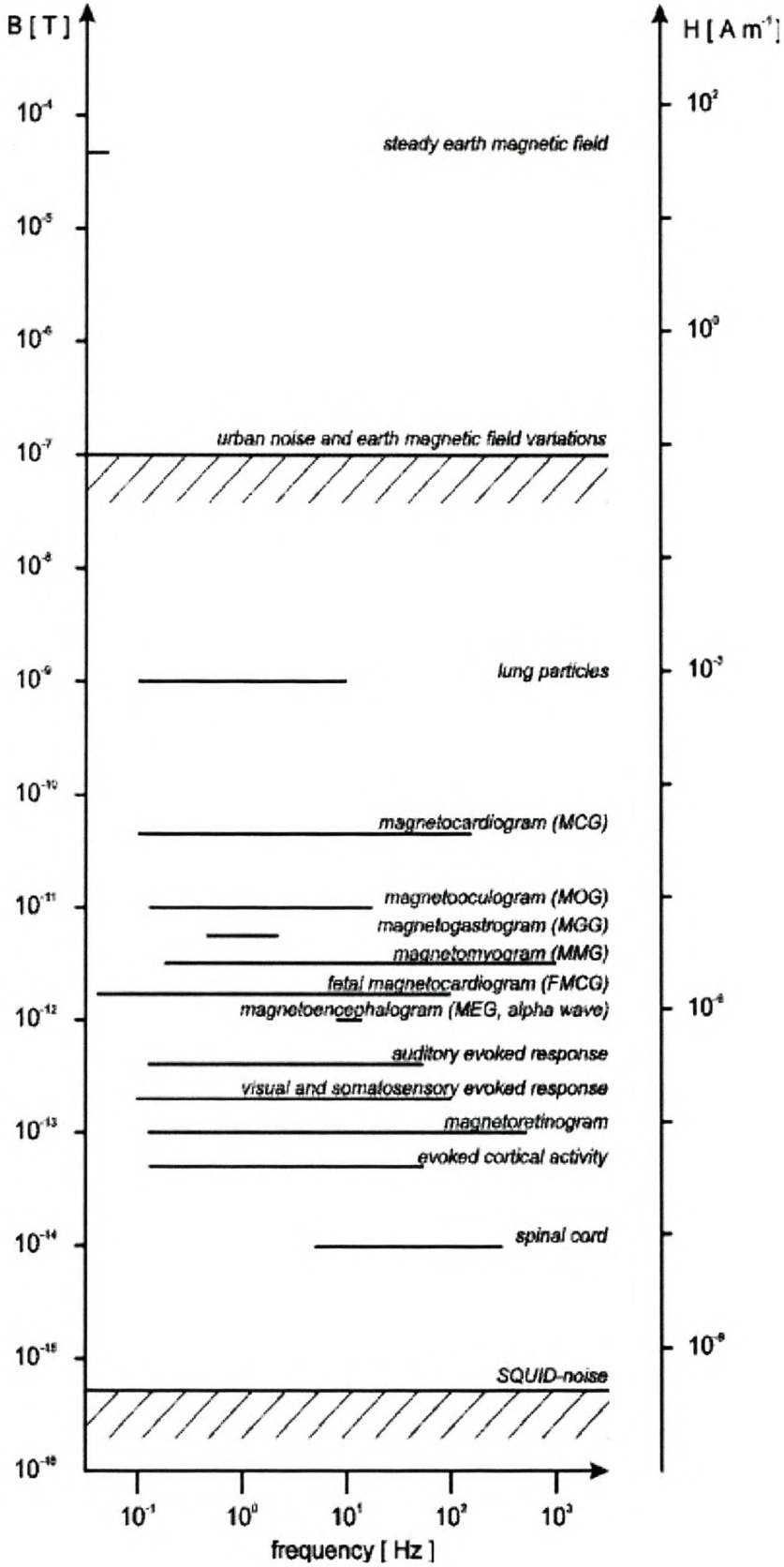


Figure 5.1: The relative sizes of various magnetic fields.

magnetic field that is measurable, although it is very weak. The advantage of measuring the magnetic field is that the currents vertical to the body surface are measured. These vertical currents mainly result from the intra-cellular current flow. Intra-cellular current flow is less distorted than volume current and this allows MEG to obtain much higher resolutions than EEG. MEG can also be used in conjunction with EEG methods, because the two measurements are complimentary.

MEG systems usually consist of an array of low-temperature SQUID sensors in a Dewar that surrounds the whole head (see fig 5.2). The array usually consists of 37 to 255 SQUID sensors, either in a gradiometer configuration or in a magnetometer configuration, with a few sensors dedicated to noise cancellation. Because of the small signal sizes, MEG measurements are always taken in a magnetically shielded room.

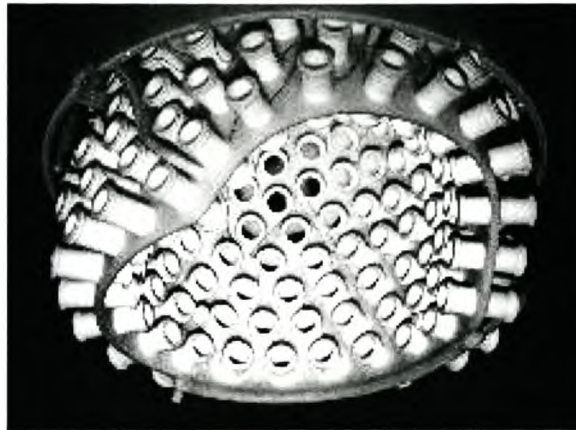


Figure 5.2: A whole-head MEG system.

5.1.1.1 Applications

MEG is used in various clinical and research applications. One example is the task of functional mapping of cortical areas, for which it is eminently suited. There are also areas in which MEG is a unique tool, areas like investigating temporal aspects of signal processing in the brain and other, even more complex brain functions. When used in conjunction with PET, MRI, fMRI and EEG, MEG provides many other unique research applications. The following is a list of a few recent applications of MEG. All the examples come from an international conference on biomagnetism [16].

In the field of Neuroscience MEG has applications in various research areas, i.e. research in vision [16, pp. 72-84], somatosensation, pain and other senses [16, pp. 85-102], motor functions [16, pp. 103-107], cognition and language [16, pp. 108-123] and auditory research [16, pp. 47- 71].

Some of the main recent advances have been in the study of object representation, where certain brain signals have been isolated to be specifically related to object representation, irrespective of whether the

object is from visual information or from memory. In the auditory field the plasticity of the auditory cortex has been measured by MEG and functional reorganisation has been observed after intense “ear training” and reversible “functional deafferentation” [16, p. 8].

The main clinical applications of MEG are the localisation of lesions as well as the localisation of the centre of epileptic discharges. In conjunction with MRI or fMRI this localisation enables accurate pre-operative planning. Another application is the planning of rehabilitation for stroke patients by determining the extent of brain damage. MEG is also used for the planning of stereotactic radiation therapy by precisely localising the primary sensory cortex through functional mapping. Through this process radiation of the cortex is kept as low as possible [16, pp. 21-24 and 124-138].

5.1.1.2 Comparison with other medical scans

The main advantage of MEG is that its temporal resolution is much higher than other imaging methods (see fig 5.3). Its main disadvantage is that it provides no anatomical information. For this reason it is often used in combination with a method like MRI.

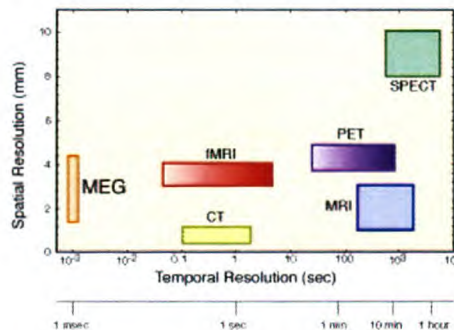


Figure 5.3: MEG vs other imaging technologies

5.1.2 Magnetocardiography (MCG)

The current flow through the heart generates a magnetic field around 50pT. This is well within the detection range of both low- and high-temperature SQUIDS. It is the first medical field where the use of high-temperature SQUIDS has become a viable alternative. MCG measures the intra-cellular current flow, which is much less distorted by the body than the volume current flow measured by EEG. MCG is also a totally non-invasive method requiring no electrodes. The main obstacle to MCG is the need for shielding. The few unshielded sensors still have to be improved before clinical application can become a reality [15].

While this is the situation at the moment it is in the process of changing. Seidel et al [44] have done MCG measurements in an unshielded laboratory environment. With these measurements they have shown that the ischaemic changes measured by a one-channel SQUID system were much plainer than ECG changes. These measurements were taken during investigations on myocardial ischaemia.

The basic MCG device, like the MEG device, consists of an array of SQUID sensors, often covering the whole chest area. Sometimes both the front and back areas are covered. The number of sensors varies from 7 to 64. All operates in a magnetically shielded room, with the exception of a few experimental models.

5.1.2.1 Applications

MCG is used for the screening of patients since the setup time is much lower than it is for ECG measurements. It has also been used to locate cardiac arrhythmias. MCG is used for the general localisation of the arrhythmia and then to map the catheter position as a more precise measurement of the area to be ablated. Research has shown that MCG can predict malignant cardiac arrhythmias with much greater accuracy than ECG. MCG is also used to predict myocardial ischaemia [16, pp. 25-28 and 139-147]. There is currently also a large amount of development in the field of fetal magnetocardiography. Fetal ECG is prone to extensive distortion due to an isolation layer called the vernix caseosa. MCG is not prone to this distortion and therefore has great clinical significance in the analysis of fetal heartbeat in high-risk pregnancies [15, pp. 176-178], [16, pp. 38-39 and 148-153].

5.1.3 Magnetoneurography

The measurement of peripheral nervous signals by means of magnetic fields is called magnetoneurography. The peripheral nervous signals are extremely small (in the order of 15fT). Because of this they can only be measured in heavily shielded rooms by very sensitive low-temperature SQUIDs. Even then special noise cancellation is needed since the magnetic disturbance coming from the heart, is almost 1000 times higher [19].

Magnetoneurography is used to locate conduction blocks or "slowing" in peripheral nerves and could serve as a diagnostic tool. This technique can also be used to locate the focal nerve in the case of acute nerve root lesion that causes severe back pain and muscle spasm [20].

5.1.4 Gastroenterology

By monitoring the magnetic signal generated by the stomach and intestines, it is possible to discern the various stages of digestion and to monitor the contractions and movements. Among the parameters

that can be measured are gastric emptying, oro-caecal transit time, esophageal transit time, pharyngeal transit time and clearance, oro-anal transit time and stomach mixing time [15, pp. 430-442], [16, p. 33]. Along with these, magnetically marked materials can be traced through the intestine in the same way that radioactive material is traced, but with no radiation. A spin-off of this technique enables pharmacists to study the path and release of solid oral dosages by studying the disintegration of magnetically marked pills [16, p. 220].

5.1.5 Magnetopneumography

A weak remnant field measurement can be taken from lungs that have been exposed to ferri-/ferromagnetic particles. These particles include metal dusts in welding and foundry fumes, grinding dust, asbestos particles and coal mine dust (among others). Some of the particles can stay in the lungs for longer than 40 years while others are absorbed after a few weeks. Using the knowledge of the remnant moment of certain particles, the amount of particles in the lung can be determined. In the case of a known amount of particles, some lung parameters can be determined.

This is done by magnetising the particles in a magnetic field and measuring the remnant magnetic field as a function of time, with a SQUID magnetometer. Since the fields are rather large, high-temperature SQUIDs can be used.

5.1.6 Liver iron susceptometry

SQUIDs are also used for non-invasively determining the amount of iron stored in the liver through a technique called susceptometry. A homogeneous magnetic field is applied to the liver area and the magnetic susceptibility is determined by measuring the disturbance in the magnetic field over the area. From this measurement the iron concentration in the liver can be determined. Due to the type of measurement, only excess concentration in liver iron can be measured [15].

5.1.7 Conclusion

This section gave a brief overview of the applications of SQUIDs in medicine. Because of noise limitations, high-temperature SQUIDs are not well-suited for magnetoencephalography and magnetoneurology. They are, however, suited to magnetocardiography and some of the other applications listed above.

5.2 High-temperature SQUID implementation

In practical MCG use –in addition to adequate sensitivity– essential issues include the system’s performance in the practical environments, its durability and stability over sufficiently long time periods and the availability of suitable MCG data acquisition and processing software [40].

In the literature only one article has been found where a high-temperature SQUID had been extensively tested in a practical biomedical environment. Zeng et al [40] reported on the characteristics and performance of their rf-SQUID gradiometer system during a period of more than 10 months of MCG measurements. They refer to another report by Weidl et al [83] which will also be discussed here.

Zeng et al [40] used YBCO rf SQUIDs with step-edge junctions in an electronic gradiometer configuration with a baseline of 10 cm. The SQUIDs are coupled through coplanar resonators similar to the ones discussed in section 4.2.2. The two resonators had different resonance frequencies, to avoid rf cross-talk between the two channels. Each SQUID and its concentrator/resonator was assembled in flip-chip configuration with a small amount of vacuum grease to ensure adhesion between the two chips.

A diagram of the readout electronics is given in figure 5.4. The electronics operated in dc lock-in mode without flux modulation. The SQUID’s signal was read out from the coplanar resonator inductively, via a single-turn matching coil. This coil, providing also the rf supply and the feedback field signal, is patterned on a printed circuit board. The distance between the resonator and the matching coil, adjustable via spacers in the range of a few millimetres, was fixed to obtain matching between the resonator and amplifier. The subtraction of the signals of the two channels with weighting factors was performed by software. An averaging process based on triggering with one of three electrocardiographic (ECG) leads, was employed to increase the signal-to-noise ratio (SNR) further. For a well-adjusted SQUID a white noise level of $10 \mu\Phi_0/\sqrt{\text{Hz}}$, corresponding to a magnetic sensitivity of $20 \text{ fT}/\sqrt{\text{Hz}}$, was obtained.

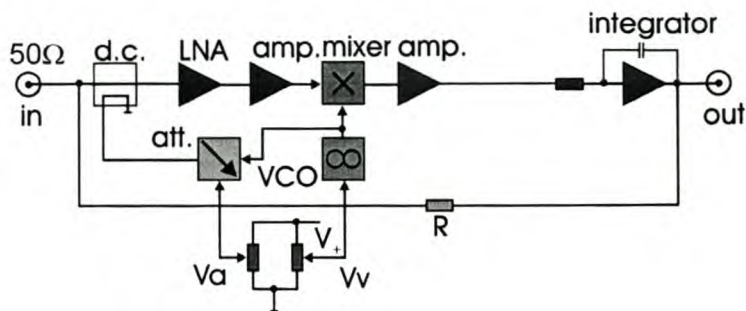


Figure 5.4: Readout electronics for the coplanar resonator [40].

A study by Seidel et al [44] confirmed these noise levels and sensitivity measurements. They found that planar high- T_c gradiometers on 10×10 mm bicrystal substrates with a baseline of about 4 mm can achieve field sensitivities between $880 \text{ fT}/\text{cm}/\text{Hz}$ and $4.2 \text{ pT}/\text{cm}/\text{Hz}$ at 1 Hz in a shielded environment.

In a disturbed environment this noise rises from 880 fT/cm/Hz to 2.4 pT/cm/Hz at 1Hz. The white noise of the planar gradiometers varies between 400 and 800 fT/cm/Hz for different geometries and is nearly independent of the environment.

This can be compared to figure 5.1, where a typical MCG signal is shown to be ≈ 80 pT. The typical size of an R-wave in fMCG is ≈ 2 pT, thus, for fetal magnetocardiography the system noise should be ≈ 20 fT/ $\sqrt{\text{Hz}}$. Although these noise levels have already been demonstrated by a few authors, it remains a challenging achievement. These low noise levels demonstrate that high-Tc SQUID systems can be used in magnetically disturbed environments for practical measurements.

5.3 Summary

SQUIDs have many applications in the biomedical field. Their main advantage is that they provide better accuracy than the EEG techniques that are usually used. This better accuracy enables more accurate and earlier diagnoses of many medical conditions.

In the area of MCG, HTc SQUIDs have already been proven to work. If such a SQUID could be manufactured at the University of Stellenbosch, it would provide many opportunities for further research in the medical field. It could also increase interest and funding for further research on SQUID magnetometers.

Chapter 6

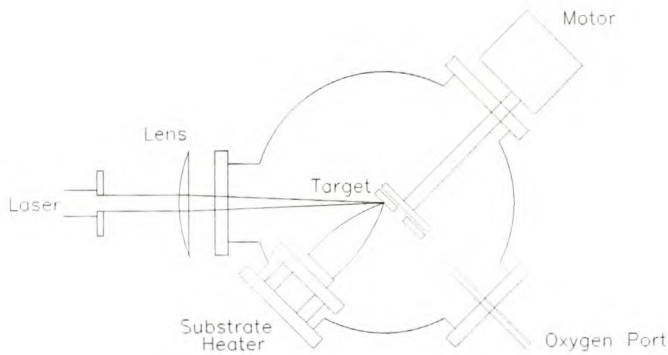
The Fabrication process

The fabrication process of a high-quality SQUID consists of a number of sub-processes. The first step in the process is the deposition of a thin layer of a superconducting material on a substrate. This substrate should contain some kind of crystalline imperfection that could lead to the formation of a grain boundary junction. This is followed by the patterning of the superconducting thin film to create the a superconducting loop and some Josephson junctions. These two steps could be repeated for a multilayer or flip-chip device. Then electrical contacts are sputtered onto the superconductor at the appropriate places and it is connected to the readout electronics. Finally the device is made passive by the deposition of a layer of amorphous YBCO on top of everything.

In this chapter the various sub-processes will be discussed in more detail starting with the deposition of the thin films. In this process we will concentrate on the pulsed laser deposition (PLD) technique. Next the way in which the pattern is transferred to the thin film will be discussed. This consists of two steps: photolithography and etching.

6.1 The deposition of YBCO thin films

The most common way of manufacturing a YBCO-coated substrate is by pulsed laser deposition (PLD), also called laser ablation. This method is preferred because of the good stoichiometry of the transfer process. The basic PLD system consists of a vacuum chamber, a laser, target material, and a substrate mounted on a substrate heater. The basic setup is shown in figure 6.1. The target and substrate are placed inside the vacuum chamber. Then in the presence of a vacuum the target is shot with a laser causing a plasma plume to be emitted in the direction of the substrate. This plume consists of the ablated material and causes it to be deposited on the substrate. For the exact PLD procedure see Appendix A.



Figuur 6.1: Schematic representation of the PLD system.

There are a lot of factors in the manufacturing of a good-quality YBCO film. These are the type of substrate, the finishing and temperature; the target, the target-substrate distance; the laser energy, spectral distribution, incidence angle, wavelength, energy distribution, pulse duration and pulse frequency; the gas mixture and pressure; the post PLD treatment annealing. In order to get a good quality YBCO film attention must be paid to all of them.

To optimise the deposition process for all these parameters an experiment was designed. This experiment accounts for a large part of the work done in this thesis and is presented in Chapter 8.1.

In this section the results of a comprehensive literature study done on the manufacturing of YBCO thin-films will be presented. The first part will discuss the results of other similar processes and will give an indication of the parameter range and other factors that must be taken into account for the deposition process. The second part will present various possible improvements to the PLD process to overcome certain inherent problems.

6.1.1 The PLD process

There are a number of different factors to take into account when the PLD process is considered. To start off, table 6.1 gives an example of a typical parameter set for the PLD process. In this case the deposition

was on an MgO substrate. A KrF laser was used with a frequency of 5Hz with a laser fluence of 1 J/cm^2 [24].

Parameter	Optimal Range
Substrate Temperature	780 - 800°C
Oxygen Pressure	400 - 500 mTorr
Target to Substrate distance	50-60 mm

Tabel 6.1: Example of a parameter set producing a rough film but a working dc SQUID

A lot of research has been done on the effect and interactions of the various parameters and their interaction in producing a high-quality YBCO surface. Below the results of some of these studies have been sorted according to three general headings; namely energy-related considerations, material-related considerations and oxygen-related considerations.

6.1.1.1 Energy-related considerations

Relationship between laser-energy density and target-substrate distance The target-substrate distance has a strong influence on the morphology of the film. One can find an explanation by looking at the properties of the plume, which consists of atoms, oxide molecules, clusters and ions. In a simple model the ablated material expands in a luminous plume until the pressure in the plume is equal to the ambient oxygen pressure [48].

Close to the target the plume species have different velocities and therefore different deposition rates. As a result, films deposited inside the plume exhibit more Ba and less Cu with respect to the 1:2:3 stoichiometry. The stoichiometry refers to the relative amount of atoms of the different elements. Outside the plume the species are thermalised and Cu condensation is preferred. The morphology of Cu enriched films is dominated by particles. Some researchers obtained the optimal electrical and morphological properties when the substrate was located at the tip of the plume emitted from the target [24, 21, 48]. Others found that films prepared at distances longer than the plume have a composition closer to 1:2:3, with the optimum composition at $1.2L$ (where L is the length of the plume) [62].

When the substrate is situated at the edge of the plume, however, the lateral expansion of the plume is not sufficient for satisfactory homogeneity of the film thickness over a substrate area of 1 cm^2 . At a distance of 100 mm the homogeneity is good (a thickness deviation of only 10% over the area), but the increased particle density is unacceptable. To attain both the optimal properties and the thickness homogeneity, one should choose a target-substrate distance of 100 mm and decrease the pressure until the substrate is at the end of the plume again. In order to maintain the position relative to the stability line of YBCO in the phase diagram, it is necessary to reduce the substrate temperature [48].

The length of the plume increases nonlinearly with the laser-energy density. According to Xu et al [21] the relationship between the plume length and the laser energy obeys the empirical equation $(E - E_{th})D^{-2} = 0.14Jcm^{-4}$, where E is the laser-energy density, E_{th} is the threshold laser-energy density which is estimated at $0.11Jcm^{-2}$ for YBCO [22]. Gareia et al [62] found that for a fluence of $1.1J/cm^2$ the length of the visible luminous plume L , generated with the YBCO target, is a function of the oxygen pressure P_{O_2} . This length was experimentally estimated to be $L = 65, 53, 61$ and 57 mm for $P_{O_2} = 0.2, 0.3, 0.4$ and 0.5 mbar respectively.

Relationship between deposition rate and film quality An orthorhombic target gives an optimal film with a pulse frequency of 10Hz, while a tetragonal target gives an underdoped film for the same frequency. Lowering the repetition rate to 1Hz, gives a optimally doped film for the tetragonal target.

This might be the result of better oxygenation of the YBCO on the substrate because of a longer nucleus ripening time. Nucleus ripening is strongly related to the oxygen saturation of the crystal structure. With the lower repetition rate another kind of outgrowth appears, elongated outgrowths that are $0.2 \mu m$ wide and between 0.5 and $4 \mu m$ long. This might be the result of surface modifications that occur on the MgO substrate at high temperatures. The lower repetition rate allows longer formation time before the substrate surface is covered by incoming ablated material [23].

Film thickness and laser fluence The target morphology depends on the laser fluence and the technique through which the laser beam is moved relatively to the target during ablation. The columnar structures frequently observed on laser deposited substrates are directed towards the laser beam; thus their formation can be suppressed by the scanning of the laser beam.

Except for the first few shots, the composition within the entire volume of the plume is the same as that of the target. One therefore averages out the spatial compositional inhomogeneity at the substrate by moving the plume relative to the substrate. To achieve this, the laser spot (demagnified by lenses to a slightly defocused circular spot of diameter of 0.3 cm at the target) was circularly scanned around the entire front surface of the target by repeating a path consisting of three concentric circles, the largest circle having a diameter close to that of the target [55].

Proyer et al [56] investigated the particulates on YBCO thin-films and their relationship to film thickness and laser fluence. They found spherically shaped particulates with sizes typically between 0.4 and a few μm . These particulates are believed to originate from a thin molten layer formed during laser-light irradiation. The number density of these droplets increased with the number of laser pulses. All droplets were found to be Y-rich and Cu-deficient.

On thicker films different types of spherically shaped particulates with pronounced surface structures were observed. They are believed to originate from misoriented growth of YBCO on droplets. Pyramidal

outgrowths also appear on thick films –they have typical sizes smaller than $1\mu\text{m}$ and a stoichiometry similar to the surrounding film. Because they can be avoided by the reduction of the film thickness the pyramidal outgrowths seem to be due to loss of epitaxy with thick films.

There were also rod-like features that have a length of up to several 100 nm and a width of less than 200nm. They appear typically on thicker films and can be suppressed by the reduction of film thickness. Their size and their tendency for 45° orientation increase with increasing film thickness. Because of this it is believed that the rods are a-axis orientated grains nucleating at a certain film thickness.

Besides droplets and rods, a variety of Cu-enriched outgrowths with different shapes were observed. The appearance of Cu-rich outgrowths depends on deposition parameters in a complex way and cannot be attributed to a single mechanism. A statistical DOE can be used to try and isolate this dependency.

Temperature dependence While for droplets no significant temperature dependence of number density is observed, the overall number density of particulates with an average diameter larger than $0.1\mu\text{m}$ shows a slight variation. At low substrate temperatures ($690\text{--}740^\circ\text{C}$) mainly droplets are observed. With increasing temperature however, irregularly shaped, Cu-rich outgrowths appear and they grow in size and number density. Their average diameter increases with T_s , but their number density shows a maximum around $T_s = 770^\circ\text{C}$ [56].

6.1.1.2 Material-related considerations

Influence of target and substrate type and finishing on the quality of the thin film The surface morphology of the substrate depends strongly on the target used but not on the substrate type. All the surfaces deposited from the soft orthorhombic target were covered with large boulders ($d = 0.5\mu\text{m}$) of number density $0.3\mu\text{m}^{-2}$. In comparison the surface of films deposited from harder tetragonal targets is almost free of boulders. The harder targets also give better results when used with higher-quality polished MgO substrates. The softer target gives better morphology with the rougher substrates. For all target-substrate combinations $T_c \leq 86\text{K}$ [23].

The quality of the film is determined in a similar way, not by the substrate type, but by the finishing of the substrate. It was determined by King et al [63] that the YBCO deposited on the as-received substrate exhibits a rough surface morphology, containing a high concentration of outgrowths. The film quality after deposition on annealed substrates (annealed for 40 min) represents a dramatic improvement. In the second case outgrowths have nearly been eliminated. This is because annealing of the MgO substrates reduces the number density of surface steps (i.e. it coarsens the microstructure), providing longer diffusion paths across terraces. Surface steps on MgO are known to act as nucleation sites for YBCO island growth. Therefore it seems logical that the density of outgrowths will be dependent on the number of available nucleation sites.

The annealing treatment was done as follows:

- The substrates were mechanically re-polished (using diamond polishing compound) to a $1\ \mu\text{m}$ finish and then either subjected to an acid wash, or rinsed in acetone followed by methanol.
- The specimens were annealed individually in air for 40 min (full anneal) at an approximate temperature of 1340°C .
- The specimens were protected from the furnace environment by encasing them within a single-crystal MgO holder, which was surrounded by high-purity MgO powder inside an alumina boat. [63]

6.1.1.3 Oxygen-related considerations

Correlation between surface resistance and oxygen pressure during the deposition process. For the applications of high-temperature superconducting (HTS) thin films, it is essential to be able to reproducibly deposit epitaxial thin-films with low surface resistance. For the deposition process it has been found that oxygen pressure has a great influence on the surface resistance R_S and critical temperature T_C . With the increase of oxygen pressure the R_S values first decrease and then increase, giving an optimum oxygen pressure which is substrate dependent. The surface resistance R_S reaches its minimum after T_C reaches its maximum. The increase of T_C at high oxygen pressures can be explained by oxygen over-doping [41].

Oxygen pressure dependence At low pressures the film surface is rough with mainly droplets but also hollows. With increasing pressure, the surface becomes smoother, but small irregularly shaped Cu-rich outgrowths occur. These cause an increase in the number of particles which has a maximum after which it decreases along with further increasing oxygen pressure. A minimum in the overall number density and the fraction of the total area covered with particulates is observed around the same pressures where optimum superconducting properties are achieved. With pressures higher than 1 mbar, irregularly shaped outgrowths occur. The occurrence of these outgrowths at high pressures is correlated to a slight Cu-enrichment within the films and a shrinkage of the length of the visible plasma plume.

It is believed that Cu-rich deposition causes segregation of a Cu-rich phase, which becomes apparent in outgrowths. Compared to Y and Ba, Cu has a smaller size, a higher initial velocity, and less stable oxides. Thus, the probability of oxide formation in the plume is bigger for Y and Ba than for Cu. This might favour the propagation of Cu atoms and ions during plume expansion, which is governed by collisions. Therefore high pressures lead to Cu-enriched deposits because there is a higher probability that Cu atoms and ions can reach the substrate. No Cu-enriched outgrowths are observed with low energies [56].

The observations above suggests that, because low pressures are required during deposition, the only way for YBCO thin films to obtain sufficient oxygenation to be superconducting is through post-annealing in an oxygen atmosphere. According to Gareia et al [62] this model disregards the presence of atomic and ionic oxygen formed by laser ablation.

They investigated the oxygenation of YBCO films during PLD as a function of the target-substrate distance at different oxygen pressures. Using a quenching process, they found that superconducting YBCO films can indeed be formed without any post-oxygenation procedure. In figure 6.2 the results for quenched films are shown. Oxygenation is higher due to the presence of active oxygen species in the laser-induced plasma, whose chemical reactivity is higher than that of molecular oxygen. While the reason for the increase of T_C with distance is still not clear, it is possibly a result of the spatial distribution of the atomic oxygen produced during the collision of O_2 atoms.

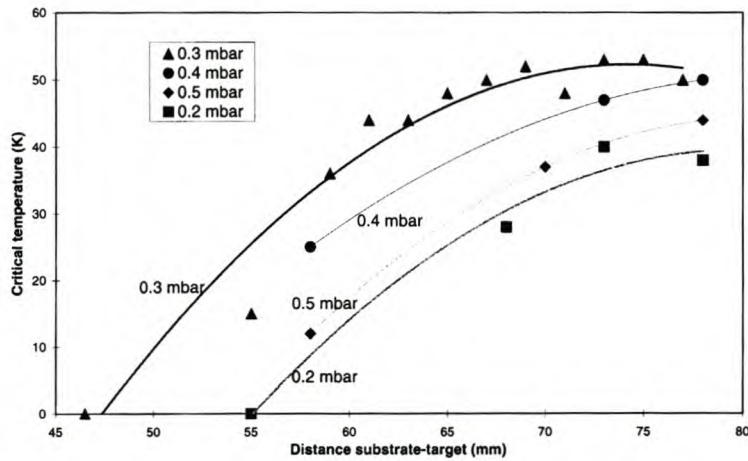


Figure 6.2: The critical temperature dependence on pressure and distance for quenched films [62].

The decrease of T_C with the laser repetition rate can be understood if we consider the decay of the atomic oxygen density after the plasma has been switched off. With each new pulse, new ablated material and atomic oxygen reach the film which increase the oxygen content of the film, but then it decreases again due to recombination. The two dominant loss mechanisms for the oxygen atoms are wall recombination and volume recombination.

Particulates on pulsed-laser deposited Y-Ba-Cu-O films There are two types of irregularities for pulsed-laser deposited Y-Ba-Cu-O films. The first is "droplets" with typical sizes of $0.2\mu\text{m}$ to $3\mu\text{m}$ and the other is big irregularly shaped particulates with diameters of around $10\mu\text{m}$. The big irregularly shaped particulates are directly transferred from the target to the substrate. The ejection of droplets from the target can be related to hydrodynamic instabilities [57], columnar structures at the target surface [58, 73, 59], and subsurface superheating [74].

There are a number of techniques to avoid particulates originating from the target. Among these are modifications of the physical properties of the target [74], special techniques for scanning the laser beam across the target, changes in deposition geometry [75, 76], mechanical masks [77] or shutters [78] between target and substrate, fractionation of particulates by means of a laser beam, deflection of particulates by means of a supersonic oxygen jet [56]. Some of the more popular methods are discussed in section 6.1.2.

6.1.2 Improvements to the PLD process

A number of efforts have been made to improve the quality and the reproducibility of YBCO films. Usually certain changes were made to the normal PLD process in an attempt to obtain better results.

6.1.2.1 Off-axis deposition

One of the preferred ways to improve the PLD process (especially the film smoothness) is by using so-called off-axis deposition.

There are two kinds of particulates that occur on the surface of a YBCO film. The first is an outgrowth, which is caused by various factors integral to the deposition process; the growth process (island vs 2D growth) and surface modification of the substrate are just two of the factors that account for the outgrowths. These particulates can be controlled by careful optimisation of the deposition process.

The other particulates are caused by laser droplets from the target. These particulates are near-spherical precipitates (diameter $\approx 1 \mu\text{m}$) that are only slightly influenced by the deposition parameters because they are an intrinsic characteristic of the PLD process. The aim of the off-axis deposition method is to remove these droplets.

The lighter particles ejected from the target by evaporation show a different behaviour than the droplets (10^{10} times more mass than the Y atoms). The droplets have a rectilinear motion with their trajectory perpendicular to the target surface; but the lighter particles have a component parallel to the target surface. Thus, if the substrate is placed perpendicular to the target, most of the droplets will not be deposited because they have no velocity component perpendicular to the substrate surface; the lighter particles, on the other hand, will be deposited [27].

Boffa et al [27] did an extensive study on off-axis deposition. For their experiment they used a 308 nm XeCl laser with an energy of 80-150 mJ at a repetition rate of 10 Hz. The substrate was placed perpendicular to the target, 5 cm from the target in a quartz tubular furnace, heated by radiation. The substrate and the target were rotated at 25 RPM. At the end of the deposition the chamber filled with O_2 up to

750 mbar and cooled at a rate of $0.15^{\circ}\text{C}\cdot\text{s}^{-1}$ to room temperature, with a 30 min dwell time at 450°C . The energy density at the target was 4 J/cm^2 .

Optimal results were achieved at a substrate temperature of 890°C , an oxygen pressure of 250 mTorr and a laser-energy density of 3 J/cm^2 . The high substrate temperature is claimed to be the result of the low kinetic energy of the particles in the off-axis deposition geometry, two orders of magnitude lower than for the on-axis geometry. To compensate for this a higher substrate temperature is necessary (this could cause a problem with a MgO substrate, causing the kind of outgrowths observed by Farnan et al [23])

A typical on-axis deposited film has droplets with a number density of $n \approx 5 * 10^6\text{ cm}^{-2}$ and some voids with a number density $n \approx 10^3\text{ cm}^{-2}$. The off-axis deposited films showed no outgrowths or voids and they had a much lower number of droplets. The films showed a T_c of 89.5K and a J_c of $2 * 10^6\text{ A/cm}^2$ at 77K.

6.1.2.2 Angled Deposition

Related to off-axis deposition is deposition at an angle. Schmauder et al [94] related this angle to the other deposition parameters as well as the electrical characteristics. They also studied the influence of the angle on SEJ SQUIDS.

The following table (6.2), gives an idea of the qualitative influence of the various angles.

Studied parameter	Fixed parameter	Changing parameter
Film thickness	Angle	Decrease with increasing angle (weaker than $\cos \alpha$ dependency)
Film thickness	Pressure	Increase for 30-50 Pa, constant for 50-70 Pa
Film thickness	Pulse energy	Increase strongly with increasing energy
Droplet density(Area)	Angle	Decrease with increasing angle ($\cos \alpha$ dependency)
Droplet density(Volume)	Pressure	Decrease with increasing pressure
Droplet density(Volume)	Pulse energy	Decrease with increasing energy

Tabel 6.2: Various effects of changing the deposition angle

With step-edge junctions the growth of the YBCO film over the step edge could cause problems. An investigation of growth as a function of deposition angle showed that deposition angles of $\alpha = 30 - 40^{\circ}$ give equal conditions for the slope and the substrate. It was also found that the film surrounding the step shows outgrowths at high angles, while at low angles the step itself shows outgrowths. For $\alpha = 36^{\circ}, 45^{\circ}$ there are no outgrowths. While the normal resistance R_n is independent of the deposition angle, the critical current I_c shows a strong dependence, peaking at $\alpha = 30 - 45^{\circ}$. For SQUIDS fabricated from these step-edge junctions the lowest white noise measured was for $\alpha = 20 - 40^{\circ}$.

6.1.2.3 Oxygen activation

The growth mode of the YBCO thin film depends on the oxygen pressure: the lower the oxygen pressure, the higher the surface quality. It would be preferable to have the oxygen pressure as low as possible while still maintaining a high enough oxygenation of the substrate to achieve good superconducting properties. There are more than one way to achieve this. Marré et al [28] used a pulsed oxygen flow and excited the oxygen with a split part of the laser used for ablation.

The laser was split in two parts; the main part focused on a 1mm^2 area on the target, the second part crossed the gas flow in front of the substrate to excite the oxygen. A mirror on a stepper motor was used to draw concentric circles on the target under PC control. This ensured a homogeneous deposition over the substrate. The oxygen entered the chamber through a pulsed valve. The opening of the valve pulse was centred on the arrival of the plume. The plume arrival was determined by a homemade ionisation gauge showing current spikes at the arrival of ionised particles. The substrate was annealed at 1000°C to optimise its smoothness.

At an oxygen pressure of 10^{-2} mbar the growth mode is tri-dimensional and it showed a large amount of particulates ($10^7 - 10^8$ particulates per cm^2). At pressures below $5 * 10^{-3}$ mbar the growth is bi-dimensional, at least for the first 15 layers – after that tri-dimensional growth appears. Still the surface shows a better smoothness with a lower particulate growth (10^5 particulates per cm^2). X-ray diffraction shows a well-oxygenated film with $T_c = 88\text{ K}$ and $J_c = 10^7\text{ A/cm}^2$ at 4.2 K .

Another approach (by Craciun et al [30]) uses UV radiation to increase the reactivity of the oxygen. They achieved this through the use of a Hg lamp.

The Hg lamp is a low-pressure lamp with a fused silica envelope. The lamp was situated 7 cm in front of the substrate, below the target. This lamp can also be used to clean the substrate of organic contaminants if it is switched on before the deposition.

The final outcome was that there is an optimum substrate temperature at which the UV radiation during PLD resulted in improvements in the film properties. If the temperature is too low, the film is amorphous and showed no improvement; if the temperature is too high, however, the extra energy provided to the oxygen by thermal energy becomes much bigger than that provided by the UV energy. In this case the UV radiation caused little improvement.

6.1.2.4 Shadow masking

Another approach to improve the surface quality is the shadow-mask method. By placing a mask between the substrate and the target the macroparticles are mostly scattered or stopped by the mask. The other particles diffuse around the mask and are deposited on the substrate.

Marcu et al [29] used this approach with the target substrate distance at 45mm and the substrate at room temperature. They inserted a mask 0.5 - 2 cm from the target surface. Two types of masks were used, plane masks of different sizes and a helical mask.

In the case of the plane mask – the bigger the mask, the lower the RMS roughness of the surface. There was, however, a radial dependence of thickness, which was most pronounced for the larger mask. To achieve a more uniform surface, a helical mask was used.

In the design of the helical mask the considerations were:

- The base of the heliod should be the same size as the substrate. This ensures that the shadowed region overlaps the substrate area.
- The transverse steps should be smaller than the wire diameter so that the helical mask is opaque for the plume.
- The longitudinal steps should increase gradually from the tip to the base of the helical mask. This is a compromise between getting a high-quality surface and keeping the surface uniform; short longitudinal steps give a high surface quality but cause a non-uniformity, while long steps give better uniformity but a poorer surface. The increase on the step lengths work because the further the plume is away from the target, the more difficult it becomes for the light particles to drive the macroparticles towards the centre.
- The target to tip-of-the-helioid distance should be optimised for stopping the macro-particles.

Using these considerations the optimal mask was designed with a wire thickness of 2mm, a transverse spacing of 1.5mm and the longitudinal spacing of 4, 5, 6.5 and 11 mm. A tip-to-target distance of 5 mm was determined to be the optimal distance.

Using this setup a YBCO film was deposited with a RMS roughness of 4nm, at a deposition rate of 0.0045 nm/pulse.

6.2 Photolithography

The most common method of pattern definition is optical photolithography; usually UV lithography is preferred because the higher wavelenghts of the light allows for the definition of finer structures.

During lithography a substrate is coated with a light-sensitive material called the photoresist. This material is usually sensitive to light of a certain range of wavelenghts. The exposure of the photoresist to

light (UV wavelength) either causes the resist to soften (positive photoresist) or to harden (negative photoresist). The coating is usually done by applying the photoresist and then spinning the sample at a high speed. The photoresist dries on contact with air. The viscosity of the photoresist and the spinning speed determine the thickness of the layer left on the sample. The sample is covered by a mask containing the pattern that has to be transferred to the photoresist and exposed to UV radiation (contact lithography). The mask is removed and the sample is developed using a chemical that removes the part of the photoresist that has been softened. Then the etching process follows where the area exposed by the process is removed. Finally the photoresist is removed through the use of a special chemical solution. This method can be used for structures in the micrometer range.

For sub-micrometer structures, projection lithography is used. Instead of placing the mask on top of the photoresist, the image of the mask is projected onto the sample through an optical microscope which reduces the size of the image.

The entire process must be done in a clean working area since dust particles and other contaminants will hinder the process. It is also important that the process continue uninterrupted because the photoresist deteriorates after being exposed to air and must be developed shortly after the film is coated.

Another method that can be used for pattern definition is electron-beam lithography. In this method the pattern is defined by scribing with an electron beam on a photoresist sensitive to this beam. This method has two advantages: very fine structures can be etched, and the need for a mask is eliminated. This method requires a high-voltage electron source that can be accurately controlled. This method has been successfully used in the fabrication of Josephson junctions between $0.5\mu\text{m}$ to $2\mu\text{m}$ [96].

6.3 Etching

6.3.1 Wet Etching

Wet etching has been a common tool for the etching of SQUID structures. It has been extensively used at the University of Stellenbosch. Although it is mostly replaced by argon milling, it is still used in some cases. The most common etchants are nonaqueous bromine in ethanol, ethylenediaminetetracetic acid (EDTA), as well as various mineral acids: sulphuric, hydrochloric, nitric and acetic.

Wet etching has the advantage of being chemically selective, that is being able to dissolve just the YBCO without causing damage to either the photoresist or the substrate. It can be used for structures down to the micron range. The disadvantage of wet etching is the high etching rates and the occurrence of under-etching. Under-etching occurs when the etchant removes some of the material underneath the photolithography mask; this is especially problematic in the etching of small structures. Other problems

with wet etching are the temperature sensitivity of the etching processes and the degradation of the superconducting properties of the YBCO (due to a chemical reaction between the YBCO and water during aqueous acid etching) [91, 90].

The most suitable wet etchant was found to be citric acid. It shows a vertical etching profile ($90^\circ \pm 5$) and a small increase in the surface resistance of the thin film. This small increase indicates that there is only a small amount of damage caused by the etchant [116]. There is another etchant, a di-sodium salt of EDTA called Trilon-B that has a much lower etching rate than the others. It also has a much lower undercut, 0-6% compared to the 12-27% of H_3PO_4 . Therefore it could be considered for structures like the flux transformers [91].

6.3.2 Ar-ion milling

6.3.2.1 Patterning of YBCO

Ar-ion milling is the preferred method for the patterning of YBCO. This method uses a stream of accelerator argon atoms to remove material. Ar-ion milling is a non-preferential method that can etch extremely small structures. We also believe that it is easier to control than chemical etching and therefore it is easier to obtain reproducible patterns. The disadvantage of this method is that it can cause damage to the YBCO by local heating, allowing the diffusion of oxygen from the thin film. This leads to a lowering of the transition temperature and an increase in the surface resistance. Furthermore, the fact that it is a non-preferential etching technique causes the photoresist to be etched away along with the YBCO, and this leads to a lower etching profile.

Both these problems can be overcome; the first by cooling the YBCO with liquid nitrogen during etching. The extremely low temperature is needed because of the poor thermal conductance of the substrate material in a vacuum [90]. The second problem can be overcome by using a two-stage reactive etching process where the photoresist mask is first transferred to a carbon mask through the use of reactive-ion etching with oxygen. In reactive-ion etching the material is bombarded with an ion with which the material reacts, leading to a much higher etching rate than usual. The carbon then forms the mask used for etching of the YBCO. Because carbon is much harder than the photoresist, this leads to a vertical etching profile. This second technique is only necessary in sub-micrometer etching – for the lower resolutions the etching profile obtained with normal photoresist is sufficient.

The etching rate can be varied by adjusting the incident angle of the beam. Schneidewind et al found an etching rate of ≈ 22 nm/min for a normal incident beam, which rises to ≈ 30 nm/min for a 20° angle (measured from the axis perpendicular to the substrate) [90]. These values are valid for a typical beam voltage of 500 V and a beam current of 1 mA/cm².

6.3.2.2 Defining step edges

Ar-ion milling is also used for the definition of the substrate steps that are used for step edges. In this section we will briefly discuss the mechanics of the etching process related to the definition of steps in the substrate.

Foley et al[37] reasoned that the ideal lowest noise step edge has a single misorientated grain boundary at the top of the step and a rounded step base that may contain some dislocation, but an insufficient number to create another grain boundary. They experimented with the various milling parameters in order to obtain such a low-noise single-grain boundary. Their work gives an indication of the mechanics of etching – the results can be used to understand the milling process better.

The experiments were done on an MgO substrate. Because the YBCO growths on MgO grow in such a way that the c-axis is always perpendicular to the MgO surface, the J_c can be controlled over 3 orders of magnitude through the variation of the step-edge angle.

The step edge was defined by using a $1.3 \mu\text{m}$ photoresist mask. They optimised the resist profile to obtain side wall angles that were as close to 90° as possible. It is possible through controlling the curing temperature, the exposure time, the ultra-violet light intensity and the development time to obtain side wall angles of 80° - 85° .

The step angle and morphology can be controlled by using different IBE orientations and the step height can be controlled by the etching time. An argon-ion beam from a Kaufman ion gun was used with a beam voltage of 500V and a neutralised beam current of 22 mA/cm^2 . The substrate holder was water cooled.

Various parameters were used to define the angle and morphology of the step. Referring to figure 6.3; α and β define the orientation of the substrate to the ion beam with the direction of the ion beam taken as the perpendicular axis; γ is the off-normal angle of the ion beam with the resist side wall; ϕ is the resultant step-edge angle and χ is the angle of the resist side wall with respect to the MgO substrate.

Effect of the α angle The etching rate varies with the α angle, increasing from perpendicular to a maximum at $\alpha = 50 - 60^\circ$ and decreasing as the glancing angles are approached. The substrate was orientated with the resist edges in such a way that the angle γ stays constant with changing α . For this orientation the etching rate of the side wall is very slow. The step angle ϕ increases with α up to 60 - 70° . For α at 50° and 60° a trench was observed and material buildup at the top for α at 60° and 70° . If the substrate is oriented in such a way that the γ angle changes with the α angle, step edges with a moderate angle $\phi = 30 - 45^\circ$ can be obtained.

Effect of the β angle. Varying the β angle can be used to vary the γ angle; this gives a step edge angle of $\phi = 35 - 40^\circ$.

Final results The etching process of a single step with $\phi = 35^\circ$ and a rounded bottom was finished by doing a final etch with $\alpha = 0^\circ$. This removes back-sputtered material and softens trenches. It also improves the surface roughness of the substrate.

6.3.2.3 Ar-ion milling for SQUID tuning

A related issue is the thinning of SQUID structures by ion milling, done to tune the SQUID devices. Amorphous YBCO (YBCO deposited at room temperature) is suggested as a milling mask. It was found that it is possible to thin the structures without damage – microbridges could be thinned down to 80nm without effecting the critical temperature [90].

It was also shown that it is possible through this thinning process to treat a step-edge junction in such a way that the t/h ratio is increased, so that the junction moves from flux-flow behaviour to RSJ-like behaviour [90].

6.4 Summary

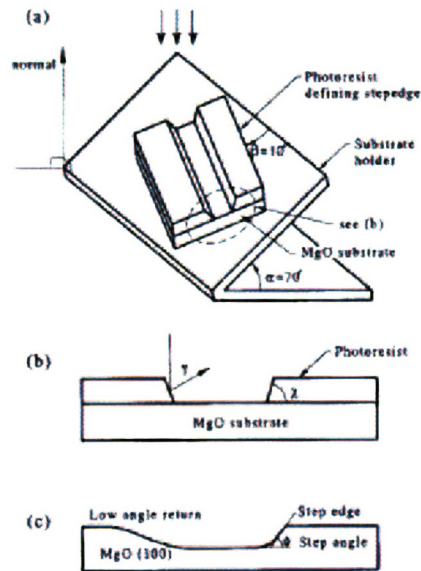
In this chapter the various fabrication steps were discussed in detail. For the PLD process the influence of the various parameters have been discussed. The important parameters in this discussion are:

- The oxygen pressure
- The substrate temperature
- The target-substrate distance
- The laser fluence
- The target and substrate quality and finishing
- The deposition rate
- Various interactions of the above-mentioned parameters

It was seen that the surface quality of the YBCO thin-film can be improved through off-axis deposition and shadow masking. The superconducting properties can be improved through annealing, oxygen activation and angled deposition.

For the photolithography the most common method is UV-lithography, although e-beam lithography has also been used successfully.

There are two types of etching: chemical etching and ion milling. Both of them have positive and negative aspects but ion milling is the preferred method. Ion milling has the added advantage that it can be used for defining step edges and for the tuning of SQUIDs.



Figuur 6.3: Definition of the various orientation angles for ion milling [37].

Chapter 7

Design of Experiment

In this chapter design of experiment is introduced, which is the method that will be used for the characterisation and optimisation of the various fabrication sub-processes. The applicability of these principles are not isolated to any one field – it could easily be extended to other fields and other areas of superconductive research. The principles of experimental design are mainly applied to analysing and optimising processes where no qualitative model of the process exists. It is also used where operator error, measurement error and random error make it difficult to distinguish between an effect for a specific input and random effects.

The field of experimental design is too great to be totally covered in this chapter. Experimental design has a foundation of statistical principles which are beyond the scope of this thesis. Therefore only the basic principles required to explain the methods used in the following chapters will be introduced at a conceptual level in this chapter.

First the author will motivate the use of experimental design. This specific approach will be compared with commonly used experimental methods and the advantages of experimental design methods pointed out. Then some of the basic concepts will be introduced. This will be followed by a discussion of the specific methods used in the rest of the research process.

7.1 Motivation

7.1.1 Terminology

Before the motivation some terminology needs to be introduced. The process on which the experiment is being performed can be seen as a “black box” This box has certain inputs, called *parameters*. Parameters are those values on a system that can be changed –*controllable parameters*; or if not changed, at least

measured –*uncontrolled parameters*. Changes in these inputs could lead to changes in the outputs of the system, these outputs are called *responses*. A response (for our purposes) can be defined as an output that provides some kind of information about the quality of the final product of the process.

7.1.2 Comparison of experimental design with the previously used method

The most common method of optimising a process is known as the *one-parameter-at-a-time* optimisation. In this process the parameters are each set at a certain value, which are usually determined by knowledge about the system concerned. A certain range over which each parameter will be varied is also chosen. Then a single parameter is varied in its range and the response is measured. The value of the parameter that corresponds to the optimal response is then chosen and the parameter is fixed at this value. Then the next parameter is optimised in the same way, until all the parameters have been optimised. The whole process is then either repeated or the system is considered as optimised.

The method described above is also the method used here at Stellenbosch during the previous efforts at optimising the PLD process [26, 25]. It is also used in most of the literature associated with the optimisation of the PLD process [76, 48, 21, 63, 56].

One-parameter-at-a-time optimisation methods can achieve good results, but they have certain inherent problems. The first is their inability to optimise for two-parameter interactions. A second problem is the fact that these methods provide relatively little information for the amount of experiments. There are also no proper mathematical tools to extract information about the relative importance of the parameters.

Experimental design on the other hand, has a solid foundation in statistical theory and supply the maximum amount of information per experiment (it also has the ability to model two- and even higher parameter interactions). Experimental design can be used both to characterise a system –providing a mathematical model through regression analysis– and to optimise the system.

These advantages show that experimental design is extremely well suited for a complex process like pulsed laser deposition (PLD) and even other less complex fabrication sub-processes like photo-lithography and Ar-ion milling. It has already been shown to give good results for the optimisation and characterisation of the PLD process. Two researchers recently used experimental design for the optimisation of the PLD process [111, 110].

At the University of Stellenbosch the high noise rejection, thanks to the statistical nature of the experimental design, compensates for some of the noise caused by poor maintenance of the equipment. The high material cost also favours the use of a more efficient method, like experimental design.

7.2 Designing experiments

This section explains functioning of and the philosophy of experimental design. A very good book on the subject was written by Douglas Montgomery [112]. In this section only a quick overview of the design process will be given. In the following sections the more advanced concepts and the methods used in the rest of the research process will be discussed. These methods are: factorial design, fractional factorial design and the Taguchi method.

7.2.1 Basic concepts

There are three concepts central to experimental design; that of replication, randomisation and blocking.

Replication refers to the repetition of the basic experiment, which enables an estimate of the experimental error. The experimental error allows one to determine whether observed differences in the data are significant or whether it could be the result of random factors.

Randomisation is the cornerstone of statistical methods in experimental design. Both the allocation of experimental material and the order in which the individual runs are performed must be random. This is because statistical methods require that the observations must be independent, random distributed variables.

Blocking is used to make a comparison between various factors more precise. There are factors (nuisance factors) which cannot be measured or which are of no interest, but which might cause differences in the response. The effect of these factors can be reduced by dividing the experiment into a block of relatively homogeneous conditions.

7.2.2 Statistical foundation

Since experimental design is based on statistical methods, a few important concepts need to be revised. This will be done by using an example.

In the UV lithography process we used a UV light through a chrome mask to expose photoresist. The photoresist is developed in a developer and then rinsed in deionised water. Let us, for the moment, assume that the quality of the SQUID is determined by the steepness of the photoresist edges after UV lithography. The parameters are chosen as the UV exposure time A and the development time B . The response is the steepness of the photoresist edge. We use three different values for both parameters. For one of the parameters (ignoring the other one for the moment) we can construct an experiment table (table 7.1).

Run no.	Exposure time (A)	Edge steepness
1	20 s	y_1
2	30 s	y_2
3	40 s	y_3

Table 7.1: Example design table for an experiment on UV lithography

We write the responses (the edge steepness) as y_i where i denotes the run. There is a certain amount of random error present, due to intensity variation of the UV light and inaccuracies of the timer among others things. If we therefore observe a difference between the response y_i and y_k for $i \neq k$, this difference could either be the result of the change in the input parameter or of random error. To determine the likelihood that the difference is the result of random error we need an estimate of the random error. This can be done if we have more than one measurement for a certain parameter value. The second measurement is usually achieved by repeating the experiment. If we suspect measurement errors as well, we could also take repeated measurements to obtain an estimate of the measurement error.

The random error is in all cases assumed to be a Gaussian distribution with a mean μ and a variance σ . The mean and variance can be estimated from repeated experiments by calculating the mean and variance of the set of values. For example: assume that we repeat the experiment in table 7.1 j times, then the mean is

$$\bar{y} = \frac{\sum_{i=1}^j y_i}{j} \quad (7.1)$$

and the variance is

$$S^2 = \frac{\sum_{i=1}^j (y_i - \bar{y})^2}{j - 1}. \quad (7.2)$$

The moment we have an estimate of the random error it is possible to calculate the probability that the difference between two responses could be due to random error. If this probability is small enough (typically $< 5\%$) we assume that the difference is due to the change in the input parameters.

Experimental design is based on these principles and is therefore extremely useful in providing information on which parameter changes have a significant influence on the response. In experimental design we change multiple parameter values between runs and in the end do an analysis similar to the one above to determine the effect of each parameter on the response. In section 7.4.1 we explain analysis of variance, this is the technique used in experimental design to analyse the experiment.

7.2.3 The design process

According to Montgomery[112] the process can be divided into the following steps:

1. **RECOGNITION OF AND STATEMENT OF THE PROBLEM.** A clear statement of the problem gives a better understanding of the phenomenon being studied and of the final solution to the problem. A list should be prepared of the specific questions and problems that should be addressed by the experiment.
2. **CHOICE OF FACTORS, LEVELS AND RANGE.** Looking at the various parameters that may influence the performance of the system, the researcher must decide which of these are potential design parameters and which are nuisance parameters. The design parameters are those that will be used in the experiment; the nuisance parameter are other parameters that could influence the response but are not included in the experiment. The effect of the nuisance parameters will manifest as noise in the experimental results. Together with the parameters the researcher must also choose the range over which these factors will be allowed to vary. To be able to do this a good knowledge of the process is required.
3. **SELECTION OF THE RESPONSE VARIABLE.** The response variable should provide useful information about the process being studied. More than one response variable can be used. An important consideration is the gauge capability (measurement error) of the response; if this is inadequate, only large parameter-effects can be distinguished. For a large spread in the measurements it is recommended to repeat some measurements several times and then take the average of these measurements.
4. **CHOICE OF EXPERIMENTAL DESIGN.** This choice involves choosing the experimental design, the sample size, the run order, whether blocking will be used and whether randomisation restrictions apply. During this part of the process the objectives of the experiment is very important.
5. **PERFORMING THE EXPERIMENT.** The execution of the experiment itself must be carefully planned, since any errors in performing the experiment will destroy the validity of the results. Montgomery also suggested that a few pilot or trial runs of the experiment should be done. This enables the researcher to obtain an estimate on the consistency of the material and the measurement- and experimental error. It might be necessary to revisit the decision made in step 1-4, based on the results of a pilot run.
6. **STATISTICAL ANALYSIS OF THE DATA.** The advantage of statistical analysis is that the results will be objective rather than subjective. Here the use of statistical software is a necessity for all experiments except the most simple. Using this software, the result can be presented in an empirical model through the use of equations based on the data. It also provides residual analysis and model adequacy checking. The statistical method does not provide an absolute measure of the optimal point or the characteristics of the system, but allows us to select the most probable results.
7. **CONCLUSIONS AND RECOMMENDATIONS.** "Once the data has been analysed, the researcher must draw practical conclusions about the results and recommend a course of action"[112]. The conclusions must be validated with further experimentation.

These guidelines will be followed to a certain extent in the research process. The next section will describe the experimental design method without the reasons for the selection of this specific method. The reasons will be treated in section 8.1.

7.3 Factorial designs

For experiments involving two or more factors factorial designs are often the most efficient method. With a factorial design, each complete trial of the experiment contains all possible combinations of the factors investigated.

It has already been mentioned that experimental design gives much more information per experiment than one-parameter-at-a-time experiments. In the case of factorial designs, this can be illustrated in the following way. Returning to the example in section 7.2.2, we have two factors: exposure time A and development time B . We assume each of them has two levels denoted as A^+ and A^- and B^+ and B^- . Now suppose we vary the factors one at a time to obtain information on both factors (one-parameter-at-a-time optimisation). Then the effect of changing A can be written as $A^+B^- - A^-B^-$ where A^+B^- and A^-B^- represents the response at the respective parameter values. The same can be written for the changing of the B parameter, $A^-B^+ - A^-B^-$. We then have three observations, A^-B^- , A^+B^- and A^-B^+ . To estimate the experimental error, we need at least two estimates of the response for changing each parameter. To achieve this we need to do a second run of the experiment, which gives a total of six observations.

For a factorial design one more observation would be added to the original experiment –the response at A^+B^+ – which gives four observations. But using this extra measurement, two estimates can be obtained for the A effect, $A^+B^- - A^-B^-$ and $A^+B^+ - A^-B^+$. The same can be done for the B effect. Thus we have two estimates of each parameter, but now using only four observations instead of the original six. These effects are just as precise as those from the one-parameter-at-a-time experiment, but with a relative efficiency of $\frac{6}{4} = 1.5$. The efficiency is obtained by looking at the amount of runs needed in each experiment to obtain a certain amount of information, this efficiency will increase as the number of factors increase [112, pp. 170-175].

This increased efficiency is useful when the raw materials are expensive or the process is time-consuming (like with PLD). One of the most common types of factorial designs is the 2^k factorial design. This design will be discussed in the next section.

7.3.1 The 2^k factorial design

“The 2^k design is particularly useful in the early stages of experimental work, when there are likely to be many factors to be investigated. It provides the smallest number of runs with which k factors can be

studied in a complete factorial design.” [112, pp. 218]

The 2^k factorial design is a special factorial design where there are k parameters, each with only two levels. The example in section 7.3 will be a 2^2 factorial design, because it has two parameters each at two levels. The parameters can be quantitative or qualitative. Because there are only two levels the response is assumed to be linear over the range of the factors chosen. This is a reasonable assumption when initially studying a system. If this assumption is of potential concern centre points can be added to the design. The number of runs in each experiment is 2^k runs if centre points are added this increase the number of runs by the amount of centre points. For a 2^2 design this gives 4 runs.

The levels of the factors can be arbitrarily called “low” and “high” –these can be represented as -1 and 1 values. The table giving the parameter values for each run of the experiment is called a *design table*. This design table typically contains only the levels 1 or -1. A separate table shows which physical value the level refers to. An example is shown in table 7.2.

Run	A	B	C	Labels
1	-1	-1	-1	(1)
2	1	-1	-1	a
3	-1	1	-1	b
4	1	1	-1	ab
5	-1	-1	1	c
6	1	-1	1	ac
7	-1	1	1	bc
8	1	1	1	abc

Table 7.2: The 2^3 full factorial design

From the observation of one complete run, the main effects as well as all the interaction effects can be determined. More on the analysis of the results will be said in section 7.4.

7.3.2 Fractional factorial designs

As the number of factors increase, the amount of total runs necessary for a full factorial design quickly becomes prohibitive. For example a complete or full factorial design with 6 parameters gives $2^6 = 64$ runs to completely characterise all main and interaction effects. But of these 63 degrees of freedom only 6 correspond to main effects and only 15 to two-parameter interactions. The remaining 42 degrees of freedom correspond to three-parameter and higher interactions. Usually these higher order interactions are negligible. Thus, the information on all the important effects can be obtained by only running a fraction of the original experiment.

Like the full factorial design, this method is most appropriate for screening experiments. After screening a more thorough investigation of the important effect could be done, using more than two levels.

In order to generate a fractional factorial design it is necessary to eliminate a fraction of the runs. A way must be found to decide which experimental runs to do and which to leave out. One would like to eliminate the higher order interactions but keep the main effect and the two-parameter interactions. Two ways of achieving this will be discussed: the first is the use of a *generator* and the second is called the *Taguchi method*. The generator will be discussed in the next section and the Taguchi method in section 7.3.3.

Because we are eliminating runs from the experiment, there is a loss of information. This loss is reflected in the fact that some of the effects become aliased with each other. This aliasing is discussed in section 7.3.2.2.

7.3.2.1 The generator

It is possible to construct a table that shows all the factorial effects in a full factorial experiment. The way in which this table is constructed will not be discussed, but most statistical packages are able to construct these tables. An example of such a table for a 2^3 factorial design is shown in table 7.3.

Treatment Combination	I	A	B	AB	C	AC	BC	ABC
(1)	+	-	-	+	-	+	+	-
a	+	+	-	-	-	-	+	+
b	+	-	+	-	-	+	-	+
ab	+	+	+	+	-	-	-	-
c	+	-	-	+	+	-	-	+
ac	+	+	-	-	+	+	-	-
bc	+	-	+	-	+	-	+	-
abc	+	+	+	+	+	+	+	+

Table 7.3: The Algebraic signs for calculating effects in a 2^3 design

This type of table can be constructed for any factorial design; every possible combination of factors is shown in the table. All columns contain an equal number of positive and negative signs.

To eliminate the higher-order interactions, only the rows for which the higher order column has either a positive or negative value are included in the experiment. The generator denotes the combination of parameters which are used. In a 2^3 experiment, which has the factors A , B and C , the generator will probably be ABC . The use of a single generator give a one-half fraction of the original experiment or a 2^{k-1} fraction. For each higher fraction another generator is added. For instance, for a one-quarter fraction or a 2^{k-2} experiment, two generators will be used.

7.3.2.2 Aliasing

Aliasing means that it is not possible to differentiate between some of the effects. For example: if A is aliased with BC , it will be impossible to tell whether a certain response is the effect of the A parameter or the BC parameter interaction. When estimating the A effect we are really estimating $A + BC$. As long as the effects (e.g. BC) which are aliased with the effect one wants to measure (e.g. A) can be assumed to be negligible this aliasing is not a problem.

To determine the alias structure the generator is multiplied with each of the factors. The result together with the knowledge that any squared parameter simply reduces to 1 gives the alias structure. For a large number of factors this can be done using statistical software packages.

7.3.2.3 Design resolution

The resolution of a design is determined by the aliasing. The resolution is indicated by a subscript, e.g. 2^{3-1}_{III} donates a resolution III design. The following resolutions are of importance:

Resolution-III designs These are designs where no main effect is aliased with any other main effect, but main effects are aliased with two-parameter interactions and two-parameter interactions may be aliased with each other. Resolution-III designs will only be used if one is sure that there are two-parameters interactions.

Resolution-IV designs These are designs where no main effect is aliased with any other main effect or any two-parameter interaction, but two-parameter interactions are aliased with each other. This design can be used if one knows that there are only a few known two-parameter interactions. The experiment must then be designed in such a way (by choosing the right generators) that the significant two-parameter interactions are aliased only with insignificant two-parameter interactions.

Resolution V designs These are designs where no main effect is aliased with any other main effect or any two-parameter interaction. Also no two-parameter interactions are aliased with each other but two-parameter interactions are aliased with third-order interactions. This design is used when one does not know which parameters interact.

7.3.3 Taguchi method

The Taguchi method use orthogonal arrays to enable the selection of certain important main parameters and two-parameter interactions in such a way that they are not aliased. Especially in situations where

resolution-IV designs are used, this enables the researcher to select the important second-order interaction so that they are not aliased with other important second-order interactions. I used the Taguchi method in my experimental design for the characterisation of the PLD process.

The Taguchi method contains many pitfalls; the generators that it produces could lower the resolution of the design and as such lead to a loss of information for instance and it is also possible for main effects to be aliased with two-parameter interactions. This can cause problems when analysing the design, these problems will be discussed in more detail in Chapter 11.

7.4 Analysis

Experimental designs are analysed by statistical methods. The principles of the statistical theory behind these methods were already discussed in section 7.2.2. As mentioned before, the response to a parameter at a certain value can be expressed as a random variable with a mean and a variance. The variance is a consequence of human error as well as the inherent variability of the process. To know whether a certain change in the response (corresponding to a change in parameters) is significant, one has to obtain an estimate of the variance of the response for identical parameters. This can then be compared to the change in the response associated with a change in the value of a parameter. From this comparison the probability that the parameter change is significant can be computed. One of the important tools for doing this is the analysis of variance treated in section 7.4.1.

Analysis of the results also involves the generation of models. Model parameters can be computed from the measurements. These models can be used to extra- and interpolate the data to obtain estimates for other data points as well as for optimising the system. An important subset of these models is the checking of the adequacy of the model.

7.4.1 The analysis of variance (ANOVA)

From the analysis of variance one can extract the variance of the noise in the system as well as the variance associated with a change in the parameter values. Comparing these two variances enables us to determine whether the parameter has a significant effect on the response.

Let us use the example in section 7.2.2 again. First consider only the exposure time A . Take the response for i levels of A and repeat the experiment j times. Each of the observation points in the experiment can be expressed as

$$y_{ij} = \mu_i + \epsilon_{ij}, \quad (7.3)$$

where μ_i is the mean and ϵ_{ij} is the error associated with the ij th observation. The same can be done the for development time B . The observation y_{ij} can also be written as

$$y_{ij} = \mu + \tau_i + \epsilon_{ij}, \quad (7.4)$$

where μ is the overall mean for the specific parameter and τ_i is a variable unique to the i th treatment, $\mu_i = \mu + \tau_i$. This can be used in hypothesis testing to determine the significance of any parameter. The null hypothesis will be $\tau_1 = \tau_2 = \dots = \tau_i$ for all i , this means that there is no difference between the means for the various levels of the parameter A and therefore that parameter A has no effect on the response. If parameter A does have an effect on the response one would be able to, by comparing the variance of τ and ϵ , determine how significant the effect is.

The analysis of variance is derived from a partitioning of the total variability into its component parts. The total corrected sum of squares is an indication of overall variability of the data. This can be partitioned into a sum of squares of the differences between the treatment averages and the overall mean (the variance of τ) and the difference within treatments from the treatment average (the variance of ϵ). The difference between the treatment averages and the overall mean is a measure of the differences between treatment means. The difference within the treatments from the treatment averages is due to random error. Thus we can obtain two estimates of σ^2 the one based on variability within treatments and the one on variability between treatments. If there is no difference between the treatments (the null hypothesis) we expect the two estimates to be similar. If they differ it is an indication that there is a difference between the treatment means.

A statistical software package is usually used for the analysis of variance. One such a package used in this thesis is Design-Expert [115].

7.4.2 Models

There are three basic models used in the analysis of the experimental data. Two of these models have already been discussed in section 7.4.1: the means model (7.3) and the effects model (7.4). In this section the regression model and the concept of model adequacy checking will be introduced.

All of these models can be reduced to contain only the parameters that have a significant effect on the response. In a fractional factorial design one cannot obtain an estimate of the error if one does not eliminate some parameters from the model. One has less runs than necessary to fully describe the system. Thus if all the possible parameters and combinations are included in the model, one is left with no degrees of freedom for the use of estimating the error. One way to solve this problem is to replicate the experiment. But another more practical, solution is to eliminate some of the insignificant parameters from the model. These parameters can then be used to provide an estimate of the error in the process.

The parameters to be included in the model are usually selected using a half-normal plot of the estimated parameter effects. Those effects that deviated from the straight line are selected as important responses. The output of the ANOVA gives an good indication of whether these parameters are sufficient or not.

7.4.2.1 Regression model

Quantitative and qualitative data are treated in exactly the same way during the initial design and analysis of the experiment. However, for the purpose of further analysis, the researcher might be interested in the quantitative data over the entire range of data, although only a few points have been considered for the purpose of the experiment. In this case an interpolation equation would be useful. Regression analysis is a general approach for fitting such empirical models. In the case of factorial analysis this would involve fitting a linear model to the data, or a quadratic model in cases where the centre point data is available.

7.4.2.2 Model adequacy checking

For all three models considered it is necessary to check the adequacy of the model, since there are certain assumptions that has to be valid for an accurate model.

One of these assumptions is that the observations are adequately described by the model, whether it is a means, effect or regression model. It is also assumed that the errors are normal and independently distributed with a mean of zero and a constant but unknown variance.

To determine the adequacy of the model used for the analysis of variance, it is useful to look at the output of the ANOVA. Below is a report produced by Design-Expert (PLD analysis of the c-axis length). We will briefly discuss some of the measures which can be used for checking the adequacy.

Use your mouse to right click on individual cells for definitions.

```
Response:      C-axis length
ANOVA for Selected Factorial Model
Analysis of variance table [Partial sum of squares]
Sum of          Mean      F
Source Squares DF      Square Value  Prob > F
Model    0.97   4      0.24   8.52   0.0022  significant
A        0.18   1      0.18   6.25   0.0295
B        0.28   1      0.28   9.75   0.0097
E        0.27   1      0.27   9.55   0.0103
BE       0.24   1      0.24   8.53   0.0139
Residual 0.31   11      0.028
Cor Total 1.28   15
```

The Model F-value of 8.52 implies the model is significant. There is only a 0.22% chance that a "Model F-Value" this large could occur due to noise.

Values of "Prob > F" less than 0.0500 indicate model terms are significant. In this case A, B, E, BE are significant model terms.

Values greater than 0.1000 indicate the model terms are not significant.

If there are many insignificant model terms (not counting those required to support hierarchy), model reduction may improve your model.

```
Std. Dev 0.17   R-Squared    0.7560
Mean    11.86  Adj R-Squared 0.6673
```

```
C.V.      1.42    Pred R-Squared  0.4838
PRESS     0.66    Adeq Precision  7.794
```

The "Pred R-Squared" of 0.4838 is in reasonable agreement with the "Adj R-Squared" of 0.6673.

"Adeq Precision" measures the signal to noise ratio. A ratio greater than 4 is desirable. Your ratio of 7.794 indicates an adequate signal. This model can be used to navigate the design space.

The F value is an indication of the significance of the model as well as the various effects. The R^2 measures the portion of the full variability of the data that is explained by the model, this gives an indication of the accuracy of the model. The problem with this value is that it will always increase if parameters are added to the model, even if they are not significant. To compensate for this, the adjusted R^2 measure is defined as R_{adj}^2 . R_{adj}^2 is adjusted for the size of the model, this measure decreases if non-significant terms are added to the model. Thus we see from the ANOVA that the model accounts for 66% of the variability of the data.

The PRESS statistic is a measure of how well the model will predict new data –the smaller the PRESS value, the more likely that the model is a good predictor of new data. Related to this is the R_{pred}^2 or prediction- R^2 statistic. This indicates how much of the variability in new data we expect the model to be able to predict. The ANOVA shown above indicates that the model is expected to explain about 48% of the variability in new data.

A power tool for checking the assumptions is the examination of the residuals. The residual for observation j in treatment i is defined as

$$e_{ij} = y_{ij} - \hat{y}_{ij} \quad (7.5)$$

where y_{ij} is the observation and \hat{y}_{ij} is an estimate of the corresponding observation. The estimate is the value predicted by the regression model. For an adequate model the residuals should be structureless –they should have no obvious patterns. There are many graphical techniques for examining the residuals of which a few will be briefly discussed below.

The Normality assumption A check of the normality assumption is made by a normal probability plot of the residuals. The plot should resemble a straight line. For small sample sizes, however, moderate deviation is acceptable. Sometimes this plot will show a residual that is significantly larger than the others. This could severely distort the analysis of variance and must be investigated. Figure 7.1 is an example of such a plot, generated by *Design-Expert*.

Plot of Residuals in Time Sequence This plot is helpful in detecting correlation between the residuals. If there is a tendency for runs of positive or negative residuals, it could imply that the error is not independent. Another common problem that can be detected is a tendency for the data to drift or become more erratic. This is an indication of a change of error variance over time and could be the result of a change in the skill of the operator as the experiment progresses. Figure 7.2 shows an example of this plot.

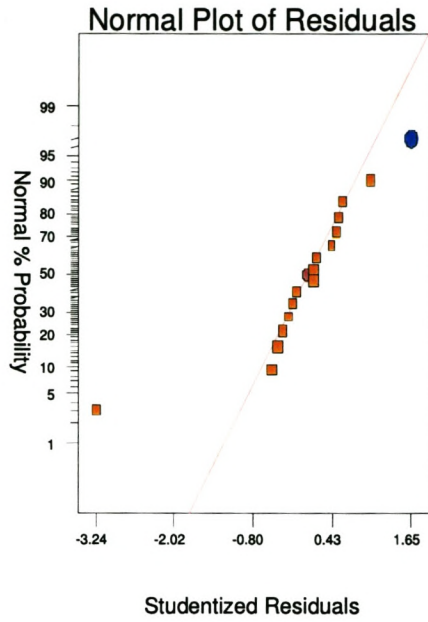


Figure 7.1: Normal probability plot of the residuals (C-axis length PLD)

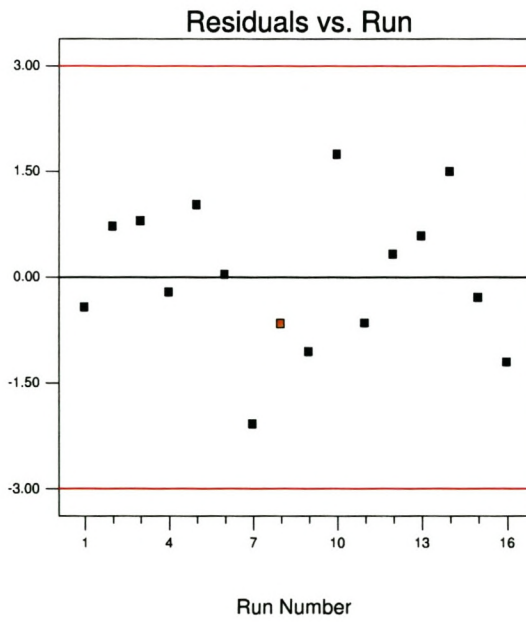


Figure 7.2: Plot of residuals versus run (Surface roughness PLD)

Plot of Residuals Versus Fitted Values For a correct model and the correct assumptions, the residuals should be structureless. If the size of the variance increases with larger observations, it could be an indications of problems with the measuring equipment. Sometimes problems in this domain can be solved using transformations of the original data. Figure 7.3 shows an example of this plot.

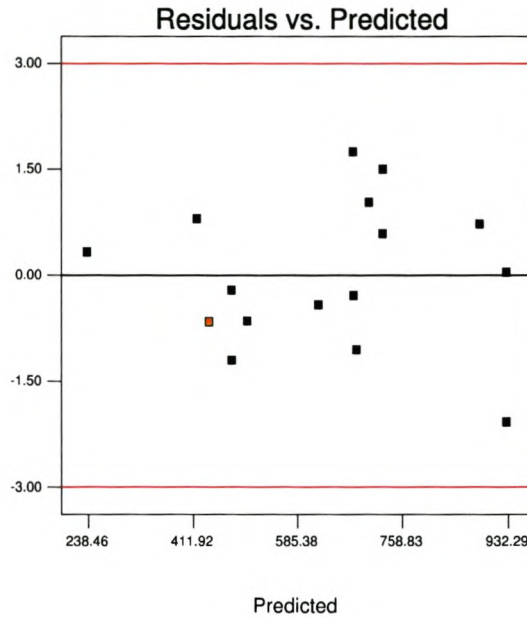


Figure 7.3: Residuals versus predicted(fitted) values (Surface roughness PLD)

7.5 Summary

This was just a basic introduction to the field of experimental design. Most of the tools that were used, were presented in this section. In the following chapter the way in which these methods were applied to the research process will be presented.

Chapter 8

Characterisation of the manufacturing process

In this chapter the various subparts of the SQUID fabrication process –with a description of the work done in the development, improvement, re-definition and characterisation of the various processes will be presented. Most of the work has been done on the pulsed laser deposition (PLD) process but substantial effort has also been put into the other two processes. The patterning and etching processes.

The work done on the design of the physical SQUID structure will be presented separately in chapter 9.

8.1 The PLD process

The basic principles of operation have already been described in section 6.1. In this section the specific PLD device used at the University of Stellenbosch will be described, as well as some of the adjustments and improvements made to the device. Then the characterisation of the process will be described, starting with the identification of the important parameters and finally a description of the DOE, the experiments, the measurements and the analysis will be given.

8.1.1 The PLD setup

The PLD system we used at the University of Stellenbosch was originally designed and built in 1995 at the National accelerator centre (NAC) –now renamed to iThemba Labs– by Maritz et al [26, pp. 46]. The system is schematically similar to the PLD device discussed in section 6.1. The schematic is reproduced here together with a photo of the actual system (figure 8.1).

The laser is a Lambda Physic EMG 203 MSC XeCl excimer laser, with a 30 ns pulse duration and a wavelength of 308 nm. The laser power is varied by adjusting the voltage on the laser electrodes

between 18–25kV. The laser frequency can also be varied between 1–100Hz. The laser is reflected at an angle of $\pm 60^\circ$ before it enters the PLD chamber where it is focused to a spot of 1.2×0.7 mm on the target.

The target is mounted on a steel holder which is attached to a carousel that allows lateral displacement and rotation of the target. The target is rotated in order to prevent that a hole is burned into the target, which could pull the plume off centre by as much as 20% [26, p. 47]. Furthermore the target is displaced laterally to get more efficient use of the target material. After each run the target must be resurfaced. This is done through the use of various degrees of sanding and finishing with a $1 \mu\text{m}$ diamond polish. There is also a pre-ablation run of ± 1 min to remove any large loose particles. During this pre-ablation the substrate is covered by a shutter to prevent deposition.

The substrate holder is heated by radiation. The assembly consists of a water-cooled reflector and a heat shield. The reflector focuses the energy on a stainless steel substrate-holder to which the substrate is attached with silver paint, to ensure good thermal contact. A overhead-projector lamp from Philips (DZJ-7804, 240V, 900W) is used to radiatively heat the substrate holder. The heat shield prevents unnecessary heating to the rest of the chamber. The photo in figure 8.2 show the substrate heating assembly.

The temperature of the substrate is determined by a K-type thermocouple attached to the substrate holder. The temperature is adjusted by a variac which adjusts the voltage on the lamp. This rather crude setup used at the moment is shown in figure 8.3.

The PLD chamber is equipped with two vacuum pumps used in conjunction with a rotary vane pump allowing a base pressure of $\pm 2 \times 10^{-6}$ to be reached. The pumping-down time to the base pressure depends on the many factors but varies between 6 hours and 24 hours.

The oxygen is passed through a commercial ozone generator before entering the chamber. The oxygen flow is controlled by a needle valve which is adjusted for a constant pressure inside the chamber. The flow is obtained by operating one turbo-molecular pump through a bypass during deposition. The ozone generator is either switched off or operated at maximum voltage.

8.1.2 Improvements to the system

8.1.2.1 The heating element

The first improvement, already described above, was the construction of a radiative heating element. A cheaper heating element was necessary after the first element failed and it became apparent that the replacement would cost in the order of R 7000. The experiment of radiatively heating the substrate holder started off with smaller Osram bulbs encased in a stainless steel cylinder. The lifetime of these bulbs were rather short due to the high temperatures (800°C). We decided to replace these bulbs with a

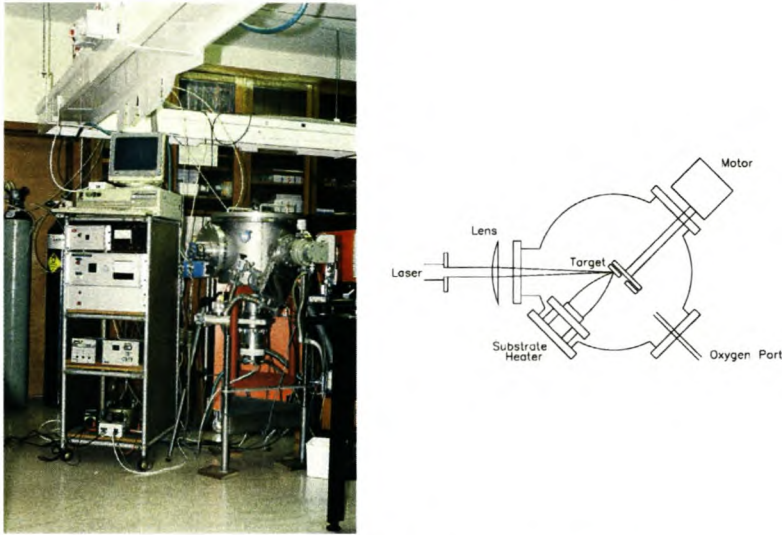


Figure 8.1: The schematic and photo of the NAC PLD system

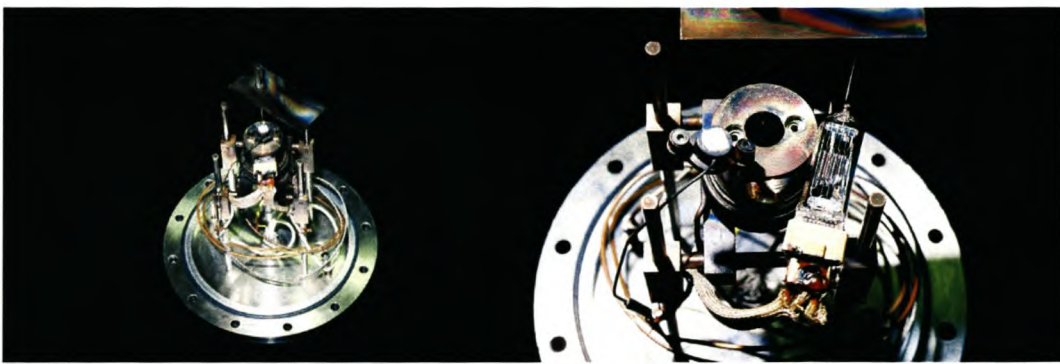


Figure 8.2: The back-plate (left) with a close up of the substrate-heater assembly (right)



Figure 8.3: The setup to control the substrate-heater.

larger bulb capable of higher power, because the previous bulbs were being operated close to their limit of 200 W.

This new bulb has proven to be much more durable and capable of reaching the required temperatures with ease. The new bulb has been operating for 3 months now, without needing replacement.

8.1.2.2 The laser beam profile

The second improvement has been to the laser beam profile. The beam profile of the excimer laser has deteriorated due to worn electrodes. It has deteriorated to such an extent that some of the main power in the beam has spread to the sidelobes. When focused on the target, the energy in the sidelobes does not provide enough energy to vaporise the surface layer of the YBCO, but could heat it up enough to make the formation of droplets energetically favourable. This could increase the surface roughness of the thin film on the substrate.

To solve this problem the laser beam was characterised using a slit scanner consisting of a metal plate with a thin slit attached to a translation stage. The slit was scanned across the laser beam and the energy coming through the slit was measured by an energy detector. This was done in the horizontal and vertical direction, so that the most homogeneous part of the beam could be found. We then constructed a rectangular aperture to filter out this part of the beam. Figure 8.4 shows the profile of the laser beam measured by the use of a vertical and horizontal slit. The red lines indicate the part that was filtered through the aperture.

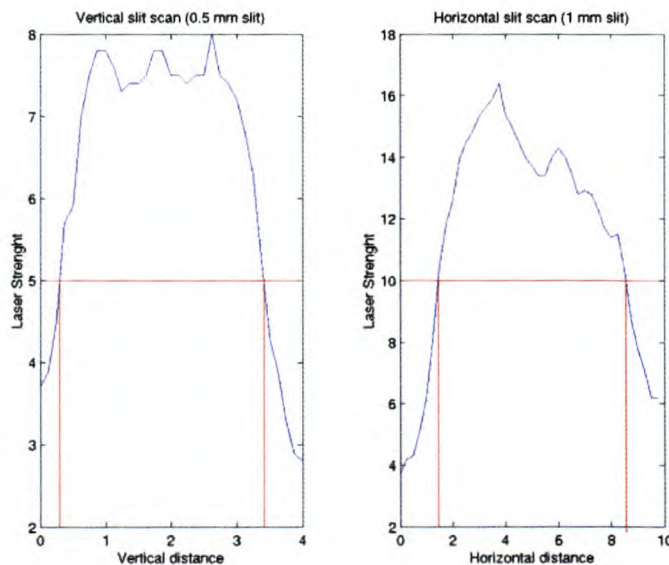


Figure 8.4: Cross-section of the laser beam

8.1.3 Experimental setup

As a substrate single crystalline MgO of $10 \times 10 \times 0.5$ mm with a lattice orientation of $\langle 100 \rangle$ was used [113]. The lattice orientation refers to the alignment of the a -, b - and c -axes of the cubic unit cell, it is written as $\langle abc \rangle$. The a - and b -axes of the YBCO unit cell will tend to line up with the a - and b -axes of the MgO unit cell. The tendency of this alignment is determined by the lattice mismatch between the YBCO and MgO crystals –in this case it is 9%. This is larger than that of SrTiO (which is 2%) but it still gives good alignment as long as the deposition conditions are optimal. Thus the MgO substrate acts as a template for the growth of the YBCO crystal.

We used $\langle 100 \rangle$ MgO because of the high anisotropy of superconductivity in YBCO, the coherence length ($\xi_{ab} = 3.1$ nm and $\xi_c = 0.51$ nm) and the critical current density is much higher in c -axis orientated crystals than in a -axis orientated crystals [26, p. 25]. In c -axis orientated crystals the long axis of the unit cell is perpendicular to the plane of the substrate onto which it was deposited. The MgO crystal is epitaxially polished by the supplier [113]. It was cleaned with acetone or ethanol before attaching it to the heater assembly.

The target was a pressed, tetragonal $\text{YBa}_2\text{Cu}_3\text{O}_{7-x}$ (99.995%) target of 1" by 1/4". It was mounted on the target carousel and prepared according to the procedure described in the previous section. The target rotation speed was adjusted according to the laser pulse frequency.

The distance between the target and substrate is adjustable between ± 20 mm and ± 70 mm. The distance was adjusted to the required distance and checked using a caliper. The accuracy was estimated at ± 5 mm.

The substrate temperature was held at the required temperature ± 10 °C during the deposition. After deposition and annealing a process was followed where the substrate was cooled down in the presence of 1 atm of O_2 . It was first cooled down at a maximum speed to 450 ± 30 °C where it was kept for 1 hour before switching off the heater to allow cooling of the substrate to room temperature.

As previously mentioned both the laser power and pulse frequency were adjusted. The deposition time was arbitrarily set to a time sufficient to have a thick YBCO layer. The PLD procedure is included in Appendix A.

8.1.4 Design of Experiment for the PLD process

The purpose of this experiment was to characterise the PLD process so that it can be optimised for both robustness and quality. To do this the important parameters must be determined as well as the effect of each of these parameters on the quality of the YBCO thin-film. To do this the researcher decided on a factorial experiment. The parameters are each set at two levels, which are their upper and lower limit.

There are six parameters of interest; for a full factorial design this would require $2^6 = 64$ runs. With expensive materials and a time requirement of ± 1 day per experiment these are too much runs. Since only the main effects and a few of the second-order effects are considered to be important, a 2^{k-2} (quarter fraction) experiment was decided upon. This gave a resolution IV design, which means no main effect is aliased with any other main effect or any two-parameter interaction, but two-parameter interactions are aliased with each other. The design requires $2^{6-4} = 16$ runs, two centre point runs were added to allow the modelling of quadratic effects. This gave a total of 18 runs.

8.1.4.1 Parameters

In this section the parameters and ranges over which they were chosen is presented. The parameters, ranges and motivation for these choices are given without references since these were discussed in section 6.1.

Laser energy The first important parameter is the laser energy –this must be above a certain threshold level for stoichiometric deposition. It is expected to have an influence on the surface roughness of the substrate and the oxygenation of the YBCO layer. The range over which it can be varied is partly determined by the available laser power, the system losses and the spot size. The energy is given in J/cm^2 and is determined by dividing the total incoming laser energy by the area on which the laser is focused, the energy loss through the system is also taken into account. An effective maximum energy of $3.5 \text{ J}/\text{cm}^2$ was determined through measurement. This is with a spot size of $0.8 \times 2.7 \text{ mm}$. A lower boundary of $2.5 \text{ J}/\text{cm}^2$ was chosen.

Oxygen pressure The second parameter was chosen to be the oxygen pressure. This parameter together with the laser energy determine the length of the plasma plume. The oxygen pressure could influence the amount of oxygenation of the YBCO layer and the critical temperature. A wide range of optimal values for the oxygen pressure is described in the literature. The lower boundary of the experiment was chosen to coincide with the lower extreme value reported in the literature. The upper bound was determined by the amount of pressure that the turbo-molecular pump could handle. From these considerations a lower bound of $5 \times 10^{-2} \text{ mbar}$ and an upper bound of $2 \times 10^{-1} \text{ mbar}$ was chosen.

Target to Substrate distance According to the literature the target-substrate distance is optimal when the substrate is located at the tip of the plume. The ratio of the plume length and this distance play an important role in the roughness and stoichiometry of the YBCO layer. Depositions made inside the plume are reported to be yttrium rich, while depositions made outside the plume are copper rich. This played a role in selecting the distance range. The upper bound was chosen just beyond the tip of the plume when

at its longest and the lower bound was chosen just inside the plume when at its shortest. This gave a range of 40 – 60 mm.

Laser pulse frequency The laser frequency could have an influence on the oxygenation of the YBCO layer because of a phenomenon known as nucleus ripening. Nucleus ripening refers to a interaction between the oxygen and the deposited layer. This interaction takes place between laser pulses. The laser frequency was chosen from the literature as the upper and lower bound reported to give optimal results. This gave a range of 4 – 10 Hz.

Ozone generator Because of the interaction of the oxygen and the YBCO layer the researcher wanted to investigate whether increasing the reactivity of the oxygen could have any positive effect on the system. It would be particularly useful if the oxygen pressure could be lowered without disturbing the level of oxygenation. This would improve the surface quality of the YBCO layer. Experiments using anatomic oxygen instead of molecular oxygen were reported in the literature but these experiments failed to consider some of the interactions that might be important. Because of the cost of anatomic oxygen the researcher decided to use ozone (O_3), which has a much higher reactivity than oxygen. The ozone was generated using a commercial ozone generator adapted to my purpose (see figure 8.5). As parameter we used $O_3 = \text{on}$ or $O_3 = \text{off}$.

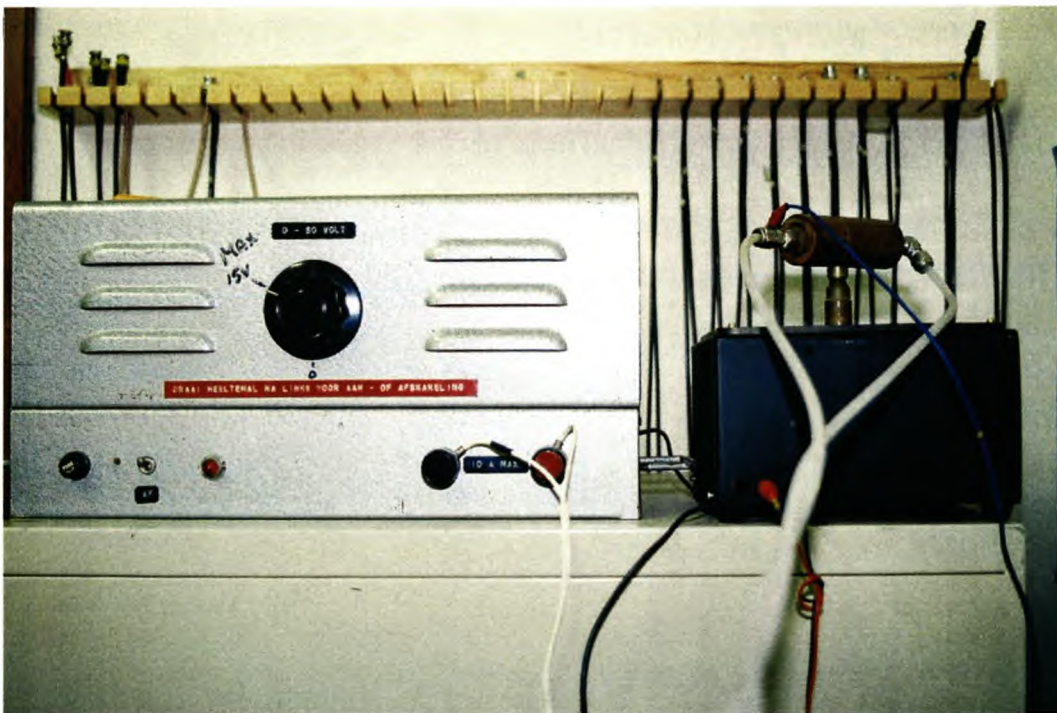


Figure 8.5: A photo of the ozone generator

Substrate temperature The last parameter is the substrate temperature. For the YBCO to be in the superconducting tetragonal state, the temperature of the substrate has to be above 680 °C. Below this point the YBCO will tend to be amorphous and non-superconducting. The temperature also has an influence on the critical temperature and the oxygenation of the YBCO layer. It is furthermore possible that high temperatures could worsen the surface quality of the substrate due to the formation of outgrowths.

As lower boundary a temperature of 720 °C was chosen. This is slightly below the optimal values reported in the literature but will allow a better observation of the effect of the oxygen activation. As upper boundary 800 °C was chosen. This is close to the maximum obtainable temperature.

8.1.4.2 Selection of interactions

A table containing all the experiments with the value for each of the parameters was created. Because we have a resolution-IV design the second-order effects will be aliased with other second-order effects. If, however, the second-order effects can be manipulated in such a way that the important effects are aliased with effects that are assumed to be negligible, the important effects can be modelled. This selection was done using the Taguchi method.

The Taguchi method (discussed in section 7.3.3) uses a set of figures like the one shown in figure 8.6. The numbers on the figures correspond to a table of orthogonal arrays. This table can be found in appendix B, the appendix also contains a complete set of the L_{16} linear graphs. To enable the modelling of certain interactions the parameters must be chosen in such a way that the important interactions are connected by a line.

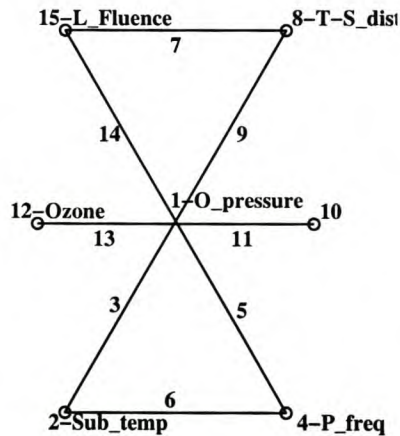


Figure 8.6: A Taguchi linear graph of L_{16}

The following interactions are considered to be important:

Oxygen pressure ⇔ **Laser energy** ⇔ **Target-Substrate distance** These three parameters interact, each in a separate two-parameter interaction and all together in a three-parameter interaction. It is impossible to model three-parameter interactions with a resolution-IV design; therefore only the two parameter interactions will be characterised.

Oxygen pressure ⇔ **Ozone** As mentioned above part of the experiment is to investigate this interaction, it will be the first time that this is done. This will show if the activation of the oxygen will allow the lowering of the oxygen pressure.

Oxygen pressure ⇔ **Pulse frequency** ⇔ **Substrate temperature** The pulse frequency determines the nucleus ripening time and the oxygen pressure determines the amount of oxygen present during the ripening time. The heat from the substrate thermally activates the oxygen close to the substrate. It is possible that a higher oxygen pressure or higher temperature will allow for higher pulse frequencies. An increase in substrate temperature could lead to a lower required oxygen pressure.

The six parameters from section 8.1.4.1 are assigned to points on the linear graph (as show in figure 8.6). The values can then be read from the corresponding columns in the orthogonal table. The run order is then randomised and this gives the experimental procedure shown in Appendix C.

8.1.4.3 Responses

In order to determine the influence of the parameters on the quality of the YBCO thin film, certain responses must be selected. These responses must correspond to the quality of the film in some way.

The researcher chose three responses: the surface roughness of the thin film, the level of oxygenation and the superconducting transition temperature.

Surface roughness The surface roughness is important for device fabrication and intrinsic noise of the Josephson junctions. If the surface roughness is too high the patterning resolution falls and it is unlikely that good junction behaviour will be observed. The surface roughness also has an effect on the intrinsic noise of the junctions, because rougher surfaces allow for easier penetration of flux vortices. The best surface reported in the literature is a boulder- and outgrowth-free surface with an rms-roughness of 4 nm. The lower the surface roughness is, the better.

The roughness is determined by anatomic force microscopy (AFM). With this method the surface of the thin film is raster-scanned using an extremely fine tip that comes into physical contact with the surface. The tip is attached to a cantilever which is attached to a piezo-electric actuator. A laser beam is reflected off the back of the tip, this allows position of the tip is determined by a photo-detector. The tip is deflected by the differing heights on the surface this gives a deflection of the laser beam. The output of

the photo-detector is fed back to the piezo-electric actuator to maintain a constant force on the tip. This output which is used to maintain the constant force gives the height data with a nanometer resolution.

The output from the AFM is processed through the use of special software, which allows three dimensional visualisation of the surface as well as determination of factors like the rms-roughness and maximum deflection height. The area that can be scanned varies from $130 \times 130 \mu\text{m}$ down to $5 \times 5 \mu\text{m}$. AFM is a non-destructive technique since the force on the tip is in the order of nanonewtons [26, p. 55]. A typical AFM picture is shown in figure 8.7.

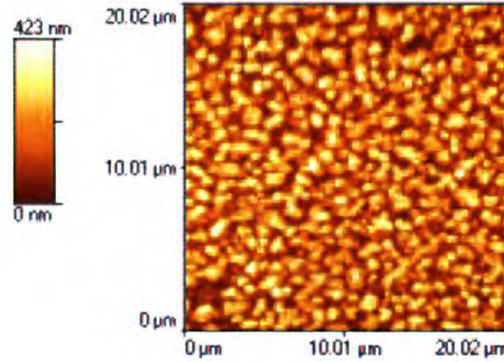


Figure 8.7: AFM measurement of sample 10 at a $20 \mu\text{m}$ resolution

In determining the surface roughness, a measurement was taken at three places on the substrate in order to get an idea of the average surface roughness. The measurements were taken at $100 \times 100 \mu\text{m}$, $20 \times 20 \mu\text{m}$ and $5 \times 5 \mu\text{m}$, which allow both the larger and smaller surface defects to be investigated. Software [114] was used to analyse the images. From the topography map the following were determined: average roughness, root mean square roughness, the ten point height, the summit density and the 5-10% height intervals. The average roughness is given by

$$S_a = \frac{1}{MN} \sum_{k=0}^{M-1} \sum_{l=0}^{N-1} |z(x_k, y_l) - \mu|, \quad (8.1)$$

where the figure is an $M \times N$ matrix, $z(x_k, y_l)$ is the height at the specific (x, y) coordinate and μ is the mean height. The root mean square average is defined as

$$S_q = \sqrt{\frac{1}{MN} \sum_{k=0}^{M-1} \sum_{l=0}^{N-1} [z(x_k, y_l) - \mu]^2}. \quad (8.2)$$

The ten point height S_z refers to the average height of the 5 highest local maximums plus the average height of the 5 lowest local minimums. The summit density S_{ds} is an indication of the number of local maximums per unit area

$$S_{ds} = \frac{\text{Number of local maximums}}{(M-1)(N-1)\delta x \delta y}. \quad (8.3)$$

The 5-10% height interval S_{dc} is related to the bearing curve. S_a , S_q , S_{ds} and S_{dc} were multiplied together to give a figure of merit shown in equation 8.4.

$$\text{Figure of merit} = S_a \times S_{ds} + \frac{S_z}{5} + S_{dc} \quad (8.4)$$

This figure of merit shows a fair agreement between the size of the figure and the roughness of the substrate. The higher this figure, the worse the quality of the substrate.

Level of oxygenation The level of oxygenation is the second response and it is important both in determining the critical temperature of the thin film and the quality of the deposition.

The level of oxygenation of the thin film was determined through X-ray diffraction (XRD) measurements. XRD provides information on the crystal structure of the sample which is measured. From this information the orientation of the crystals as well as the length of the various axes can be determined. Because the amount of oxygen has an influence on the length of the c-axis of the YBCO crystal, this information allows determination of the amount of oxygenation of the thin film.

During XRD the sample is radiated with x-rays. These rays reflect from the various crystalline planes in the sample and undergo constructive and destructive interference with each other. This provides information on the crystalline structure of the sample. In order to explain this phenomenon more thoroughly diffraction and Bragg's law will be discussed.

The atoms in crystalline solids form a regular array that acts as a diffraction grating for electromagnetic waves if the wavelength is of the same order as the space between the atoms. The wavelength of x-rays are of the same order as the space between atoms (≈ 1 nm). In a crystal many sets of parallel planes can be drawn through the positions of the atoms and the planes of every set are separated by characteristic distances. Each family of parallel planes can be seen as a set of slit-type diffraction gratings for x-rays. For every family the rays will scatter from a given plane for which the reflection angle equals the incident angle, because at that reflection angle the wavelets emitted by each atom add constructively. Because the x-rays penetrate the crystal, this reflection will occur at different planes. If the path length between two planes are a integer multiple of the wavelength the reflections will also experience constructive interference. The difference between two path lengths can be written as $2d \sin \theta$, where d is the separation between the planes. Thus

$$2d \sin \theta = n\lambda \text{ where } n = 1, 2, 3, \dots \quad (8.5)$$

This expression is known as Bragg's law. If this condition is satisfied, constructive interference will occur. The spacing between the maxima in the interference pattern is correlated to d , the separation. By rotation of the x-ray beam and the detector around the sample, various crystal plane separations can be determined. From the intensity of the reflection a deduction can be made about the amount of atoms in the crystalline plane. This information can be correlated to a database containing standard x-ray

diffraction angles in order to determine the crystalline structure of the specific sample. Figure 8.8 shows a typical XRD plot, the blue lines are data from the database for $\text{YBa}_2\text{Cu}_3\text{O}_7$.

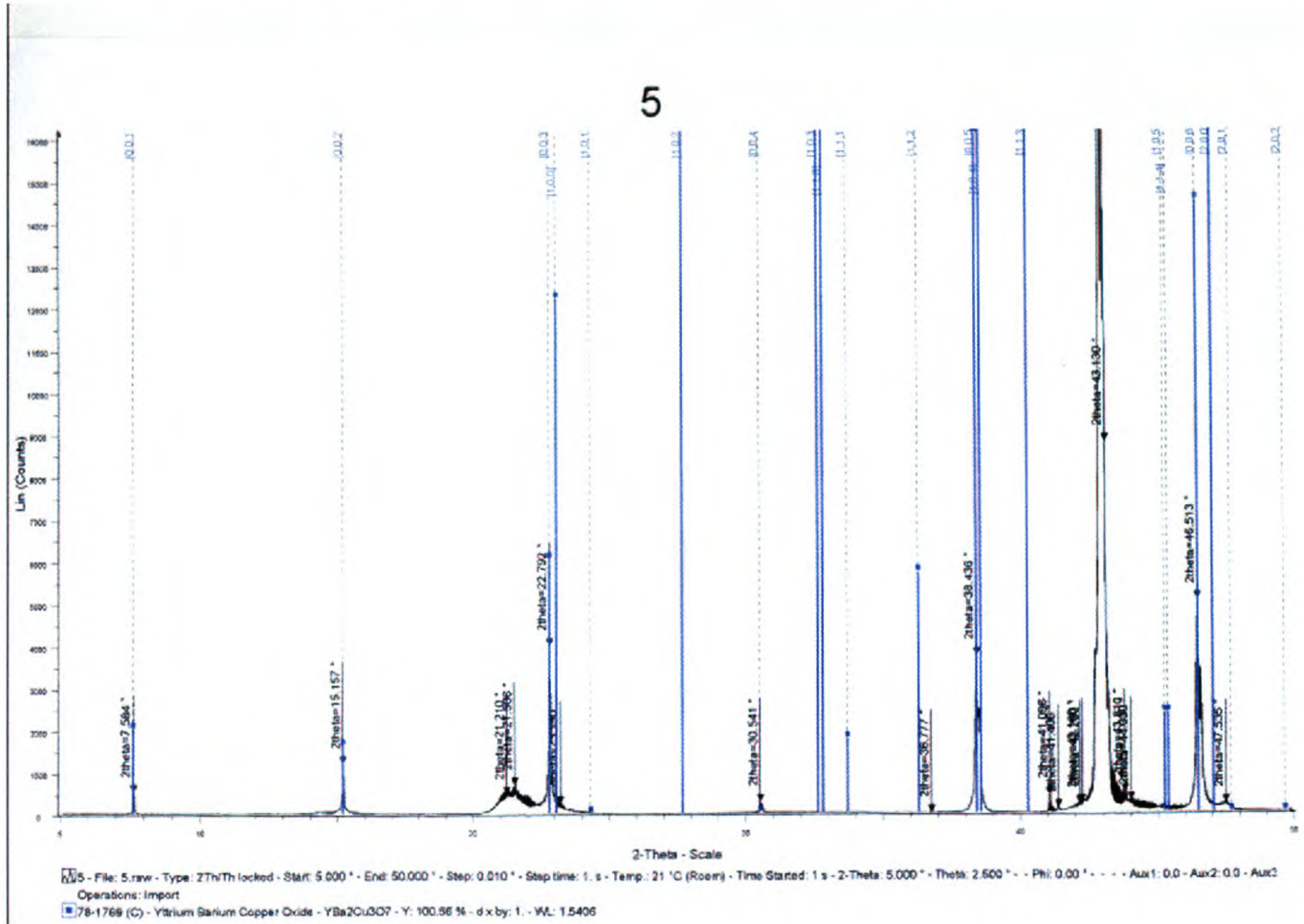


Figure 8.8: A XRD measurement of YBCO thin film

From the position of the peaks in the XRD plot the c -axis length can be calculated (using equation 8.5) for peaks of which the Miller index is $\langle 00n \rangle$, this indicates that the measurement is in the c -direction. The shorter the c -axis the better the oxygenation of the sample.

Critical Temperature The critical temperature is the third response and it gives a good indication of the quality of the YBCO thin film. The higher the temperature at which the superconducting transition takes, place the better the quality of the thin film. A critical temperature transition point above 88 K is preferable. The critical temperature, T_c can be measured in two ways. The first is a four-point-probe measurement, the second is a susceptibility measurement. The four-point-probe measurement is more widely used, but we were not able to get the four point probe measurement to work. We therefore used the susceptibility measurement.

The susceptibility measurement gives a good overall picture of the quality of the film, since it uses the Meissner effect to determine T_c . It also causes no damage to the substrate, compared to moderate damage caused by the four-point-probe method. The susceptibility measurement measures the ac magnetic susceptibility of the thin film. The test apparatus consist of two coils; a planar coil and a cylindrical coil, attached to a cold finger. The whole assembly is placed inside a vacuum to provide thermal isolation. The cold finger is cooled down using a liquid helium cryo-cooler. This whole assembly is shown in figure 8.9.



Figure 8.9: Magnetic susceptibility measurement setup

The sample is placed between the two coils. The cylindrical coil is driven by a 1 MHz sinusoid to generate a magnetic field perpendicular to the surface of the sample –the magnetic field is picked up using the planar coil. After amplification and filtering the voltage is plotted as a function of the temperature of the cold finger. As the sample passes through T_c and become superconducting, the magnetic field penetrating the sample is expelled according to Meissner's theory. This causes a drop in the voltage measured over the sensing coil. From this measurement the transition point can be determined. Figure 8.10 shows a typical susceptibility measurement. The drawback of this measurement is that the position of the transition point is affected by the film thickness as well as the strength of the magnetic field. This measurement is taken by using the cryo-cooler to cool down the sample while the susceptibility is monitored via a computer. The cryo-cooler can achieve temperatures down to 20K after about 3 hours. For more information on the susceptibility meter please refer to the operating manual [125].

8.2 The patterning process

The current patterning facility at the university of Stellenbosch is a UV-lithography setup. The setup consists of a resist spinner, a forced air convection oven, a digitally controllable hot plate and a Karl Süss MJB3 mask aligner. As photoresist we used Shipley S1818 and Shipley MF319 as developer.

The patterning of microstructure, using this setup, has already been characterised by several researchers [25, 26, 116]. It is believed that the results they achieved show that it is possible to define a pattern at the required resolution. For the purpose of this thesis the method developed by Knox-Davies [26] is preferred with a few adaptations to ensure better repeatability.

Knox-Davies proposed use of professionally manufactured chrome contact masks; he has proven these masks to give a superior quality pattern definition. Using these masks he was able to define patterns down to $1\mu\text{m}$, although there are doubts about the repeatability. Using these techniques, however, it is definitely possible to define patterns down to $4\mu\text{m}$ without problems. Knox-Davies points out the importance of fresh photoresist and developer.

We made certain adjustments to try and improve the quality and repeatability of the patterning process. The first was the manufacturing of a temperature bath to keep the temperature of the developer at a constant $21\text{ }^{\circ}\text{C}$. This was done because of the sensitivity of the development speed to the temperature. This temperature bath is shown in figure 8.11. The developer was put inside a water bath, the temperature of this bath was regulated using a controllable heating element. The room was kept at a temperature of $18\text{ }^{\circ}\text{C}$, the water bath was isolated from the room using polystyrene plates.

The flow diagram of the UV-lithography process is shown in figure 8.12. The detailed method for executing each one of the steps is compiled in instruction manuals available at the micro-fabrication lab. The last few steps in this diagram refer to the chemical etching of the thin film. The etching will be discussed in the next section (section 8.3).

For every new batch of photoresist and developers the pattern definition process needs to be tuned to maintain the process at its optimal point. This can be done using a one-parameter-at-a-time optimisation or a fractional factorial design. The important parameters in this process are firstly the development and exposure times and secondly (perhaps less important) the soft-bake type and the temperature. The soft-bake type refers to the way of baking. There are two ways of baking: baking in a forced air convection oven and baking on a hotplate. The hard bake is seen as part of the etching process and is therefore not important at this time. If all four factors are tuned at the same time, this will give a 2^{4-k} experiment with a maximum of 16 runs for a full characterisation. However, for the purpose of tuning the process only the soft-bake time, development time and exposure time is considered. The soft-bake temperature was fixed at the manufacturer's recommended temperature of $90\text{ }^{\circ}\text{C}$. This gives a 2^3 factorial experiment which consists of 8 runs. The table of factors and levels will be given in Appendix D. These experiments were not executed, but this is the suggested method for tuning the process at the start of every new batch.

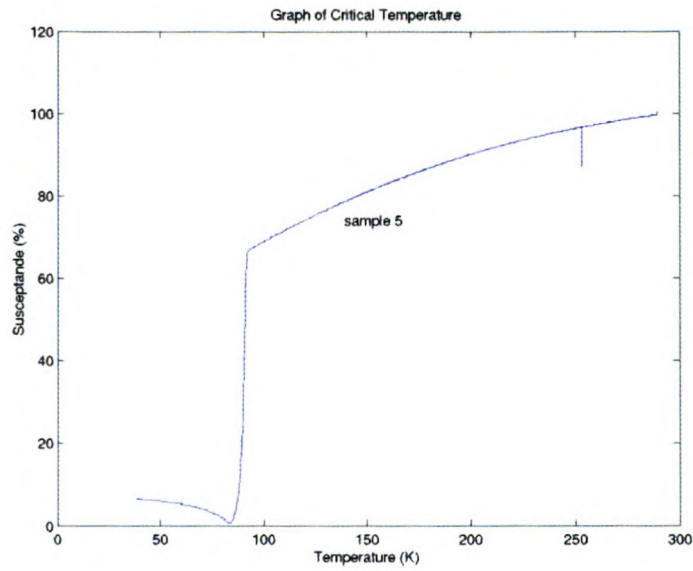


Figure 8.10: The susceptibility measurement, plotted as % susceptibility against critical temperature.

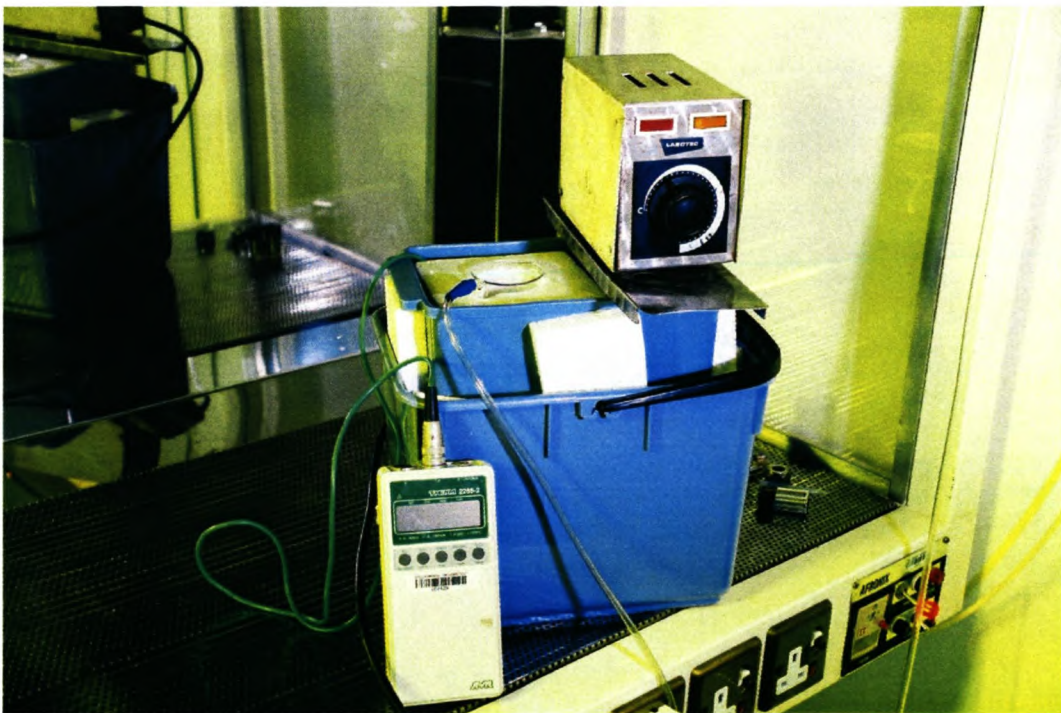


Figure 8.11: Isolated temperature bath

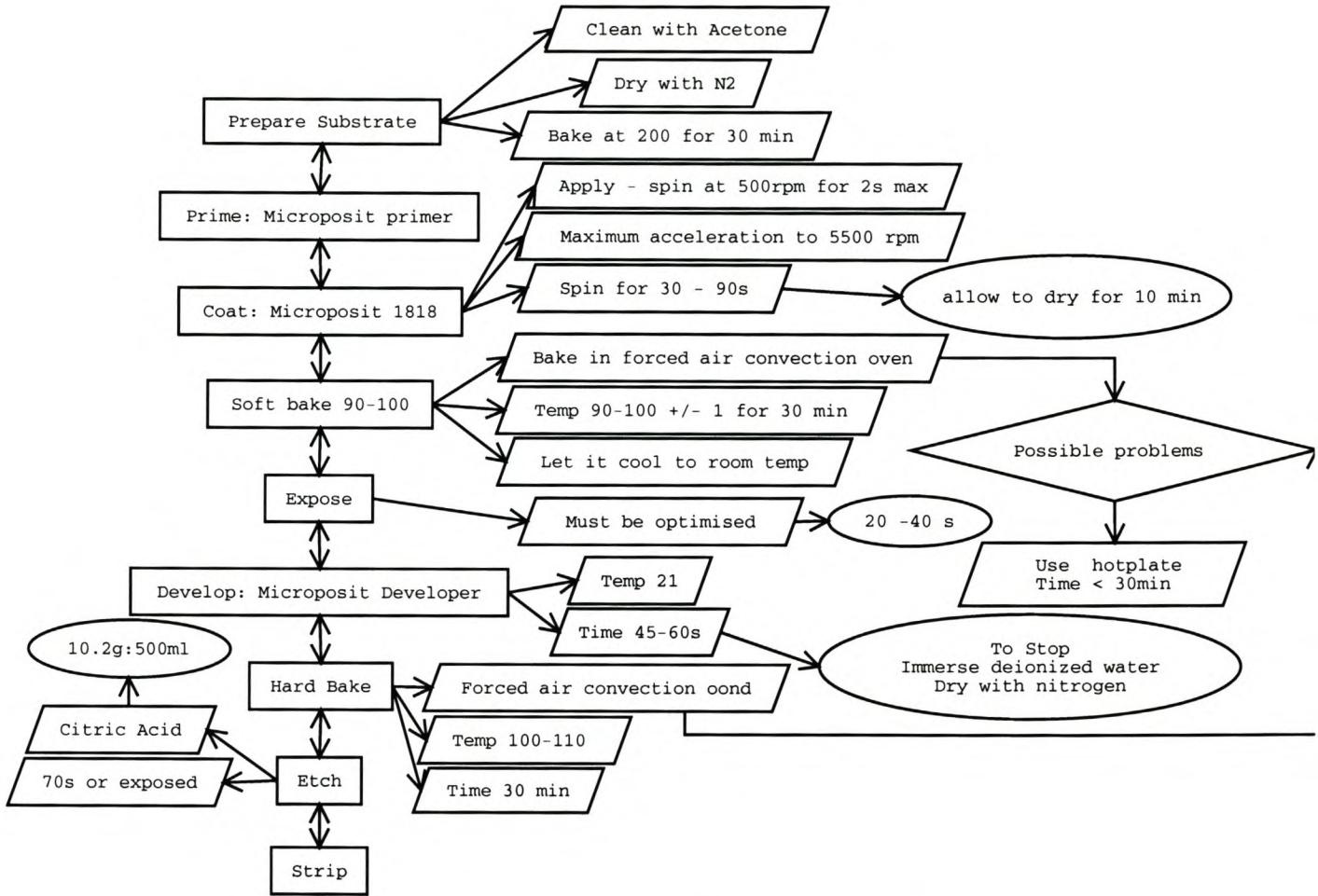


Figure 8.12: Flow diagram of the UV lithography process

8.3 The etching process

There are two types of etching: wet etching and dry etching. Wet etching or chemical etching uses a chemical substance that dissolves the YBCO thin film in the places where it is not covered by the photolithography mask described in the previous section. Dry etching or ion milling uses a stream of particles to physically remove the YBCO, by bombardment, in places not covered by the photoresist.

It was decided to use Ar-ion milling for the etching process, all the considerations leading to this decision were covered in section 6.3.2. However, at the present there is only one ion-milling facility in South Africa and the researchers were unable to obtain permission to use this commercial facility. Therefore it was decided to develop an Ar-ion mill.

8.3.1 Principles of ion milling

An ion mill consists of a discharge chamber where the ions are produced and an ion-extraction system that extracts and accelerates these ions. Ions are produced when electrically neutral atoms lose or gain electrons, giving them a positive or negative charge. These charged ions can now be manipulated using electric and magnetic fields. There are many ways in which atoms can be ionised, which lead to a large variety of ion sources. The ion source we decided to build is called an rf multicusp ion source.

RF ion sources use a radio-frequency energy source to ionise the chosen gas. In these sources the RF energy is coupled to the gas in an inductive manner using a coil. The energy causes the induced electron flow to ionise the gas molecules. Through individual electron-gas molecule collisions kinetic energy is transferred, leading to the dissociation of the atoms into positively charged atoms and free electrons. Such a charged gas is called a plasma. In a multicusp source, permanent magnets are attached on the outside of the discharge chamber in such a way that a longitudinal line-cusp field is formed (see figure 8.13).

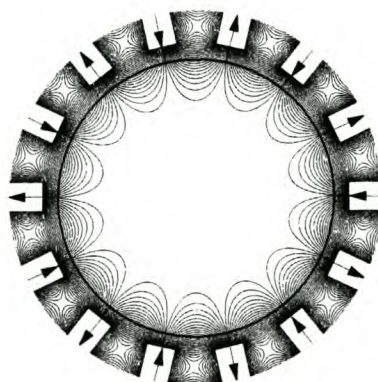


Figure 8.13: The radial magnetic flux lines of a line cusp, calculated by D. Wutte et al [117] using Poisson.

As this figure indicates, the multicusp magnets generates a strong field close to the chamber walls but the centre of the chamber is virtually field free. This field confines the electrons and enhances the plasma density and uniformity. This provides a large uniform beam for the etching of the substrate. Other advantages of RF multicusp sources include: the rf discharge can be operated with all gasses, including reactive gasses; there is no short-lived components in the source; the plasma is free from contamination and the rf power supplies can be operated at ground level [118, 119].

The extraction of the positive ionised atoms is achieved by electric fields. This is done using extraction electrodes. There are three electrodes in this system: the first, which encloses the chamber at the bottom, is called the plasma electrode, the second is the extraction electrode and the third the ground electrode. The electrodes consist of metallic conductors containing one or more apertures. The plasma electrode is either connected to the chamber or left floating, depending on the gas used. The extraction electrode is at a negative potential compared to the chamber and the last electrode is grounded. The charged ions are pulled towards the extraction electrode by the applied electric field. As they travel towards this electrode these ions are accelerated, gaining kinetic energy. They are projected through the apertures onto the substrate where they collide with the surface atoms, causing them to be removed from the surface.

8.3.2 Ion-mill design

For the patterning of YBCO the following ion mill characteristics are required:

- An ion current of 2 - 3 mA
- Ion acceleration of 500 eV
- A beam diameter larger than 1 cm
- A homogeneous beam profile

The reasons it was decided to use an rf multicusp ion source include its high beam homogeneity, high current capability and the fact that we already had a 400 W rf source operating at 13.56 MHz available. The researcher contacted D. Boonyawan from Chiang Mai University, Thailand, to obtain the designs used in their construction of an ion source [119].

The ion source was constructed according to their design at the central mechanical services (SMD) of Stellenbosch University. The source consists of a cylindrical discharge chamber, an rf antenna coil, permanent magnets and an ion-extraction system. A schematical representation of the system is given in figure 8.14. The discharge chamber is made from stainless steel, with an inner diameter of 10 cm and a length of 9 cm. The inner wall is surrounded by 16 columns of Sm-Co₅ magnets arranged alternately

with N and S facing the inner wall, producing the cusp fields. The magnets are enclosed by an outer cylinder, with cooling water circulating between the magnets and the inner wall. There are also 4 bars of Sm-Co₅ magnets on the top flange.

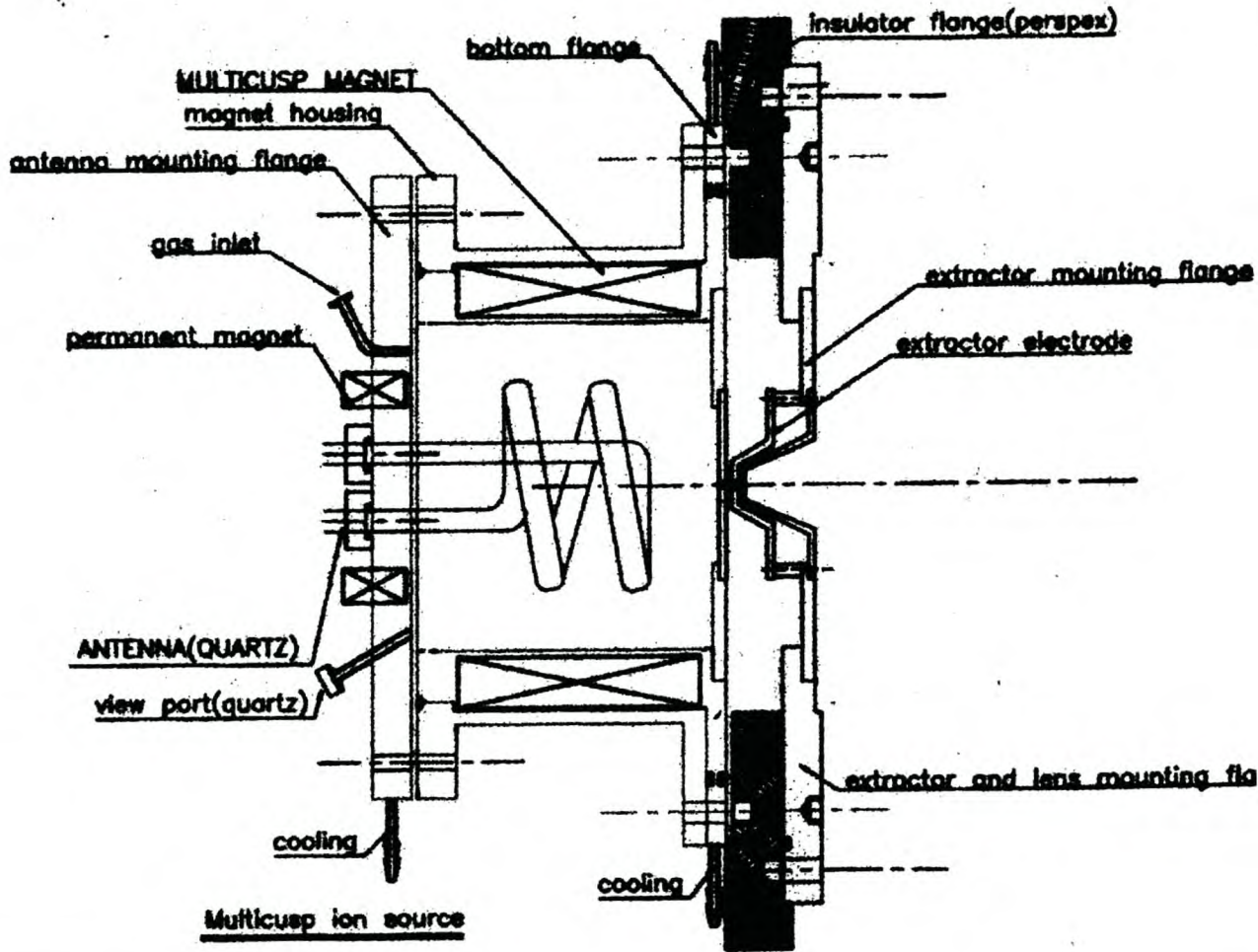


Figure 8.14: Schematic diagram of the rf multicusp ion source

The antenna, 6 cm in diameter, is made from copper tubing coated with a thin layer of glass. This coating is done, firstly to reduce the degree of sputtering of the antenna material, and secondly to double the efficiency of the source (the reason for this is unknown). The antenna is also cooled by water circulating through the tubing. The rf source delivers up to 400 W of rf energy at 13.56 MHz into a 50 Ω load. The rf matching is done through an isolation transformer and two adjustable capacitors (see figure 8.15). The extraction system consists of three electrodes with a single 4 mm diameter beam aperture. The electrodes are separated by 4 mm. The complete design of the mill is included in Appendix E.

The ion source is mounted on an old Technics argon mill stand containing a diffusion pump as well as two variable high-voltage (HV) sources (0-6 kV). In order to obtain a higher ion current, a turbo-molecular pump was added to the setup. The ion current is partly the result of the volume flow of argon through the system, a higher pumping rate increases the available current. The milling stage and the Faraday cup of the old ion mill was re-used with the new ion source going on top of the sample chamber. The Faraday cup is a device for measuring ion current. It consists of a conduction metal cup that is connected to ground via a resistor. By measuring the voltage across the resistor we are able to determine the ion current. It works because the positive ions, when they collide with the metal, combine with electrons to form neutral atoms. This recombination causes a flow of electrons through the resistor generating a potential. Figure 8.16 shows a photo of the base on which the ion source is mounted.

The water cooling is done in a closed-loop system using deionised water. Deionised water is used to prevent leaking from the high voltage to ground. Argon is used as etching gas, it is inert and easy to ionise and accelerate. After pumping the chamber down to a base pressure of 5×10^{-6} Torr, argon gas is introduced to a pressure of 4×10^{-5} Torr. These pressures are measured in the vacuum chamber. The gas is ionised using an rf power of 200 W. To ignite the gas the argon pressure is raised to 4×10^{-4} Torr for a few seconds. After ionisation the impedance of the plasma changes and the matching must be readjusted. The chamber is connected to the positive side of one of the variable HV sources set at ≈ 4 kV, the plasma electrode is connected to the chamber, the extraction electrode is connected to the ground and the ground terminal is left floating. Figure 8.17 shows the complete ion mill setup. The structure on top of the source chamber is the matching network.

Using this setup we were able to obtain an ion current of 1.1 mA for a gun current of 1.6 mA and an extraction voltage of 5500 V. The ion current can be adjusted by varying the rf power and the extraction voltage. An ion current of 1.1 mA is slightly on the low side for the etching of the YBCO, but it just means that the etching rate would be slower. The etching of test pieces show that the ion beam is of a sufficient diameter (27-34 mm) and voltage to be used for the etching of structures.

This process has not yet been optimised. optimisation of this process would involve the use of software to simulate the behaviour of the ions in the presence of the electric and magnetic fields. This will enable

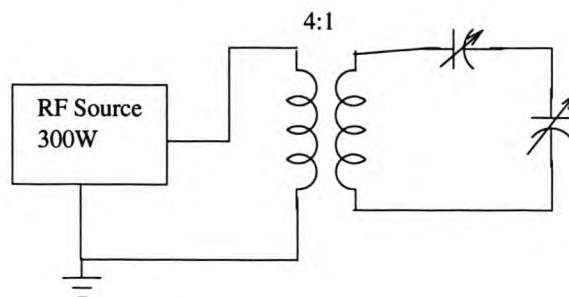


Figure 8.15: The rf matching network

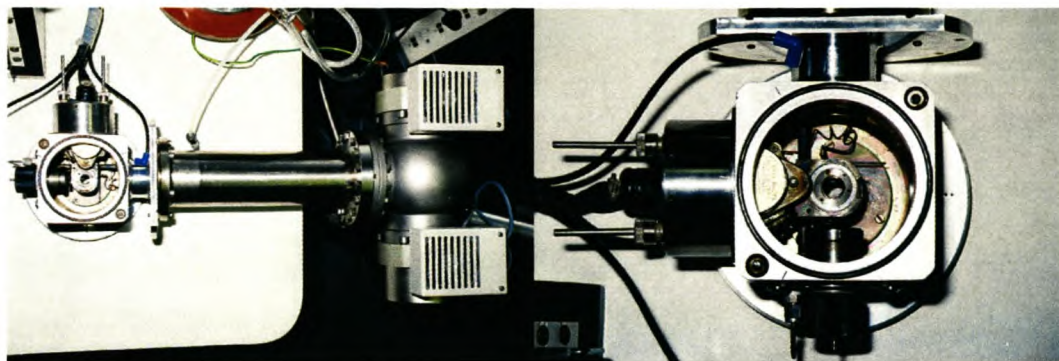


Figure 8.16: The base on which the ion mill was mounted: the base with the turbo-pump attached (left) and a close-up of the base showing the substrate holder and the Faraday cup (right).

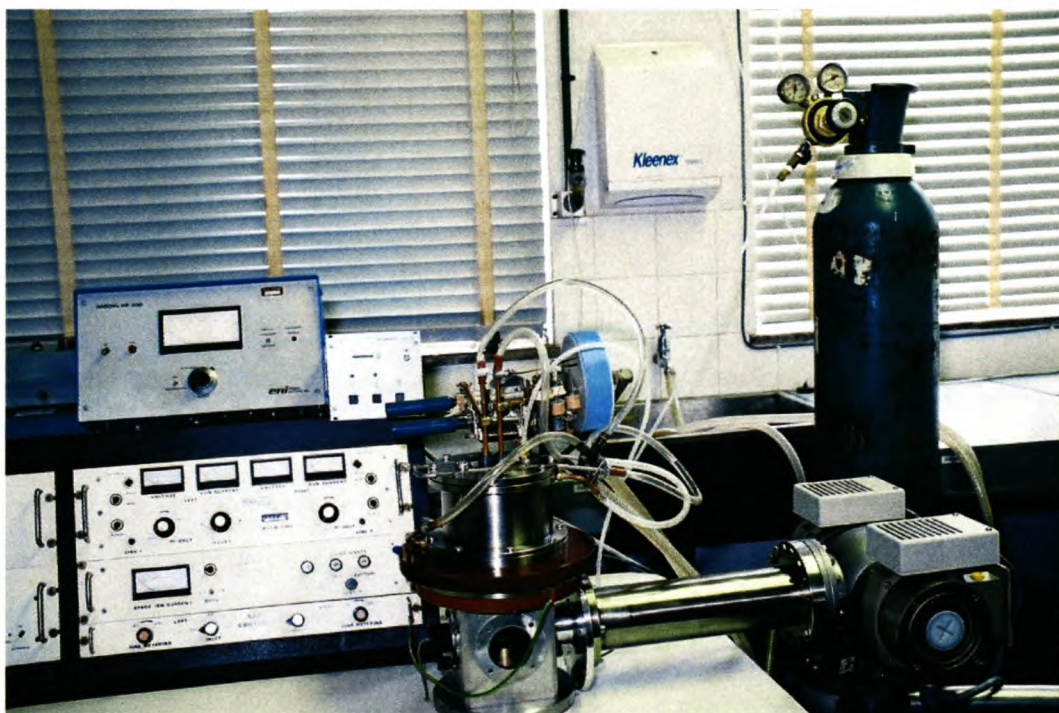


Figure 8.17: Complete Ar-ion milling setup

the optimisation of the extraction system in terms of voltages, aperture sizes and electrode separation. For possible software, see Zaim et al [120].

The final additions to the system is a liquid nitrogen cooling stage, (to cool the sample during etching) and some device to measure the beam acceleration. These must still be constructed.

Chapter 9

Improvements to existing SQUID designs

At the time of this research, two SQUID structures have already been designed and simulated at the University of Stellenbosch [25, 26]. In this chapter these designs will be critically discussed, some of the deficiencies will be pointed out and improvements will be suggested.

This thesis focuses on the establishment of an entire process for fabricating a high-quality SQUID. The design of the SQUID as such should also be discussed. To do this by designing a SQUID structure is, however, beyond the scope of this thesis. Therefore, instead of designing another structure, the knowledge gained from the extensive literature study done on the subject (Chapter 4) is applied to the evaluation of the SQUID structures already designed by previous researchers. Because of the deficiencies in the fabrication process the manufacturing of these SQUID structures has not yet been realised.

Before evaluating these designs, a overview of some of the important requirements of SQUIDs operating in unshielded conditions will be given.

9.1 Requirements

For unshielded applications, highly balanced large-baseline systems, which can be positioned at different measurement locations are required [42, 46]. They must be highly sensitivity but still be able to operate in magnetically unshielded environments for a long time and they need to be simple in handling (including cooling) [44]. If any type of electronic compensation is used, this compensation must provide low levels of noise even at very low frequencies. High system dynamics and linearity are also required [51].

Another important requirement for the unshielded SQUID operation is a large flux-to-voltage transfer function. This is not only necessary for obtaining low flux-noise, but is especially important to ensure stable operation of SQUID electronics without flux modulation in strongly disturbed environments [49].

Other than these requirements which are specific to operation in unshielded environments there is also the the general requirements of a high $I_c R_n$ product and a β in the order of 1 as well as ease of fabrication and reproducibility.

9.2 Evaluation of previous designs

The two SQUID designs done at the University of Stellenbosch both followed similar design procedures. These design are shown in figure

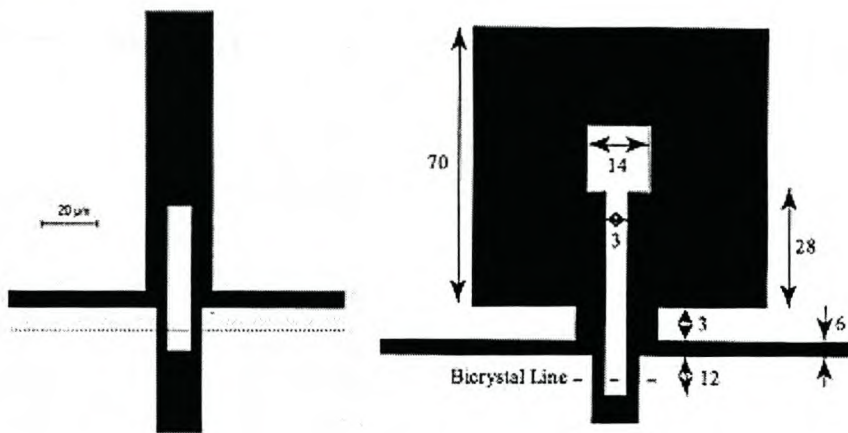


Figure 9.1: The SQUID designs by Knox-Davies [26] (left) and Conradie [25] (right).

9.2.1 Pickup loop design

The pickup loop was designed to provide the maximum effective area and to carry enough current to effectively screen the earth's magnetic field [26, pp. 28-29]. This approach fails to consider the noise effects and hysteresis caused by the screening current as it drives flux vortices into the conductor. Because the two halves of the loop are never completely balanced, part of this screening current is also coupled into the SQUID loop. This causes loss of sensitivity and added noise. The principle behind having such a large screening current capability is to enable the gradiometer to screen out the earth's magnetic field. If the magnetic field is larger than the capability of the loop, superconductivity will be lost.

An alternative to the thick lines is to have a number of thinner lines each containing a flux dam. These can be designed to have enough capability to shield out variations in the static magnetic field but, let through the largest part of the magnetic field. Lower screening currents means less noise and the thinner lines has less hysteresis.

9.2.2 SQUID loop design

This design was approached by the determination of the required SQUID inductance. This was determined from the literature and empirical formulas. The square washer design was used in both cases and the dimensions were adjusted to give the required inductance [25, 26]. Other considerations was increasing the length of the legs to simplify manufacturing as well as simplifying the washer structure [26]. In both cases the β_L was found to be above optimal. This was mainly a result of the width of the Josephson junctions, that was limited to sizes above $1\mu\text{m}$ by the fabrication process. A possible problem with both designs is the width of the lines in the SQUID loop –lines wider than $4\mu\text{m}$ allow the penetration of flux vortices, leading to high noise in unshielded operation.

To find a solution to the other problem, the large β_L we need to investigate the equation

$$\beta_L = \frac{2LI_c}{\Phi_0}. \quad (9.1)$$

To decrease β_L either the inductance L or the critical current I_c must be lowered. The inductance can be lowered by using inductive coupling between the pickup loop and the SQUID loop or introducing slots and holes in the SQUID body. The critical current can be lowered by using step-edge junctions, where it is possible to lower I_c by adjusting the t/h ratio of the step.

9.2.3 Simulation

A large amount of numerical simulations has been done on these SQUIDs. The models used in these simulations were, however, low-temperature SQUID models. In section 4.3 some possibilities for equivalent circuit models and analytical models were introduced. The use of these models would allow more accurate modelling and prediction of the behaviour of the SQUIDs. Using these models would also make it easier to diagnose problems with the final device.

9.3 Possible alternatives

One alternative to the dc SQUIDs designed above would be to rather use rf SQUIDs. Advantages are the simplification of the SQUID design and improved chances of success as well as reproducibility (only one junction instead of two). The modelling of rf SQUIDs is also easier and much more accurate. An rf-SQUID design is currently used in a very successful unshielded MCG probe, recently demonstrate the IEEE conference on Applied superconductivity [121].

With rf SQUIDs the readout becomes more problematic. The readout must be done inductively using an rf-tank circuit. However, this moves the problem to an area where we are better equipped to solve it –rf

electronics. In the case of an rf SQUID we are also required to use an inductively coupled pickup loop. This can be patterned on a separate substrate and flip-chip joined to the SQUID.

Another issue that must be addressed is the use of electronic compensation. Because of the lack of appropriate HTS wire, hardware gradiometers are restricted to planar ones which have small baselines and often suffer from poor balance. A possible solution is the formation of highly balanced electronic or software gradiometers via additional reference-SQUID channels [51]. In section 4.6 electronic compensation and the necessary background for developing software gradiometry are presented. Again, while the precise patterning of a gradiometer loop is a new challenge, the use of electronic balancing is old territory. Therefore it might be simpler to design a magnetometer and to use electronic compensation for balancing the uniform magnetic field.

Chapter 10

Experimental Results

The results of my experiments will be presented in three sections, which will be the PLD results, the patterning results and the etching results. The analysis and interpretation will be included. In the next chapter my conclusions will be presented as well as a critical discussion based on these results.

10.1 PLD results

10.1.1 The experiment, parameters and responses

The DOE was presented in section 8.1. The following table (10.1) gives a summary of the parameters used:

Parameters	+1 Values	-1 Values
Oxygen pressure	0.4 mbar	0.05 mbar
Substrate temperature	800 °C	720 °C
Target-Substrate distance	60 mm	40 mm
Laser energy	3.5 J/cm ²	2.5 J/cm ²
Ozone generator	on	off
Laser pulse frequency	10 Hz	4 Hz

Table 10.1: The DOE parameters and values

The responses were discussed in detail in section 8.1, they are :

- The oxygenation, determined by the c-axis length from the x-ray diffraction measurements.

- The critical temperature T_c , determined by susceptibility measurements.
- The surface roughness, determined by AFM measurements.

The 18 run experiment was executed over a time of 6-8 months. Over this period a number of components associated with the PLD system failed. These had to be replaced and sometimes redesigned. All this led to a large amount of random error in the experiment. At the completion of the experiment the samples were measured.

10.1.2 Results

The measurements are presented at the end of the chapter. For each sample there were a x-ray measurement, a susceptibility measurement and 9 atomic force microscope (AFM) measurements. This gives a total of 198 measurements. Some of the measurement had to be executed more than once and some samples had to be redeposited when the measurements showed that there has been some error in the process. The real amount of samples processed was in the order of 30 samples with approximately 300 measurements.

Since this is an enormous amount of data only a selection of the results will be given. Three AFM measurements, the susceptibility measurement and the x-ray diffraction measurement of 17 of the samples will be given. These 17 samples are the ones that were used in the final analysis of the PLD process.

10.1.3 Analysis of the results

The measurements were analysed using Design-Expert [115], using the following steps:

- For each response the data were first plotted in a normal plot of the estimated parameters. Then, from this plot, the significant parameters were selected. These are the parameters that deviate from the straight line plotted through the data points.
- After selecting these parameters an analysis of variance (ANOVA) was done. The output of the ANOVA gave an indication of whether a model based on the selected parameters accounts for a sufficient amount of the variation of the data to be considered adequate.
- The first step was repeated until an adequate model was obtained. The model was considered adequate if the model F value indicated the model to be significant (less than a 5% chance that the model occurs due to noise) and the adjusted R^2 was larger than 50 %. The researcher also tried to obtain the highest possible R_{pred}^2 .

- Finally the diagnostic graphs were checked to see whether the assumptions of independence, adequacy and randomisation were satisfied. These graphs also indicate some possible problem areas, for instance outliers. Outliers are responses that differ a lot from the average and could decrease the accuracy of the model.
- When the diagnostics graphs indicated that the model was adequate the interaction graphs were obtained.

10.1.3.1 Analysis of variance (ANOVA)

The ANOVA showed that the most important parameters and interactions are:

- the oxygen pressure, substrate temperature, ozone and the substrate-temperature \leftrightarrow ozone interaction for the c-axis length.
- the substrate temperature and target-substrate-distance \leftrightarrow laser-energy interaction for the RMS roughness.
- the oxygen pressure, target-substrate distance, ozone, oxygen-pressure \leftrightarrow ozone interaction and the laser-frequency \leftrightarrow laser-energy interaction.

10.1.3.2 Diagnostic graphs

The diagnostic graphs of the c-axis length measurements showed that samples 2, 3, 10 and 11 have excessive values. For the other responses the values of all the measurements were within the acceptable range. The problem probably lies with the x-ray diffraction measurements. As soon as the x-ray diffraction apparatus is repaired it is advisable to do these measurements again. At the moment, although it might reduce the accuracy of the analysis slightly, the samples do not lie far enough from the median to have a serious effect.

10.1.3.3 Interaction diagram

From the interaction graphs an interaction diagram was constructed. This diagram, shown in figure 10.1, shows the final results of the statistical analysis. The diagram shows the effect of every parameter on the response variables. The lines show the effects; the multiplication boxes denote the interactions. The graphs indicate the type of interaction, whether it has a positive or negative effect on the particular response variable. The graphs with two lines denote the interactions, the red-and-black line signifies the high and low levels of the one parameter, and the other parameter is plotted against the response

variable. From this graph one can see the way in which the changing of the parameter effects the response. Those parameters that have no line connecting it to the response have no –or a very small– effect on the response. The red lines indicate the three-parameter interaction referred to earlier. This interaction cannot be modelled by the DOE, but does exist, and could by aliasing make some other effects seem larger they actually are.

There are several points of interest in this diagram:

1. C-axis length

- The use of ozone improves the oxygenation and reduces the temperature sensitivity.
- The other important factors are the oxygen pressure and the laser energy.

2. T_c

- The use of ozone also improves T_c and reduces its sensitivity to the oxygen pressure
- The model predicts some strange, counter-intuitive effects, like a laser frequency \Leftrightarrow laser energy interaction and a T_c which decreases with increasing temperature.

3. RMS Roughness

- The use of ozone also seems to improve the surface quality of the thin film.
- We find the strange laser frequency \Leftrightarrow laser energy interaction occurring again.

The obvious deduction is that ozone certainly has a very positive effect on the PLD process. The strange interaction effects are possibly a result of some noise in the DOE, this will be discussed in Chapter 11.

10.1.3.4 Optimisation of the process

The final step in the analysis was to find a possible optimum deposition condition. Since the various responses have different optimum points, the final optimisation consists of finding a compromise between the various points that delivers the thin film of the best quality .

From the experiment a regression model was derived for each response and using iterative search the best combination was found. To verify the accuracy of the model a sample was prepared using the parameter set suggested by the optimisation. This sample was measured and the results were compared with the predicted results. The optimal parameter set is shown in table 10.2. The responses, predicted and measured, are shown in table 10.3.

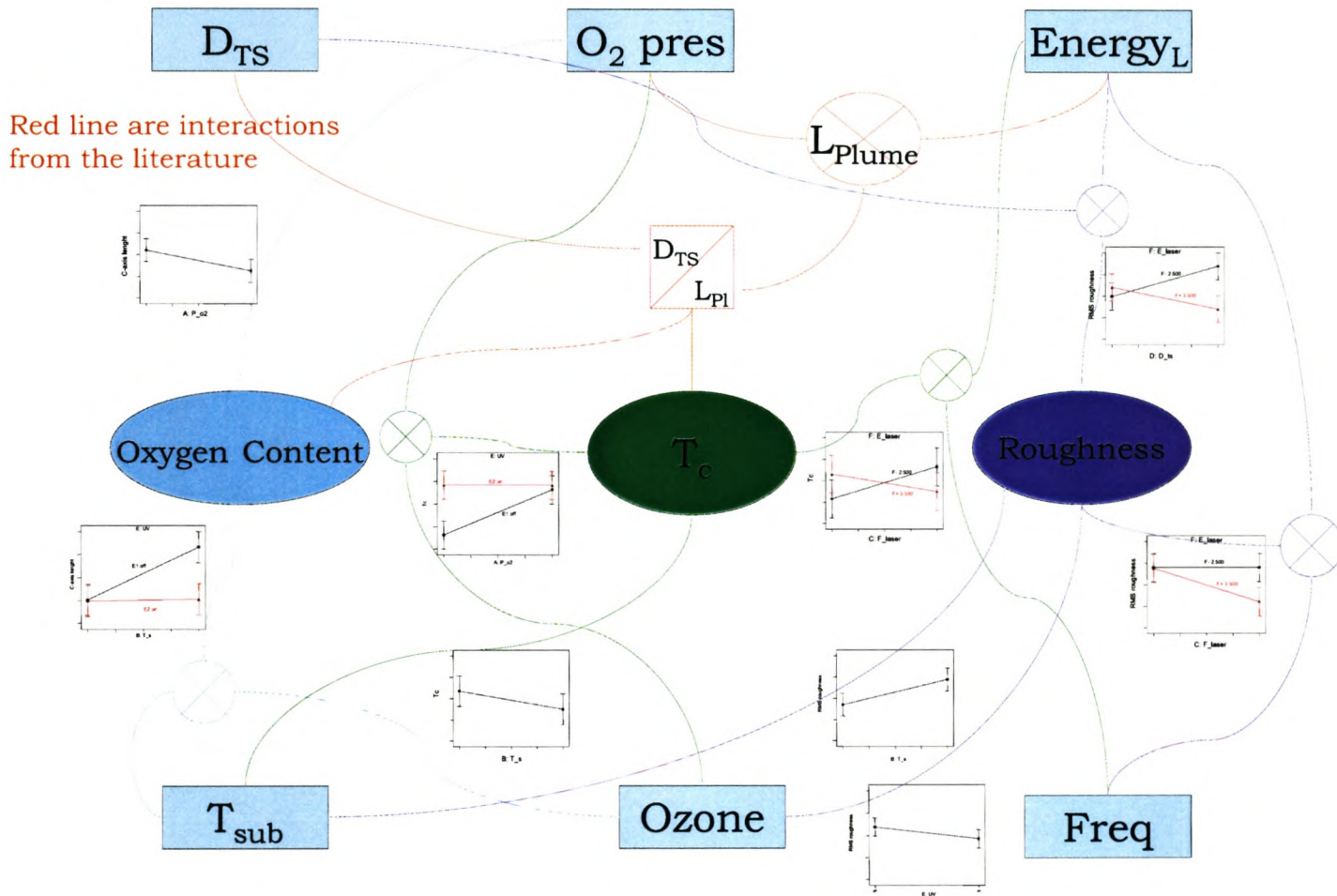


Figure 10.1: The PLD interaction diagram

The x-ray diffraction apparatus was not available for measuring the oxygen content of the final sample. The surface roughness, although it appears to be low in the analysis, was on looking at the AFM plot, quite rough containing a lot of boulders. This indicates that although the model for the roughness figure is reasonably accurate, the figure does not accurately represent the true surface roughness. This indicates that, to truly characterise the surface roughness, the equation for the roughness figure must be reconsidered. The susceptibility graph and AFM pictures are shown in figure 10.22.

10.2 Patterning results

Preliminary experiments were done through the method described by Knox-Davies [26], with the improvements described in section 8.2.

The preliminary experiment consisted of 8 runs done at various levels of the important parameters. For etching the chrome test mask, developed by Knox-Davies and manufactured by Pico systems, was used. The mask design is shown in figure 10.2. After the development of the photoresist the surfaces were analysed by scanning electron microscopy (SEM). The results of this analysis are shown in figure 10.3. Clearly the results were far from optimal and this process must be tuned using the method suggested in section 8.2.

Parameter	Value
Oxygen pressure	0.4 mbar
Substrate Temperature	720 °C
Ozone generator	on
Target-Substrate distance	40 mm
Laser pulse frequency	10 Hz
Laser energy	3.4 J/cm ²

Table 10.2: The optimal parameter set

Response	Predicted Value	Measured Value
Critical Temperature	91.4 K	91 K
Surface Roughness	374.55	305

Table 10.3: Predicted and measured responses for the optimal parameter set

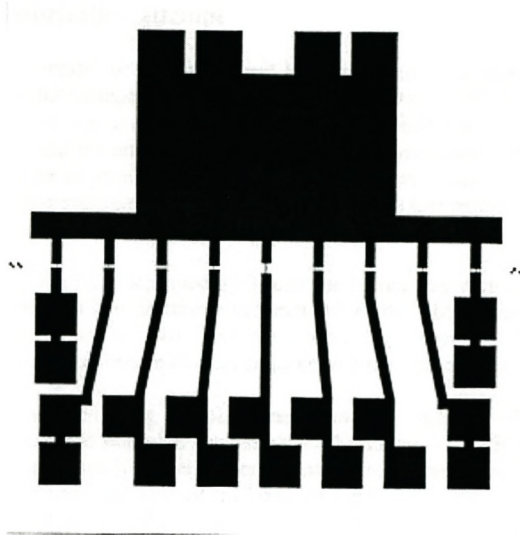


Figure 10.2: The test mask used for the patterning and etching of test structures

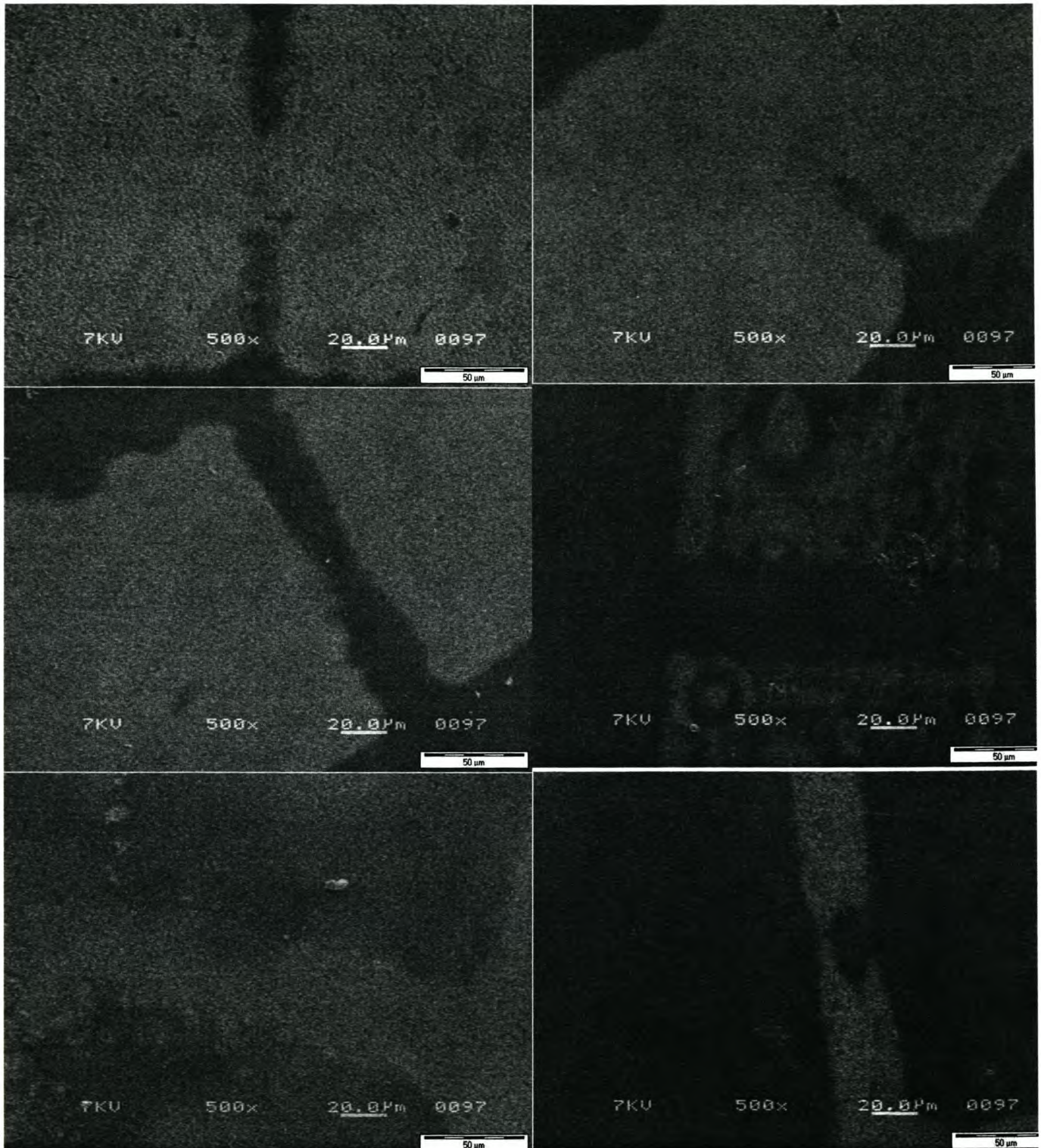


Figure 10.3: SEM pictures of the various runs of UV lithography

The DOE described in section 8.2 was designed for this purpose, but due to time constraints and logistical problems with the installation of a new SEM apparatus at the University, this could not be completed. The DOE is presented in Appendix D and should be used for this purpose. The simplicity of this DOE

would make it a good starting point for somebody interested in applying and learning about the technique and it has a much lower cost per experiment than for instance the PLD DOE.

10.3 Etching results

To prove the success of the newly build ion mill the best of the photoresist masks from the previous characterisation was used it for Ar-ion milling of the substrate. The milling conditions is shown in table 10.4, the ion current has to be kept very low due to the absence of the cooling stage. The SEM photo of the milled substrate is shown in figure 10.4 –clearly the definition of the thin film is very good.

Parameter	Setting
rf Power	200 W
Extraction voltage	3500 V
Gun current	0.9 mA
Ion current	300 μ A
Substrate angle	10 ^o

Table 10.4: Milling conditions for the first experimental etch.

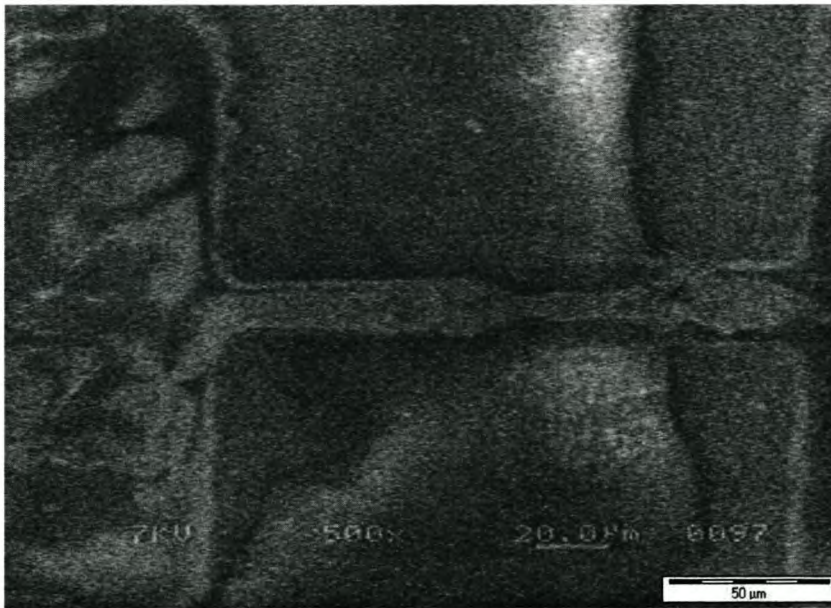


Figure 10.4: SEM picture of initial Ar-ion milling result

The superconductivity of the thin film is destroyed due to the absence of a cooling stage, but the result shows that Ar-ion milling does indeed work much better than wet etching. For comparison a SEM picture

of a wet etched YBCO thin film is shown (figure 10.5). The same test mask (shown in figure 10.2) was used in both cases.

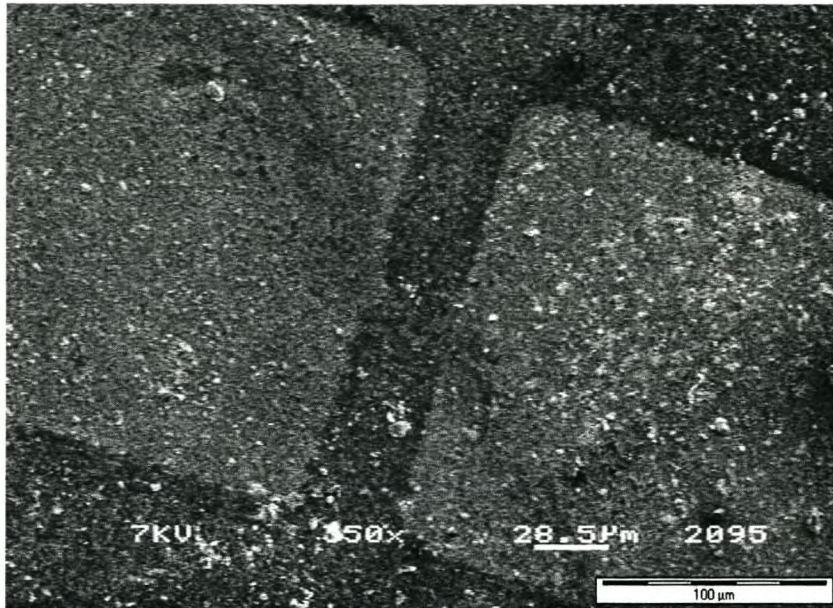
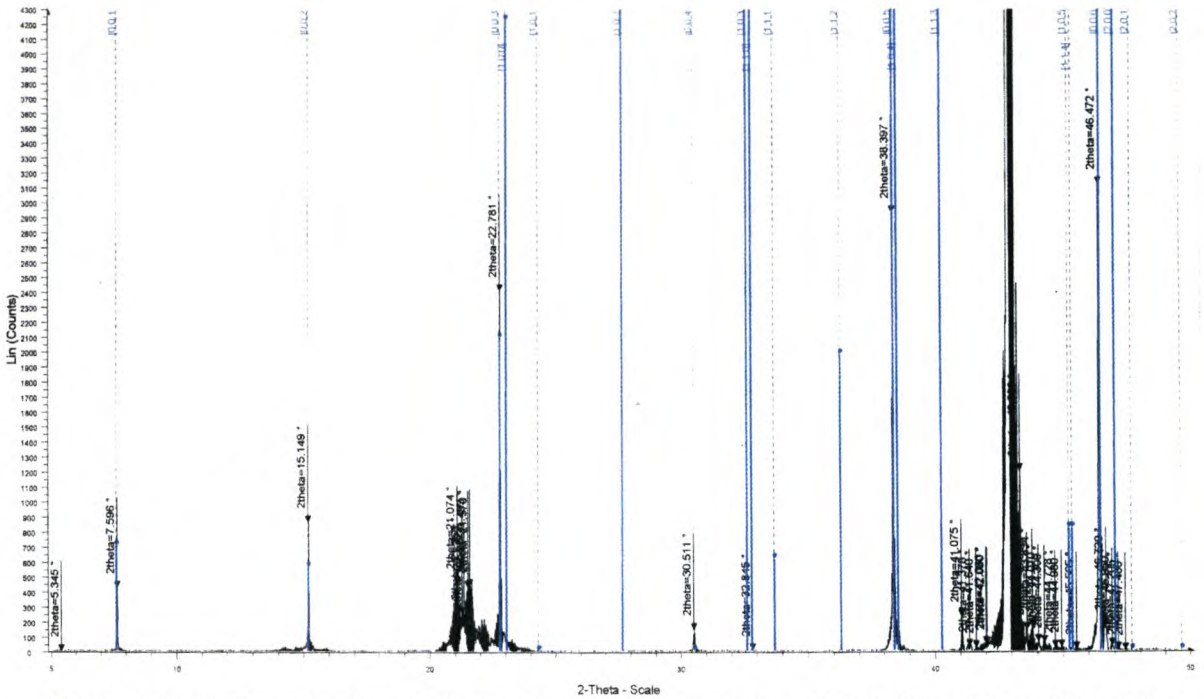
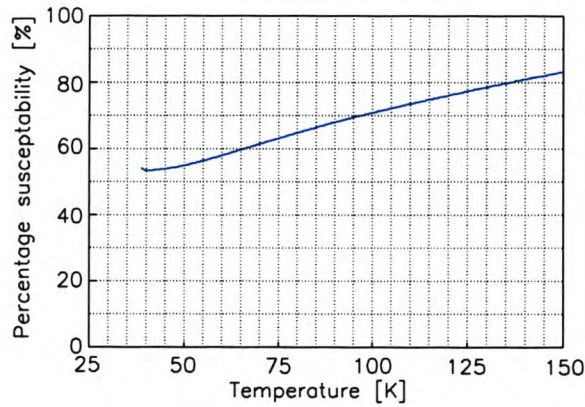


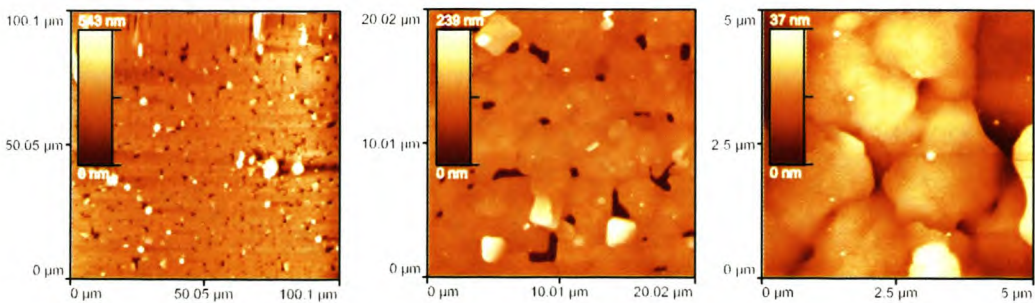
Figure 10.5: A wet-etched YBCO thin film



(a)

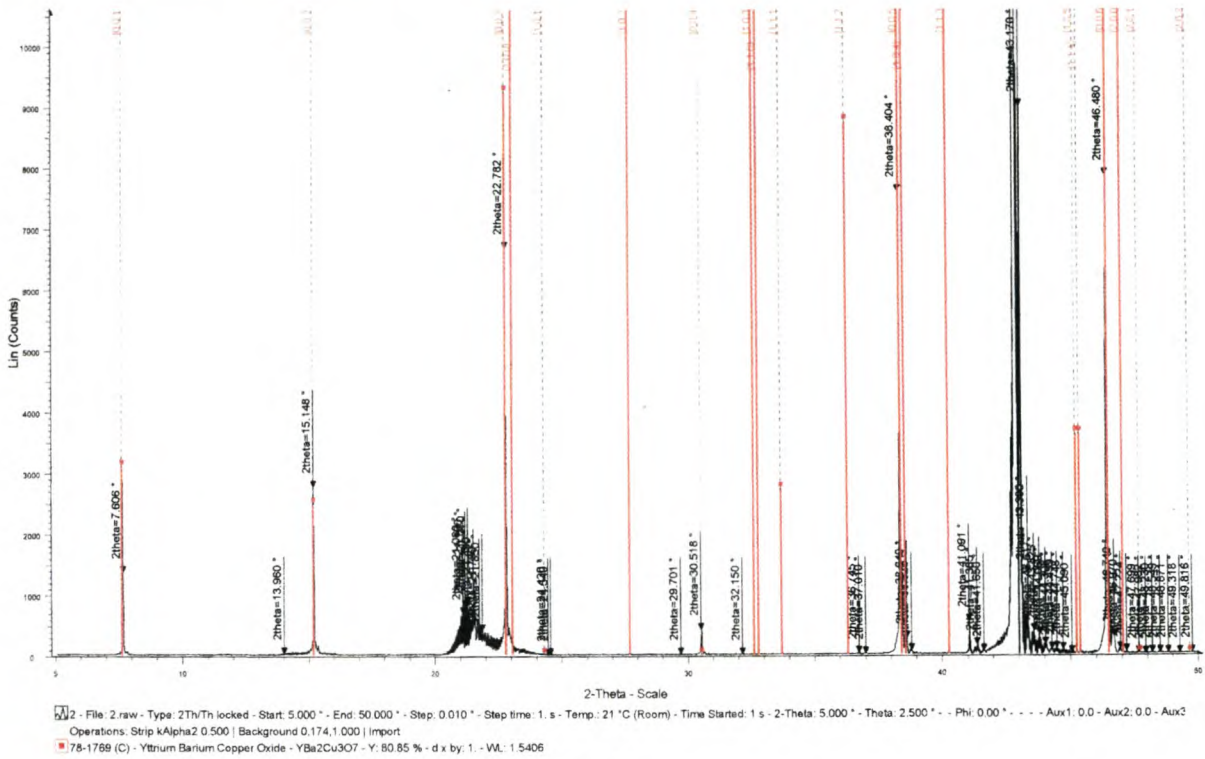


(b)

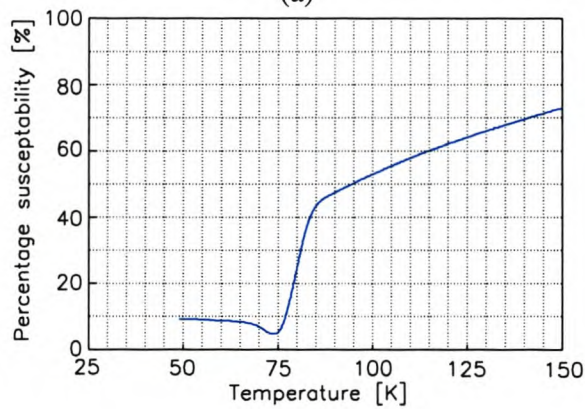


(c)

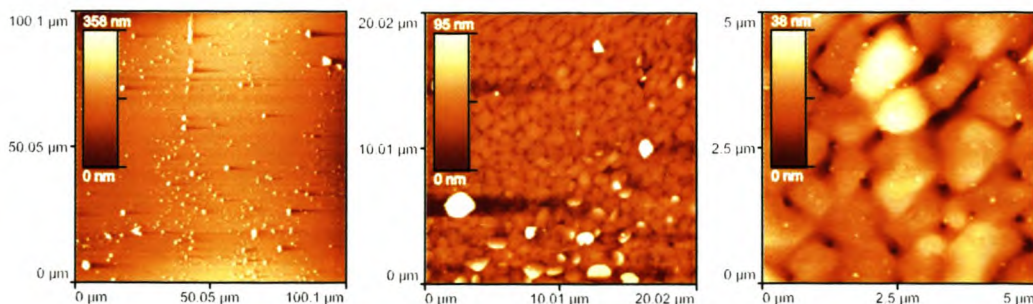
Figure 10.6: Measurements on Sample 1 with (a) X-ray diffraction, (b) magnetic susceptibility and (c) Atomic Force Microscopy (AFM).



(a)

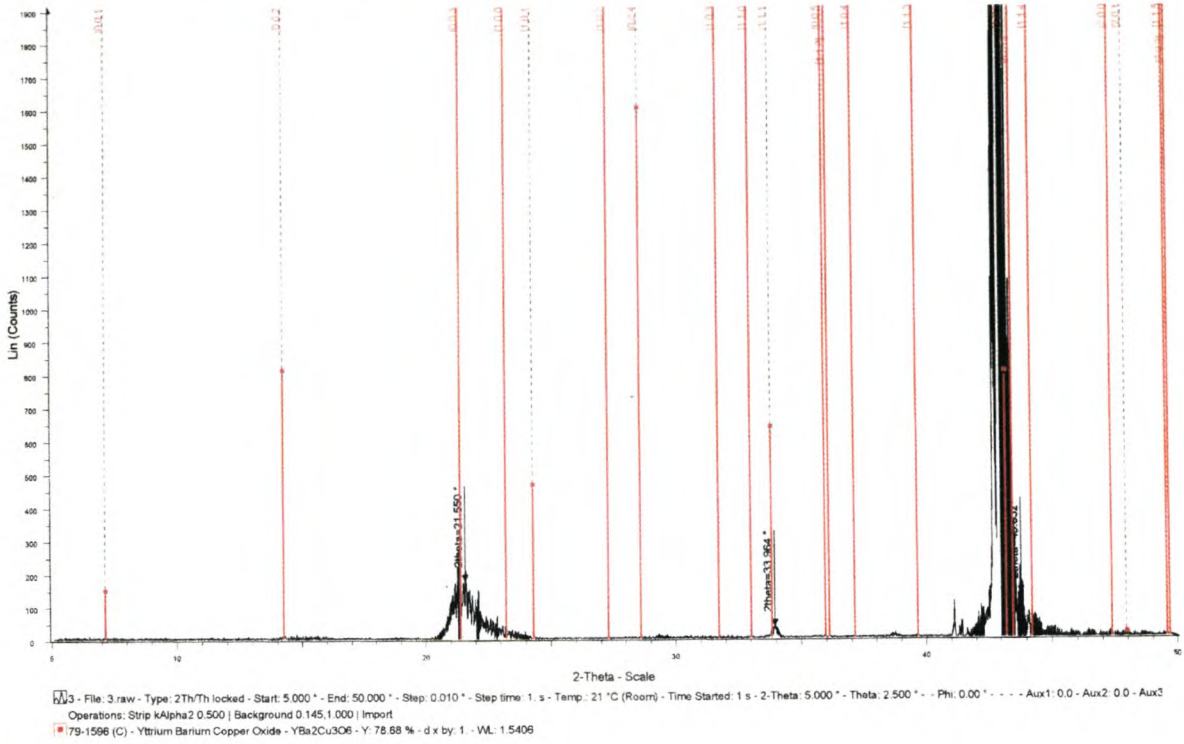


(b)

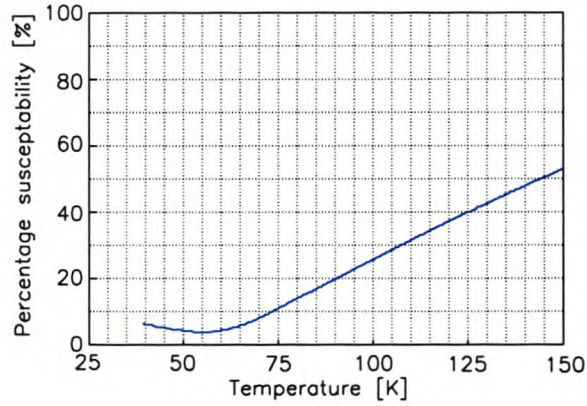


(c)

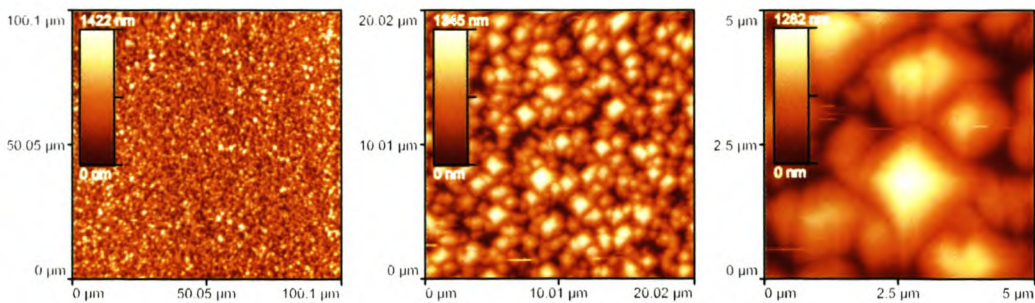
Figure 10.7: Measurements on Sample 2 with (a) X-ray diffraction, (b) magnetic susceptibility and (c) Atomic Force Microscopy (AFM).



(a)

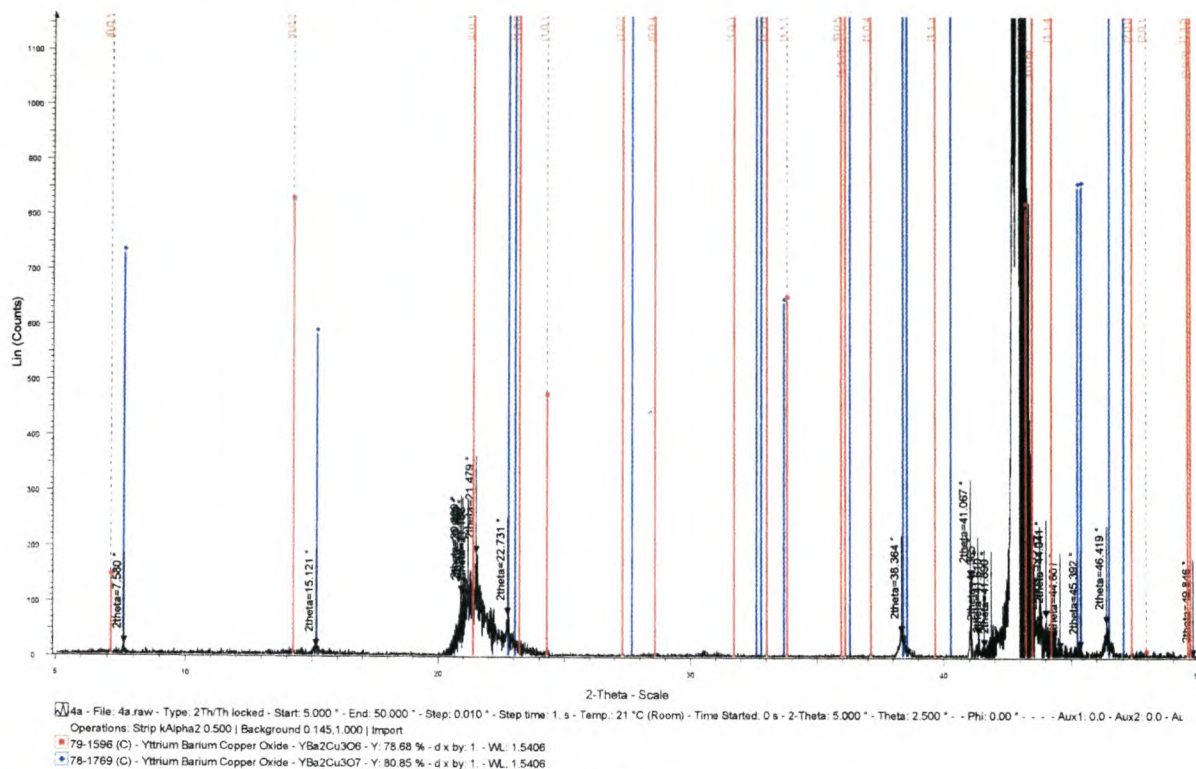


(b)

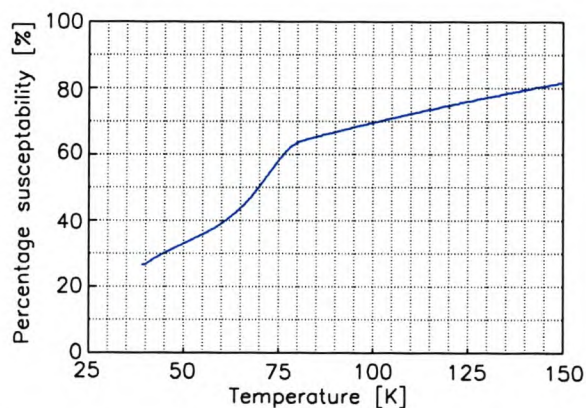


(c)

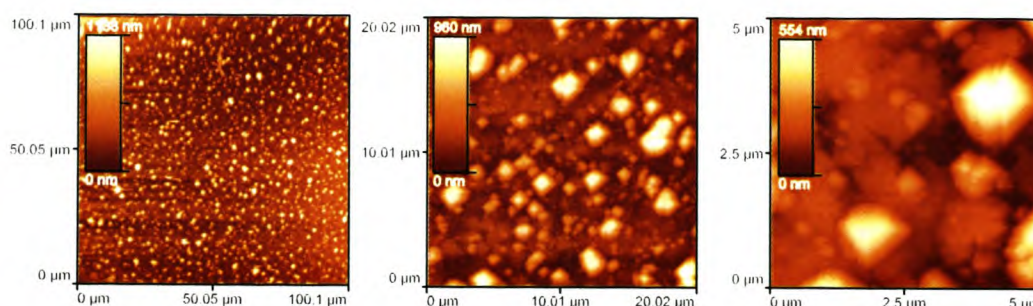
Figure 10.8: Measurements on Sample 3 with (a) X-ray diffraction, (b) magnetic susceptibility and (c) Atomic Force Microscopy (AFM).



(a)

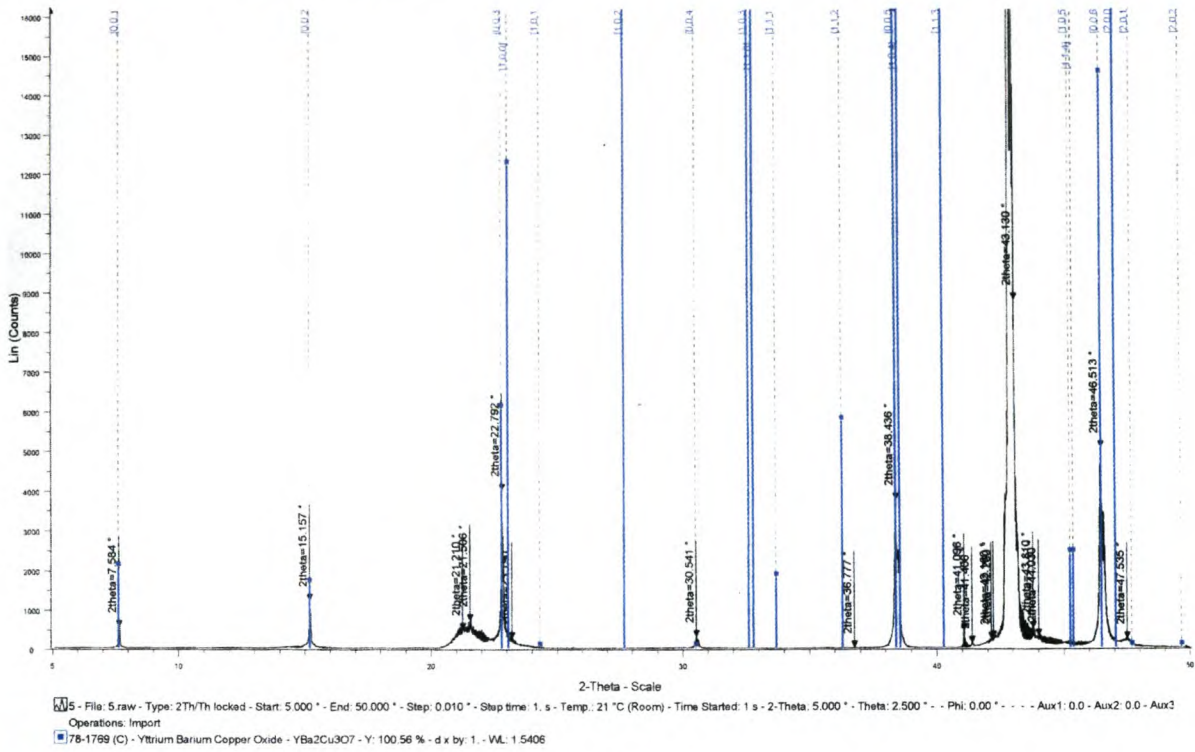


(b)

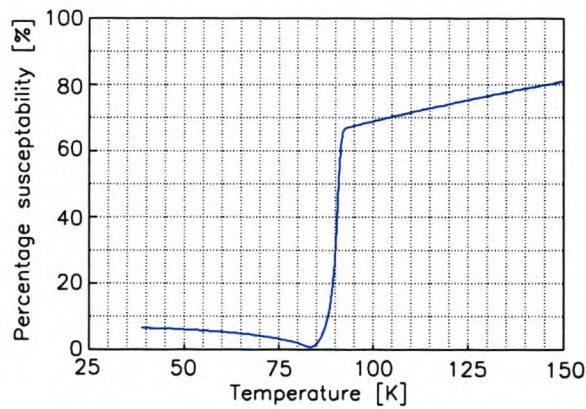


(c)

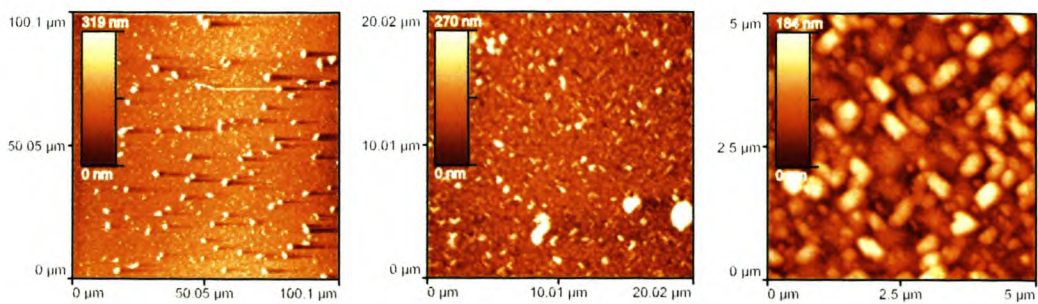
Figure 10.9: Measurements on Sample 4 with (a) X-ray diffraction, (b) magnetic susceptibility and (c) Atomic Force Microscopy (AFM).



(a)

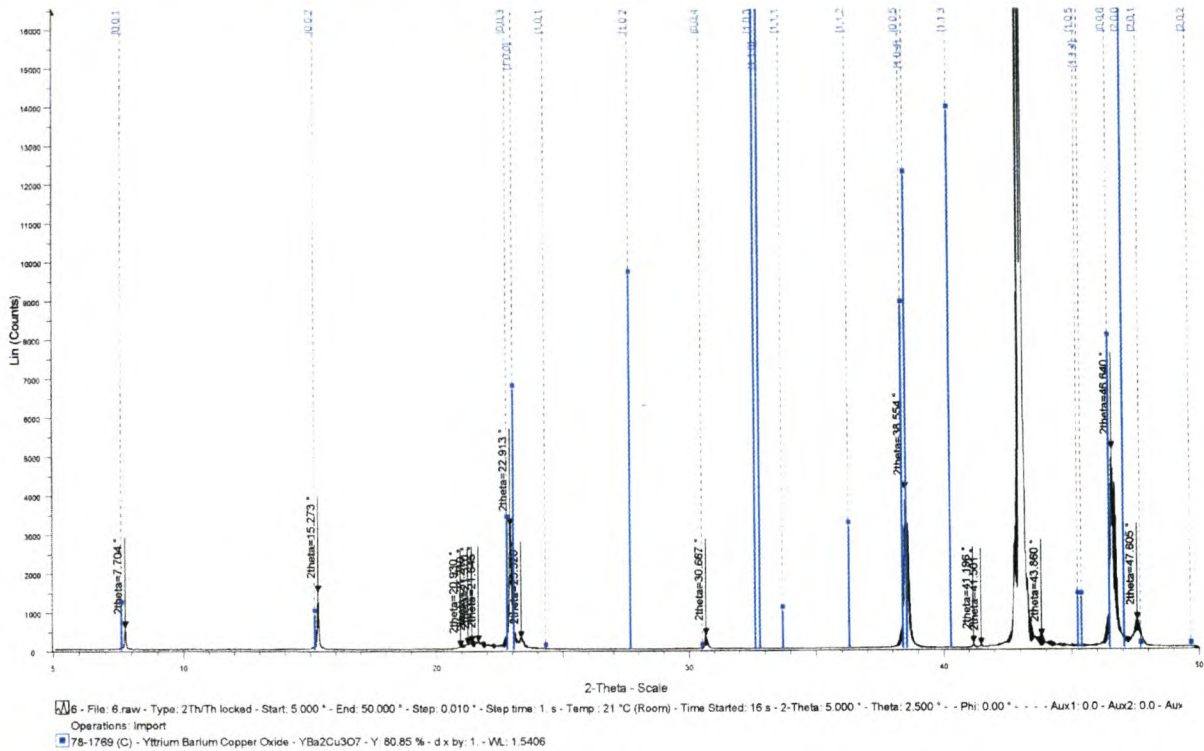


(b)

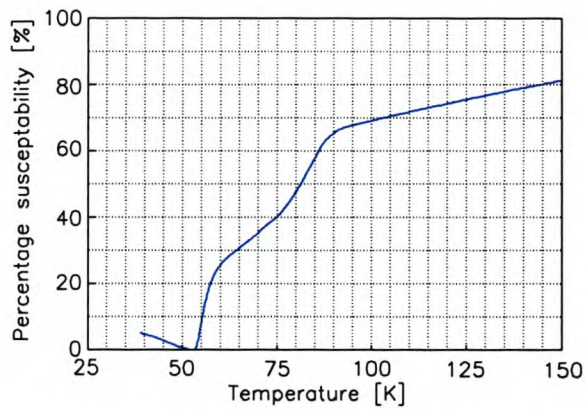


(c)

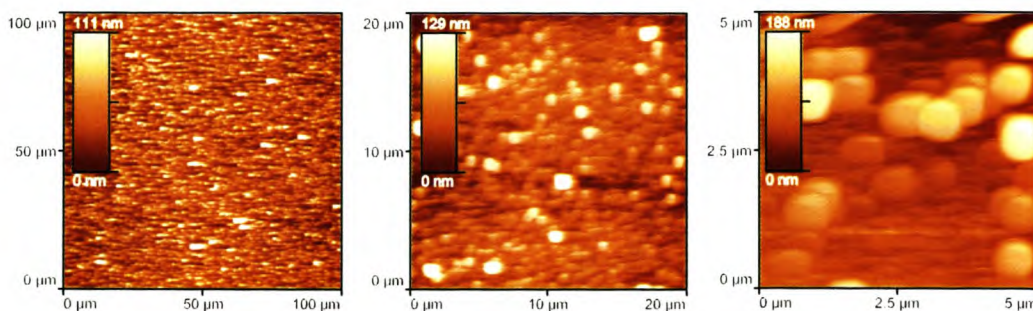
Figure 10.10: Measurements on Sample 5 with (a) X-ray diffraction, (b) magnetic susceptibility and (c) Atomic Force Microscopy (AFM).



(a)

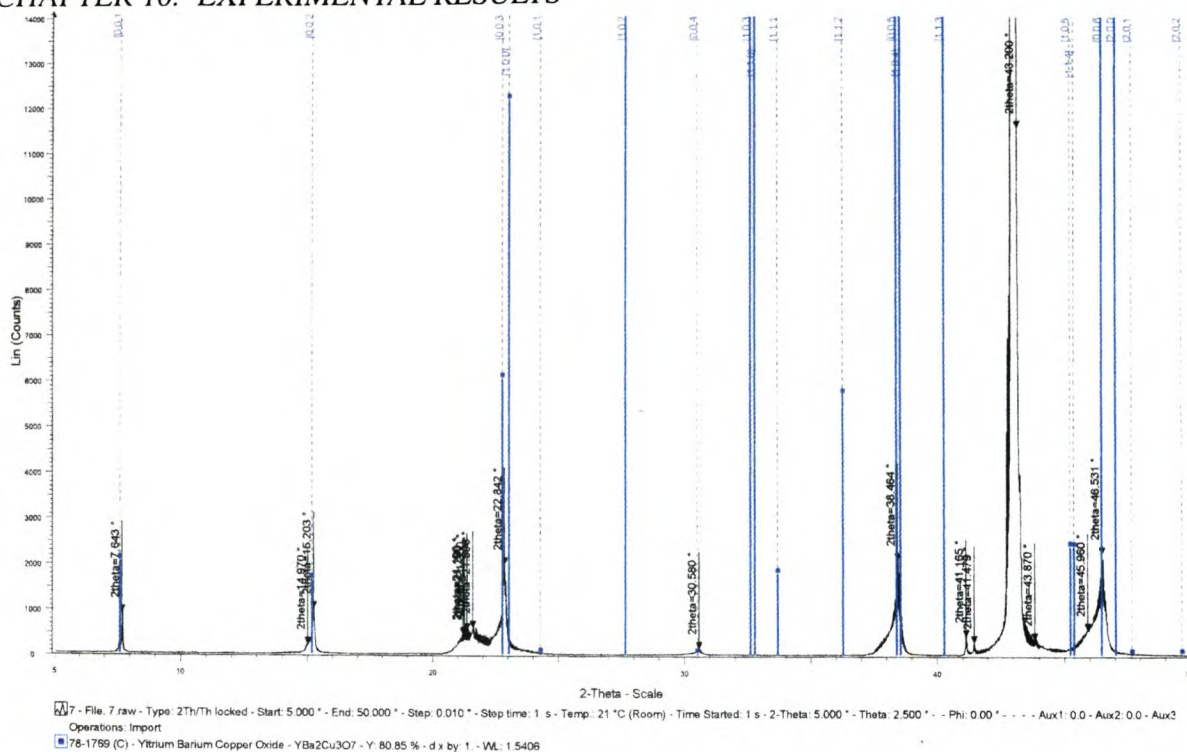


(b)

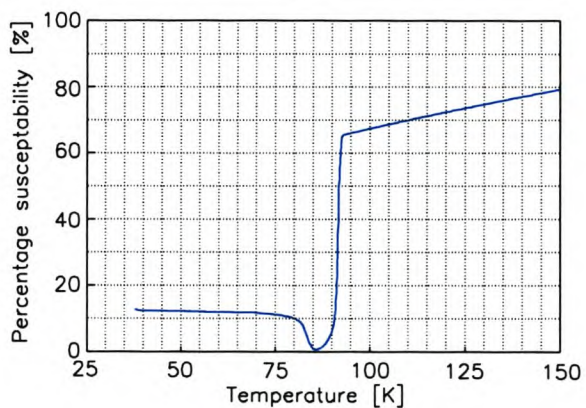


(c)

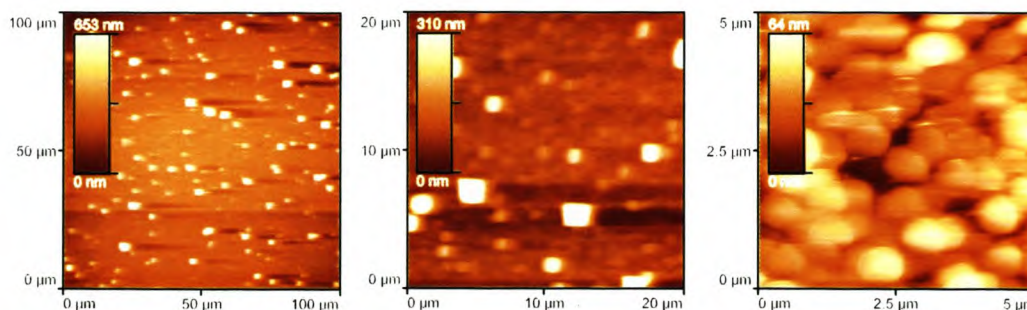
Figure 10.11: Measurements on Sample 6 with (a) X-ray diffraction, (b) magnetic susceptibility and (c) Atomic Force Microscopy (AFM).



(a)

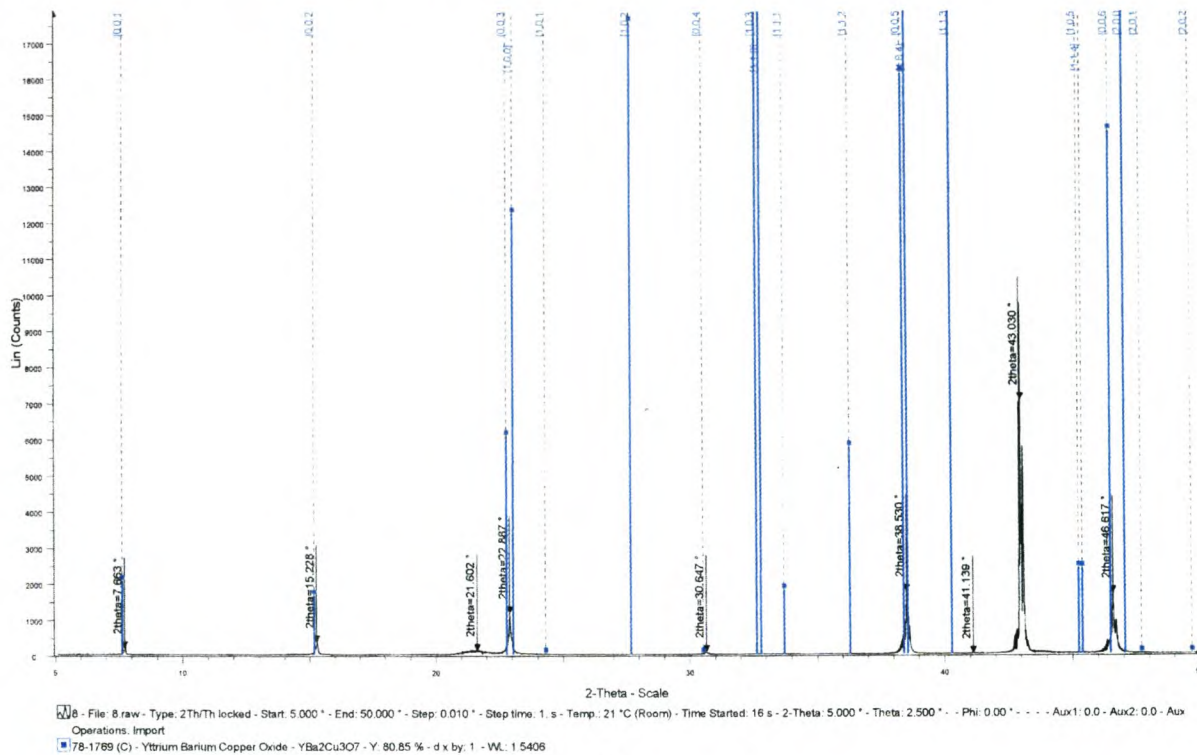


(b)

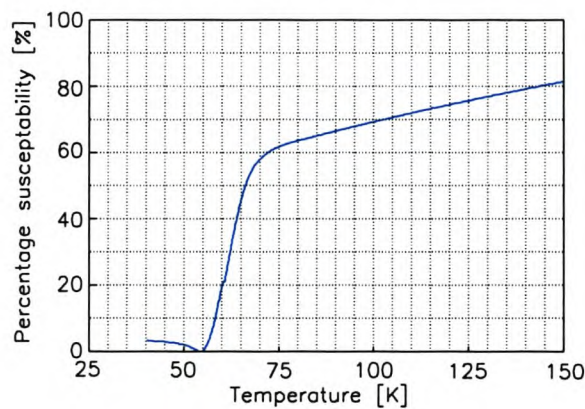


(c)

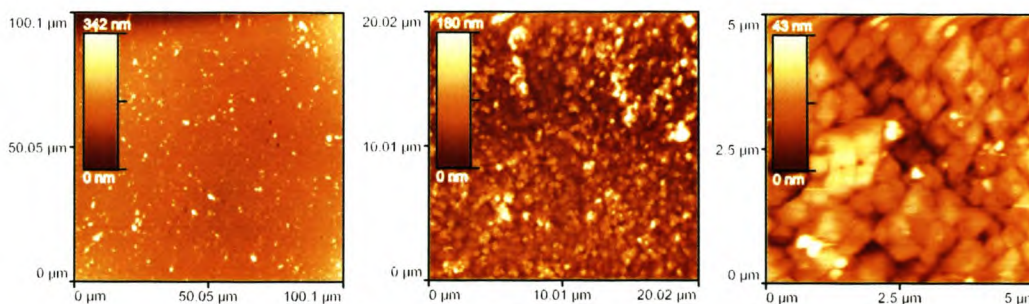
Figure 10.12: Measurements on Sample 7 with (a) X-ray diffraction, (b) magnetic susceptibility and (c) Atomic Force Microscopy (AFM).



(a)

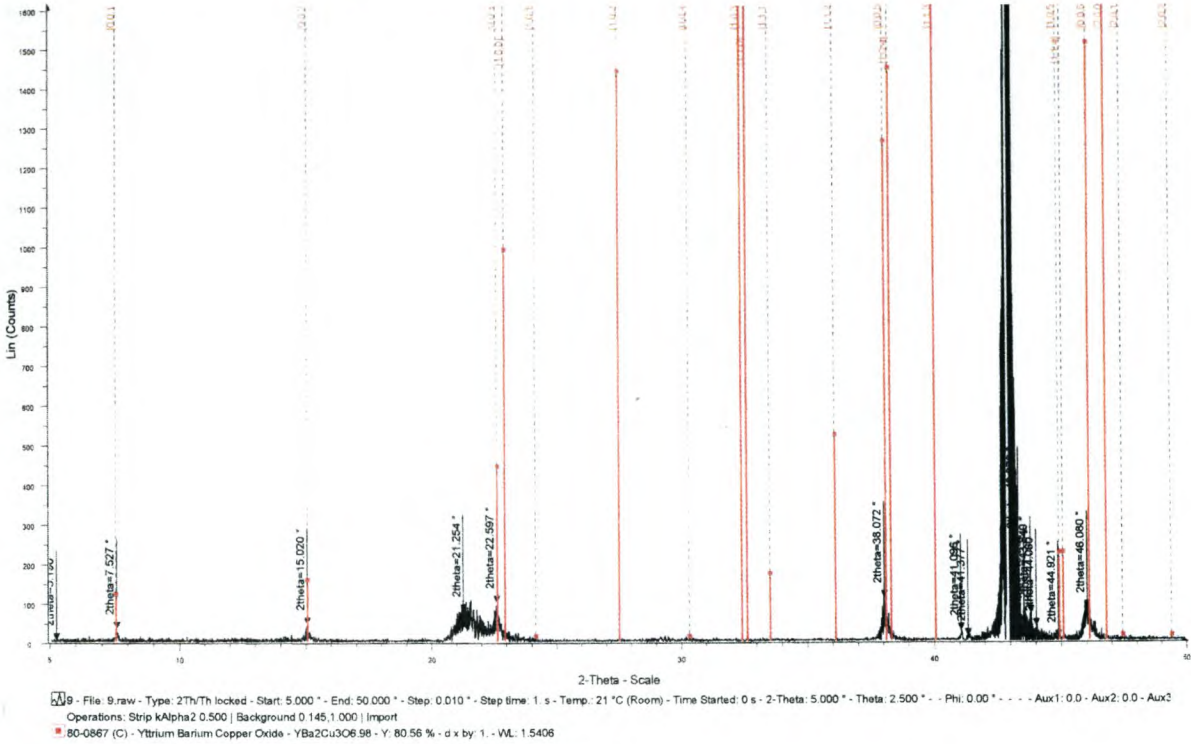


(b)

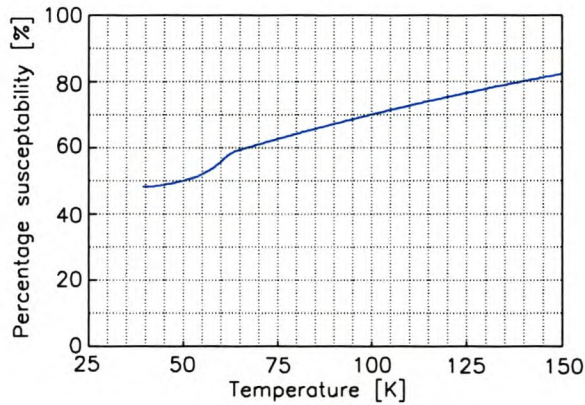


(c)

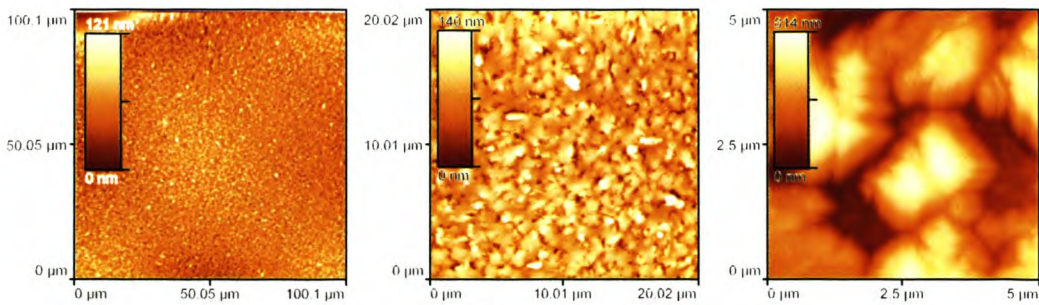
Figure 10.13: Measurements on Sample 8 with (a) X-ray diffraction, (b) magnetic susceptibility and (c) Atomic Force Microscopy (AFM).



(a)

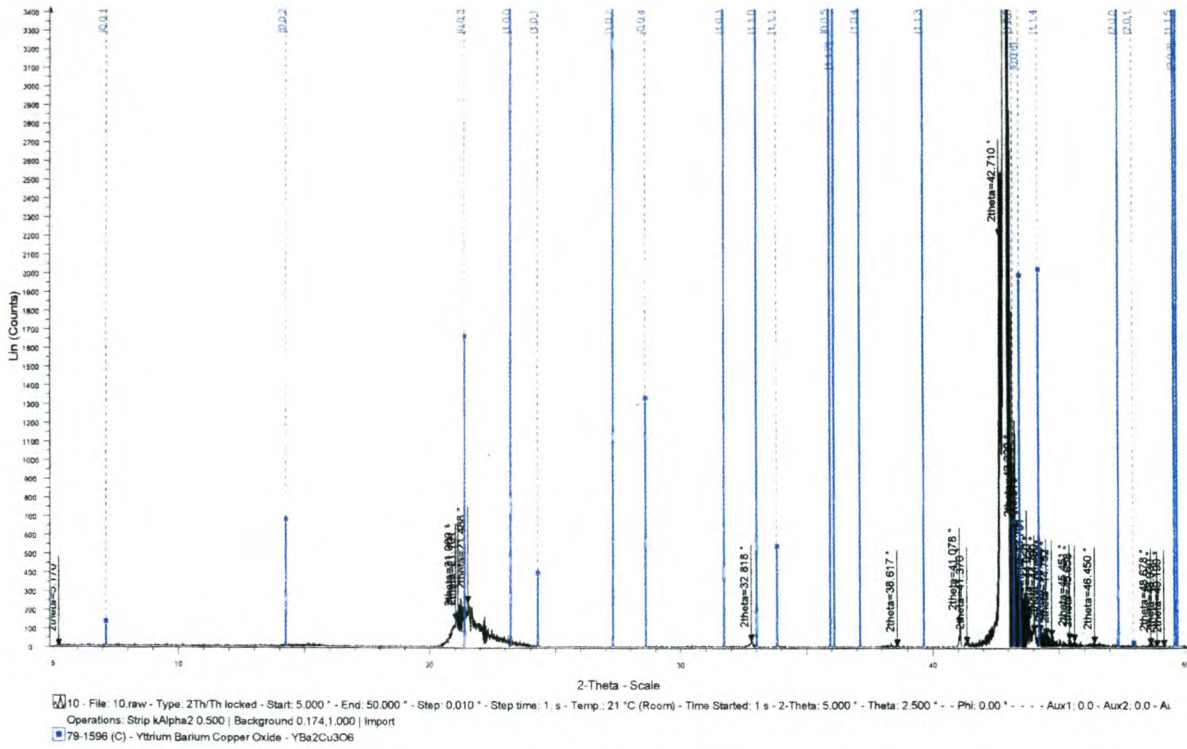


(b)

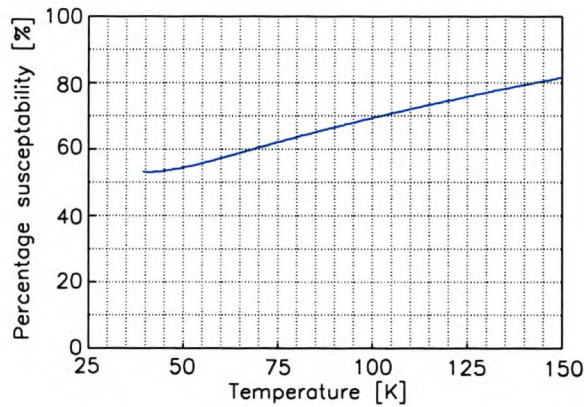


(c)

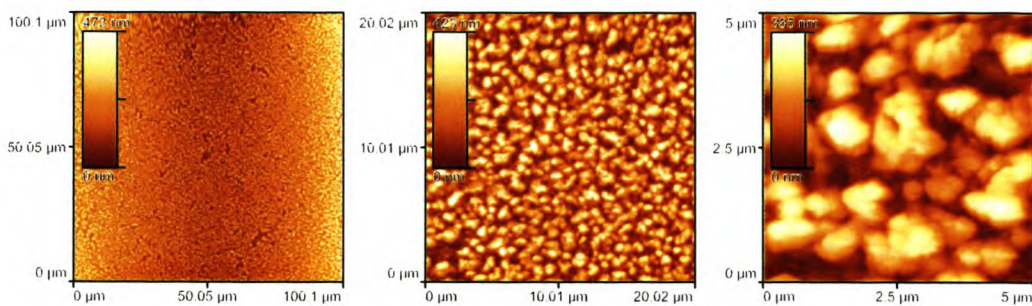
Figure 10.14: Measurements on Sample 9 with (a) X-ray diffraction, (b) magnetic susceptibility and (c) Atomic Force Microscopy (AFM).



(a)

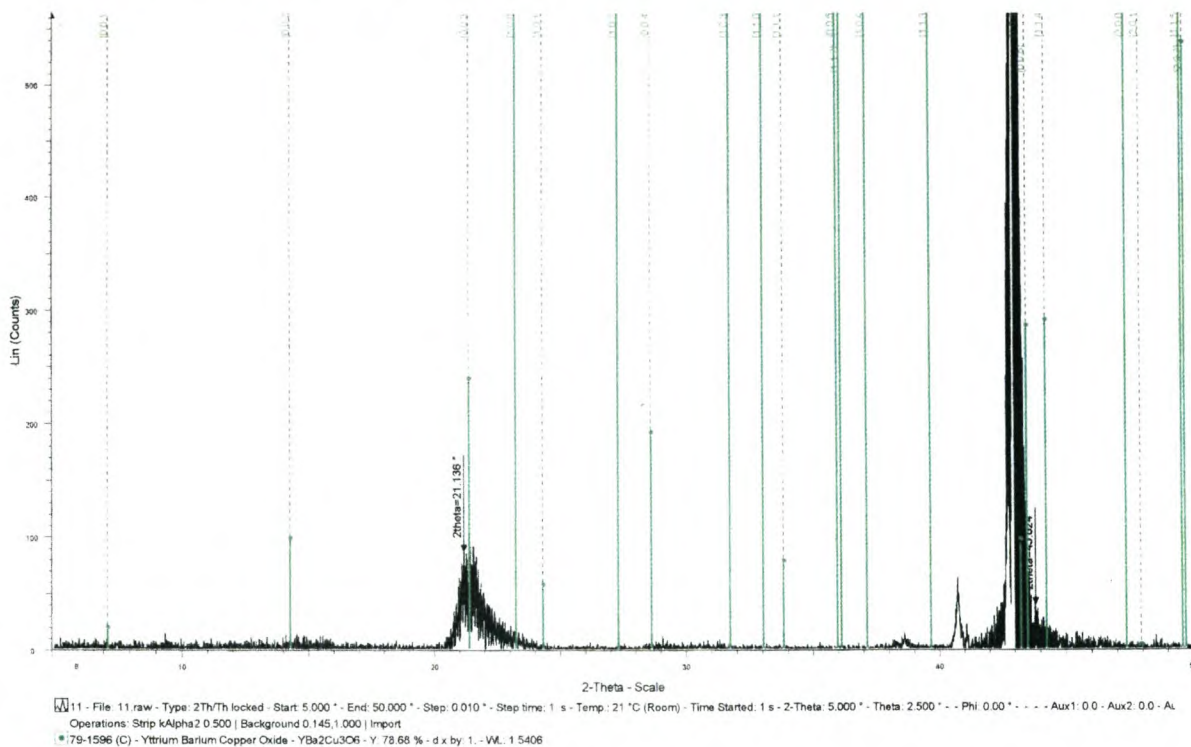


(b)

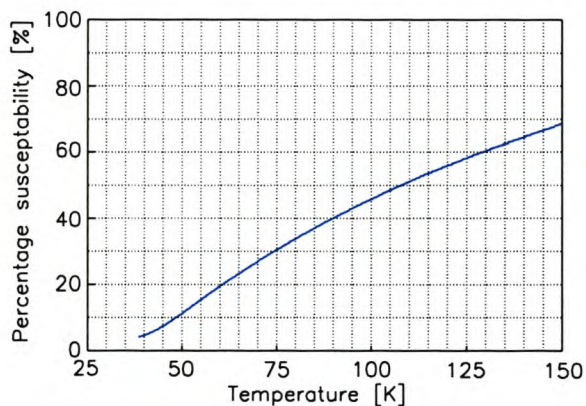


(c)

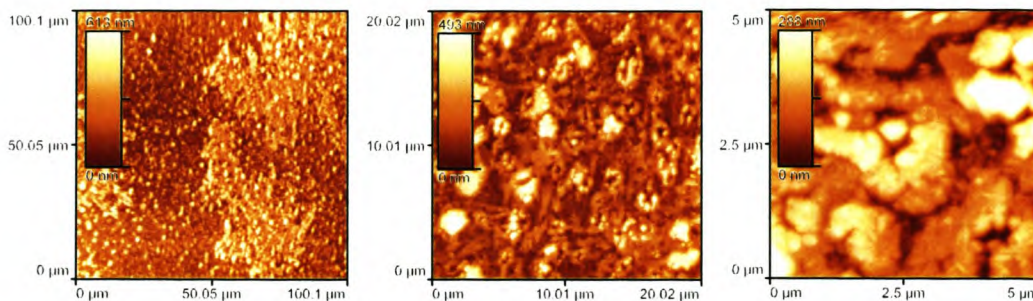
Figure 10.15: Measurements on Sample 10 with (a) X-ray diffraction, (b) magnetic susceptibility and (c) Atomic Force Microscopy (AFM).



(a)

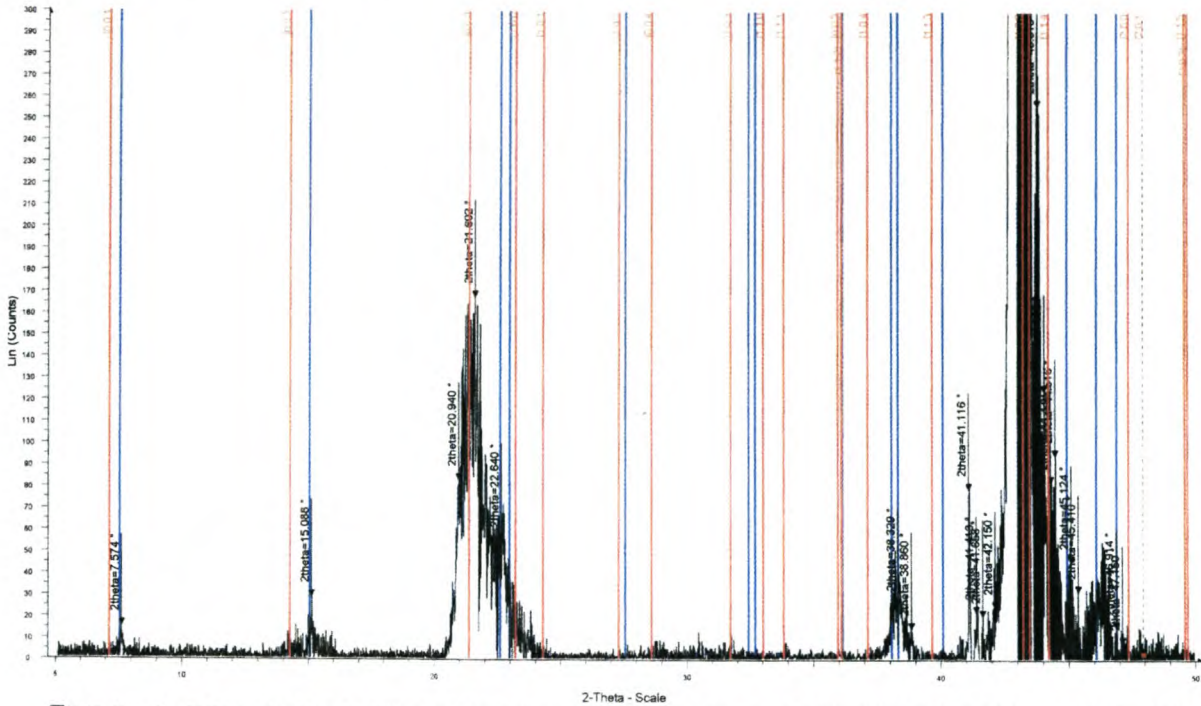


(b)

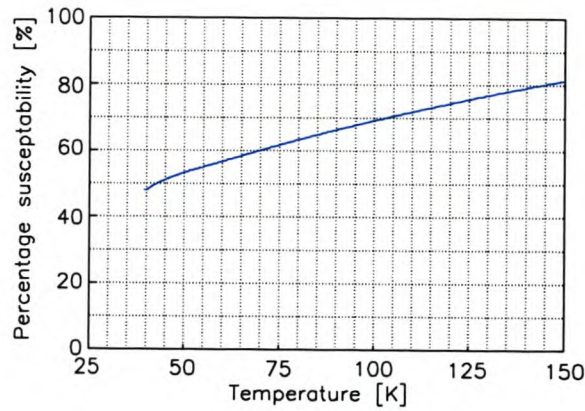


(c)

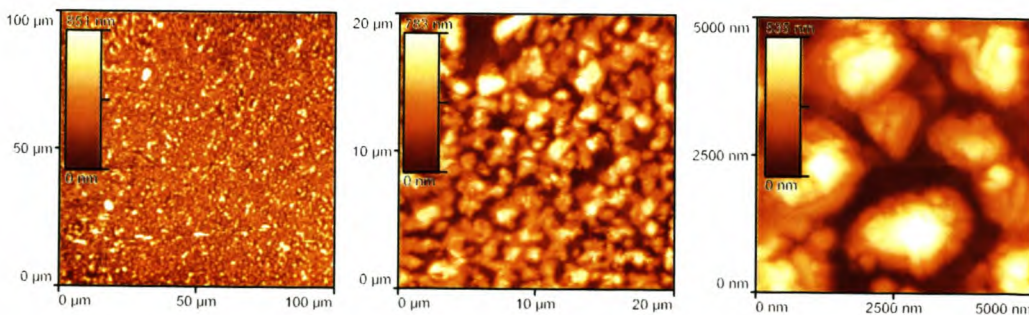
Figure 10.16: Measurements on Sample 11 with (a) X-ray diffraction, (b) magnetic susceptibility and (c) Atomic Force Microscopy (AFM).



(a)

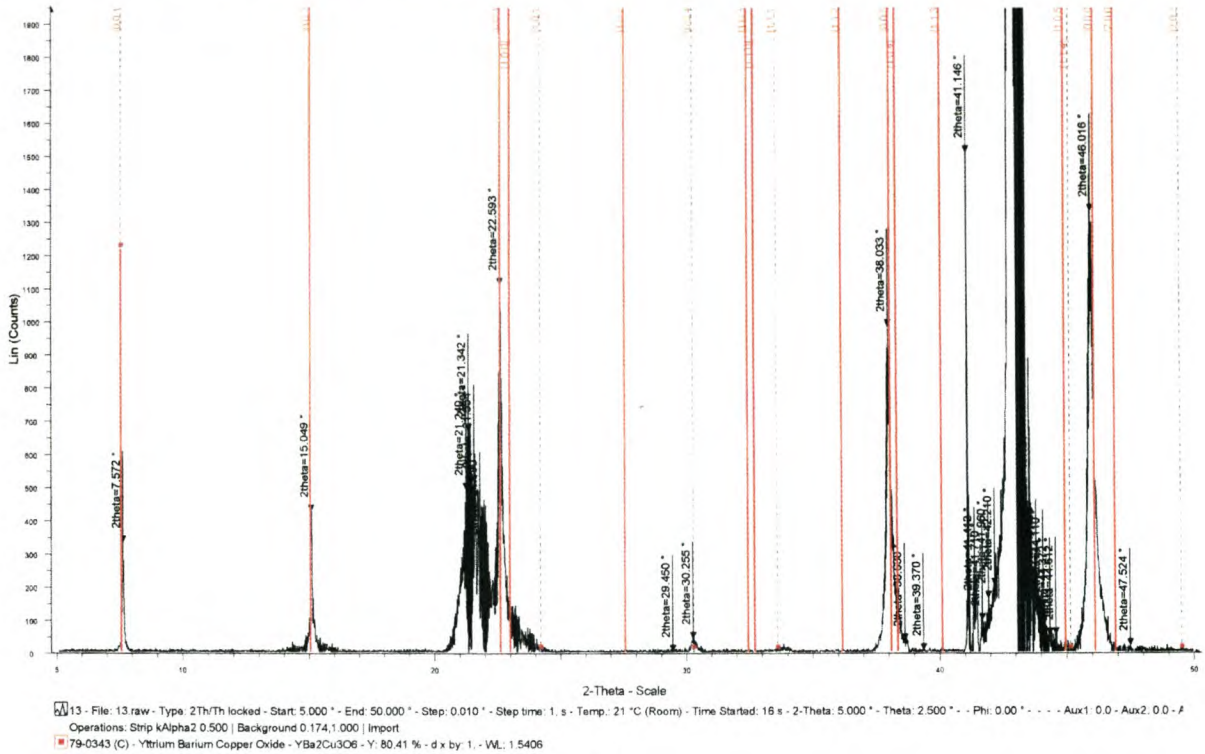


(b)

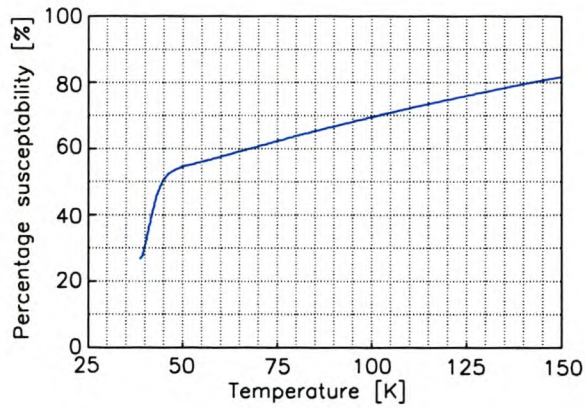


(c)

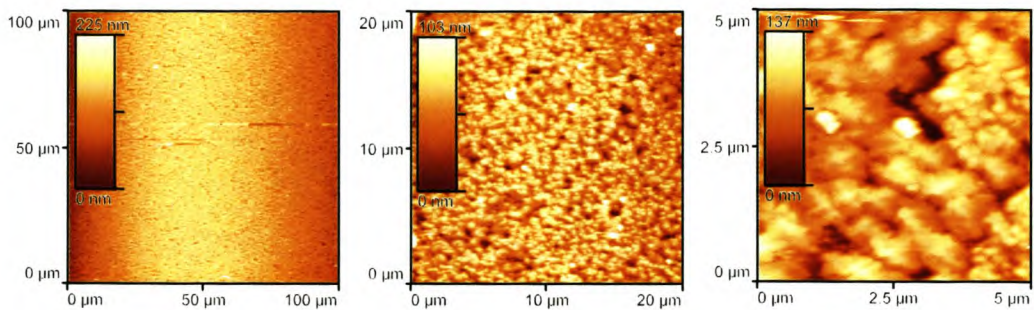
Figure 10.17: Measurements on Sample 12 with (a) X-ray diffraction, (b) magnetic susceptibility and (c) Atomic Force Microscopy (AFM).



(a)

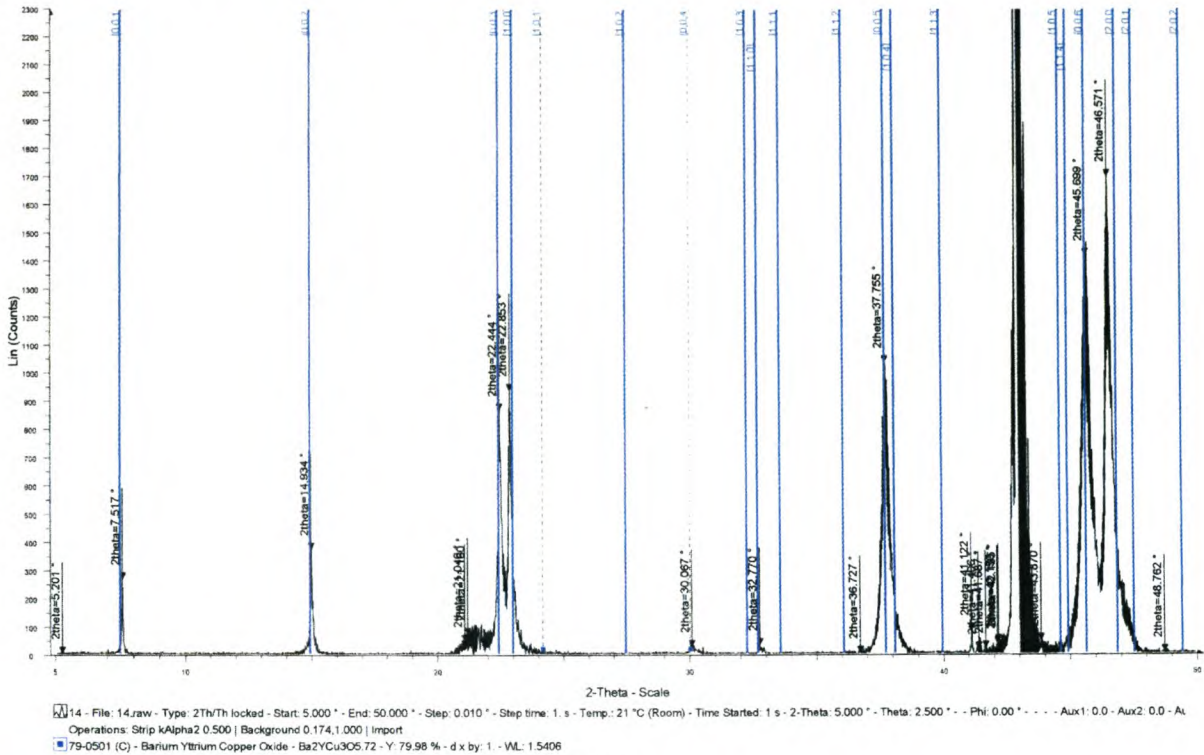


(b)

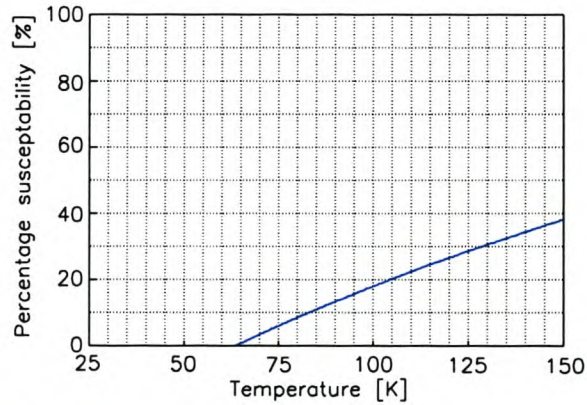


(c)

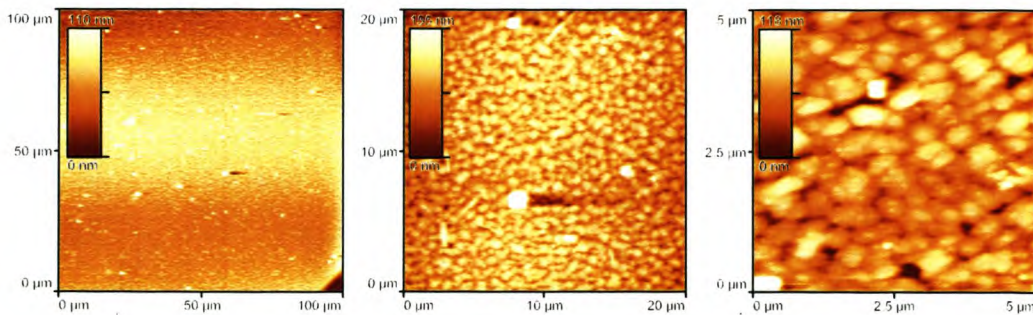
Figure 10.18: Measurements on Sample 13 with (a) X-ray diffraction, (b) magnetic susceptibility and (c) Atomic Force Microscopy (AFM).



(a)

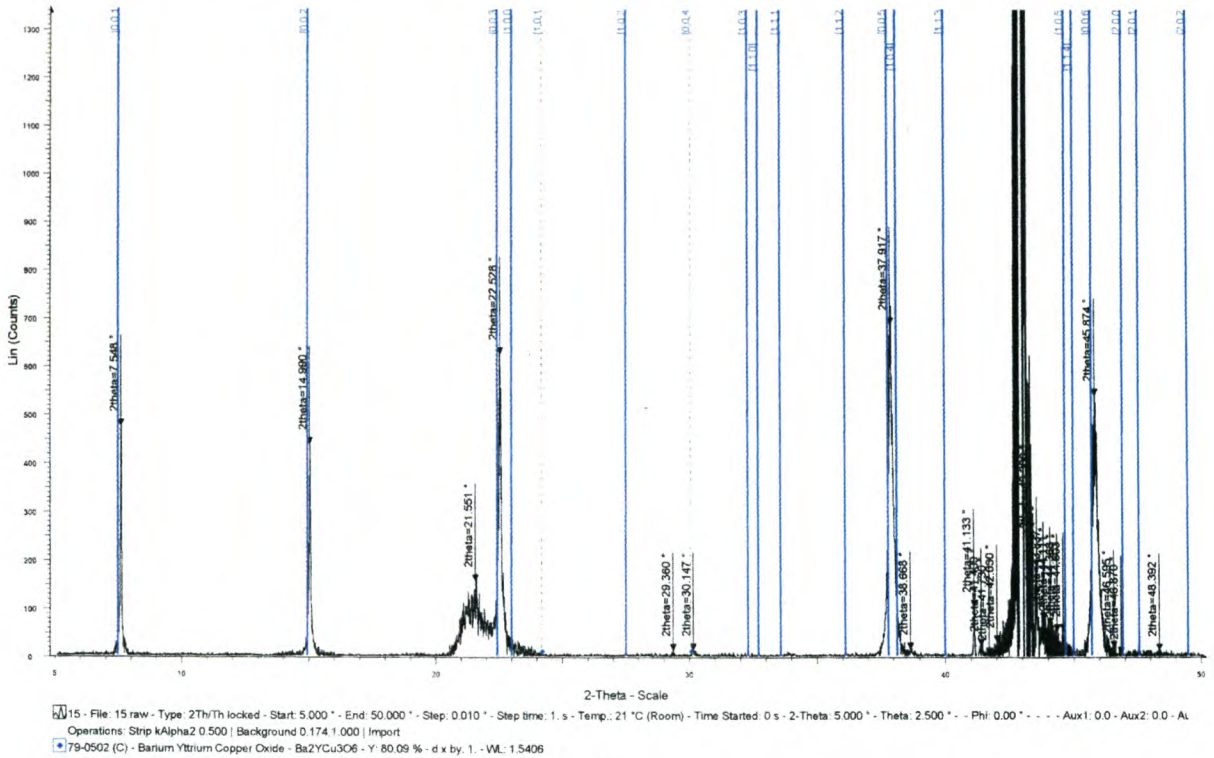


(b)

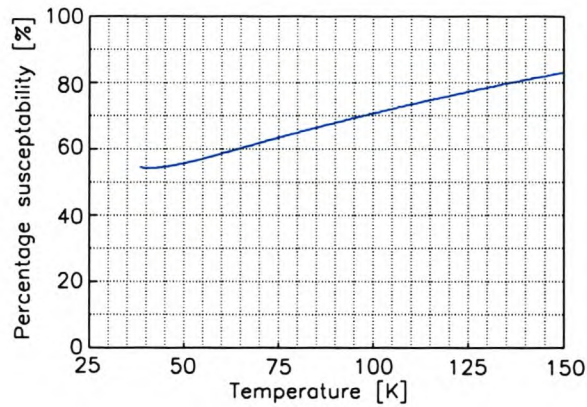


(c)

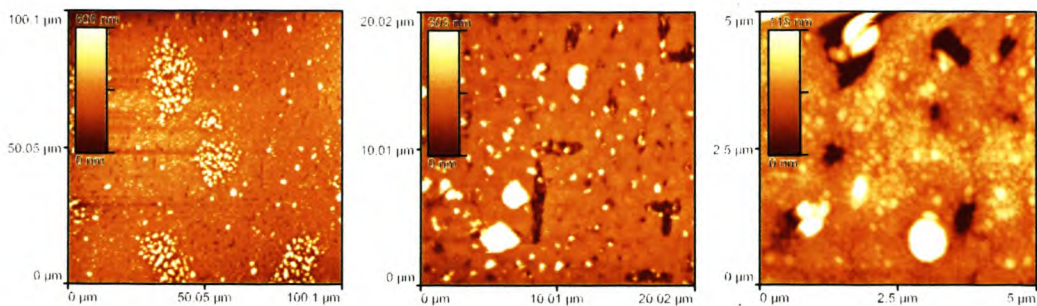
Figure 10.19: Measurements on Sample 14 with (a) X-ray diffraction, (b) magnetic susceptibility and (c) Atomic Force Microscopy (AFM).



(a)

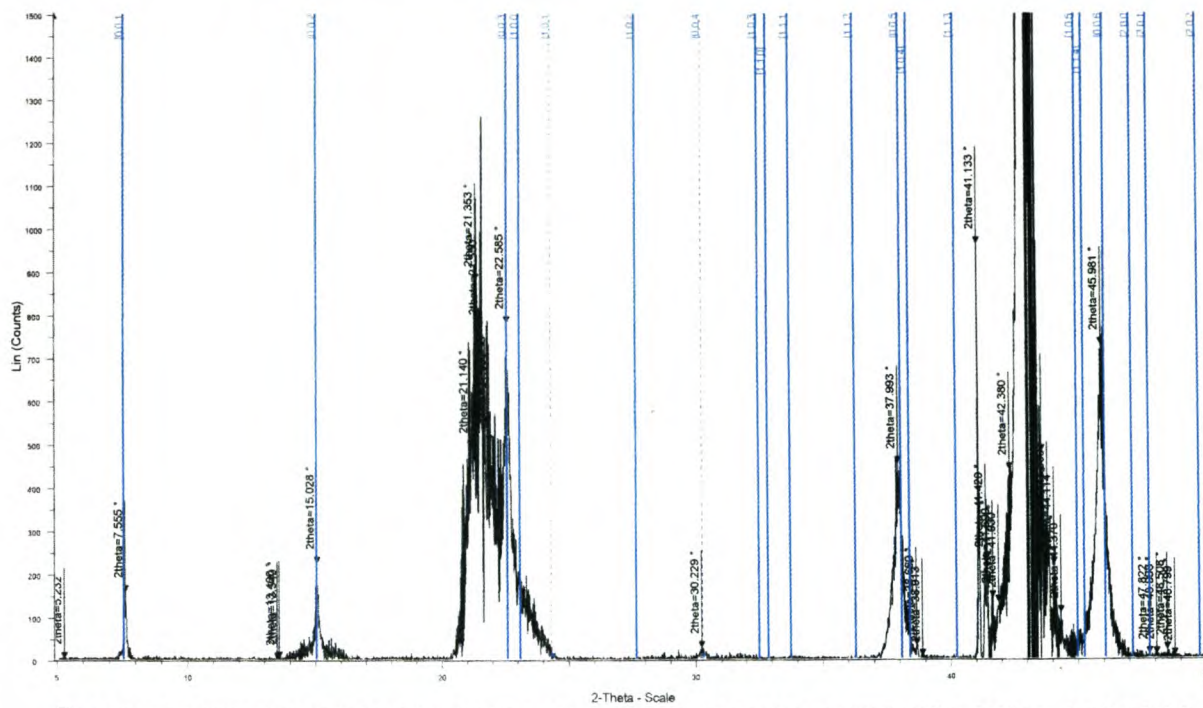


(b)

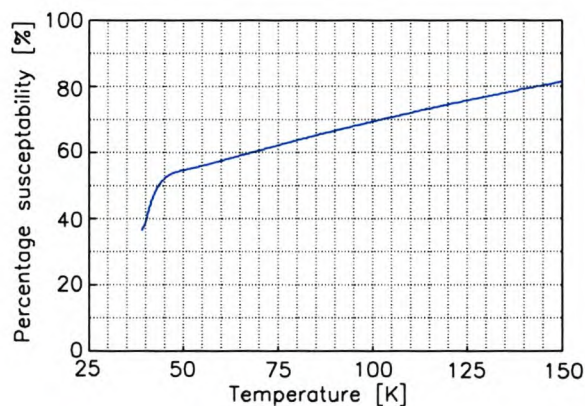


(c)

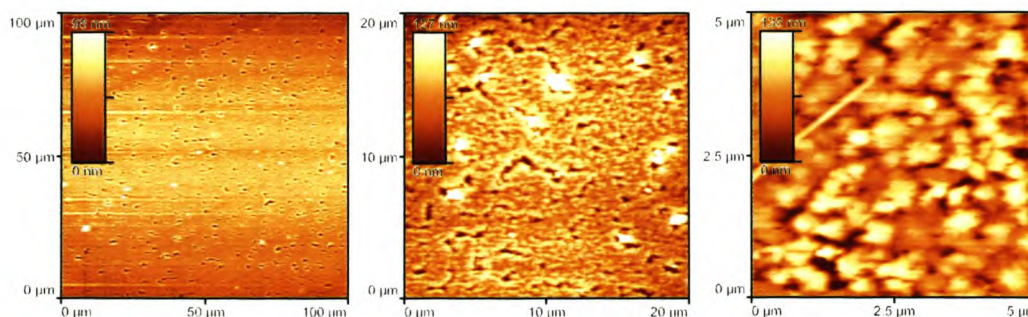
Figure 10.20: Measurements on Sample 15 with (a) X-ray diffraction, (b) magnetic susceptibility and (c) Atomic Force Microscopy (AFM).



(a)

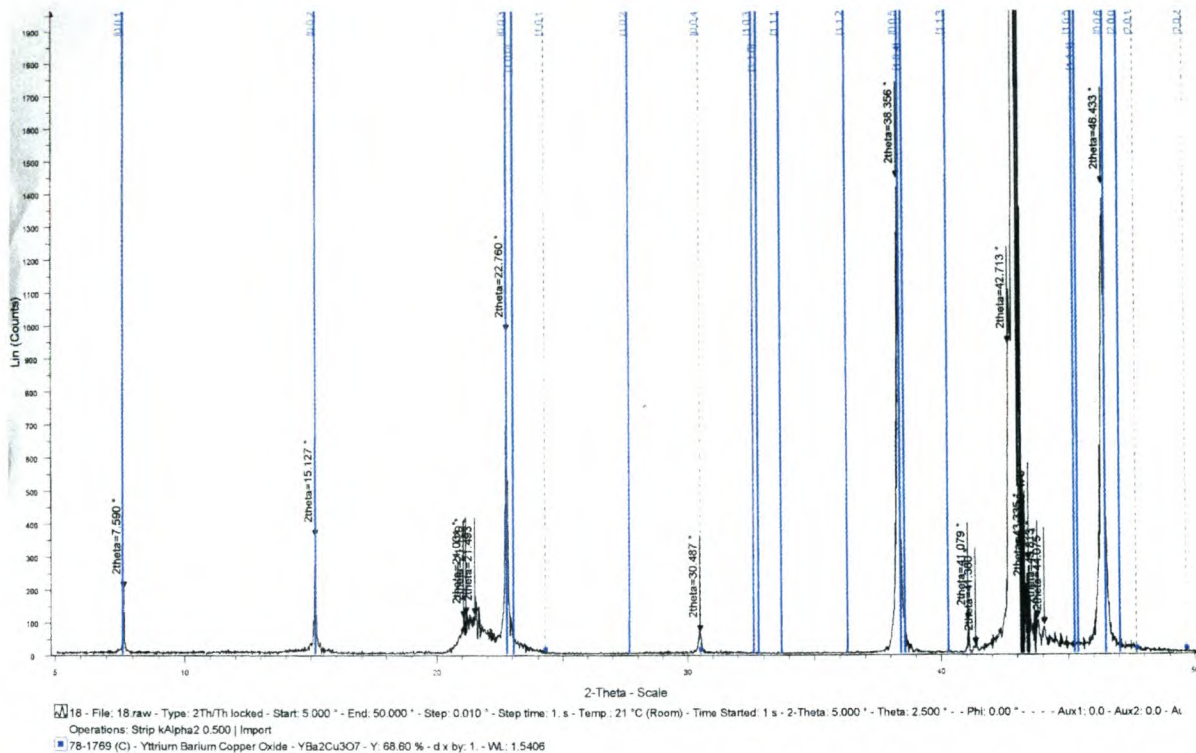


(b)

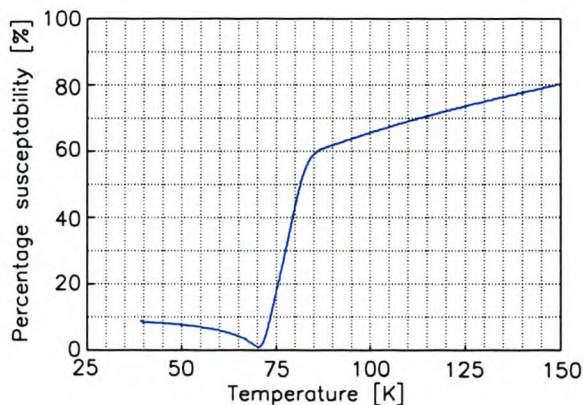


(c)

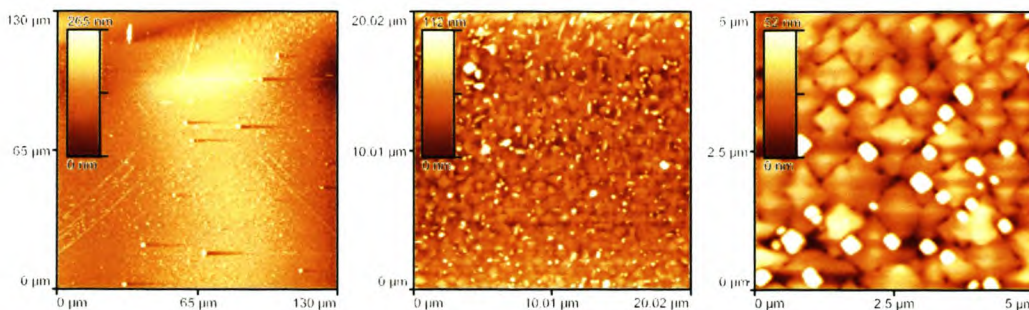
Figure 10.21: Measurements on Sample 16 with (a) X-ray diffraction, (b) magnetic susceptibility and (c) Atomic Force Microscopy (AFM).



(a)

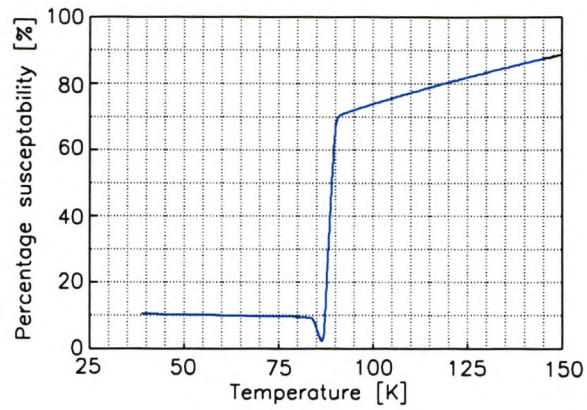


(b)

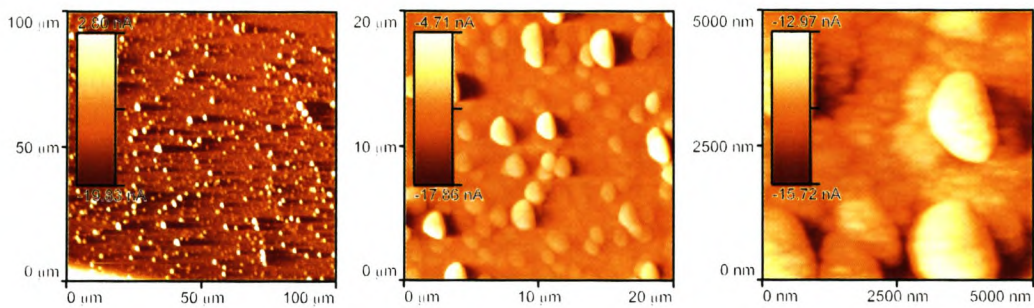


(c)

Figure 10.22: Measurements on Sample 18 with (a) X-ray diffraction, (b) magnetic susceptibility and (c) Atomic Force Microscopy (AFM).



(a)



(b)

Figure 10.23: Measurements on optimum sample with (a) magnetic susceptibility and (b) Atomic Force Microscopy (AFM).

Chapter 11

Conclusions

In this thesis the successful development, re-definition, improvement and characterisation of a process for the fabrication of high-quality HTc SQUIDs was described. The most important achievements during my work have been the following:

- A literature review summarising the most important work done in the field of the fabrication, design and modelling of HTc SQUIDs in recent years. Additionally, a review of the application of SQUID technology in the field of Biomagnetics is presented. This information is a good guide and a starting point for advanced research (PhD).
- The establishment of the use of experimental design in the re-engineering of the HTc SQUID fabrication process. This has important implications, both for the understanding of processes like PLD and for the continuous optimisation of other processes that are difficult to model. DOE has proven itself as an extremely useful tool.
- The characterisation of the PLD process. The characterisation has been successful in pointing out the important interactions, showing weaknesses in the process and indicating the areas of optimal deposition. This will allow future use and tuning of this process to proceed rapidly and cost-effectively.
- It is the first time that the influence of ozone during the PLD process on the quality of YBCO superconductors has been systematically investigated. This research is new and it adds useful knowledge to the field of YBCO fabrication. The positive effect ozone has on increasing the robustness of the PLD process was received with great interest at the IEEE conference on Applied Superconductivity (2002).
- During the process of characterisation several permanent improvements was made to the PLD system that improved the reliability, the efficiency and quality of the process.

- The development of the ion mill enables easy high-quality patterning of HTc SQUIDs. The development also increased the scope for research and development at the university beyond the area of superconductivity. Through the ion mill, new areas of research, like nano-technology will become viable.
- As a direct result of the work and research in this thesis the researcher also started development of a electron-beam lithography facility. In the first place this will enable the fast prototyping of different SQUID structures, but this facility will also be useful in a wide variety of other fields, like the nano-technology field mentioned above. The road-map for the continuing development of this facility will be given in Chapter 12.
- Except for its academic value in terms of knowledge gained and the physical value of improvement to the various systems and development of new systems, this thesis also had the effect of establishing an amount of expertise in the technical staff of the university. Forgotten methods and equipment have been repaired and improved and their use were studied. Perhaps the most useful of all this is that somebody on the permanent technical staff now knows how to operate the equipment to produce high-quality results.
- Finally, this thesis –due to its broad scope and the fact that some of the important problems associated with the fabrication process have finally been overcome or properly characterised– has opened up several avenues for further research in the field of high-temperature superconductivity. The most important of these fields are perhaps that of high-temperature logic.

Except for these main conclusions there were several other aspects which must be concluded.

11.1 The Literature review

11.1.1 Josephson junctions and SQUIDs

For both high-temperature Josephson junctions and SQUIDs there has been a lot of development in recent years. Although the basic phenomenon is not yet understood, the mathematical models are approaching usefulness. There are also numerous practical developments, especially in the fields of rf SQUIDs and electronic compensations. These developments place practical HTc magnetocardiographs well within reach.

The literature review contains a lot of information on all aspects of SQUID design and should be a useful source of information for somebody who wants to develop a high-quality SQUID. Because of the vastness of the field everything could not be covered, therefore the focus was on the practical aspects and the theory that had practical application. The focus was also more on new research than on work that had already been compiled in a textbook.

11.1.2 Biomedical applications of SQUIDS

It has been shown that the field of biomagnetism presents great challenges, and some of these challenges can be met only through the use of SQUID technology. In our own country this is a field that is very underdeveloped. The benefits of being able to develop and understand this technology are significant.

11.2 Design of experiment

The use of experimental design can make a great difference in the characterisation of processes. It is superior to the one-parameter-at-a-time experiments frequently used for this purpose. The correct application of experimental design requires a good understanding of the underlying statistical principles. If these principles are fully understood and applied, DOE becomes a powerful tool for characterising and optimising processes.

Another area where DOE is frequently used in the industry is the improvement of the robustness of a process. In the fabrication of YBCO superconductors this is of extreme interest since it is very important to have a reproducible process. The greater the robustness of the process towards parameter variations, the easier it is to obtain reproducible results. This application of DOE could not be done within the allocated time but must be considered for future optimisations.

11.3 The PLD process

During the characterisation of the PLD process several improvements were made to the system and some interesting lessons were learned on the behaviour of the system and the application of DOE.

11.3.1 The improvements

Both the improvements to the substrate heater and the laser beam have been proven to work reliably with good results. The ozone generator also performed well. The first improvements to the heater failed frequently because the bulbs were being operated too close to their limits. After being replaced with a much stronger bulb, the system stabilised.

11.3.2 The application of DOE

The DOE provided a large amount of new and useful information on the influence of the various parameters in the PLD process. These were discussed in section 10.1. The strength of this method was its high rejection of noise. By enabling us to compare variance of the noise with the responses to parameter changes it allowed us to be sure that the parameters we identified as significant are truly significant.

Due to several factors the noise has been higher than it might have been. This would have invalidated the results of a one-parameter-at-a-time experiment, but with DOE we simply lost some of the weaker effects, while the strong effects remained evident.

If the various constraints are considered it becomes obvious that the use of a DOE achieved good results in circumstances where it would have been impossible to do so otherwise. In the following sections a few of the factors and constraints that could have had a influence on the noise are considered and ways to lower them are proposed.

11.3.3 Dealing with equipment failures

One of the problem that frequently occurred was the failure of equipment. A related issue, the continuous redesigning of the equipment has already been mentioned. These issues gives rise to extra variability in the process, since factors that were considered fixed in the original design could possibly change. In these kind of circumstances blocking is a good method to use.

The concept of blocking allows a big experiment to be divided into sub-blocks that can be done under homogeneous circumstances. It also allows the verification of results before the whole experiment is complete and this could allow certain problems to be fixed without the need to repeat a large experiment. Blocking requires a slightly larger amount of samples. The exact amount depend on the number of blocks.

In uncertain circumstances, especially with equipment that has been irregularly used the extra samples required for blocking is justified by the increased noise resistance. At the start of the characterisation of a complex system it is a good idea to allow for the possibility that certain parameter ranges and perhaps even parameters might have to be changed. Blocking in these cases is advisable.

11.3.4 Measurements conditions

With characterisation measurements one must remember that the operator and the measurement apparatus have a definite effect on the result. This was the case for the AFM measurements, done by three different operators on two different microscopes.

It was found by visual inspection of the results that both the operator and the microscope play a large role in the final result. This is probably due to the large number of measurement parameters set by the operator and the sensitive nature of the microscope. In this type of circumstances it would be good to record the operator and measurement apparatus of each sample. This could be used to generate a plot of the residual sorted by operator and microscope that would show any pattern in the measurements.

As a whole, the roughness results contain a large amount of noise, due to poor measurement accuracy and large spreads of measured values. The poor accuracy leads to uncertainty about whether the mean of the measurements is at the correct place. The large spread in measurements give a large variance, making it difficult to determine whether any effect is significant.

11.3.5 Parameter interactions

In the Taguchi method none of the specified interactions are aliased to one another or to main parameters, but main parameters could be aliased with non-specified two-parameter interactions. This is seldom a good idea since a main effect could then look like a two-parameter interaction and the other way around. However, it is reasonably easy to check the aliasing table after using the Taguchi method to make sure that this is not the case.

A better approach would be to avoid the Taguchi method entirely and rather use an ordinary fractional factorial design. Usually there are quite a few possible combinations of higher-order generators that will not cause this problem. The generators can be used and alias tables can be calculated until a suitable combination of two-parameter interactions is found.

In cases where the main effect is already aliased with the two-parameter interaction the main effect must be separated from the interaction. This is done by conducting a separate mini-experiment.

11.3.6 Optimisation with fractional-factorial experiments

2^k Factorial analysis is originally intended for screening experiments. As a consequence of the lack of resources one is sometimes forced to use the results of the factorial analysis for optimisations as well. As was seen in section 10.1 this does give good results. Still, this is not the recommended way to do it.

A better approach is to use the initial 2^k factorial experiments for screening and perhaps indicating the direction of the optimal. For optimising a second experiment is recommended. In this experiment the 2^k analysis could be mixed with a 3^k analysis in cases where sharp peaks are suspected. 3^k refers to having k factors at three levels each. The factors for this second experiment will be the ones pointed out in the initial 2^k fractional factorial experiment to be the significant parameters. This new experiment can also

be reduced to a fractional factorial experiment and all the statistic tools can still be used. The advantage is that this new experiment allows higher resolution of the selected effect because all other parameters are fixed or truly random. The use of allowing some parameters to have 3 values is that higher order surfaces can be fitted to the data. These surfaces have the ability to clearly indicate the maxima as well as the robustness of the process. The robustness is determined by the slope of the surface near the maximum point.

In Chapter 12 we will propose a way in which this approach can be applied to the current optimisation of the PLD process.

11.3.7 Treatment of other noise sources.

The following aspect also added noise to the outcome of the experiment, the reason for the noise will be explained and a solution suggested.

Critical parameters Even after an extensive literature study one is not able to be absolutely sure of the importance of the various parameters. Because it is not possible to include all parameters in the experiment the situation arises where an important parameter is allowed to vary randomly, thereby introducing extra noise in the system. In the PLD process the researcher suspect the number of shots to be such a parameter. The number of shots are suspected to influence both the responses T_c and surface roughness. The deposition time was, however, included in the results, from this and the laser frequency it is possible to estimate the number of shots with a reasonable accuracy. Thus the number of shots can be included in the model as a nuisance parameter. Doing this will allow some of the noise to be reduced.

Precision in executing experiments One of the determining factors in a DOE is the precision with which the experiment is executed. All possible factors that can be controlled must be held as constant as possible to reduce the noise in the experiment. Lack of control over things like substrate and target cleanness caused unnecessary noise. Some of the substrates has not been properly cleaned and it was found that finger marks led to severe degradation of the thin film in certain places. These experiments had to be repeated.

11.4 The development of the ion mill

The broad area of application of the ion mill has already been emphasised at the beginning of the chapter. We saw that the results from a sample etched with the ion mill is superior to the sample etched using wet etching. The resolution of the ion mill is much higher than that of wet etching. At the moment the UV

lithography is the limiting factor in the fabrication and not the milling anymore. Once the electron beam lithography unit has been fully develop it will be possible to pattern sub-micron junctions on the YBCO.

The mill can also be used –as mentioned in section 4.8.1– for the tuning and improvement of SQUIDs. It also enables the fabrication of step edges using the fabrication method described in section 3.3.2. Step-edge junctions are superior to bi-crystal junctions because the junctions are freely positionable and it is possible to achieve β_L values in the order of 1 with junction widths of $4\ \mu\text{m}$. Junction widths of $4\ \mu\text{m}$ is easily achievable by a well optimised UV lithography process.

The development of the ion mill has vastly increased the number opportunities for the fabrication of SQUIDs as well as other research areas.

11.5 Final remarks

This thesis was successful in achieving the development, re-definition and characterisation of the SQUID fabrication process. I believe that the work begun in this thesis should be continued upon, to establish a fully functional SQUID development facility. I also believe that the development of an MCG should be continued, based on the foundation established in this work. To enable the continuation of this work the issues that still need to be addressed as well as suggestions on how it could be addressed will be presented in the next chapter. The researcher should still be able to complete a number of these issues before the end of the year. The rest will have to be resolved in a separate project.

Just before the finalisation of this thesis the researcher attended the IEEE conference on Applied Superconductivity (2002), where he presented his work. From the response of the scientific community it is clear that the issues addressed in this thesis also present problems for other researchers even in technologically more advanced countries. While enormous progress has been made in developing mass fabrication techniques for HTc superconducting wires and magnets, a lot of opportunities in the fabrication of HTc devices still remain. There are technologies that are better suited to mass fabrication than PLD. As a research tool, however, PLD is still preferred. From this conference it became clear that superconductivity is entering the marketplace and will prove to be a strong competitor in areas like telecommunication, satellites, information processing and medicine.

This thesis has achieved a lot in establishing a research facility and opportunities that is unique in South Africa. Because of the work presented in this thesis as well as the work of the other researchers at this university, the University of Stellenbosch is in a good position to gain from these global trends. It is vital that the University of Stellenbosch continues to maintain and enhance these facilities and continue to add new expertise in the field of superconductivity.

Chapter 12

The way forward

As seen in the previous chapter a lot was achieved in terms of the final fabrication of a SQUID for the use in magnetocardiography (MCG). In this chapter the a road-map for the continuing development and improvement of several of the aspects started in this thesis will be presented.

The first part of this chapter will address the outstanding issues in the fabrication process. These include the optimisation and robustness analysis of the PLD process and the characterisation of the lithography and ion milling process.

The second part will address additional improvements and developments as well as research stemming from the work presented in this thesis. Some of the proposals for future research include research on step-edge junctions, the development and testing of rf SQUIDs, research on high-temperature logic and development of a sub- μm etching capability.

12.1 Finalising the fabrication process

12.1.1 Optimising the PLD process

After the important parameters of the PLD process have been identified and an initial optimisation has been done, a final experimental design still remains.

Experimental design is an iterative process –using one big experiment for both the characterisation and optimisation is a dangerous principle. The parameter screening has been successful, but having determined the important parameters, the next step is to design a separated experiment in the smaller design space specified by the interaction diagram and optimise the process using this experiment.

The important parameters from the results are shown in table 12.1. There are two parameters present as interactions but not as main parameters. This means that although changing the individual parameters has little effect on the system, changing them together does have a significant effect on the system.

Main parameters	Interactions
oxygen pressure	substrate-temperature \leftrightarrow ozone
target-substrate distance	target-substrate-distance \leftrightarrow laser-energy
substrate temperature	oxygen-pressure \leftrightarrow ozone
ozone	laser-frequency \leftrightarrow laser-energy

Table 12.1: The important parameters and interactions

For a uniform thickness of the thin film, the target-substrate distance has to be fixed at a range of 70-100 mm. This eliminates one parameter from the final optimisation. From the distance \leftrightarrow laser-energy interaction in the interaction diagram the laser energy should be as high as possible for the longer distance. This makes sense in terms of the plume length as well. The plume should be longer so that the substrate is located near the tip of the plume. For the remaining parameters two values should be chosen around the value lying at the optimum point. The optimum point is determined from the results of the PLD characterisation.

It is debatable whether it is necessary to include the laser frequency parameter in the optimisation experiment. It might be possible to resolve the counter-intuitive laser-frequency \leftrightarrow laser-energy interaction by including it. My suggestion is that it is included in the experiment.

These parameters gives a 2^4 full factorial experiment. In this case, however, only a half fraction is required. This gives 8 runs. The results of these experiments can be combined with the previous fractional factorial experiment by generating a mixed factorial design.

12.1.2 Robust design of the PLD process

It is possible to optimise a process in such a way that the process is robust to noise or small parameter variations. This means that the output remains relatively stable in the presence of noise or small parameter variations.

To optimise a process to be robust, the noise factors must be controlled for the purpose of the experiment, although they are assumed to be random for the actual process. The experiment is then separated in noise parameters and control parameters.

For the PLD process the size of this experiment would be roughly similar to the original experiment. In this case it would be advisable to introduce the robustness analysis as part of the routine fabrication

process. To do another separate large run would consume too much time and too many resources. The robustness analysis could be included in the regular process by setting aside a separate day per week in between the normal production process. The design itself can be generated using software like Design-Expert [115]. The theoretical background can be found in the book by Montgomery [112, pp. 488-500].

12.1.3 Monitoring and improving the PLD process

The process will tend to drift from the optimal values because of variations in the operator, raw material, age of the component and environmental changes. One method of continuous monitoring and improvement is called Evolutionary Operation (EVOP).

With EVOP small variations in the levels of the operating parameters under consideration are systematically introduced. These variations are determined by an ordinary 2^k design. The changes must be large enough that improvement will be noticeable but not so large that it causes serious disturbances in the yield or quality of the process.

The responses should be easy to measure and non-destructive. AFM and susceptibility measurements might be best suited to this purpose. For the theory and application of the process the reader is again referred to Montgomery [112, pp. 484-488].

12.1.4 Characterisation of the UV lithography and Ar-ion milling process

The argon mill has been built and tested but the parameter setting for optimum patterning of the YBCO still has to be determined. It is also suggested that the UV lithography should be optimised along with the argon milling process after the initial tuning. This is because aspects like the resist thickness and baking time will have an influence on the argon milling process.

The tuning of the UV lithography process is treated in appendix D. This process will definitely be completed before the end of the year. However, the characterisation of the Ar-ion milling process still has to be considered.

The milling current is easily measured but the electron voltage still has to be considered. This voltage determine the velocity of the electrons and thus the force with which it impacts on the YBCO surface. The literature (see section 6.3.2) suggests a very low electron voltage of ≈ 500 V. To obtain a precise measure of the voltage some type of energy meter is necessary. These measurements can be done at iTemba Labs.

In the meantime the acceleration voltage can be used as an estimate of the electron voltage. The acceleration voltage is the voltage applied between the extraction electrode and the ground electrode. To

accurately estimate the ion energy a simulation will have to be used. An overview of possible simulation packages is given by Zaim et al [120].

Once these have been determined the following parameters need to be included in the experimental design:

- The ion current.
- The ion voltage.
- The angle of the substrate relative to the ion beam.
- The chamber pressure

As an initial experiment a resolution-III design can be used. The response variables will be:

- The percentage of degradation of the YBCO, determined by four-point-probe measurements before and after milling.
- The resolution of the milling, determined by SEM measurements.
- The milling rate.

Once the ion milling process has been characterised separately it would be useful to determine the effect of the photoresist thickness and hard-baking time on the final result. A DOE combining the two processes can be used for this purpose.

The optimum will be the parameter set producing the steepest edges with the least degradation of the YBCO surface in the shortest time.

12.2 New developments and research

12.2.1 Electron-beam lithography

Electron-beam lithography uses an electron beam to expose an electron-sensitive photoresist in the same way UV light exposes the photoresist in the UV lithography process. While UV lithography utilises a mask through which the pattern is exposed on the photoresist, e-beam lithography scribes directly on the photoresist with a thin bundle of electrons. The bundle is typically in the order of a few nanometers and this allows e-beam lithography to obtain much higher resolutions than UV lithography. E-beam

lithography also allows for rapid prototyping because a design can be written directly onto the photoresist without having to make a mask first. While the scribing process is too slow (in the order of a hour) to be of use in a production environment, it is ideal for a research environment like the University of Stellenbosch.

During the development of the ion mill the researcher became aware of a retired transmission electron microscope. The idea originated to modify this device to obtain an e-beam lithograph. The necessary modifications are quite simple. There is a company that sells kits for converting old electron microscopes into e-beam lithographs, but the kits are very expensive (in the order of 35 000 USD) [126]. Therefore it was decided to attempt the conversion ourselves.

With the basic conversion one replaces the module that scans the electron beam over the surface of the sample with a computer controlled module that allows the beam to be steered. The computer analyses the design and determine a scan pattern to reproduce the design on the photoresist. The beam is then scanned at a speed determined by the sensitivity of the photoresist. The photoresist is developed in a process similar to the UV lithography process and the sample is ion-milled.

The electron microscope was obtained and in the process of being converted to an e-beam lithograph. This device will vastly expand the research possibilities at the University of Stellenbosch.

12.2.2 Future research proposals

12.2.2.1 Step-edge junction

Step-edge junctions can be easily manufactured using the newly developed Ar-ion mill. The steps are defined by milling away part of the substrate before deposition of the YBCO layer. UV lithography and conventional photoresist can be used for transferring the step patterns. Alternatively there are more elaborate processes which gives steeper step edges or variable step profiles. These were described in section 3.3.2.

It is suggested that more research should be done on this aspect of SQUID manufacture; the newly developed facilities are sufficient for research of this kind. The SQUID obtained with step-edge junctions are just as good as the much more rare and expensive bi-crystal junction.

12.2.2.2 rf-SQUIDs

As was mentioned in the Chapter 9, the rf SQUID should be seriously considered as an alternative to the dc SQUID (the design and readout electronics of the rf SQUID was described in detail in chapter 4).

Research on rf-SQUID magnetometers would benefit from a good background in rf-electronics. The design of the magnetometer itself is less problematical than that of a dc SQUID but the readout and coupling of the pickup coil would present an interesting rf-design challenge.

12.2.2.3 High-temperature superconducting logic

The area of expertise at Stellenbosch is superconducting logic. A lot of work has been done on the design and simulation of RFSQ logic as well as improving the robustness of the circuits to parameter variations. The parameter variations in high-temperature Josephson junctions is one of the factors limiting the implementation of superconducting logic. This improved robustness together with a well characterised fabrication process could provide a way of implementing high-temperature logic.

Research involving the patterning of a few highly optimised gates on YBCO thin film would be relatively simple once the e-beam lithograph is operational. The design of the readout electronics might be more problematic due to the lower voltages of HTc junctions compared to low-temperature junctions.

12.2.2.4 Sub-micrometer patterning

For high-temperature superconducting logic to be truly viable, sub- μm patterning is necessary. This requires a multi-layer etching technique where the photoresist pattern is first transferred to a carbon mask using reactive ion etching and then the carbon mask is used to etch the YBCO thin film.

The multilayer technique has already been developed [87], but the implementation and optimising of the process would take at least 6 months.

Bibliography

- [1] James D. Doss, "Engineer's Guide to High-Temperature Superconductivity", John Wiley & Sons, 1989.
- [2] P.F. Dahl, "Kammerlingh Onnes and the discovery of superconductivity: The Leyden years, 1911-1914", *Historical Studies in the Physical Sciences*, Vol. 15, Part 1, pp. 1-37, 1984.
- [3] P. F. Dahl, "Superconductivity after World War I and circumstances surrounding the discovery of a state $B = 0$ ", *Historical Studies in the Physical and Biological Sciences*, Vol. 16, Part 1, pp. 1-58, 1986.
- [4] F. London, "Superfluids, Macroscopic Theory of Superconductivity", Vol. 1, John Wiley & Sons, New York, pp 3-4, 1950.
- [5] J. Bardeen, L. N. Cooper and J. R. Schrieffer, "Theory of Superconductivity", *Physical Review*, Vol. 108, No. 5, pp 1175-1204, December 1957.
- [6] I. Giaever, "Energy gap in superconductors measured by electron tunneling", *Physics Review Letters*, Vol. 5, No. 4, pp 147-148, August 1960.
- [7] B.D. Josephson, "Possible new effects in superconductive tunneling", *Physics Letters*, Vol. 1, No. 7, pp 251-253, July 1962.
- [8] J.G. Bednorz and K.A. Müller, "Possible High T_c Superconductivity in the Ba-La-Cu-O System", *Applied Physics B - Condensed Matter*, Vol. 64, pp. 189-193, 1986.
- [9] M.K. Wu, J.R. Ashburn, C.J. Thorng, P.H. Hor, R.L. Meng, L. Gao, Z.J. Huang, Y.Q. Wang and C.W. Chu, "Superconductivity at 93K in a New Mixed-Phase Y-Ba-Cu-O Compound System at Ambient Pressure", *Physics Review Letters*, Vol. 58, No. 9, pp. 908-910, 1987.
- [10] T. P. Orlando, K. A. Delin, "Foundations of Applied Superconductivity", Addison-Wesley Publishing Company, 1991.
- [11] T. Van Duzer, C. W. Turner, "Principles of Superconductive Devices and Circuits", Second edition, Prentice Hall PTR, 1999.

- [12] R. Gross, L. Alff, A. Beck, O.M. Froehlich, D. Koelle and A. Marx, "Physics and Technology of High Temperature Superconducting Josephson Junctions", *IEEE Transactions on Applied Superconductivity*, vol. 7, no. 2, pp. 2929-2935, June 1997.
- [13] K.A. Delin, A.W. Kleinsasser, "Stationary Properties of High-Critical-Temperature proximity effect Josephson junctions", *Superconducting Science and Technology*, Vol. 9, pp. 227-241, 1996.
- [14] WRSPICE, Whitley Research Inc, Sunnyvale, USA, www.wrcad.com.
- [15] W. Andrä and H. Nowak, "Magnetism in Medicine: a handbook", Wiley-VCH, 1998.
- [16] Biomag 2000,"Book of Abstracts",12th international conference on Biomagnetism, August 13-17, 2000, Helsinki University of Technology, Espoo, Finland.
- [17] J.W. Burgoyne, P.D. Daniels, K.W. Timms and S.H. Vale, "Advances in Superconducting Magnets for Commercial and Industrial Applications", *IEEE Transactions on Applied Superconductivity*, vol. 10, no. 1, pp. 703-709, March 2000.
- [18] R. G. McNeil, R. C. Ritter, B. Wang, M. A. Lawson, G. T. Gillies, K. G. Wilka, E. G. Quate, M. A. Howard III and M. S. Grady, "Characteristics of an Improved Magnetic-Implant Guidance System", *IEEE Transactions on Biomedical Engineering*, vol. 42, no. 8, pp. 802-807, August 1995.
- [19] M. Burghoff, B.-M. Mackert, W. Haberkorn, G. Curio and L. Trahms, "High resolution magnetoneurography", *Applied Superconductivity*, vol. 6, nos 10-12, pp. 567-575, 1998.
- [20] B.-M. Mackert, G. Curio, M. Burghoff, L. Thrahms and P. Marx, "Magnetoneurographic 3D localization of conduction blocks in patients with unilateral S1 root compression", *Electroencephalography and clinical Neurophysiology*, vol. 109, p 315-320, 1998.
- [21] S.F. Xu, Y.J. Tian, H.B. Lü, D.F. Cui, Z.H. Chen, L. Li and G.Z. Yang,"The effect of laser energy density and target substrate distance on the quality of $\text{YBa}_2\text{Cu}_3\text{O}_{7-x}$ thin films", *Superconducting Science and Technology*, no 7, pp. 435-437, 1994.
- [22] A. Inam, X. D. Wu, T. Venkatesan, S. B. Ogale, C. C. Chang and D. Dijkkamp, "Pulsed laser etching of high Tc superconducting films" *Applied Physics Letters*, vol. 51, pp. 1112-1114, 1987.
- [23] G.A. Farnan, M.P. McCurry, C.C. Smith, R.J. Turner and D.G. Walmsley,"Growth of $\text{YBa}_2\text{Cu}_3\text{O}_{7-\delta}$ thin films in pulsed laser deposition: influence of target, substrate and deposition rate.", *Superconduction Science and Technology*, no. 13, pp. 262-272, 2000.
- [24] E.-H. Lee, S.J. Park, I.H. Song, I. Song, J. Gohng, J. Sok and J.W. Lee,"Fabrication of High Quality $\text{YBa}_2\text{Cu}_3\text{O}_y$ Thin Films using Pulsed Laser Deposition", *IEEE Transactions on Applied Superconductivity*, vol. 7, no. 2, pp. 1193-1196, 1997.

- [25] E. H. Conradie, "The Design and Fabrication of DC SQUID Magnetometers", Master's thesis, Stellenbosch, University of Stellenbosch, 1998.
- [26] E. C. Knox-Davies, "The Design and Fabrication of a High- T_c DC SQUID Gradiometer", Master's thesis, Stellenbosch, University of Stellenbosch, 1999.
- [27] V. Boffa, T. Petrisor, L. Ciontea, U. Gambardella, S. Barbanera, "High-quality surface YBCO thin films prepared by off-axis pulsed laser deposition technique", *Physica C*, no 276, p 218-224, 1997.
- [28] D. Marré, A. Diaspro, C. Ferdeghini, G. Grassano, I. Pallecchi and A. S. Siri, "Two-dimensional growth of atomically smooth YBCO epitaxial films deposited by PLD in a pulsed oxygen flow", *Superconducting Science and Technology*, no 11, p 737-743, 1998.
- [29] A. Marcu, C. Grigoriu, W. Jiang and K. Yatsui, "Pulsed laser deposition of YBCO films in a shadow mask configuration", *Thin Solid Films*, no. 360, pp. 166-172, 2000.
- [30] V. Craciun, R. K. Singh, "Ultraviolet-assisted pulsed laser deposition of thin oxide films", *Applied Surface Science*, no. 168, pp. 239-243, 2000.
- [31] J.P. Sydow, M. Berninger, R.A. Buhrman and B.H. Moeckly, "Effects of Oxygen Content on YBCO Josephson Junction Structures", *IEEE Transactions on Applied Superconductivity*, vol. 9, no. 2, pp. 2993 - 2996, 1999.
- [32] C. Horstmann, P. Leinenbach, A. Engelhardt, R. Gerber, C.L. Jia, R. Dittmann, U. Memmert, U. Hartmann and A.I. Braginski, "Influence of ramp shape and morphology on the properties of YBCO-ramp-type junctions", *Physica C*, no. 302, pp. 176-182, 1998.
- [33] R. Dittmann, J.-K. Heinsohn, A.I. Braginski and C.L. Jia, "Fabrication of $\text{YBa}_2\text{Cu}_3\text{O}_7$ Ramp-Type Junctions by Interface Treatments", *IEEE Transactions on Applied Superconductivity*, vol. 9, no. 2, pp. 3440-3443, 1999.
- [34] K.-O. Subke, S. Krey, H. Burkhardt and M. Schilling, "Technology for $\text{YBa}_2\text{Cu}_3\text{O}_7$ SNS- and SIS-Josephson Junctions", *IEEE Transaction on Applied Superconductivity*, vol. 9, no. 2, pp. 3125-3128, 1999.
- [35] J.B. Bulman, "Magnetic Field Behaviour of SNS Edge Josephson Junctions", *IEEE Transactions on Applied superconductivity*, vol. 9, no. 2, pp. 3149 - 3152, 1999.
- [36] H.-W. Yu, M.-J Chen, H.-C. Yang, S.Y. Yang and H.E. Horng, "Characterisation of Grain Boundaries in $\text{YBa}_2\text{Cu}_3\text{O}_y$ Bicrystal Junctions", *IEEE Transaction on Applied Superconductivity*, vol. 9, no. 2, pp. 3101 - 3104, 1999.

- [37] C.P. Foley, E.E. Mitchell, S.K.H. Lam, B. Sankrithyan, Y.M. Wilson, D.L. Tilbrook and S.J. Morris, "Fabrication and Characterisation of YBCO Single Grain Boundry Step Edge Junctions", *IEEE Transactions on Applied Superconductivity*, vol. 9, no. 2, pp. 4281-4284, June 1999.
- [38] C. Francke, M. Offner, A. Krämer, L. Mex and J. Müller, "Fabrication of $\text{YBa}_2\text{Cu}_3\text{O}_7$ step-edge Josephson junctions for low noise dc-SQUIDs", *Superconducting Science and Technology*, no. 11, pp. 1311-1316, 1998.
- [39] J.C. Nie, L. Chen, L. Li, T. Yang, M.Q. Huang, P.J. Wu, G.R. Liu and Z.X. Zhao, "A simple lift-off process for sharp step edges and $\text{YBa}_2\text{Cu}_3\text{O}_7$ Josephson junctions." *Superconducting Science and Technology*, no. 9, pp. 1087-1091, 1996.
- [40] X.H. Zeng, H. Soltner, D. Selbig, M. Bode, M. Bick, F. Rüdgers, J. Schubert, W. Zander, M. Banzet, Y. Zhang, H. Bousack and A.I. Braginski, "A high-temperature rf SQUID system for magnetocardiography", *Measurement Science and Technology*, no. 9, pp. 1600-1608, 1998.
- [41] R.X. Wu, S.Z. Yang, Y.L. Zhou, B.B. Jin, M. Qian, P.H. Wu, J.H. Gu, and D.S. Ding, "Correlation between surface resistance of $\text{YBa}_2\text{Cu}_3\text{O}_7$ thin films and oxygen pressure during deposition process", *Physica C*, no. 282-287, pp. 591-592, 1997.
- [42] J. Borgmann, A. P. Rijpma, H.J.M. ter Brake, H. Rogalla and P. David, "Highly Balanced Gradiometer Systems Based on HTS-SQUIDs for the Use in Magnetically Unshielded Enviroments", *IEEE Transactions on Applied Superconductivity*, vol. 9, no. 2, pp. 3680-3683, June 1999.
- [43] C.M. Pegrum, A. Eulenburg, E.J. Romans, C. Carr, A.J. Millar and G.B. Donaldson, "High-temperature single-layer SQUID gradiometers with long baseline and parasitic effective area compensation", *Superconducting Science and Technology*, no. 12, pp. 766-768, 1999.
- [44] P. Seidel, F. Schmidl, S. Wunderlich, L. Dörrer, T. Vogt, H. Schneidewind, R. Weidl, S. Lösche, U. Leder, O. Solbig and H. Nowak, "High-Tc SQUID Systems for Practical Use", *IEEE Transactions on Applied Superconductivity*, vol. 9, no. 2, pp. 4077-4080, June 1999.
- [45] J.W. Purpura, "High-Temperature Superconducting Pickup-Loop Hysteresis for Magnetometer and Gradiometer Configurations" *IEEE Transactions on Applied Superconductivity*, vol. 9, no. 2, pp. 4404-4407, June 1999.
- [46] D.F. He, H.-J. Krause, Y. Zhang, M. Bick, H. Soltner, N. Wolters, W. Wolf and H. Bousack, "HTS SQUID Magnetometer with SQUID Vector Reference for Operation in Unshielded Environment", *IEEE Transactions on Applied Superconductivity*, vol. 9, no. 2, pp 3684-3687, June 1999.
- [47] S. Wunderlich, F. Schmidl, L. Dörrer, H. Schneidewind and P. Seidel, "Improvement of Sensor Performance of High-Tc Thin Film Planar SQUID Gradiometers by Ion Beam Etching", *IEEE Transactions on Applied Superconductivity*, vol. 9, no. 1, pp. 71-76, March 1999.

- [48] F. Goerke and A. Thorns, "Influence of target-substrate distance and oxygen pressure on morphology, orientation and homogeneity of laser-deposited $\text{YBa}_2\text{Cu}_3\text{O}_7$ films on MgO (100)" *Physica C*, no. 251, pp. 247-254, 1995.
- [49] V. Schultze, V. Zakosarenko, R. IJsselsteijn, J. Ramos and H.-G. Meyer, "Investigation of Multiple SQUID Arrangements in Single Layer High T_c Magnetometers" *IEEE Transactions on Applied Superconductivity*, vol. 9, no. 2, pp. 3279-3282, June 1999.
- [50] J. Schubert, M. Siegert, M. Fardmanesh, W. Zander, M. Prömpers, Ch. Buchal, J. Lisoni and C.H. Lei, "Superconducting and electro-optical thin films prepared by pulsed laser deposition technique", *Applied Surface Science*, no. 168, pp. 208-214, 2000.
- [51] F. Ludwig, J. Beyer, D. Drung, S. Bechstein, and Th. Schurig, "High-performance High- T_c SQUID Sensors for Multichannel Systems in Magnetically Disturbed Environment" *IEEE Transactions on Applied Superconductivity*, vol. 9, no. 2, pp. 3793-3796, June 1999.
- [52] D. Drung, E. Dantsker, F. Ludwig, H. Koch, R. Kleiner, J. Clarke, S. Krey, D. Reimer, B. David and O. Doessel, "Low noise $\text{YBa}_2\text{Cu}_3\text{O}_{7-x}$ SQUID magnetometers operated with additional positive feedback", *Applied Physics Letters*, vol. 68, no. 13, pp. 1856-1858, 1996.
- [53] H.-M. Cho, R. McDermott, B. Oh, K.A. Kouznetsov, A. Kittel, J.H. Miller Jr. and J. Clarke, "Low Frequency Noise in Field-Cooled, Directly Coupled Magnetometers" *IEEE Transactions of Applied Superconductivity*, vol 9, no 2, pp. 3294-3297, June 1999.
- [54] J. Beyer, D. Drung, F. Ludwig, T. Minotani and K. Enpuku, "Low-noise $\text{YBa}_2\text{Cu}_3\text{O}_{7-x}$ single layer dc superconducting quantum interference device (SQUID) magnetometer based on bicrystal junctions with 30° misorientation angle", *Applied Physics Letters*, vol. 72, no. 2, pp. 203 - 205, January 1998.
- [55] A. Wong, R. Liang, M. Gardner and W.N. Hardy, "Reproducible growth of highly crystalline $\text{YBa}_2\text{Cu}_3\text{O}_7$ thin films on SrTiO_3 by scanning pulsed laser deposition", *Journal of Applied Physics*, vol. 82, no. 6, pp. 3019-3023, September 1997.
- [56] S. Proyer, E. Stangl, M. Borz, B. Hellebrand and D. Bäuerle, "Particulates on pulsed-laser deposited Y-Ba-Cu-O films", *Physica C*, no. 257, pp. 1 - 15, 1996.
- [57] A. B. Brailovsky, S. V. Gaponov, V. I. Luchin, "Mechanisms of melt droplets and solid-particle ejection from a target surface by pulsed laser action", *Applied Physics A*, vol. 61, no. 1, pp. 81-86, 1995.
- [58] E. van de Riet, C.J.C.M. Nillesen and J. Dieleman, "Reduction of droplet emission and target roughening in laser ablation and deposition of metals", *Journal of Applied Physics*, vol. 74, no. 3, pp. 2008-2012, 1993.

- [59] S.R. Foltyn, R.C. Dye, K.C. Ott, E. Peterson, K.M. Hubbard, W. Hutchinson, R.E. Muenchausen, R.C. Estler and X.D. Wu, "Target modification in the excimer laser deposition of YBaCuO", *Applied Physics Letters*, vol. 59, pp. 594 - 596, 1991.
- [60] C. Carr, A. Eulenburg, E. Romans, C.M. Pegrum and G.B. Donaldson, "Planar SQUID Gradiometers Fabricated on 24° and 30° SrTiO₃ Bicrystals", *IEEE Transactions on Applied Superconductivity*, vol. 9, no. 2, pp. 3105 - 3108, June 1999.
- [61] Y. Zhang, D.F. He, N. Wolters, R. Otto, K. Barthels, X.H. Zeng, H.R. Yi, H.-J. Krause, A.I. Braginski and M.I. Faley, "Radio Frequency Bias Current Scheme for dc Superconducting Quantum Interference Device" *IEEE Transactions on Applied Superconductivity*, vol. 9, no. 2, pp. 3813 - 3816, June 1999.
- [62] J. Gareía López, D.H.A. Blank, H. Rogalla and J. Siejka, "Role of the oxygen plasma during in situ growth of YBa₂Cu₃O_{7-x} thin films by pulsed laser deposition", *Physica C*, no. 307, pp. 298 - 306, 1998.
- [63] S. King, L. Coccia and I.W. Boyd, "SEM observations of YBCO on as-received and heat-treated MgO substrates", *Applied Surface Science*, no. 86, pp. 134 - 139, 1995.
- [64] M.S. Dilorio, K.-Y. Yang, S. Yoshizumi, S.G. Haupt, D. Haran, R.H. Koch, F.P. Milliken, J.R. Rozen, D.K. Lathrop, S. Kumar and H.S. Trammell III, "Sensitive High-T_c SQUID Magnetometers for Unshielded Operation", *IEEE Transactions on Applied Superconductivity*, vol. 9, no. 2, pp. 4428-4431, 1999.
- [65] M.A. Espy, E.R. Flynn, R.H. Kraus Jr. and A.N. Matlashov, "Two methods for a first order hardware gradiometer using two HTS SQUIDs", *IEEE Transactions on Applied Superconductivity*, vol. 9, no. 2, pp. 3302-3305, June 1999.
- [66] M. Fardmanesh, J. Schubert, M. Banzet, W. Zander, Y. Zhang and H.J. Krause, "Effects of the step structure on the yield, operating temperature, and the noise in step-edge Josephson junction rf-SQUID magnetometers and gradiometers", *Physica C*, vol. 354, pp. 40-44, 2001.
- [67] M. Vaupel, G. Ockenfuss and R. Wördenweber, "Magnetic field behaviour of small sputtered step-edge junctions", *Applied Physics Letters*, vol. 68, no. 25, pp. 3623-3625, April 1996.
- [68] R.H. Koch, W. Eidelloth, B. Oh, R.P. Robertazzi, S.A. Andrek, and W.J. Gallagher, "Identifying the source of 1/f noise in SQUIDs made from high-temperature superconductors", *Applied Physics Letters*, vol. 60, pp. 507-509, 1992.
- [69] O. Dössel, B. Davids, M. Fuchs, W.H. Kullman, K.-M. Lüdeke, "A modular low noise 7-channel SQUID-magnetometer" *IEEE Transactions on Magnetics*, vol. 27, pp. 2797-2800, 1991.

- [70] J.M. Jaycox and M.B. Ketchen, "Planar Coupling Scheme for Ultra Low Noise dc SQUIDS", IEEE Transaction on Magnetics, vol. 17, pp. 400, 1981.
- [71] T. Mitzuka, K. Yamaguchi, S. Yoshikama, K. Hayashi and Y. Enomoto, "The Microstructure and I-V Characteristics of Step-Edge Josephson Junctions", Physica C, vol. 218, pp. 229-239, 1993.
- [72] C.P. Foley, S.Lam, B. Sankrithyan, Y. Wilson, J.C. Macfarlane and L. Hao, "The Effects of Step Angle on Step Edge Josephson Junctions on MgO", IEEE Transactions on Applied Superconductivity, vol 7, no. 2, pp. 3185-3188, 1997.
- [73] R. Pinto, S.P. Pai, C.P. Dsouza, L.C. Gupta, R. Vijayaraghaven, D. Kumar and M. Sharon, "Optimization of KrF laser ablation parameters for in-situ growth of $\text{YBa}_2\text{Cu}_3\text{O}_{7-\delta}$ thin films", Physica C, no. 196, pp. 264-270, 1992.
- [74] R.K. Singh and D. Bhattacharya, "Control of surface particle density in pulsed laser deposition of superconducting $\text{YBa}_2\text{Cu}_3\text{O}_7$ and diamondlike carbon thin films", Applied Physics Letters, no. 61, p. 483, 1992.
- [75] B. Holzapfel, B. Roas, L. Schultz, P. Bauer and G. Saemann-Ischenko, "Off-axis laser deposition of $\text{YBa}_2\text{Cu}_3\text{O}_7$ [delta] thin films", Applied Physics Letters, no. 61, p. 3178, 1992.
- [76] S.-G. Lee, D.-S. Hwang, Y.K. Park and J.-C. Park, "Deposition angle-dependent morphology of laser deposited $\text{YBa}_2\text{Cu}_3\text{O}_7$ thin films" Applied Physics Letters, no. 65, p. 764, 1994.
- [77] K. Kinoshita, H. Ishibashi and T. Kobayashi, "Improved Surface Smoothness of $\text{YBa}_2\text{Cu}_3\text{O}_{7-y}$ Films and Related Multilayers by ArF Excimer Laser Deposition with Shadow Mask Eclipse Method", Japanese Journal of Applied Physics, no. 33, p. L417, 1994.
- [78] D. Lubben, S.A. Bame, K. Suzulci, S. Gorbatkin and J.E. Green, "Laser-induced plasmas for primary ion deposition of epitaxial Ge and Si films", Journal of Vacuum Science and Technology B, no. 3, p. 968, 1985.
- [79] Y. Zhang, M. Mück, K. Herrmann, J. Schubert, W. Zander, A.I. Braginski and C. Heiden, "Low-noise $\text{YBa}_2\text{Cu}_3\text{O}_7$ rf SQUID magnetometer", Applied Physics Letters, no. 60, pp. 645, 1992.
- [80] F.-M. Kamm, A. Plettl and P. Ziemann, "Superconducting $\text{YBa}_2\text{Cu}_3\text{O}_{7-\delta}$ nanobridges prepared by a self-limiting wet chemical etching process", Superconducting Science and Technology, no. 11, pp. 1397-1400, 1998.
- [81] D. Grundler, R. Echart, B. David and O. Dössel, "Origin of 1/f noise in $\text{Y}_1\text{Ba}_2\text{Cu}_3\text{O}_{7-x}$ step-edge dc SQUIDS", Applied Physics Letters, no. 62, vol. 17, pp. 2134, April 1993.

- [82] Y. Zhang, W. Zander, J. Schubert, F. Rüdgers, H. Soltner, M. Banzet, N. Wolters, X.H. Zeng and A.I. Braginski, "Operation of high-sensitivity radio frequency superconducting quantum interference device magnetometers with superconducting coplanar resonators at 77 K", *Applied Physics Letters*, Vol. 71, no. 5, pp. 704, August 1997.
- [83] R. Weidl, S. Brabetz, F. Schmidl, F. Klemm, S. Wunderlich and P Seidel, "Heart monitoring with high-Tc dc SQUID gradiometers in an unshielded environment", *Superconducting Science and Technology*, vol. 10, pp. 95-99, February 1997.
- [84] J. Borgmann, G. Ockenfuss, R. Otto, J. Schubert, W. Zander, A. I. Braginski and P. David, "Compensation techniques for high-temperature superconducting quantum interference device gradiometers operating in unshielded environment", *Review of Scientific Instruments*, vol. 68, no. 8, pp. 2730-2734, 1997.
- [85] V. Schultze, R. Ijsselsteijn, V. Zakosarenko, F. Thrum, E. Il'ichev and H. -G. Meyer, "High Tc SQUIDs with two or three junctions for application in disturbed environment", *Applied Superconductivity*, vol. 5, pp. 221-225, August 1998.
- [86] E. Dantsker, S. Tanaka, and J. Clarke "High-Tc super conducting quantum interference devices with slots or holes: Low $1/f$ noise in ambient magnetic fields", *Applied Physics Letters*, vol. 70, pp. 2037-2039, April 1997.
- [87] R. IJsselsteijn, H. Elsner, W. Morgenroth, V. Schultze, and H.-G. Meyer, "Bicrystal submicrometer Josephson junctions and dc SQUIDs", *IEEE Transactions on Applied Superconductivity*, vol. 9, no. 2, pp. 3933-3936, June 1999.
- [88] K. Enpuku, H. Doi, G. Tokita and T. Maruo, "Modulation voltage of high Tc DC superconducting quantum interference device with damping resistance", *Japanese Journal of Applied Physics*, vol. 33, part 2, no. 5B, pp. L722-L725, 1994.
- [89] R. H. Koch, J.Z. Sun, V. Foglietta and W.J. Gallagher, "Flux dam, a method to reduce extra low frequency noise when a superconducting magnetometer is exposed to a magnetic field", *Applied Physics Letters*, vol. 67, no. 5, pp. 709-711, July 1995.
- [90] H. Schneidewind, F. Schmidl, S. Linzen and P. Seidel, "The possibilities and limitations of ion-beam etching of $\text{YBa}_2\text{Cu}_3\text{O}_{7-x}$ thin films and microbridges", *Physica C*, vol. 250, pp. 191-201, 1995.
- [91] S.F. Karmenenko, A. A. Semenov, I. A. Khrebtov, V. N. Leonov, T. H. Johansen, Y. M. Galperin, A. V. Bobyl, A. I. Dedoboretz, M. E. Gaevski, A. V. Lunev and R. A. Suris, "Fabrication process and noise properties of antenna coupled microbolometers based on superconducting YBCO films", *Superconducting Science and Technology*, vol. 13, pp. 273-286, 2000.

- [92] B. A. Davidson, J. E. Nordman, B. M. Hinaus, M. S. Rzchowski, K. Siangchaew and M. Libera, "Superconductor-normal-superconductor behaviour of Josephson junctions scribed in $Y_1Ba_2Cu_3O_{7-\delta}$ by a high brightness electron source", *Applied Physics Letters*, vol. 68, no. 26, pp. 3811, 1996.
- [93] R. Gross, P. Chaudhari, M. Kawasaki and A. Gupta, "Scaling behaviour in electrical transport across grain boundaries in $YBa_2Cu_3O_{7-\delta}$ superconductors", *Physical Review B*, vol. 42, no. 16, pp. 10735-10737, 1990.
- [94] T. Schmauder, A. Waldauf, H. Wald and P. Seidel, "Influence of target-substrate angle on properties of laser deposited $YBa_2Cu_3O_{7-\delta}$ thin films and step-edge Josephson junctions", *Physica C*, vol. 333, pp. 23-30, 2000.
- [95] T. Minotani, K. Enpuku and Y. Kuroki, "Effect of capacitive feedback on the characteristics of direct current superconducting quantum interference device coupled to a multturn input coil", *Journal of Applied Physics*, vol. 82, pp. 457-463, 1997.
- [96] M. Kawasaki, P. Chaudhari, T. H. Newman and A. Gupta, "Submicron $YBa_2Cu_3O_{7-\delta}$ grain boundary junction SQUIDs", *Applied Physics Letters*, vol. 58, no. 22, pp. 2555, 1991.
- [97] M.I. Faley, U. Poppe, K. Urban, D.N. Paulson, T.N. Starr and R.L. Fagaly, "HTS dc-SQUID flip-chip magnetometers and gradiometers", unpublished.
- [98] F. Dillmann, V.N. Glyantsev and M. Siegel, "Performance of $YBa_2Cu_3O_{7-\delta}$ direct current SQUIDs with high-resistance step-edge junctions", *Applied Physics Letters*, vol. 69, no. 13, pp. 1948, 1996.
- [99] V.N. Glyantsev, Y. Tavrín, W. Zander, J. Schubert and M. Siegel, "The stability of dc and rf SQUIDs in static ambient fields", *Superconducting Science and Technology*, vol. 9, pp. A105-A108, 1996.
- [100] N.I. Firsov, I.L. Novikov, R.F. Khusnutdinov and S.B. Kvasov, "The High- T_C Rf-SQUID Magnetometer with a Copper Flux Transformer", unpublished.
- [101] S-G. Lee, Y. Hwang, B-C. Nam, J.-T. Kim, Y.K. Park and G.Y. Sung, "Second-order dc SQUID gradiometer from single layer of high temperature superconducting film", *IEEE Transactions on Applied Superconductivity*, vol. 9, no. 2, pp. 3286-3289, June 1999.
- [102] K. Enpuku, T. Minotani, F. Shiraishi, A. Kandori and S. Kawakami, "High T_C dc SQUID Utilizing Bicrystal Junctions with 30 Degree Misorientation Angle", *IEEE Transactions on Applied Superconductivity*, vol. 9, no. 2, pp. 3109-3112, June 1999.
- [103] A.I. Braginski, K. Barthel, B. Chesca, Y. Greenberg, R. Kleiner, D. Koelle, Y. Zhang and X. Zeng, "Progress in Understanding of High-Transition-Temperature SQUIDs", *Physica C*, vol. 341-348, pp. 2555-2559, 2000.

- [104] T. Minotani, S. Kawakami, T. Kiss, Y. Kuroki and K. Enpuku, "High Performance DC superconducting Quantum Interference Device Utilizing a Bicrystal Junction with a 30° Misorientation Angle", *Japanese Journal of Applied Physics*, vol. 36, part 2, no. 8B, pp. L1092-1095, 1997.
- [105] T. Minotani, S. Kawakami, Y. Kuroki and K. Enpuku, "Properties of Josephson Junctions Fabricated on Bicrystal Substrate with Different Misorientation Angles", *Japanese Journal of Applied Physics*, vol. 37, part 2, no. 6B, 1998.
- [106] K. Barthel, D. Koelle, B. Chesca, A.I. Braginski, A. Marx, R. Gross and R. Kleiner, "Transfer function and thermal noise of $\text{YBa}_2\text{Cu}_3\text{O}_{7-\delta}$ direct current superconducting quantum interference device operating under large thermal fluctuations", *Applied Physics Letters*, Vol. 74, no. 15, pp. 2209, 1999.
- [107] Ya.S. Greenberg, V. Schultze and H.-G. Meyer, "Theory of the voltage-current characteristics of high T_C DC SQUIDs and its experimental verification", *Physica C*, vol. 368, pp. 236-240, 2002.
- [108] X. H. Zeng, Y. Zhang, B. Chesca, K. Barthel, Ya. S. Greenberg and A. I. Braginski, "Experimental study of amplitude-frequency characteristics of high-transition-temperature radio frequency devices", *Journal of Applied Physics*, vol. 88, no. 11, pp. 6781-6787, 2000.
- [109] Y. Zhang, N. Wolters, R. Otto and H.- J. Krause, "Non-constant bias current for dc SQUID operation", *Physica C*, vol 368, pp. 181-184, 2002.
- [110] J. -K. Heinsohn, D. Reimer, A. Richter, K. -O. Subke and M. Schilling, "Interaction of process parameters in the laser deposition of $\text{YBa}_2\text{Cu}_3\text{O}_7$ films", *Physica C*, vol. 299, pp. 99-112, 1998.
- [111] A. Eulenburg, E.J. Romans, Y.C. Fan and C.M. Pegrum, "Pulsed laser deposition of $\text{YBa}_2\text{Cu}_3\text{O}_{7-\delta}$ and $\text{NdBa}_2\text{Cu}_3\text{O}_{7-\delta}$ thin films: a comparative study", *Physica C*, vol. 312, pp. 91-104, 1999.
- [112] D. C. Montgomery, "Design and analysis of experiments", 5th edition, ISBN 0-471-31649-0, John Wiley & Sons, 2001.
- [113] Escete Single Crystal Technology B.V., Enschede, The Netherland, escete@eschete.com.
- [114] SPIP, The Scanning Probe Image Processor, version 2.3037, Image Metrology ApS, www.ImageMet.com.
- [115] Design-Expert, release 6.0.3, Stat-Ease, Inc. www.statease.com.
- [116] C. van Niekerk, "An Investigation into the Manufacture and Measurement of Superconducting Microwave Devices", M thesis, Electric and Electronic engineering, University of Stellenbosch, South Africa, 1995.

- [117] D. Wutte, S. Freedman, R. Gough, Y. Lee, M. Leitner, K.N. Leung, C. Lyneis, D.S. Pickard, M.D. Williams and Z.Q. Xie, "Development of an rf driven multicusp ion source for nuclear science experiments", *Nuclear Instruments and Methods in Physics Research B*, vol. 142, pp. 409-416, 1998.
- [118] K.N. Leung, D.A. Bachman, P.R. Herz and D.S. McDonald, "Rf driven multicusp ion source for pulsed or steady state ion beam production", *Nuclear Instruments and Methods in Physics Research B*, vol 74, pp. 291-294, 1993.
- [119] D. Boonyawan, P. Suanpoot and T. Vilaithong, "A 13.56 MHz multicusp ion source for gaseous ion-beam production", *Surface and Coatings Technology*, vol. 112, pp. 314-317, 1999.
- [120] H. Zaim and G.D. Alton, "Computational design studies for an ion extraction system for the oak ridge national laboratory ecr ion source", *Proceedings of the 2001 Particle Accelerator Conference*, Chicago.
- [121] Jülicher SQUID GmbH, The Jülich SQUID Company(JSQ), <http://www.jsquid.com>, Jülich, Germany.
- [122] Ya. S. Greenberg, "Determination of the parameters of High-Tc RF SQUID from its small signal voltage-frequency characteristics", *Journal of Low-Temperature Physics*, vol. 114, pp. 297-315, 1999.
- [123] B. Chesca, "Analytical theory of DC SQUIDS operating in the presence of thermal fluctuations", *Journal of Low Temperature Physics*, vol. 112, pp. 165-196, 1998.
- [124] B. Chesca, "Theory of RF SQUIDS operating in the presence of large thermal fluctuations", *Journal of Low Temperature Physics*, vol. 110, pp. 963-1001, 1998.
- [125] W.F. van Rooyen, "Cryostat Measurement System, Technical Manual", SED, University of Stellenbosch, Stellenbosch, South Africa, 2002.
- [126] JC Nability Lithography, Bozeman, USA, www.jcnability.com, private communication.
- [127] G. Taguchi and S. Konishi, "Orthogonal Arrays and Linear graphs", ASI Press, ISBN 0-941243-01-X, 1987.
- [128] E.J. Maritz, "A Study of Superconducting Three-Terminal Transistorlike Devices", M.Sc. Thesis, University of Stellenbosch, 1994.

Appendix A

PLD deposition instructions

A.1 Preperation Procedure for YBCO thin film Deposition

When working inside the PLD chamber wear gloves at all times !

1. Clean the substrate holder with acetone to remove all old silver paste.
2. Remove the target holder with the target.
3. Use sanding paper (120G) to sand YBCO surface until no indication of grooves remain. Finish with 180G and 500G sanding paper.
4. Then polish on diamond polish machine, until smooth.
5. Replace target holder.
6. Replace MgO substrate using silver paint to attach to substrate heater.
7. Replace heat shield and make sure substrate is centered in the opening.
8. Observe main O-ring gasket for dust particles or hair. If present remove using lintless cloth and acetone.
9. Replace lid and start roughing pump.
10. Open roughing pump side valve until pressure reaches 10-2 mbar. Close side valve.
11. If no pumping down required switch off roughing pump otherwise start pumping down procedure.

A.2 Deposition Procedure for YBCO thin film deposition

1. Note the vacuum pressure as the base pressure in the experiment sheet, this value should be below 10⁻⁵. Also note the pumping time on the experiment sheet.
2. Heat the substrate up to the desired temperature using the following procedure:
 - (a) Switch on the multimeters
 - (b) Check that the variac is set to 0
 - (c) Switch on the temperature controller
 - (d) Switch on the controller box next to the variac
 - (e) Adjust the variac until the voltage is around 60V
 - (f) The actual temperature depend on the voltage, this varies with the age of the bulb.
 - (g) DO NOT EXCEED 70V
3. Switch on the laser and measure the note the laser counter setting and your name in the laser logbook.
4. Measure the laser power between the laser and the mirror with the laser voltage set at 25KV.
 - (a) If the power is lower than 450mV reload the HCl gas following the reloading procedure published.
 - (b) After refilling measure the power again.
 - (c) This measurement should be noted in the experiment sheet as well as the laser logbook - also indicate whether the laser has been refilled or not.
5. Set the laser frequency to the value specified on the parameter sheet using the occilloscope to determine the frequency.
6. Measure the laser power between the mask and the lens of the PLD chamber. This value must be set to the value specified in the parameter set follow the procedure below:
 - (a) Read the required laser voltage from the value sheet.
 - (b) Adjust the laser voltage until the required voltage on the occilloscope is reached.
 - (c) Note the value on the experiment sheet.
7. Make sure the substrate is covered by the cover plate, switch on the stepper motor and do a pre-ablation run for 2 minutes. Note the pre-ablation time as well as the rotation speed on the experiment sheet.

8. Check that the temperature is stable at the desired value and note it on the experimental sheet.
9. Open the oxygen cylinder and adjust the pressure control that the pressure gauge shows 300kPa.
10. Open the oxygen valve and set the pressure to the value specified by the parameter set using the flow control valve.
11. Note the value on the experiment sheet.
12. Uncover the substrate by moving the cover plate.
13. CHECK the TARGET ROTATOR, the OXYGEN pressure and the SUBSTRATE TEMPERATURE. Check that all values pertaining to the deposition run are filled in on the experiment sheet.
14. Note the number on the laser pulse counter, add the number of shots to it.
15. Switch on the laser and watch the laser pulse counter, when the required number of shots is reached. Switch the laser off, now proceed with the post-annealing procedure

A.3 Post deposition annealing procedure.

1. Switch off the laser.
2. Switch off the target rotator.
3. Start lowering the temperature to 500°C by lowering the voltage to about 27V.
4. Close side and bottom valve. Switch off both turbo-pumps. Slowly open the roughing pump side valve, taking care not to overload the turbo-pumps. Wait 5 minutes.
5. Increase the Oxygen pressure to 1000mbar.
6. Increase the voltage until the temperature stabilises at 500°C.
7. Make sure the temperature is stable, let the system run at this setting for 1 hour.
8. Note the post deposition settings in the experiment sheet.
9. After the annealing time is over shut the heater off.
10. When the temperature reaches 30°C the sample can be removed.
11. Close main oxygen valve - wait until regulator pressure drops to zero, close the flow control valve on PLD chamber.
12. Open nitrogen main valve, open PLD chamber valve.

13. Switch off the roughing pump and close roughing pump side valve.
14. Wait until nitrogen starts escaping through lid gasket.
15. Close nitrogen main valve, wait until regulator pressure drops to zero. Close PLD nitrogen valve.
16. Put on gloves.
17. Remove lid, remove temperature shield from substrate holder.
18. Remove substrate carefully.
19. Attach number to back of substrate and put in correct place in numbered container.
20. Mark experiment as done on parameter sheet.
21. Make sure experiment sheet is completed and numbered.
22. File experiment sheet in correct envelope.

Appendix B

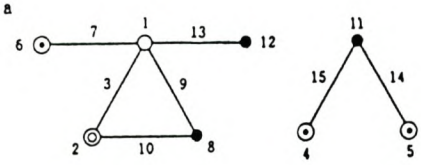
Taguchi method

The Taguchi method uses the linear graphs on page 197 together with the orthogonal array on page 198 to produce the DOE. The numbers on the nodes of the linear graphs correspond to the columns in the orthogonal array that gives the parameter levels. These graphs are taken from Taguchi et al [127].

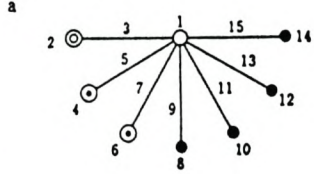
$L_{16} (2^{15})$ cont'd

$L_{16} (2^{15})$ cont'd

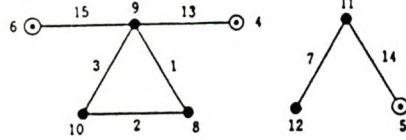
(3)



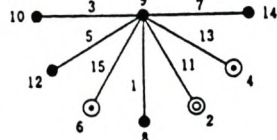
(4)



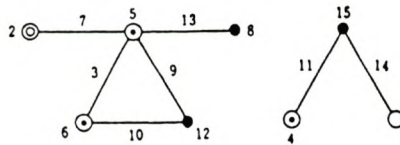
b



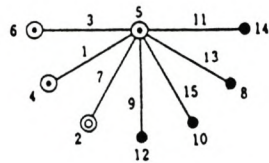
b



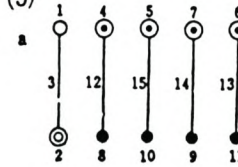
c



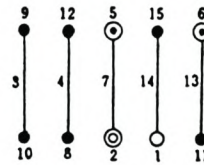
c



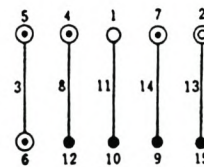
(5)



b

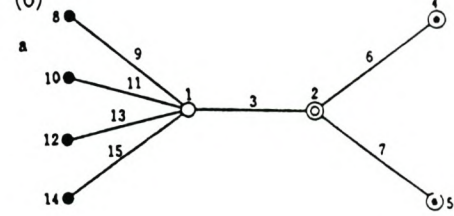


c

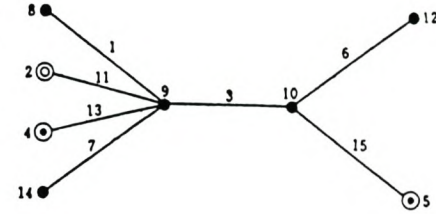


L 2ⁿ

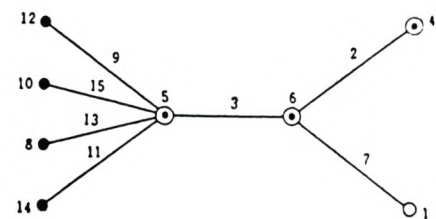
(6)



b



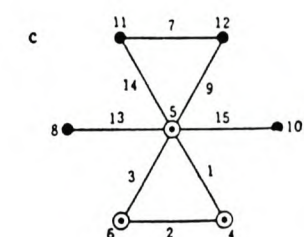
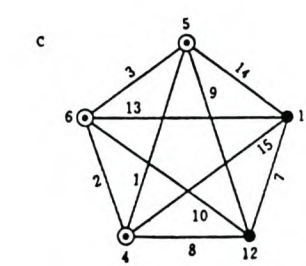
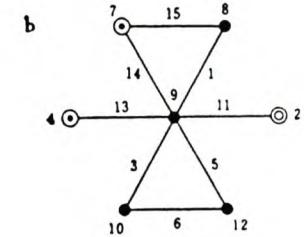
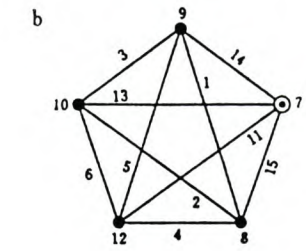
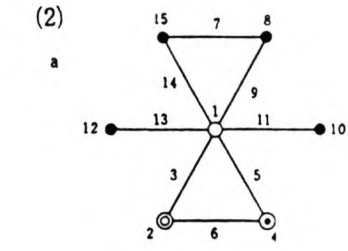
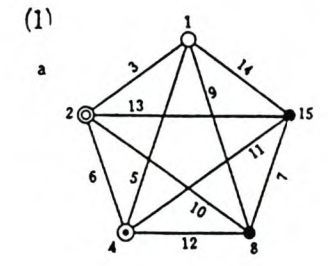
c



$L_{16} (2^{15})$

No.	1	2	3	4	5	6	7	8	9	10	11	12	13	14	15
1	1	1	1	1	1	1	1	1	1	1	1	1	1	1	1
2	1	1	1	1	1	1	1	2	2	2	2	2	2	2	2
3	1	1	1	2	2	2	2	1	1	1	1	2	2	2	2
4	1	1	1	2	2	2	2	2	2	2	2	1	1	1	1
5	1	2	2	1	1	2	2	1	1	2	2	1	1	2	2
6	1	2	2	1	1	2	2	2	2	1	1	2	2	1	1
7	1	2	2	2	2	1	1	1	1	2	2	2	2	1	1
8	1	2	2	2	2	1	1	2	2	1	1	1	1	2	2
9	2	1	2	1	2	1	2	1	2	1	2	1	2	1	2
10	2	1	2	1	2	1	2	2	1	2	1	2	1	2	1
11	2	1	2	2	1	2	1	1	2	1	2	2	1	2	1
12	2	1	2	2	1	2	1	2	1	2	1	1	2	1	2
13	2	2	1	1	2	2	1	1	2	2	1	1	2	2	1
14	2	2	1	1	2	2	1	2	1	1	2	2	1	1	2
15	2	2	1	2	1	1	2	1	2	2	1	2	1	2	1
16	2	2	1	2	1	1	2	2	1	1	2	1	2	2	1
	a	b	a	c	a	b	a	d	a	b	a	c	a	b	a
		b	b	c	c	c	b	d	d	d	b	d	c	d	b
							c				d				c
															d
Group	1	2	3	4											

Linear Graphs for $L_{16} (2^{15})$



$L_{16} (2^{15})$ Interactions Between Two Columns

	1	2	3	4	5	6	7	8	9	10	11	12	13	14	15
(1)	3	2	5	4	7	6	9	8	11	10	13	12	15	14	
(2)		1	6	7	4	5	10	11	8	9	14	15	12	13	
(3)			7	6	5	4	11	10	9	8	15	14	13	12	
(4)				1	2	3	12	13	14	15	8	9	10	11	
(5)					3	2	13	12	15	14	9	8	11	10	
(6)						1	14	15	12	13	10	11	8	9	
(7)							15	14	13	12	11	10	9	8	
(8)								1	2	3	4	5	6	7	
(9)									3	2	5	4	7	6	
(10)										1	6	7	4	5	
(11)											7	6	5	4	
(12)												1	2	3	
(13)													3	2	
(14)														1	

Appendix C

DOE for the PLD process

From the DOE of the PLD process the design table on page 200 was generated to give the parameter levels. The actual parameter values corresponding to these levels are shown on page 201, the run order is randomised for statistical purposes. The calculations of the amount of laser energy lost through the system and an estimation of the required number of shots to give a thin film of the required thickness is also shown. For each experiment an experiment sheet is completed recording all relevant information to double-check the accuracy of each experiment. An example experiment sheet is shown on page 202.

PLD Design of Experiment: Design Table

Experiment Number	Substrate Temperature	Laser Fluence	Oxygen Pressure	Target-Substrate Distance	Pulse Frequency	UV
17	0	0	0	0	0	0
10	1	1	-1	-1	1	-1
4	1	1	1	-1	-1	1
6	-1	1	1	-1	1	-1
14	-1	-1	-1	-1	1	-1
11	1	1	-1	1	-1	-1
3	1	-1	1	1	-1	-1
9	1	-1	-1	1	1	1
1	1	1	1	1	1	1
16	-1	1	-1	-1	-1	1
2	1	-1	1	-1	1	-1
7	-1	1	1	1	-1	-1
13	-1	1	-1	1	1	1
5	-1	-1	1	1	1	1
15	-1	-1	-1	1	-1	-1
12	1	-1	-1	-1	-1	1
8	-1	-1	1	-1	-1	1
18	0	0	0	0	0	0

Supplementary information for PLD DOE

Parameter value

Parameter	-1 value	+1 value	Center point
Substrate Temperature	720 °C	800 °C	760 °C
Laser Fluence	2.5 J/cm ²	3.5 J/cm ²	3 J/cm ²
Oxygen Pressure	0.05mbar	0.4mbar	0.225mbar
Target-Substrate distance	40 mm	60 mm	50 mm
Laser Frequency	4 Hz	10 Hz	7 Hz

Energy loss Calculations

Without lens	With lens	Energy difference (%)
0.21	0.15	40
0.24	0.18	29.12
0.27	0.2	34
		34.37

Required Laser voltage

Required Fluence	Laser Voltage (mV)
2.5 J/cm ²	159.63
3.5 J/cm ²	223.48
3 J/cm ²	191.56

Number of shots depend on the parameter set (use this table as a guide)

Laser Fluence (Lf)	Oxygen Pressure	Target-Substrate distance	Number of Shots
1	1	1	6000-9000
-1	1	1	8000-10000
1	-1	1	5000-8000
-1	-1	1	6000-9000
1	1	-1	4000-6000
-1	1	-1	5000-7000
1	-1	-1	2000-4000
-1	-1	-1	3000-5000

Results Sheet for YBCO deposition by PLD

EXPERIMENT NUMBER: 13

Preparation parameters

Target material	YBCO
Target preparation	polished and sanded.
Target density	7.4 g/cm ³
Target - Substrate distance	60 mm
Substrate material	MgO
Substrate finishing	opti polished.

Deposition parameters

Base pressure	3×10^{-6}	
Pumping time	3 hours	
Laser power (at laser)	450 mV	
HCl reloaded ? (Yes/No)	No	
Laser power (at laser after reload)	—	
Laser power (at lens)	215,4 mV	
Laser power (in chamber)	—	
Pulse frequency	10 Hz	
Laser fluence	3.5 J/cm ²	
Spot size	2,6 x 0,8	0.025 cm ²
Laser voltage	22 kV	
Pre-ablation time	1 min	
Rotation speed	6 s	
Temperature	720°C - 710°C	
Heater current	10,55 A 23,8 V	
UV - Radiation	on	
Oxygen pressure	5×10^{-2} mbar	
Deposition time	10 min	
Number of Shots	18000	

Post deposition

Laser power (after deposition)	212,5 mV
Annealing time	1 hour
Oxygen pressure	1 Atm
Temperature	650°C

Appendix D

DOE for the UV Lithography process

The design sheet and parameter values is shown below. The values were chosen from the datasheets for the various chemicals. The soft-bake type, whether a hotplate or forced air convection oven also used as a parameter. It is used to investigate the claim by Knox-Davies [26] that the hotplate produces superior results. The experiment is divided into two blocks. The idea is that each block should be completed on a single day with a fresh batch of developer used each day.

DOE for UV-Lithography

Design Sheet

Experiment nr.	Blocks	Bake type	Bake temp	Ekspose time	Develop time
2	1	-1	1	-1	1
4	1	-1	1	1	-1
1	1	1	-1	-1	1
3	1	1	-1	1	-1
8	2	1	1	1	1
6	2	1	1	-1	-1
5	2	-1	-1	-1	-1
7	2	-1	-1	1	1

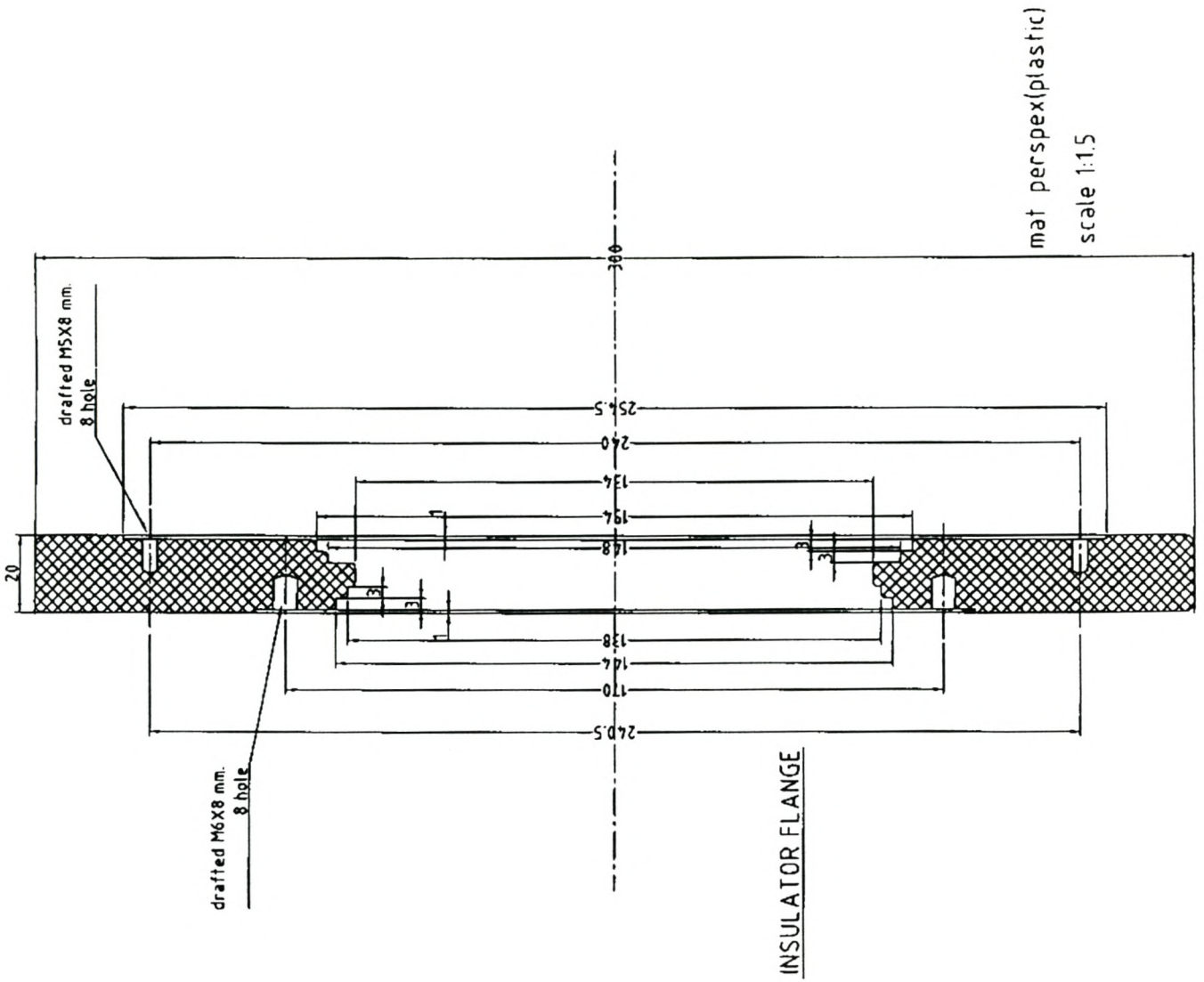
Parameter values

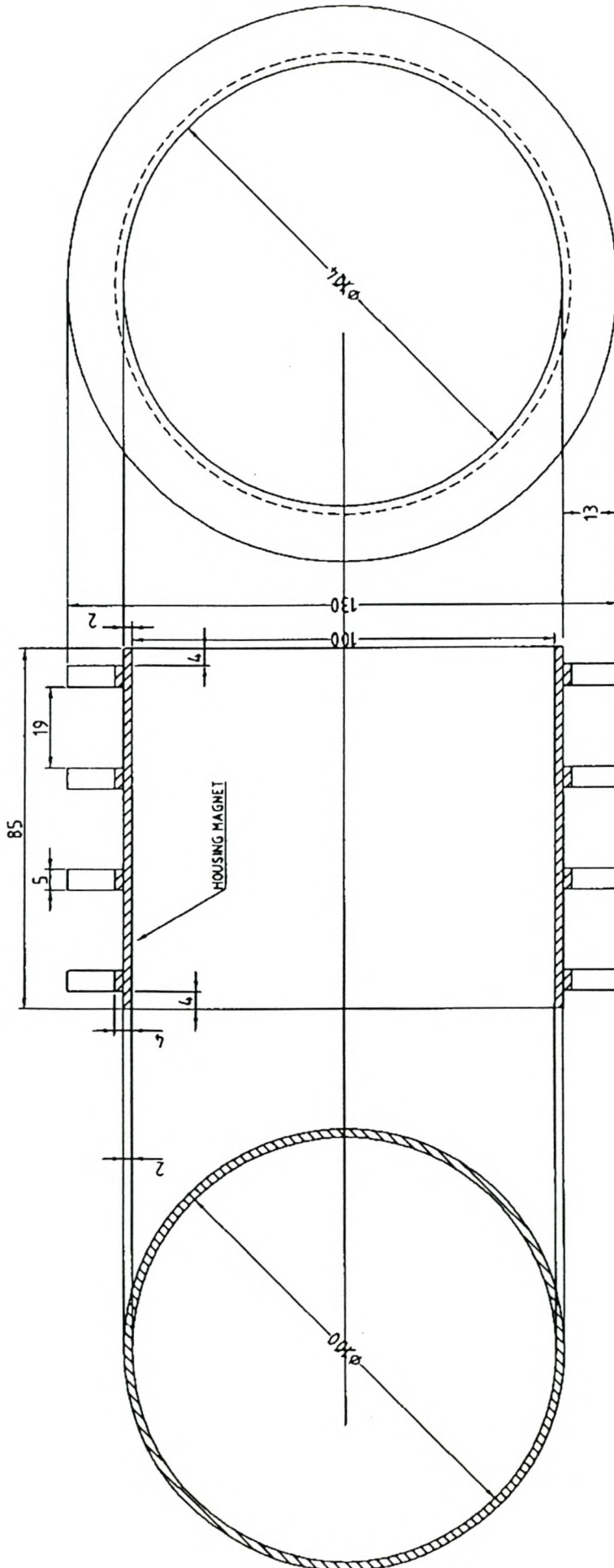
Parameter	-1 Value	+1 Value
Bake type	Hotplate	Oven
Bake temperature	90 °C	100 °C
Exposure time	20 s	40 s
Development time	45 s	60 s

Appendix E

Design of rf multicusp ion mill

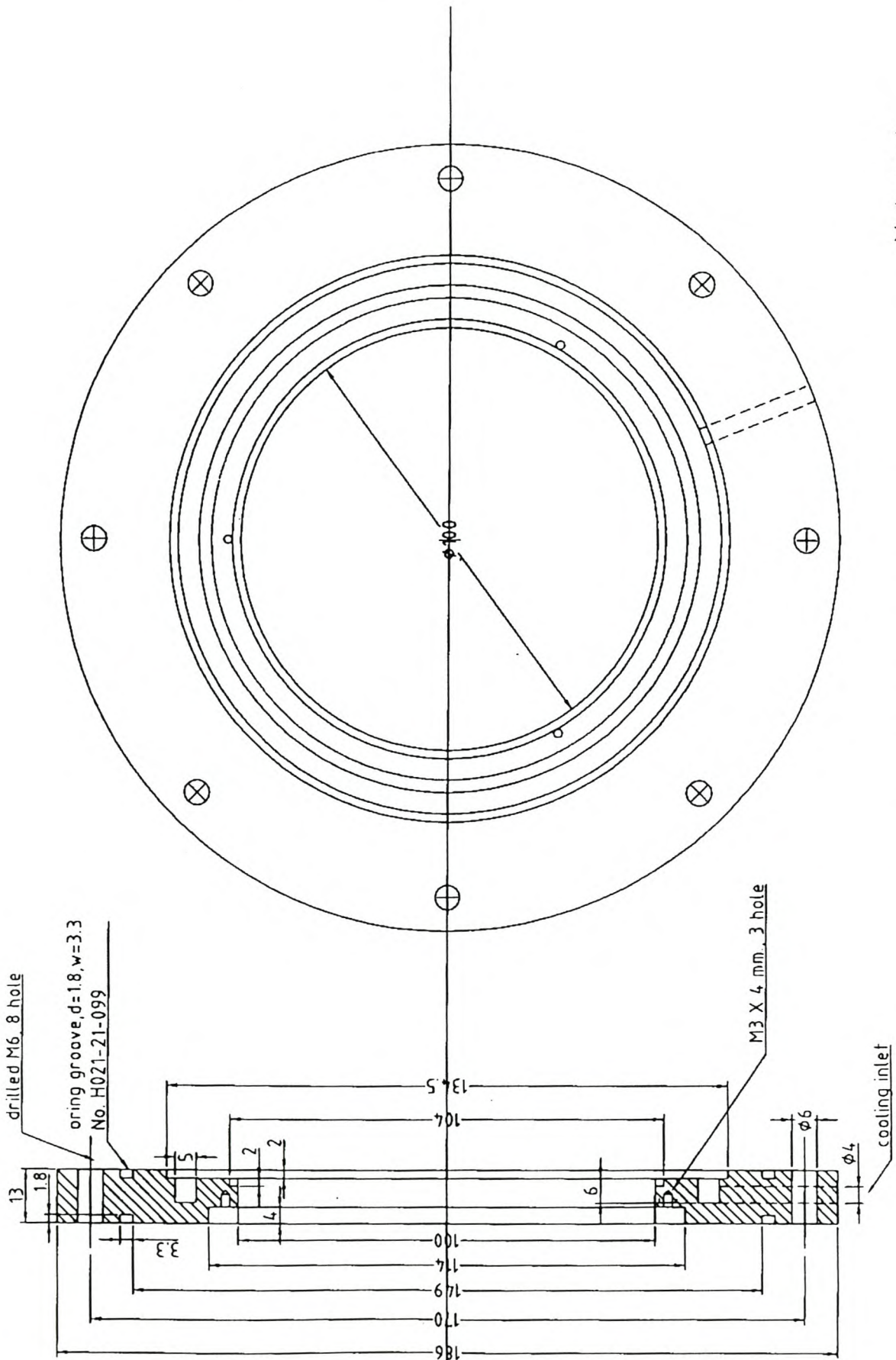
Over the next few pages the blueprint of the rf multicusp ion mill as designed by Boonyawan et al [119] will be given.





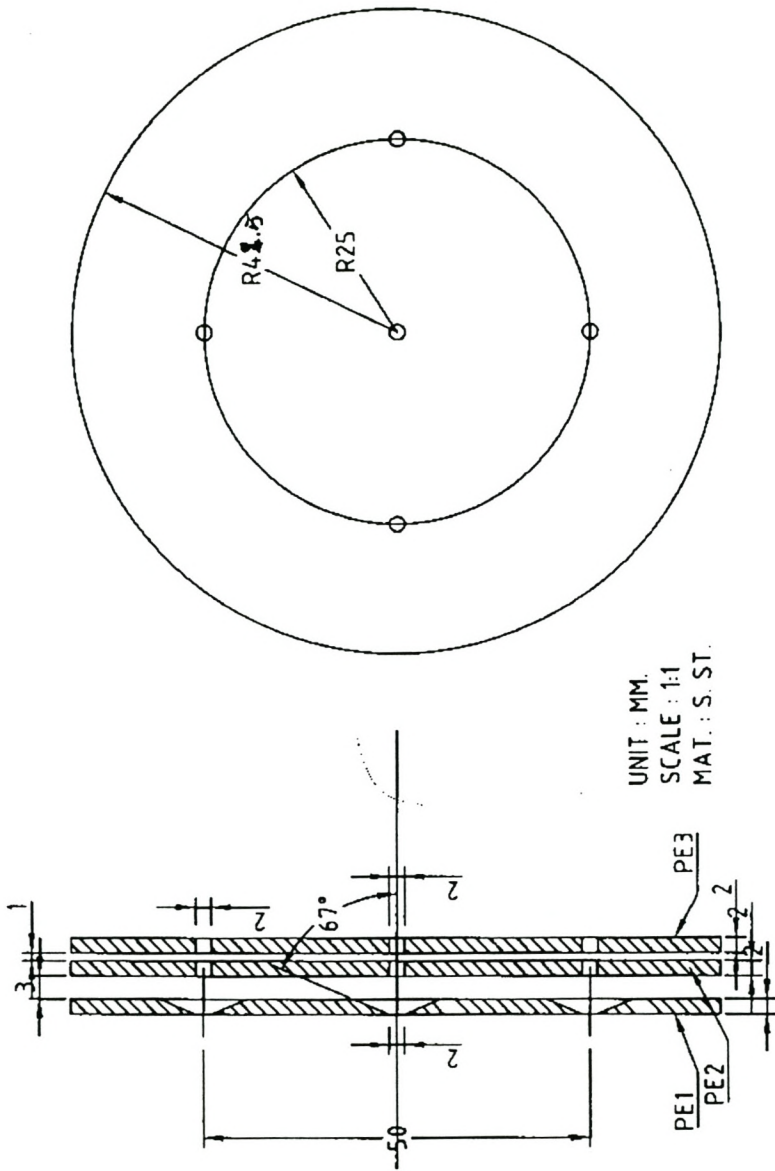
mat: s.st.
scale 1:1.5
unit: mm.

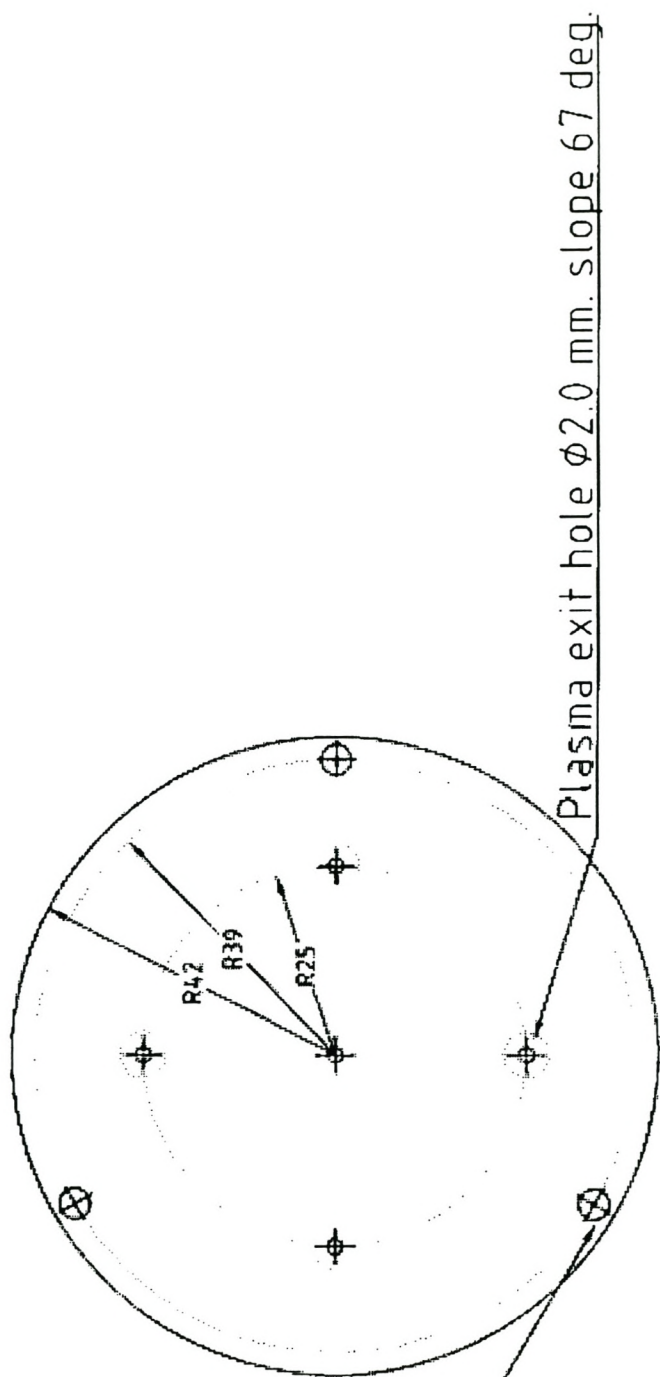
HOUSING MAGNET



Mat: s s t
scale 1:1.5

Plasma electrode mounting flange





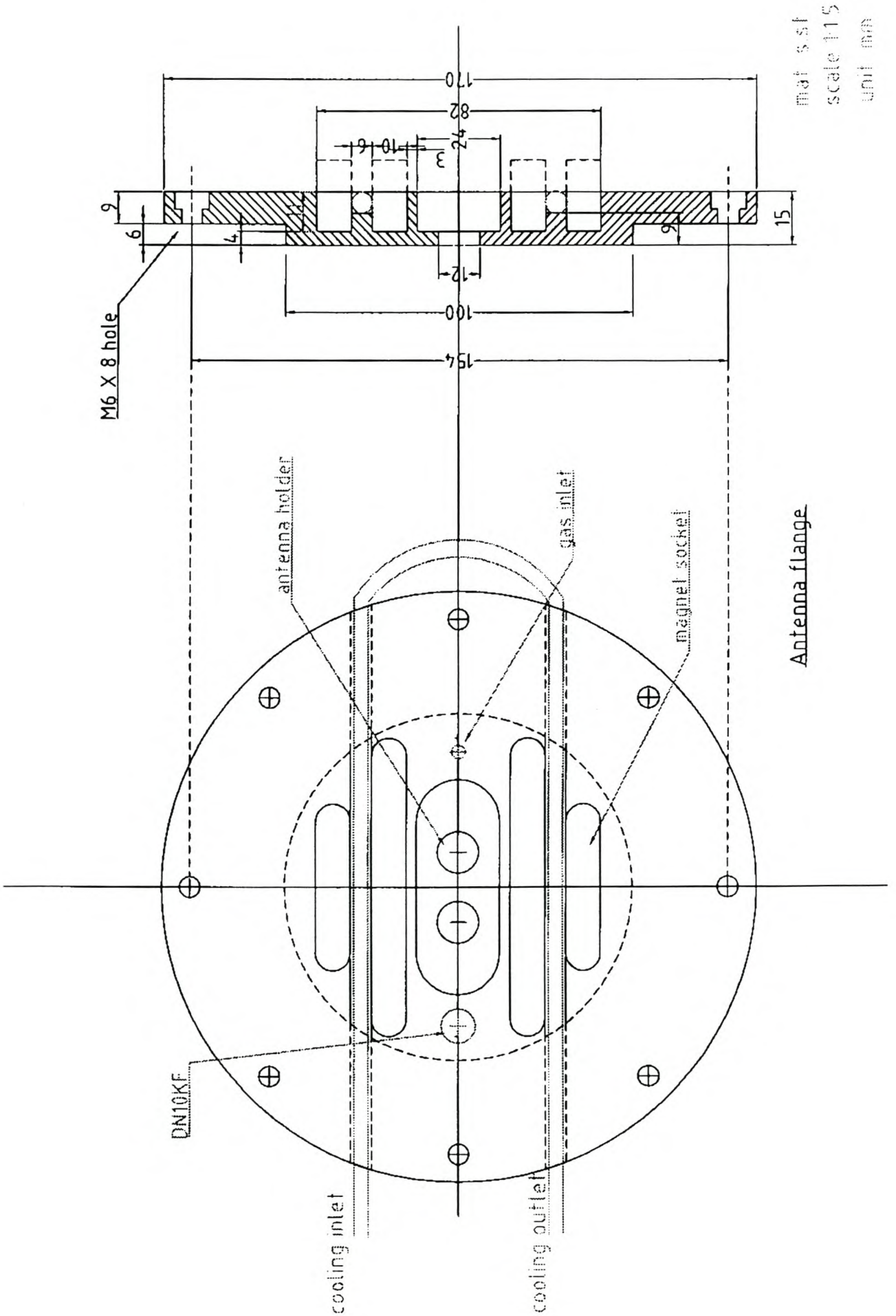
Mounting hole, M2 drill

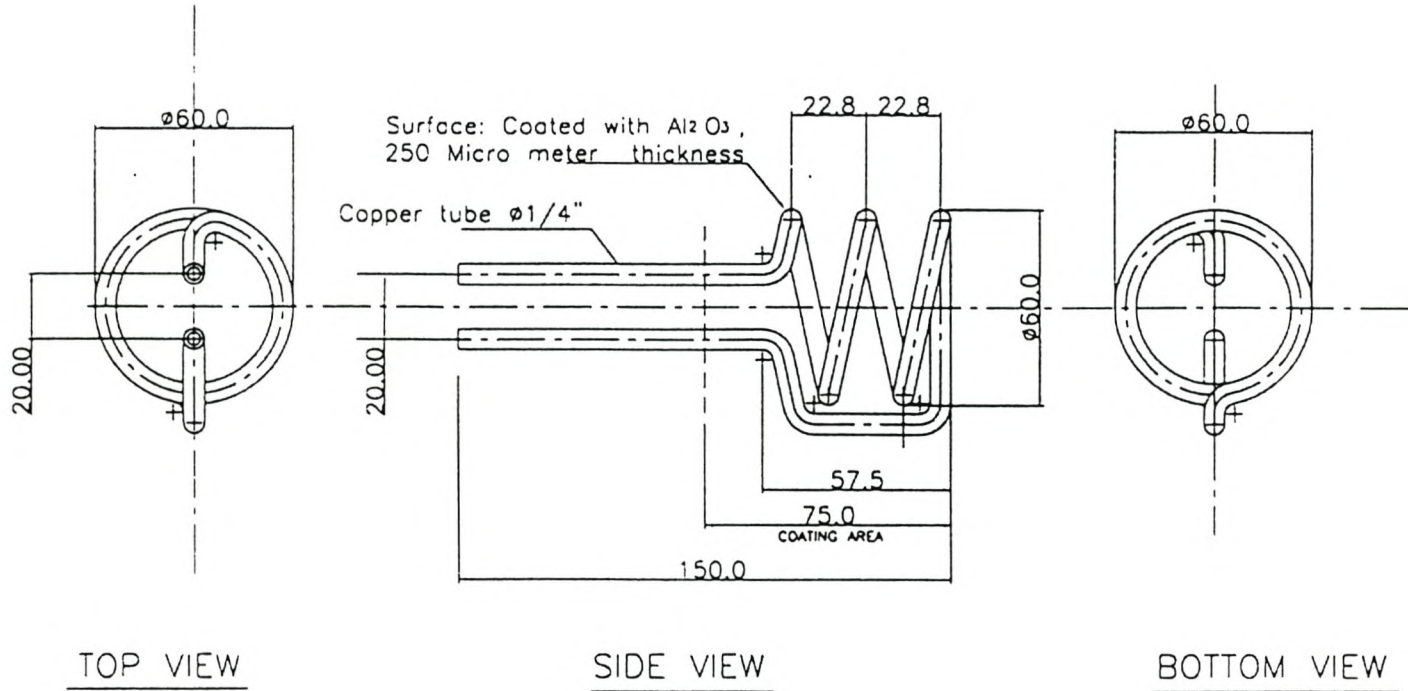
Plasma exit hole ϕ 2.0 mm, slope 67 deg.

Plasma electrode

unit : mm.

material : s. st. thickness 2.0 mm.





PART No.	PART NAME	MATERIAL	QUANTITY	REMARKS
UNLESS OTHERWISE SPECIFIED				
DIMENSIONS IN MM		SCALE 1:2	DRAWN BY Rachen	DATE 9/11/00
TOLERANCE	± 0.1	± 0.2	± 0.5	± 1.0
ANGULAR	R. 0.2000		DESIGN BY Dherawan	DATE
OTHER	ASSY NAME COPPER ANTENNA		APP'D BY	DATE
FILE LOCATION	ASSY USED ON		PROJECT	
FNRf		DESCRIPTION		DATE
Drawing Not Instrumentally Checked Not TOLERABLE		COPPER ANTENNA WITH Al ₂ O ₃ COATING		10/11/00

REVISIONS	CHANGE OR ADDITION	MADE BY	DATE	APP'D BY	DATE

